PANJAB UNIVERSITY
RESEARCH JOURNAL (SCIENCE)

VOL. 70 2020

PANJAB UNIVERSITY RESEARCH JOURNAL (SCIENCE)
VOLUME 70, 2020

Chief Patron :
Prof. Raj Kumar, Vice Chancellor, PU, Chandigarh

Editor-in-Chief :
Prof. Devinder Mehta, Department of Physics, PU, Chandigarh
Editor :
Prof. Jagtar Singh, Department of Bio-technology, PU, Chandigarh

Editorial Board:
Dr. A.K. Bhalla (Pediatrics), PGIMER, Chandigarh
Prof. Rajat Sandhir (Biochemistry), PU, Chandigarh
Prof. A.S. Ahluwalia (Botany), PU, Chandigarh
Prof. R.K. Wanchoo (UICET), PU, Chandigarh
Prof M.L. Garg (Biophysics), PU, Chandigarh
Prof. Kalpana K. Mahajan (Statistics), PU, Chandigarh
Prof. Jagdeep Kaur (Biotechnology), PU, Chandigarh
Prof. S.K. Mehta (Chemistry), PU, Chandigarh
Prof. Manjit Kaur (Physics), PU, Chandigarh
Prof. Karan Vasisht (UIPS), PU, Chandigarh
Prof. R.K. Singla (DCSA), PU, Chandigarh
Prof. Sanjay Chhibber (Microbiology), PU, Chandigarh

Advisory Board:
Dr. Krishan Lal, NPL, New Delhi.
Prof. A.K. Sood, Indian Institute of Science, Bangalore
Prof. R.K. Sinha, Director, CSIO, Chandigarh
Dr. Girish Sahni, Former Director General, CSIR, New Delhi
Prof. K.K.Mishra, Former Director, IGRMS, Bhopal
Prof. Y.K. Chawla, Former Director, PGIMER, Chandigarh.
Dr. Vishwa Mohan Katoch, Former Director General, ICMR, New Delhi.
Prof. A.K. Chakraborty, NIPER, Mohali
Sh. Ashwagosha Ganju, Former Director, SASE, Chandigarh.
Dr. Manjit Singh, Director, TBRL, Chandigarh
Dr. S.K. Shukla, Former Director, CFSL, Chandigarh
Dr. Rakesh Tuli, UIET, PU, Chandigarh

The subscription of the journal may be sent in the form of a Bank Draft payable to ***The Registrar*, *Panjab University, Chandigarh*** and addressed to The Editor-in-Chief on the following address:

Research Journal (Science)
Old Corresponding Building,
Panjab University, Chandigarh -160 014, (India)

The manuscripts for publication or any other enquiry is also to be addressed to the Editor-in-Chief

---

Subscription fee:

	Inland	Foreign
Annual Subscription	Rs.400/-	US$ 50
Life Membership	Rs. 3000/-	US$ 250

Printed in 2021

CONTENTS

Volume 70 (2020)

Pb. Univ. Res. J (Sci.) Vol. 70, 2020, pp 1-6

ELECTRON EMISSION AT LOW TURN-ON FIELDS FROM CNT/ZnO HYBRIDS

I. Sameera* **and Ravi Bhatia**

Department of Physics, Guru Jambheshwar University of Science & Technology, Hisar-125001, India.

ABSTRACT

Field emission of multiwall carbon nanotubes (MWCNTs) decorated with crystalline zinc oxide nanoparticles (ZnO NPs) was studied. MWCNT/ZnO NPs hybrid samples were synthesized by wet chemical route. ZnO NPs loading onto the surface of MWCNTs was tuned to form three different hybrid structures and their characterization using scanning electron microscopy is presented. Further, the field emission of the hybrid nanostructures indicates a shift in turn on field from 3.5 V/µm (bucky paper) to 1.0 V/µm by increasing the ZnO NPs:MWCNT ratio from 0.2 to 0.9, with an increase in enhancement factor from ~2000 to ~4900. Thus, the hybrid nanostructures exhibit enhanced field emission performance in comparison to bucky paper, with threshold fields as low as 1.4 V/µm and emission currents as high as 50µA/cm^2.

Keywords: Multiwall carbon nanotubes, Zinc oxide nanoparticles, Enhanced field emission

INTRODUCTION

Zinc oxide (ZnO), is one of the most promising semiconducting materials, due to its wide band gap (~3.37 eV) and large exciton binding energy (~60 meV). During the last decade, considerable amount research thrust has been dedicated to one dimensional (1D) nanostructures of ZnO, owing to their potential applications in lasers, solar cells, light emitting diodes, and nanogenerators (Huang *et al.*, 2001; Law *et al.*, 2005; Xu *et al.*, 2006; Wang *et al.*, 2006b). 1D nanostructures of ZnO are found to be ideal candidates for designing high quality field emission devices due their high aspect ratio, high thermal stability and high oxidation resistance. Field emission performance of various 1D nanostructures of ZnO such as nanowires, nanopencils, nanotubes, nanotetrapods, needle-like nanowires and nanowires grown on carbon cloth, have been studied by various research groups (Lee *et al.*, 2002; Tseng *et al.*, 2003; Li *et al.*, 2007; Ham *et al.*, 2005; Wang *et al.*, 2005, 2006a; Shen *et al.*, 2005; Gupta *et al.*, 2010; Zhu *et al.*, 2003; Li *et al.*, 2004; Jo *et al.*, 2004). Considerable progress has been made in proving the ZnO nanowires as the efficient field emitters, in terms of their stable emission behavior and resistance in harsh environment. A major hurdle with the field emission from ZnO nanostructures is their high turn-on field and low current density, which limits their field emission capa bilities. In view of this, hybrid structures of ZnO have received much attention, as they can provide the desired material properties that are not easily achievable with ZnO. For example, carbon nanotubes (CNT)-ZnO hybrid materials are found to exhibit excellent field emission as compared to ZnO nanostructures (Green *et al.*, 2006; Liu *et al.* , 2011). Pyramid like micro-patterns of CNT/ZnO heterostructures, CNT bundle arrays grown on vertically self-aligned ZnO nanorods, are fabricated and their field emission have been reported by different research groups (Yan *et al.*, 2008; Li *et al.*, 2007a). Liao *et al.* (2005) have reported the coating of amorphous carbon (a-C) and carbon nitride (CN$_x$) on ZnO nanowires results in better field emission performance than bare ZnO nanowires. Zheng et al. (2009) have reported the field emission of ZnO nanowires covered with graphene sheets and demonstrated a lowering in turn-on field from 2.5 V/µm to 1.3 V/µm after the coating. Furthermore, the heterostructures of ZnO with ZnS, GaN, Al_2O_3, Si and SiO_2 have also been synthesized for demonstrating various nanodevices (Bae *et al.*, 2004). However, the development of new heterostructures with controlled morphology still remains a challenging task. In the present work, synthesis, characterization and field emission of multiwall carbon nanotubes (MWCNTs) coated with ZnO nanoparticles (NPs) are studied.

EXPERIMENTAL

MWCNTs were grown by chemical vapor deposition of toluene and ferrocene mixture, and the details of the synthesis are presented elsewhere (Sameera *et al.*, 2013). MWCNTs were chemically functionalized by sonicating with concentrated nitric acid in order to activate the inert surface of MWCNTs. This treatment is used to produce carboxyl and hydroxyl groups on the surface of MWCNTs (Hiura *et al.*, 1995; Ebbesen *et al.,* 1996). The resulting suspension of MWCNTs

---

* Corresponding Author: sameeraivaturi@gmail.com (I. Sameera)

MS Received: August 9, 2020, Accepted: September 10, 2020

was washed with de-ionized water several times and dried in oven at 100 °C. About 5 mg of acid treated MWCNTs were dispersed in methanol by sonication. Then required amount of zinc acetate solution (0.001 M) was added to MWCNTs suspension. Sodium hydroxide solution (0.015 M) was then added drop wise and sonicated for two hours. The final product was obtained after centrifuging and washing with de-ionized water several times, so as to remove the byproducts formed in the reaction and dried in oven. The overall composition of the hybrid can be conveniently controlled by varying ratio of the components in the liquid phase, i.e., by varying the NPs concentration and keeping the MWCNTs concentration constant. We have prepared three different samples by weight ratio of ZnO NPs: MWCNTs as 0.2:1, 0.5:1, 0.9:1 and these are labelled as sample *A*, sample *B*, and sample *C*, respectively. FEI SIRION scanning electron microscope (SEM) with energy dispersive X-ray analysis (EDAX) facility was used for studying the morphology of hybrid structures.

RESULTS AND DISCUSSION

Figures 1(a)-(c) represent the SEM micrographs of MWCNT/ZnO NPs hybrid with increasing ZnO NPs content. The coating of ZnO NPs on to the surface of MWCNTs, and increase in nanoparticle loading can be clearly observed from the SEM micrographs. The average diameter of ZnO NPs ranges from 7-10 nm. The EDAX of sample *C* (shown in figure 1(d)), provides the elemental information, indicating the presence of Zn and O in the sample. Further, Fe and C peaks arise from the MWCNT. Furthermore, the crystallinity of the sample studied using X-ray diffraction (XRD) and was reported elsewhere (Sameera *et al.*, 2010).

The field emission measurements on the MWCNT/ZnO NP hybrid were carried out by casting the three samples on Si substrate. The field emission J-E characteristics are shown in figure 2(a). The results are compared with that of bucky paper. It can be observed that the field emission from the bucky paper can be improved by anchoring ZnO NPs on the surface of MWCNT. A shift in turn-on field (at 1 μA/cm^2) from 3.5 V/μm (bucky paper) to 1.0 V/μm by increasing the ZnO NPs content is observed.

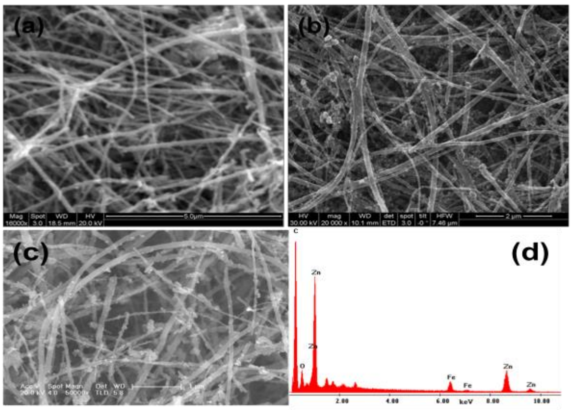

Fig. 1: SEM micrographs of MWCNT/ZnO NPs hybrid (a) sample *A*, (b) sample *B*, and (c) sample *C*, (d) EDAX of sample *C*.

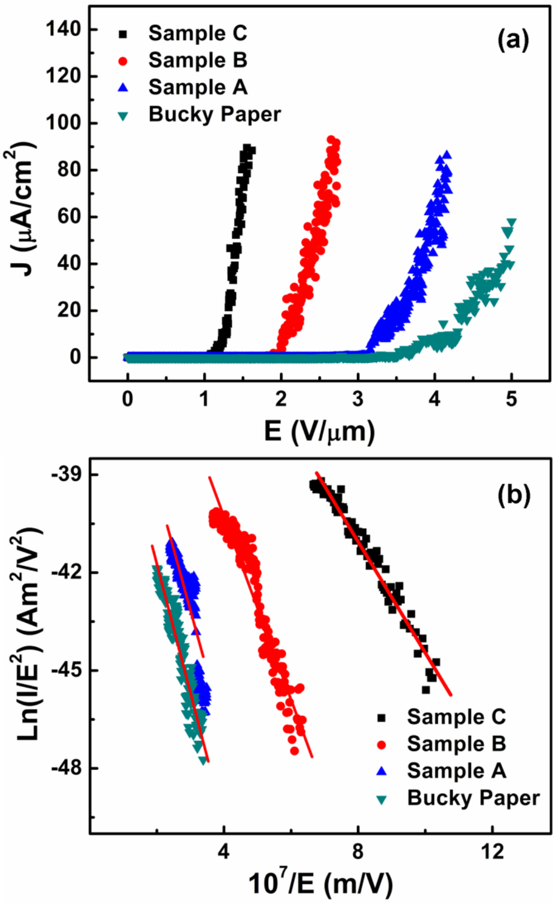

Fig. 2: (a) A comparison of field emission J-E characteristics of MWCNT/ZnO hybrids with bucky paper, and (b) corresponding FN plots.

The emission current-voltage characteristics are analyzed by Fowler-Nordheim (FN) equation for the field emission,

$$\ln(I/E^2) = \ln(A\alpha\beta^2/\varphi) - B\varphi^{3/2}/\beta E \qquad (1)$$

where, I is the emission current, A=1.56 x 10^{-6} AeV/ V^2, B=6.83 x 10^9 V/e$V^{3/2}$ m, β is a field enhancement factor, φ is the work function, α is effective emission area, E=V/d is the applied field, d is the distance between the anode and the cathode, and V is the applied voltage. Here, the effective field enhancement factor β is calculated from slope of the FN plot by taking the work function of ZnO as 5.3 eV (Li *et al.*, 2007a). The enhancement factor for bucky paper is ~2000, whereas for MWCNT-ZnO NPs hybrid the enhancement increases with ZnO NP loading and is maximum for sample *C* (β ~4900). The values of turn-on field, threshold field (50 µA/cm^2) and enhancement factor are listed in Table 1 for comparison.

Table. 1: A comparison of field emission parameters of MWCNT/ZnO NPs hybrid with bucky paper.

Sample name	Turn on field (1 µA/cm^2)	Threshold field (50 µA/cm^2)	Enhancement factor
Sample *C*	1.1	1.4	4900
Sample *B*	1.9	2.4	3000
Sample *A*	3.2	3.9	2200
Bucky paper	3.5	4.9	1900

In general, a significant increase in field enhancement factor is strongly attributed to the geometrical parameters of a field emitter. In our case, the ZnO NPs in the hybrid can act as emission sites, because of their small size and spherical shape, leading to an enhanced local field at the surface of MWCNT. As the NPs content increases, the number of emission sites increases, and hence the decrease in turn-on field and increase in enhancement factor observed with a ZnO NPs loading. It is very interesting to compare the field emission of hybrid nanostructures with that of ZnO nanowires reported in literature (Liao *et al*., 2005; Zhend *et al*., 2009). Table 2. represents a comparison of field emission results of MWCNT-ZnO NPs hybrid with various other hybrid nanostructures as well as with ZnO nanowires. The turn-on field for bare ZnO nanostructures is reported to be in the range 6-18 V/µm with higher threshold fields; some of the ZnO samples are unable to produce sufficient current density (see Table 2), while the turn-on fields and threshold fields for MWCNT/ZnO NPs hybrid lie in the range 1.1-3.2 and 1.4-3.9 V/µm, respectively. In general, ZnO nanowires possess high resistance, and lacks effective back contact from the electrode, which increases the turn-on field and limits the current density. The hybrid morphology provides highly conducting MWCNTs as effective back electrode for ZnO NPs and enhances the field emission performance significantly.

Table 2: Comparison of field emission results of MWCNT/ZnO hybrid with similar studies in the literature.

Sample	Ref.	Turn-on field (V/µm)	Threshold field (V/µm) (at 1 mA/cm^2)
CNT/ZnO pyramid like patterns	Yan *et al.* (2008)	1.8 V/µm (10µA/cm^2)	2.7
Carbon nanotube bundle arrays grown on self-aligned ZnO nanorods	Li *et al.* (2007a)	1.5 V/µm (0.1µA/cm^2)	4.5
Composite of graphene sheets and ZnO nanowires	Zheng *et al.* (2009)	1.3 (1 µA/cm^2)	2.5
Vertically well-aligned zinc oxide nanowires	Lee *et al.* (2002)	6.0 (0.1 µA/cm^2)	11
Needle like ZnO nanowires	Tseng *et al.* (2003)	18 (0.01 µA/cm^2)	24 (0.1 mA/cm^2)
ZnO nanowire arrays	Li *et al.* (2007b)	7.4 (1 µA/cm^2)	13
Vertically well-aligned zinc oxide nanowires	Ham *et al.* (2005)	6.2 (0.1 µA/cm^2)	15
MWCNT/ZnO NPs hybrid (Sample *C*)	Present work	1.1 (1 µA/cm^2)	1.4 (50 µA/cm^2)

Under the action of electric field, the MWCNT bucky paper acts as effective back contact and facilitate the electron emission from the hybrid structure. So, the hybrid morphology lowers the turn-on field by lowering the barrier for emitting electrons and then collects the electrons from all over the surface of the bucky paper, and enhances current density. Although, in the present study hybrid nanostructures are not aligned and patterned unlike as shown in the other works available in the literature, they exhibit similar competitive behavior in terms of the turn-on and threshold fields.

SUMMARY

Field emission study of MWCNT/ZnO NPs hybrids indicate, the emission from the bucky paper can be improved by anchoring ZnO NPs on the surface of MWCNT. A shift in turn-on field from 3.5 V/µm (bucky paper) to 1.0 V/µm by increasing the ZnO NPs content is observed, with increase in enhancement factor from ~1900 to 4900. Thus, the hybrid nanostructures exhibit enhanced field emission performance with threshold fields as low as 1.4 V/µm with emission currents as high as 50µA/cm^2, in comparison to bucky paper and the other hybrid nanostructures reported in the literature.

REFERENCES

Bae S.Y., H.W. Seo, H.C. Choi, J. Park, and J. Park, 2004. Heterostructures of ZnO Nanorods with Various One-Dimensional Nanostructures, J. Phys. Chem. B 108, 12318.

Ebbesen T.W., 1996. Wetting, filling and decorating carbon nanotubes, J. Phys. Chem Solids 57, 951.

Green J.M., L. Dong, T. Gutu, J. Jiao, 2006. ZnO-nanoparticle-coated carbon nanotubes demonstrating enhanced electron field-emission properties, J. Appl. Phys. 99, 094308.

Gupta B.K., D. Haranath, S. Chawla, H. Chander, V.N. Singh, and V. Shanker, 2010. Self-catalytic synthesis, structure and properties of ultra-fine luminescent ZnO nanostructures for field emission applications, Nanotechnology 21, 225709.

Ham H., G. Shen, J.H. Cho, T.J. Lee, S.H. Seo, and C. J. Lee, 2005. Vertically aligned ZnO nanowires produced by a catalyst-free thermal evaporation method and their field emission properties, Chem. Phys. Lett. 404, 69.

Hiura H., T.W. Ebbesen, and K. Tanigaki, 1995. Opening and purification of carbon nanotubes in high yields, Adv**.** Mater**.** 7, 275.

Huang M.H., S. Mao, H. Feick, H. Yan, Y. Wu, H. Kind, E. Weber, R. Russo, and P. Yang, 2001. Room-Temperature Ultraviolet Nanowire Nanolasers, Science 292, 1897.

Jo S.H., D. Banerjee, and Z.F. Ren, 2004. Field emission of zinc oxide nanowires grown on carbon cloth, Appl. Phys. Lett. 85, 1407.

Law M., L.E. Greene, J.C. Johnson, R. Saykally, and P. Yang, 2005. Nanowire dye-sensitized solar cells, Nat. Mater. 4, 455.

Lee C.J., T.J. Lee, S.C. Lyu, and Y. Zhang, H. Ruh, and H. J. Lee, 2002. Field emission from well-aligned zinc oxide nanowires grown at low temperature, Appl. Phys. Lett. 81, 3648.

Li Y.B., Y. Bando, and D. Golberg, 2004. ZnO nanoneedles with tip surface perturbations: Excellent field emitters, Appl. Phys. Lett. 84, 3603.

Li C., G. Fang, L. Yuan, N. Liu, L. Ai, Q. Xiang, D. Zhao, C. Pan, and X. Zhao, 2007a. Field emission from carbon nanotube bundle arrays grown on self-aligned ZnO nanorods, Nanotechnology 18, 155702.

Li M.K., D.Z. Wang, Y.W. Ding, X.Y. Guo, S. Ding, and H. Jin, 2007b. Morphology and field emission from ZnO nanowire arrays synthesized at different temperature, Mater. Sci. Eng. A 452, 417.

Liao L., J.C. Li, D.F. Wang, C. Liu, C.S. Liu, Q. Fu, and L.X. Fan, 2005. Field emission property improvement of ZnO nanowires coated with amorphous carbon and carbon nitride films, Nanotechnology 16, 985.

Liu N., G. Fang, W. Zeng, H. Long, and X. Zhao, 2011. Giant Enhancement of Field Emission from Selectively Edge Grown ZnO–Carbon Nanotube Heterostructure Arrays via Diminishing the Screen Effect, J. Phys. Chem. C 115, 14377.

Sameera I., R. Bhatia, and V. Prasad, 2010. Preparation, characterization and electrical conductivity studies of MWCNT/ZnO nanoparticles hybrid, Physica B 405, 1709.

Sameera I., Bhatia Ravi, and V. Prasad, 2013. Characterization and magnetic response of multiwall carbon nanotubes filled with iron nanoparticles of different aspect ratios, Physica E 52, 1.

Shen X.P., A.H. Yuan, Y.M. Hu, Y. Jiang, Z. Xu, and Z. Hu, 2005. Fabrication, characterization and field emission properties of large-scale uniform ZnO nanotube arrays, Nanotechnology 16, 2039.

Tseng Y.K., C.J. Huang, H.M. Cheng, I.N. Lin, K.S. Liu, and I.C. Chen, 2003. Characterization and Field-Emission Properties of Needle-like Zinc Oxide Nanowires Grown Vertically on Conductive Zinc Oxide Films, Adv. Funct. Mater. 13, 811.

Wang R.C., C.P. Liu, J.L. Huang, and S.J. Chen, 2006a. Growth and field-emission properties of single-crystalline conic ZnO nanotubes, Nanotechnology 17, 753.

Wang Z.L. and J. Song, 2006b. Piezoelectric Nanogenerators based on Zinc Oxide Nanowire Arrays, Science 312, 242.

Wang R.C., C.P. Liu, J.L. Huang, S.J. Chen, Y.K. Tseng, and S.C. Kung, 2005. ZnO nanopencils: Efficient field emitters, Appl. Phys. Lett. 87, 013110.

Xu W.Z., Z.Z. Ye, Y.J. Zeng, L.P. Zhu, B.H. Zhao, L. Jiang, J.G. Lu, H.P. He, and S.B. Zhang, 2006. ZnO light-emitting diode grown by plasma-assisted metal organic chemical vapor deposition, Appl. Phys. Lett. 88, 173506.

Yan X., B.K. Tay, and P. Miele, 2008. Field emission from ordered carbon nanotube-ZnO heterojunction arrays, Carbon 46, 753.

Zheng W.T., Y.M. Ho, H.W. Tian, M. Wen, J.L. Qi, and Y.A. Li, 2009. Field Emission from a Composite of Graphene Sheets and ZnO Nanowires, J. Phys. Chem. C 113, 9164.

Zhu Y.W., H.Z. Zhang, X.C. Sun, S.Q. Feng, J. Xu, Q. Zhao, B. Xiang, R.M. Wang, and D.P. Yu, 2003. Efficient field emission from ZnO nanoneedle arrays, Appl. Phys. Lett. 83, 144.

Pb. Univ. Res. J (Sci.) Vol. 70, 2020, pp 7-12

INFORMATION THEORETIC CONCEPTS OF MODIFIED HYLLERAASPLUS EXPONENTIAL ROSEN MORSE POTENTIAL

Aarti Sharma* **and Anil Kumar**†‡
*Department of Physics, SGGS Khalsa College, Mahilpur-146 105, Punjab, India.
†Department of Physics, JC DAV College, Dasuya-144 205, Punjab, India

ABSTRACT

The information theoretic concepts are influential in the study of quantum mechanical systems. In this paper, the information entropy of modified Hylleraas plus exponential Rosen Morse potential is analyzed in position and momentum space as a function of Hylleraas parameters and distance from equilibrium position. The information density in position and momentum space is graphically demonstrated for different states. The entropy densities have asymmetric shape which depends on the values of quantum numbers. The information entropy is numerically obtained for distinct levels of the potential and Bialynicki-Birula and Mycielski inequality is tested for various states using different parameters of the potential.

Keywords: Hylleraas plus exponential, Rosen Morse potential, Information density and entropy.

INTRODUCTION

In recent times, there has been increasing interest in the studies on information theoretic measures for quantum mechanical systems. The concepts of information theory have been utilized to study its applications in chemical science, biology, nuclear physics, solid state physics, statistical physics, computer science and mathematical physics (Preston & Bhaduri, 1975; Greiner, 2000; Kim, 2017). The information entropy has a versatile framework to study unpredictability and uncertainty. It measure the information content present in a system. The probability densities ρ(r) in position space and ρ(p) in momentum space are used as input to information entropy. The information entropy in position and momentum space respectively, of the single particle distribution is given by

$$S_{pos} = -\int \rho(r) \ln \rho(r)\, dr \quad (1)$$

$$S_{mom} = -\int \rho(r) \ln \rho(r)\, dr \quad (2)$$

The information entropies in position space and momentum space, for various systems like ultracold trapped interacting bosons (Haldar *et al.*, 2013), modified Tietz-Hua potential (Onate *et al.*, 2018), the position depen- dent mass Schr¨odinger equation (Falaye *et al.*, 2016), conditionally exactly solvable potential (Dutta & Roy, 2011), Rydberg-like harmonic states (Dehesa *et al.*, 2017), the Morse potential (Aydiner *et al.*, 2008), isospectral potential (Kumar, 2005; Pooja, 2020), Dirac-Delta-like potentials (Bouvrie *et al.*, 2011), the Po¨schl-Teller potential (Atre *et al.*, 2004), spherical confined hydrogen atom (Jiao *et al.*, 2017), the static screened coulomb potential (Isonguyo *et al.*, 2018), the harmonic oscillator potential (Yan´ez *et al.*, 1994), infinite circular potential well (Song *et al.*, 2015), squared tangent potential well (Dong *et al.*, 2014), the Kratzer potential (Yahya *et al.*, 2014), the hyperbolic double-well potential (Sun *et al.*, 2015), the hyperbolic potential function (Valencia-Torres *et al.*, 2015), Mobius square potential (Ikot *et al.*, 2020a), exponential-type potential (Ikot *et al.*, 2020b) and parity-restricted harmonic oscillator (Shi *et al.*, 2017) have been recently studied.

Quantum information entropy measure the uncertainty associated with a random variable which is related to the degree of localization-delocalization. It has been analyzed for some confined systems such as atoms and ions in hard spherical boxes where the information entropy has local maxima and minima as a function of confinement radius (Aquinoa *et al.*, 2013). The spreading of the quantum mechanical probability cloud for mass Schro¨dinger equation submitting solitonic profile with a squared hyperbolic cosecant potential is studied in reference (Serrano *et al.*, 2016). The information theoretic measures have capability to unveil the hidden structure of the chemical reactions through phenomenological concepts revealing the asynchronous or synchronous behaviour of the reactions. These measures are also employed to describe a three center chemical reaction detecting the transition state and stationary points which study the bond forming and bond breaking regions (Esquivel *et al.*, 2010a, 2010b).

The information entropies, in position space and momentum space, connect information theory and quantum mechanics. The Position-momentum uncertainty relations have been found for many important quantum systems. The entropic relation was investigated by Hirschman (1957) and Everett (1973) in the many worlds interpretation context considering position and momentum observables and later proved by Bialynicki-Birula and Mycielski (1975). It plays an important role in numerous fields and has now become a universal concept in classical statistical physics. It states that for wave functions normalized to unity, in a d-dimensional system

---

‡ Corresponding author: anilkumarphys@gmail.com
MS Received: November 6, 2020, Accepted: December 20, 2020

$$S_{pos} + S_{mom} \geq d(1 + \ln \pi) \tag{3}$$

The decrease in information entropy in position space is related to increase in information entropy momentum space and vice-versa. A general formulation of information theoretic uncertainty relations, for the different conjugate pair of observables, is described which works for all the systems and dimensions (Werner, 2016). The analytical results of position space and momentum space information entropy are quite difficult and have been obtained only for a few particular solvable quantum mechanical systems. For the simple harmonic oscillator and Eckart potential, the information entropies were exactly calculated for the ground state in both coordinate and momentum state, for which the BBM inequality is saturated (Majernik & Opatrny, 1996; Pooja, 2016).

In this paper, we study the information entropy of Hylleraas plus exponential Rosen Morse potential (Ikot *et al.,* 2013; Pooja, 2017) in terms of Hylleraas parameters and equilibrium distance. This potential is widely used to study the quantum mechanical problems in chemistry and physics. It illustrates the advantage of representing the uncertainty of position and momentum in terms of their entropies instead of their dispersions. In section 2, the Fourier transform of position space eigenfunctions is used to obtain momentum space eigenfunctions in analytical form which are useful in physics and mathematics. The characteristic features of information density are also investigated. The information entropy of the potential is analyzed for Hylleraas parameters and equilibrium distance which were not considered earlier and the BBM inequality is verified in section 3. The information entropy is reduced both in position as well as momentum space with careful selection of various parameters. The conclusion of the current work is given in section 4.

INFORMATION DENSITY

The information density illustrates the compactness in terms of the amount of information. The Hylleraas potential is an interesting chemical and physical problem in quantum me- chanics over the years and has been one of the most useful potential models to describe the interaction between two atoms in a diatomic molecule. The potential reads

$$V(r) = -\frac{V_0}{b}\left[\frac{a+e^{-2\alpha(r-r_c)}}{1+e^{-2\alpha(r-r_c)}}\right] - \frac{4V_1 e^{-2\alpha(r-r_c)}}{\left(1+e^{-2\alpha(r-r_c)}\right)^2} + V_2\left[\frac{1-e^{-2\alpha(r-r_c)}}{1+e^{-2\alpha(r-r_c)}}\right], \tag{4}$$

where V_0, V_1, V_2 are the potential depths, α is adjustable parameter, a and b are the Hylleraas parameters and r_c is the distance from the equilibrium position. The Schrödinger equation for the potential ($\overline{h} = m = 1$) is

$$\frac{dU_{nl}^2}{dr^2} + 2\mu\left[E_{nl} - V(r) - \frac{l(l+1)}{2\mu r^2}\right]U_{nl} = 0 \tag{5}$$

The radial wave function for the potential reads (Ikot *et al.*, 2013).

$$R_{nl}(s) = N_{nl}(1-s)^{\frac{1+\kappa}{2}} s^{\frac{\varepsilon}{2}} P_n^{\varepsilon,\kappa}(1-2s), \tag{6}$$

using the transformation $s = -e^{-2\alpha(r-rC)}$ and

$$\varepsilon = 2\sqrt{-\frac{\mu E}{2\alpha^2\hbar^2} - C}\,, \qquad \kappa = 2\sqrt{\frac{1}{4} - (A+B+C)}$$

$$A = \frac{\mu V_0}{2\alpha^2\hbar^2 b}(V_0 + V_2 b) - \frac{l(l+1)a_1}{4\alpha^2}$$

$$B = \frac{\mu V_0}{2\alpha^2\hbar^2 b}(a+1) - \frac{2\mu V_1}{\alpha^2\hbar^2} + \frac{l(l+1)a_1}{2\alpha^2}\left(a_1 + \frac{a_2}{2}\right)$$

$$C = \frac{\mu}{2\alpha^2\hbar^2 b}(V_0 a - V_2 b) - \frac{l(l+1)}{4\alpha^2}(a_1 + a_2 + a_3).$$

$$a_1 = \frac{1}{r_c^2}\left[1 + \frac{3}{2\alpha r_c} + \frac{3}{4\alpha^2 r_c^2}\right]$$

$$a_2 = \frac{1}{r_c^2}\left[\frac{2}{\alpha r_c} + \frac{3}{2\alpha^2 r_c^2}\right], \qquad a_3 = \frac{1}{r_c^2}\left[\frac{1}{2\alpha r_c} + \frac{3}{4\alpha^2 r_c^2}\right]$$

$P_n^{\varepsilon,\kappa}(s)$ are the Jacobi polynomials and N_{nl} is the normalization constant. The wave function $\psi(r, \theta, \varphi)$ is written in terms of radial wave function and spherical harmonics $Y_{lm}(\theta, \varphi)$ as

$$P_n^{\varepsilon,\kappa}(s)$$
$$\psi(r,\theta,\phi)$$
$$Y_{lm}(\theta,\phi),$$
$$\psi(r,\theta,\phi) = \frac{R(r)}{r}Y_{lm}(\theta,\phi), \tag{7}$$

To study the information densities in momentum space, the Fourier transforms of corresponding position space eigen function are obtained. For ground state, the wave function is calculated as

$$\psi_0(p) = \frac{1}{\sqrt{2\pi}}\sqrt{\frac{1}{\beta[1+\varepsilon,2+\kappa]}}\,\Gamma\left[1+\frac{\varepsilon}{2}\right]\Gamma\left[\frac{3+\kappa}{2}\right]\zeta_1,$$
$$\zeta_1 = F\left[\frac{2+\varepsilon}{2}, \frac{1}{2}(5+\varepsilon+\kappa), -\imath p\right], \tag{8}$$

where $F\left[\frac{2+\varepsilon}{2}, \frac{1}{2}(5+\varepsilon+\kappa), -\imath p\right]$ is the hypergeometric regularized function and β is beta function. After some calculations, the excited state wave functions are obtained as

$$\psi_1(p) = \frac{1}{2\sqrt{2\pi}}\sqrt{\frac{\Gamma[5+\varepsilon+\kappa]}{(4+3\kappa+\kappa^2+\varepsilon(3+\kappa))\Gamma[2+\varepsilon]\Gamma[2+\kappa]}}$$
$$\Gamma\left[1+\frac{\varepsilon}{2}\right]\Gamma\left[\frac{3+\kappa}{2}\right]\left(2(1+\varepsilon)\zeta_1 - (2+\varepsilon)(2+\varepsilon+\kappa)\zeta_2\right), \tag{9}$$
$$\zeta_1 = F\left[\frac{2+\varepsilon}{2}, \frac{1}{2}(5+\varepsilon+\kappa), -\imath p\right]$$

$$\zeta_2 = F\left[\frac{4+\varepsilon}{2}, \frac{1}{2}(7+\varepsilon+\kappa), -\imath p\right].$$

$$\psi_2(p) = \frac{1}{2\sqrt{\pi}}\frac{1}{\Gamma\left[\frac{1}{2}(5+\varepsilon+\kappa)\right]}(2+\varepsilon)\Gamma\left[1+\frac{\varepsilon}{2}\right]\Gamma\left[\frac{3+\kappa}{2}\right]$$
$$\sqrt{\frac{(4+\varepsilon+\kappa)(5+\varepsilon+\kappa)(6+\varepsilon+\kappa)\Gamma[3+\varepsilon+\kappa]}{(12+\varepsilon(5+\kappa)+\kappa(5+\kappa))\Gamma[3+\varepsilon]\Gamma[3+\kappa]}}$$
$$\left((1+\varepsilon)\zeta_1 - \frac{2(2+\varepsilon)(3+\varepsilon+\kappa)\zeta_2}{(5+\varepsilon+\kappa)} + \frac{2(4+\varepsilon)(3+\varepsilon+\kappa)(5+\varepsilon+\kappa)\zeta_3}{(5+\varepsilon+\kappa)(7+\varepsilon+\kappa)}\right) \tag{10}$$

$$\Gamma\left[1+\frac{\varepsilon}{2}\right]\Gamma\left[\frac{3+\kappa}{2}\right]\left(2(1+\varepsilon)\zeta_1 - (2+\varepsilon)(2+\varepsilon+\kappa)\zeta_2\right),$$

$$\zeta_1 = F\left[\frac{2+\varepsilon}{2}, \frac{1}{2}(5+\varepsilon+\kappa), -\imath p\right]$$

$$\zeta_2 = F\left[\frac{4+\varepsilon}{2}, \frac{1}{2}(7+\varepsilon+\kappa), -\imath p\right].$$

$$\zeta_3 = F\left[\frac{6+\varepsilon}{2}, \frac{1}{2}(9+\varepsilon+\kappa), -\imath p\right].$$

The position space and momentum space eigen functions are used for further numerical calculations. The different features of information density in position space and momentum space are graphically plotted for various levels of the potential in figures 1 and 2, respectively. These characteristic features have been illustrated for particular values of different quantum numbers. There exist sharp peaks for the momentum probability density function of the potential. The development of dip and asymmetric shape of the entropy densities depends on the quantum numbers *n* and *l*. The position density function also reflects dissimilar behavior for various values of the parameter. The figure clearly indicates a strong dependence of the number of minima along with their corresponding depth on different parameters.

INFORMATION ENTROPY

The position space and momentum space information entropy calculations have been performed for the potential using equations (1) and (2). The analytical results of information entropy are quite difficult due to complications in the integral. The eigenfunctions are used to perform the numerical calculations of information entropy.

The ground state information entropy values in position space, momentum space and the entropy sum are presented in table 1, for different values of the parameter α. There is a change in position and momentum space information entropy for α values but the sum is bounded above inequality. The BBM inequality is satisfied and tend to saturate for lower values of the α. The variation of information entropy with Hylleraas parameter *a* is shown in Table 2. The existence of highly localized states in position space are shown in table 1 and 2. The effect of the distance from equilibrium position on the ground state information entropy values in position space, momentum space has been represented in table 3. It is found that sum of the entropies in position and momentum space is reduced for carefully selected values of the parameters. The lower bound can be reached only by a class of Gaussian wave packets. It is interesting to note that information sum is reduced for lower values of r_c and α. The BBM inequality presents an irreducible lower bound to the entropy sum. The position and momentum space information entropies have an inverse relationship with each other. A strongly localized distribution in the momentum space corresponds to widely delocalized distribution in the position space.

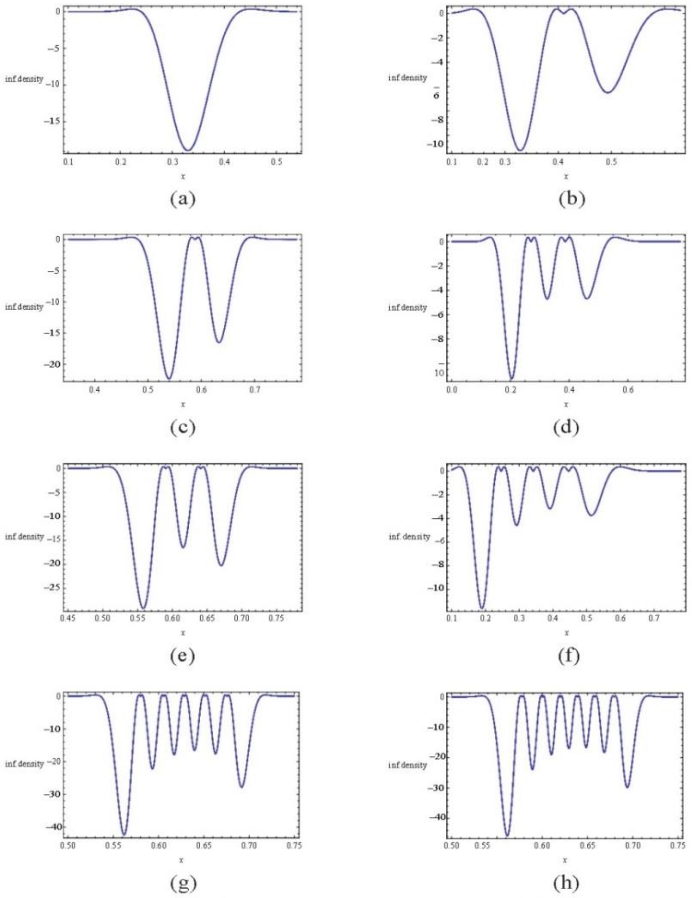

Fig. 1: Position space information densities of the potential for $\alpha = 0.11, a = 1.1, b = 1.5$ and (a) $n = 0, l = 0$ (b) $n = 1, l = 0$ (c) $n = 1, l = 1$ and (d) $n = 2, l = 0$ (e) $n = 2, l = 2$ (f) $n = 3, l = 0$ (g) $n = 5, l = 5$ (h) $n = 6, l = 6$.

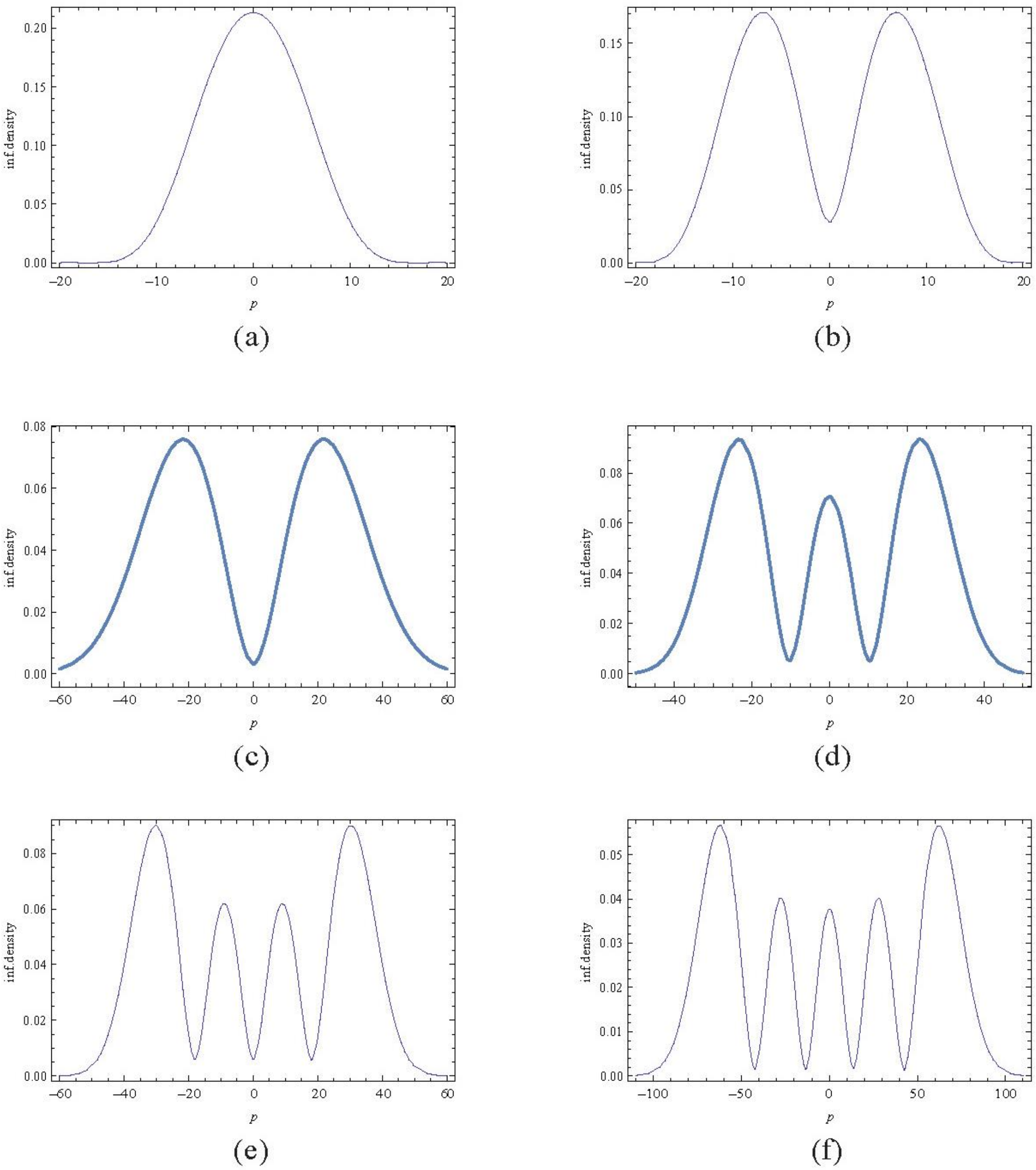

(a) (b) (c) (d) (e) (f)

Fig. 2: Momentum space information densities of the potential for $\alpha = 0.1, a = 10, b = 13$ and (a) $n = 0, l = 0$, (b) $n = 1, l = 0$, (c) $n = 1, l = 1$, (d) $n = 2, l = 1$, (e) $n = 3, l = 1$ and (f) $n = 4, l = 4$.

Table 1: The variation of information entropy for the ground state of the modified Hylleraas plus exponential Rosen Morse potential as a function of α for $a = 0.01$, $b = 0.02$, $V_0 = 0.0007$, $V_1 = 0.0006$, $V_2 = 0.099$, $r_c = 0$, $a_1 = 1$, $a_2 = 150$ and $a_3 = 100$.

α	*Spos*	*Smom*	*Spos + Smom*	α	*Spos*	*Smom*	*Spos + Smom*
0.0008	2.4366	-0.2844	2.1522	10	-0.9021	3.3304	2.4283
0.0010	2.3297	-0.1756	2.1541	15	-1.3071	3.7354	2.4283
0.0050	1.6178	0.5695	2.1873	20	-1.5946	4.0229	2.4283
0.0070	1.4954	0.7056	2.2010	30	-1.9999	4.4282	2.4283
0.0200	1.2565	1.0114	2.2679	40	-2.2876	4.7159	2.4283
0.0500	1.3623	0.9708	2.3331	50	-2.5107	4.9390	2.4282
0.1000	1.6573	0.7064	2.3637	80	-2.9807	5.4090	2.4283
1	1.3135	1.1085	2.4220	100	-3.2038	5.6321	2.4283
2	0.6853	1.7413	2.4266	200	-3.8969	6.3253	2.4284
3	0.2925	2.1351	2.4276	300	-4.3024	6.7308	2.4284
5	-0.2118	2.6398	2.4280	500	-4.8132	7.2416	2.4284
8	-0.6795	3.1077	2.4282	1000	-5.5063	7.9347	2.4284

Table 2: The variation of information entropy for the ground state of the modified Hylleraas plus exponential Rosen Morse potential as a function of a for $\alpha = 0.1$, $b = 0.02$, $V_0 = 0.0007$, $V_1 = 0.0006$, $V_2 = 0.099$, $a_1 = 1$, $a_2 = 150$ and $a_3 = 100$.

a	*Spos*	*Smom*	*Spos + Smom*	*a*	*Spos*	*Smom*	*Spos +Smom*
0.001	1.6561	0.7075	2.3636	10	2.5664	-0.1968	2.3696
0.010	1.6573	0.7064	2.3637	12	2.0752	0.2901	2.3653
0.100	1.6687	0.6951	2.3638	15	1.6212	0.7424	2.3636
1.0	1.7903	0.5737	2.3640	20	1.1482	1.2148	2.3630
1.5	1.8650	0.4993	2.3643	25	0.8289	1.5339	2.3628
2.0	1.9459	0.4187	2.3646	30	0.5874	1.7753	2.3627
2.5	2.0341	0.3309	2.3650	40	0.2304	2.1321	2.3625
3.0	2.1310	0.2346	2.3656	50	-0.0320	2.3945	2.3625
4.0	2.3599	0.0073	2.3672	60	-0.2397	2.6022	2.3625
5.0	2.6618	-0.2908	2.3710	70	-0.4115	2.7741	2.3626
6.0	3.1140	-0.7318	2.3822	80	-0.5581	2.9207	2.3626
7.0	4.1666	-1.7078	2.4588	90	-0.6860	3.0485	2.3625
8.0	3.7069	-1.2920	2.4149	100	-0.7993	3.1618	2.3625
9.0	2.9617	-0.5843	2.3774	120	-0.9935	3.3560	2.3625

Table 3: The variation of information entropy for the ground state of the modified Hylleraas plus exponential Rosen Morse potential as a function of r_c for $\alpha = 0.1$, $a = 0.001$ $b = 0.02$, $V_0 = 0.0007$, $V_1 = 0.0006$, $V_2 = 0.099$, $a_1 = 1$, $a_2 = 150$ and $a_3 = 100$.

r_c	S_{pos}	S_{mom}	$S_{pos} + S_{mom}$
5	0.6778	2.4389	3.1167
6	0.7394	2.3815	3.1209
7	0.7841	2.3403	3.1244
8	0.8174	2.3097	3.1271
9	0.8429	2.2861	3.1290
10	0.8629	2.2674	3.1303

CONCLUSION

The information entropy provides a deeper insight into the internal structure of the quantum mechanical systems. We have investigated information theoretic concepts of modified Hylleraas plus exponential Rosen Morse potential. The characteristic properties of information density of the potential are graphically analyzed for one-dimensional potential. The number of minimas and their depth depends on the values of quantum numbers. The information entropy of the potential is obtained in position and momentum states and the BBM inequality is verified. It is interesting to find that information entropy gets reduced for lower distances from equilibrium position and parameter α. The eigenfunctions will be more concentrated for reduced values of information entropy and the particle is accurately localized.

ACKNOWLEDGMENTS

The authors are thankful to Dr. C.N. Kumar, Department of Physics, Panjab University, Chandigarh for many useful discussions.

REFERENCES

Aquinoa N., A. Flores-Riverosb, 2013. J.F. Rivas-Silva, *Phys. Lett. A* 377; 2062.

Atre R., A. Kumar, C. N. Kumar and P. K. Panigrahi, 2004. *Phys. Rev. A* 69; 052107.Preston M. A. and R. K. Bhaduri, 1975. *Structure of Nucleus*, (Addison-Wesley Reading,).

Aydiner E., C. Orta and R. Sever, 2008. *Int. J. Mod. Phys. B* 22; 231.

Bialynicki-Birula I. and J. Mycielski, 1975. *Commun. Math. Phys.* 44; 129.

Bouvrie P. A., J. C. Angulo and J. S. Dehesa, 2011. *Physica A* 390; 2215.

Dehesa J. S., I. V. Toranzo and D. Puertas-Centino, 2017. *Int. J. Quantum Chem.* 117; 48.

Dong S., G. H. Sun, S. H. Dong and J. P. Draayer, 2014. *Phys. Lett. A* 378; 124.

Dutta D. and P. Roy, 2011. *J. Math. Phys.* 52, 032104.

Esquivel R.O., N. Flores-Gallegos, C. Iuga, E.M. Carrera, J.C. Angulo and J. Antolin, 2010a. *Phys. Lett. A* 374; 948.

Esquivel R.O., N. Flores-Gallegos, J.S. Dehesa, J.C. Angulo, J. Antolin, S. Lopez-Rosa and K.D. Sen, 2010b. *J. Phys. Chem. A* 114; 1906.

Everett H., 1973. The Many Worlds Interpretation of Quantum Mechanics, (Princeton University Press, Princeton, NJ).

Falaye B. J., F. A. Serrano and S. H. Dong, 2016 *Phys. Lett. A* 380, 267.

Greiner W., 2000. *Relativistic Quantum Mechanics*, (Springer-Verlag Berlin, Heidelberg, New York).

Haldar S. K., B. Chakrabarti, T. K. Das and A. Biswas, 2013. *Phys. Rev. A* 88; 033602.

Hirchman I.I., 1957. *Am. J. Math.* 79; 152.

Ikot A. N., G. J. Rampho, P. O. Amadi, M. J. Sithole, U. S. Okorie and M. I. Lekala, 2020a. *Eur. Phys. J. Plus* 135; 503.

Ikot A. N., G. J. Rampho, P. O. Amadi, U. S. Okorie, M. J. Sithole and M. L. Lekala, 2020b. *Results Phys.* 18; 103150.

Ikot A.N., A.D. Anita, I.O. Akpam and O.A. Awoga, 2013. *Rev. Mex. de Fisica* 59; 46.

Isonguyo C. N., K. J. Oyewumi and O. S. Oyun, 2018. *Int. J. Quantum Chem.* 118; 25620.

Jiao L. G., L. R. Zen, Y. Z. Zhang and Y. K. Ho, 2017. *Int. J. Quantum Chem.* 117; 25375.

Kim S., 2017. *New Phys.: Sae Mulli* 67; 226.

Kumar A., 2005. *Ind. J. Pure* & *App. Phys.* 43; 958.

Majernik V. and T. Opatrny, 1996. *J. Phys. A: Math. Gen.* 29; 2187.

Onate C. A., M. C. Onyeaju, E. E. Ituen, A. N. Ikot, O. Ebomwonyi, J. O. Okoro and K. O. Dopamu, 2018. *Indian J. Phys.* 92; 487.

Pooja, Gupta R., A. Sharma and A. Kumar, 2020. *New Phys. Sae Mulli* 70, 778.

Pooja, Kumar R., G. Kumar, R. Kumar, A. Kumar, 2016. *Int. J. Quantum Chem* 116; 1413.

Pooja, Sharma A., R. Gupta and A. Kumar, 2017. *Int. J. Quantum Chem* 117; 25368.

Serrano F.A., B.J. Falaye and S.H. Dong, 2016. *Physica A* 446; 152.

Shi Y. J., G. H. Sun, J. Jing and S. H. Dong, 2017. *Laser Phys.* 27; 125201.

Song X. D., G. H. Sun and S. H. Dong, 2015. *Phys. Lett. A* 379; 1402.

Sun G. H., S. H. Dong, K. D. Launey, T. Dytrych and J. P. Draayer, 2015. *Int. J. Quantum Chem.* 115; 891.

Valencia-Torres R., G. H. Sun and S. H. Dong, 2015. *Phys. Scr.* 90, 035205.

Werner R.F., 2016. *Front. Phys.* 11; 110305.

Yahya W. A., K. J. Oyewumi and K. D. Sen, 2014. *Ind. J. Chem. A* 53; 1307.

Yan´ez R. J., W. V. Assche and J. S. Dehesa, 1994. *Phys. Rev. A* 50; 3065.

Pb. Univ. Res. J (Sci.) Vol. 70, 2020, pp 13-24

A SOPHISTICATED APPROACH FOR ASSIGNING SPIN, PARITY AND EXCITATION ENERGY TO THE YRAST SUPERDEFORMED NUCLEAR BANDS

Sham S. Malik*
Department of Physics, Panjab University, Chandigarh-160014, India

ABSTRACT

A more sophisticated approach for obtaining the complete set of characteristics, like spin-parity and excitation energy, of the observed yrast super-deformed bands is presented. The primary motive of this approach is two-fold. Firstly, it extracts the band-head characteristics from the systematic studies, which involve the experimental data of available positive as well as negative parity normal deformed states and the yrast super-deformed states in a given nucleus. A plateau behavior is seen in the observed $\frac{E_\gamma(I)}{E_\gamma(I+2)}$ ratio of the super-deformed band that supports a smooth gradual increase of its moment of inertia with increasing angular momentum. These systematics not only assign the spin, parity and excitation energy of the super-deformed spectra reasonably, but also ensure the contribution of pairing correlations among the nucleons for explaining their spectra. The band-head predictions drawn from the systematic study are then confirmed by using the quantum mechanical models, like the cranked shell model and the two-center-shell model. These formalisms (systematic study plus quantum approach) are tested in three mass regions, namely, A ~ 130, 150 and 190 where the maximum number of super-deformed spectra have been observed. These findings may resolve in near future the anomalies like identical band phenomena among the neighboring super-deformed nuclei, and the absence or presence of linking transitions from the super-deformed states to the normal deformed states in a given nucleus.

Keywords : Nuclear mass regions A ~ 130, 150 and 190, Superdeformed bands, Spin-parity, excitation energy.

INTRODUCTION

In 1986, Twin and co-workers (1986) observed for the first time super-deformed (SD) rotational band in rare-earth nucleus ^{152}Dy. Just after this discovery an immense interest had exploded and within two-decade or so more than 335 yrast as well as excited SD bands have come-up in five mass chains A∼60, 80, 130 150 and 190 (Singh, Zywine, Firestone, 2002; Sonzogni, 2008). In 1996, Khoo and co-workers (Khoo *et al.*, 1996) were able to observe the linking transitions between the SD states of ^{194}Hg and its low-lying normal deformed (ND) states; and hence established the spin-parity as well as the excitation energy of this yrast SD band. Within a couple of years later, Lauritsen and co-workers (Lauritsen *et al.*, 2002) had also successfully observed the linking transitions between the SD and ND states of ^{152}Dy. Similar experiments were repeated in the following years for the remaining SD nuclei, but these linking transitions were completely untraceable, except for very few more cases (Hackman *et al.*, 1997; Hauschild *et al.*, 1997). Therefore, the γ-ray energies are the only spectroscopic information universally available in almost all the SD bands without knowing the discrete linking transitions between SD and ND states.

The identical band phenomenon is one of the prominent observed features among SD bands (Byrski *et al.*, 1990). These findings are not only limited to SD domain but has also been extended to the ND bands (Ahmad *et al.*, 1991; Casten *et al.*, 1992; Baktash *et al.*, 1992). The various theoretical explanations for their (*i.e*, ND bands) identicity may be found in Refs. (Baktash *et al.*, 1995; Malik and Mazumdar, 2019). It is noticed that the similarities among their moment of inertia is one of major criteria for deciding their identical nature. An exact determination of moment of inertia requires an unambiguous assignment of the angular momentum, parity and excitation energy to the SD states. Therefore, the band-head characteristics are crucial for explaining the identical band phenomenon. Theoretical techniques are the only way-out for fixing the band-head characteristics of SD bands. Several formalisms were tested successfully for assigning an appropriate band-head spin (Bohr and Mottelson, 1975; Shalaby, 2004; Shalaby, 2006; Harris, 1964; Wu *et al.*, 1992; Wu and Zhou, 1997; Holmberg and Lipas, 1968; Liu, 1998; Liu, 1998; Liu *et al.*, 1999; Liu and Gao, 2001; Liu *et al.*, 2001a; Liu *et al.*, 2001b). However, these studies were unable to pinpoint the complete information of the SD band-head, e.g., a definite spin, the parity and the excitation energy with respect to low lying ND states.

In this paper we have used two entirely different approaches for assigning the band-head spin (I_b), parity (Π) and excitation energy (E*) of the yrast SD bands. The first one is the systematic empirical approach which involves the experimental data of available positive as well as negative parity ND states and the yrast SD states in a given nucleus. The plateau behavior in the observed $\frac{E_\gamma(I)}{E_\gamma(I+2)}$ ratio in SD bands support a gradual increase of moment of inertia with angular momentum. On the basis of this observation, a finite pairing correlation among the nucleons is included in our quantum mechanical based calculations. Secondly, the predictions drawn from the systematic studies for the SD band-head are also confirmed by the cranked-shell model (CSM) and the two-center-shell model (TCSM). Out of five mass

---

* Corresponding Author: shammalik@yahoo.com
MS Received : May 16, 2020, Accepted: August 25, 2020.

regions A~ 60, 80, 130 150 and 190 in which the SD bands are reported, large number of SD bands are available only in three, *i.e.*, A~ 130 150 and 190 (Singh, Zywine, Firestone, 2002; **Sonzogni,** 2008). Therefore, this two-way approach is performed for the three mass regions, selecting at least one nucleus from each region and its success is highlighted in comparison with the available experimental data; and is presented below in the following Tabular form.

Technique	Nucleus	I^π ħ, E^* (MeV) Predicted values	I^π ħ, E^* (MeV) Exp. Values (Lauritsen *et al*., 2002; 2003)
Empirical	^{194}Hg ^{152}Dy ^{131}Ce	8^+, ~3.2-4.5 24^+, 9.5 14.5^+, 6.7	6^+, 6.4 24^+, 10.6 -
Cranked shell model	^{194}Hg ^{152}Dy ^{131}Ce	8.3^+ 24.7^+ at ħω~0.3 MeV 19.5^+ at ħω~0.3 MeV	
Tilted-cranked shell model	^{194}Hg	E^*~6.5 MeV	

Using the available experimental data of ND and SD states, the systematic studies are carried out in section II for predicting the spin, parity and excitation energy of the yrast SD spectrum. Section III deals with the CSM calculations. In this section the band-head characteristics as extracted in section II, are confirmed by reproducing the complete spectra and the electromagnetic transitions properties of the yrast SD bands of ^{131}Ce, ^{152}Dy and ^{194}Hg. Further, following the Strutinsky shell correction technique (Strutinsky, 1967; Strutinsky, 1968) a shape dependent macroscopic-microscopic formalism has already been developed (Scharnweber *et al*., 1971; Brack *et al*., 1972) for obtaining the deformation energy surfaces of nuclei. These surfaces are found to be quite useful in explaining the fission isomeric states in actinides. Using the TCSM technique (Scharnweber *et al*., 1971), the excitation energy of the band-head of yrast SD spectrum with respect to the ND state of a given nucleus is estimated in section IV. Finally, the conclusions are summarized in section V.

SYSTEMATIC EMPIRICAL STUDIES FOR THE YRAST SD BANDS

These systematic calculations are based on the observed data of positive as well as negative parity ND and the yrast SD states of a given nucleus. Within this formalism, the band-head characteristics of yrast SD states, namely, (i) spin, (ii) parity and (iii) excitation energy with respect to ND states, are investigated. In order to extract these prominent features, a preliminary estimate of band-head spin is required, which will subsequently be confirmed by the cranking model. Using the observed γ-rays of yrast SD spectrum, a reasonable estimate of band-head angular momentum is extracted and the underlying procedure is discussed below.

A. Spin determination

Wu and co-workers (1992) have already claimed that two-parameter equation for $E_\gamma(I) = a\left[\sqrt{1+bI(I+1)} - \sqrt{1+b(I-2)(I-1)}\right]$, a and b being the parameters) is quite effective in reproducing the band-head spin of SD nuclei and its (two-parameter formula) equivalence with the microscopic derivation based on Bohr Hamiltonian has already been shown (Wu and Zeng, 1987). We have used its generalized version, as discussed below, for obtaining the band-head spin,

$$E_\gamma(I) = a\left[\begin{array}{l}\sqrt{1+b(I_b+2n)(I_b+2n+1)} - \\ \sqrt{1+b(I_b+2n-2)(I_b+2n-1)}\end{array}\right] \tag{1}$$

These three parameters, namely, band-head angular momentum, I_b, the inertia equivalent parameter, a and softness parameter, b, are obtained by a best least-square fit method involving the experimentally known SD E_γ with $1 \le n \le 10$. In these calculations, we generally start with a threshold value of I_b and increase it by one unit till the calculated E_γ coincide with the observed values excellently.

Firstly, we carry out the least square fit calculations for ^{194}Hg, in which the band-head spin using linking transitions between the yrast SD states and the low-lying states of ND is well known experimentally (Khoo *et al*., 1996). Fig.1 shows the plot of $\Delta E_\gamma = (E_\gamma)_{exp}-(E_\gamma)_{cal}$ vs the angular momentum I. The band-head spin is varied within the limits $7ħ \le I_b \le 9ħ$ and the corresponding ΔE_γ for each case is shown. It is quite evident from this plot that the difference in observed and calculated γ-rays, *i.e.*, ΔE_γ emerges ≤ ±1 keV only in case of $I_b = 8ħ$. This angular momentum, *i.e.*, $I_b = 8ħ$ is one of the most appropriate choice for the SD band of ^{194}Hg and is remarkably in agreement with the observed value (Khoo *et al*., 1996).

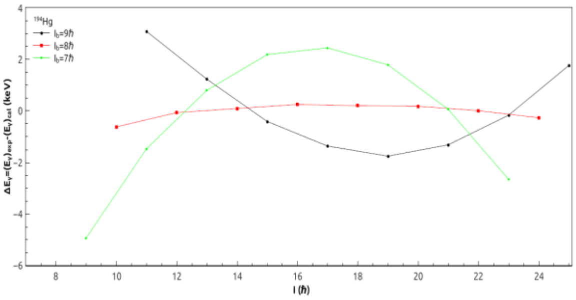

Fig. 1. Difference between experimental and least square fitted (using equation (1)) values of E_γ for various band-heads in case of yrast SD band of ^{194}Hg.

Similar procedure is also repeated for the remaining two mass regions, *i.e.*, A ~ 130 and 150, particularly, for yrast bands of ^{131}Ce and ^{152}Dy. The best fit as well as the observed E_γ for the yrast SD bands of ^{194}Hg, ^{152}Dy and ^{131}Ce, are shown as a function of angular momentum, respectively, in Fig. 2(a)-Fig.2(c). The appropriate band-head spin along with the other fitted parameters a and b are indicated on each of these plots. The extracted band-head spins of ^{152}Dy and ^{194}Hg are, respectively, 24$\hbar$ and 8$\hbar$ and are fully in agreement with their corresponding experimental band-head spins (Khoo *et al.*, 1996; Lauritsen *et al.*, 2003). On the basis these observations we have assumed that I_b = 14.5 $\hbar$ is a true band-head for ^{131}Ce-SD band.

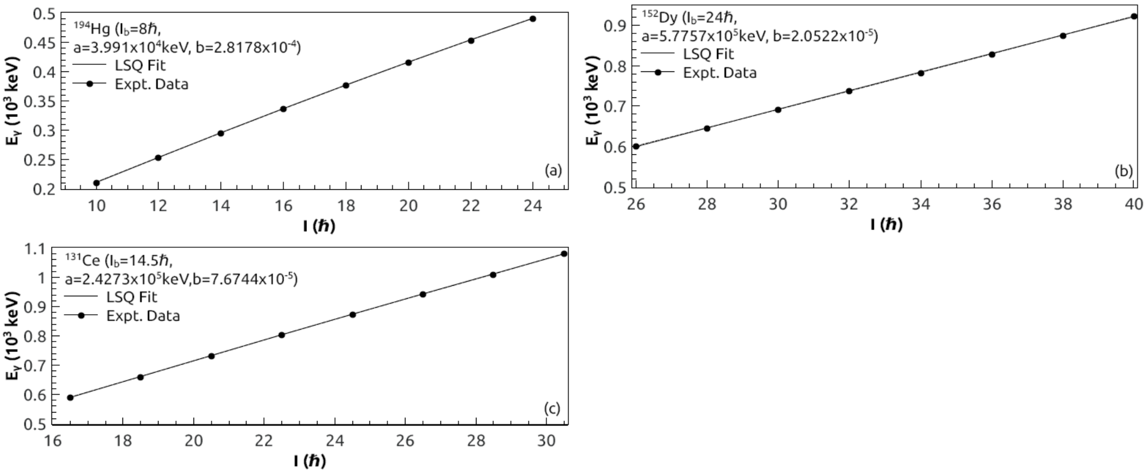

Fig. 2. Least square fit to the experimental E_γ by using equation (1) of the yrast SD bands of ^{194}Hg, ^{152}Dy and ^{131}Ce. The fitted parameters are also shown in each case.

Further, using these fitted parameters (i.e., a and b), we have calculated the moments of inertia (defined as $\Theta = \hbar^2/ab$ of each SD band and it comes out to be $\Theta(^{194}\mathrm{Hg}) = 89\ \hbar^2/\mathrm{MeV}$, $\Theta(^{152}\mathrm{Dy}) = 84.4\ \hbar^2/\mathrm{MeV}$ and $\Theta(^{131}\mathrm{Ce}) = 53.7\ \hbar^2/\mathrm{MeV}$. It is quite interesting to notice here that the moment of inertia of yrast SD band is nearly ~50% higher than that of ND band, *i.e.*, $\Theta_{ND} = (\hbar^2/2E_\gamma)\,(4I-2)$ whereas it (SD band moment of inertia) is nearly ~15%-20% less than their corresponding rigid-rotor value (*i.e.*, $\Theta_{\text{Rigid-rotor}} = (2/5)\,AmR^2[1+(1/3)\beta]$, A, R, m and β being, respectively, mass number of the nucleus, nuclear radius, nucleon mass and deformation parameter). Thus, an equality $\Theta_{ND} < \Theta_{SD} < \Theta_{\text{Rigid-rotor}}$ discards the pure rigid-rotor character of the yrast SD band below band termination. Hence, the pairing correlations among the nucleons, even though it is small, still must be required for explaining the SD rotational spectra.

Knowing a reasonable value of the band-head spin of yrast SD states, the parity and excitation energy with respect to the ND states are extracted in a following way.

B. Estimation of parity and excitation energy

The moment of inertia of ND bands generally varies with an increase in angular momentum due to (i) the stretching effect (ii) the Coriolis anti-pairing effect and (iii) the rotation alignment. Further, a variation in moment of inertia with angular momentum between two consecutive states having angular momentum I and I+2 is mainly decided by the ratio $E_\gamma(I)/E_\gamma(I+2)$. At some critical angular momentum, this varied moment of inertia may approach close to that of the yrast SD band. Keeping these points in mind, we have plotted the experimental ratio $E_\gamma(I)/E_\gamma(I+2)$ vs the angular momentum I for all available positive as well as negative parity ND-bands together with the yrast SD band in a given nucleus. Figures 3-5 show, respectively, the plots of these ratios for ^{194}Hg, ^{152}Dy and ^{131}Ce nuclei. Following interesting points emerge from these plots.

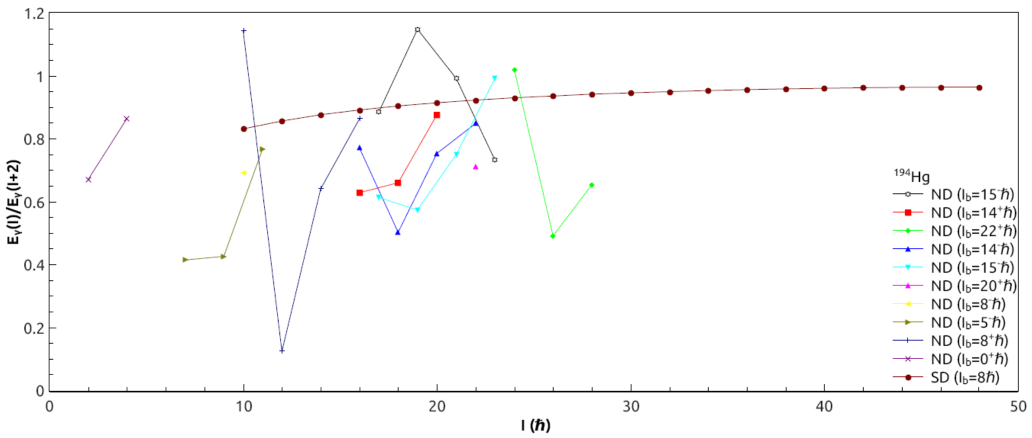

Fig. 3. The ratio E_γ (I) / E_γ (I+2) vs angular momentum I for ND and yrast SD states of ^{194}Hg.

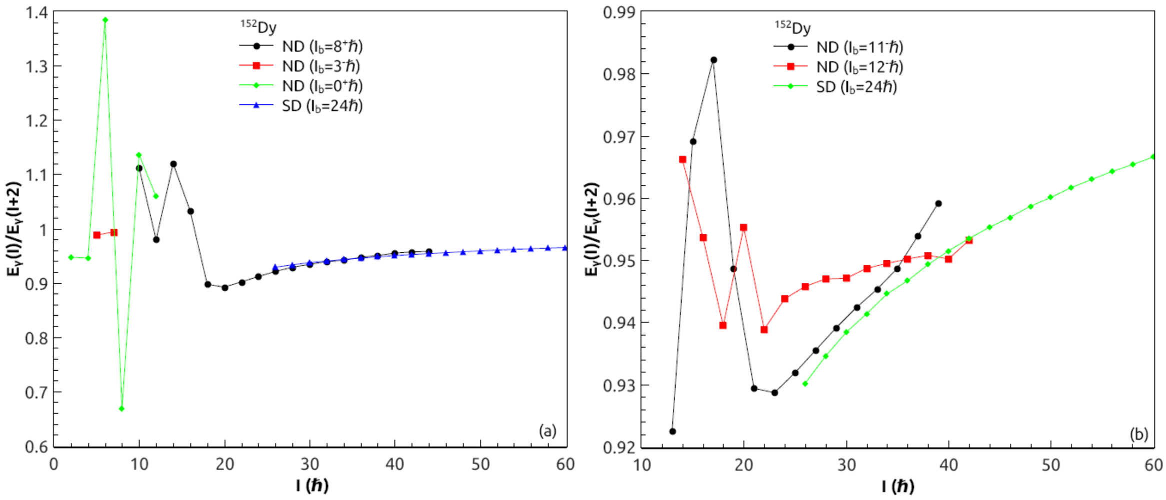

Fig. 4: The ratio E_γ (I) / E_γ (I+2) vs angular momentum I for ND and yrast SD states of ^{152}Dy.

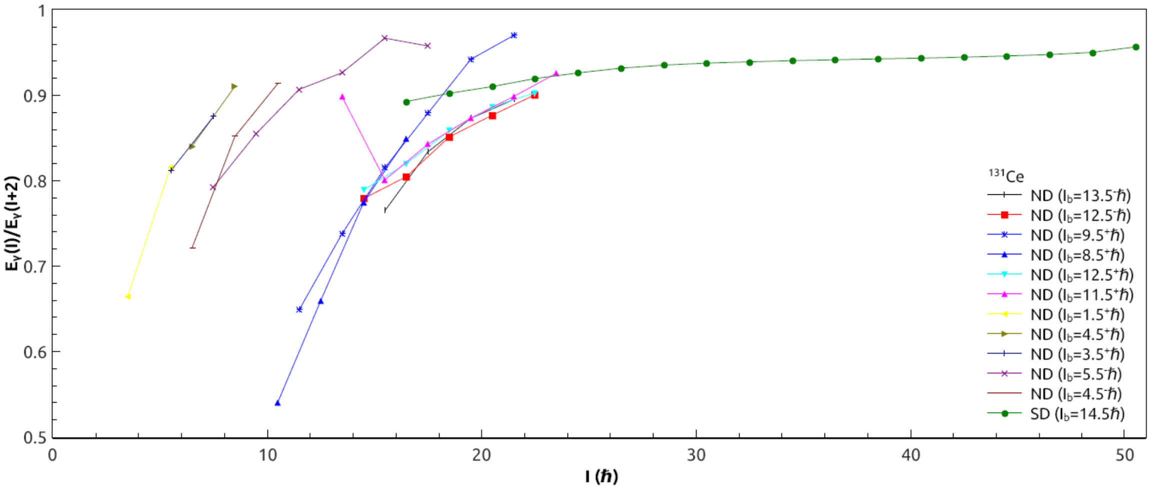

Fig. 5: The ratio E_γ (I) / E_γ (I+2) vs angular momentum I for ND and yrast SD states of ^{131}Ce.

(i) The ratio $E_\gamma(I)/E_\gamma(I+2)$ shows a nearly constant behavior for the yrast SD states in each case. This constant behavior supports a smooth increase in moment of inertia with increasing angular momentum. This gradual increase in moment of inertia implies that even though SD bands are observed in the most deformed region, still they exhibit substantial deviation from the rigid-rotor behavior in a considerable range of angular momenta. On the other-hand, for ND states this ratio varies drastically with angular momentum and attains a plateau region either for the positive or for the negative parity states near their band termination.

(ii) In case of ^{194}Hg (as shown in Fig. 3), the positive parity ND states beginning with band-head I_b = 8ħ attains a plateau behavior similar to that of yrast SD states near its (*i.e.*, ND state) terminating angular momentum $16^+\hbar$. Also, another positive parity ND states beginning with band-head I_b = $14\hbar$ attains a plateau behavior near the terminating angular momentum $20^+\hbar$. Whereas such type of plateau behavior is not seen in any negative parity ND states while terminating close to the SD structure. On the basis of this observation one may assign positive parity to the yrast SD states and is fully consistent with the experimental observation made by Khoo and co-workers (1996).

An estimate of threshold excitation energy of SD band-head with respect to the ND states is another milestone of this equality in the relative ratio of γ-rays between the SD and the terminating ND states, *i.e.*, $\left[\frac{E_\gamma(I)}{E_\gamma(I+2)}\right]_{SD} = \left[\frac{E_\gamma(I)}{E_\gamma(I+2)}\right]_{ND}$. Since the excitation energy of the terminating ND state is known to us. This excitation energy should be assigned to the coinciding angular momentum of yrast SD-state. For example, the positive parity ND state with band head I_b = $8\hbar$ at the terminating point coincides with yrast SD state with assigned angular momentum $16\hbar$, therefore, the excitation energy of this SD state is same as that of terminating ND state, i.e., 4274.8 keV. Just by subtracting the sum of remaining known γ-ray energies below the coinciding angular momentum of the SD state (i.e., $16\hbar$ with 4274.8 keV) one may obtain an estimate of band-head energy of the yrast SD band. In this case there are four available γ-rays just below I =

16ℏ (i.e., $E_\gamma(I = 10\to8) = 211.6$ keV, E_γ $(I = 12\to10) = 254$ keV, E_γ $(I = 14\to12) = 296$ keV and E E_γ $(I = 16\to14) = 377.4$ keV). Therefore, just subtracting their sum from 4274.8 keV, it gives ~3.2 MeV threshold excitation energy for its band-head. Also, the positive parity ND state with band head $I_b = 14\hbar$ at the terminating point coincides with yrast SD state with assigned angular momentum 20ℏ, therefore, the excitation energy of this SD state is 6349.4 keV. By subtracting the known energy sum of remaining γ-rays below 20ℏ in this case, fixes the threshold band-head excitation energy value ~4.5 MeV.

Our systematic study predicts the positive parity as well as the threshold excitation energy ~3.2-4.5 MeV for the yrast SD band-head of ^{194}Hg and both these predictions are reasonably supported by the experimentally observed values (Khoo *et al.*, 1996).

(iii) In case of ^{152}Dy, the ratio E_γ (I)/E_γ (I+2) for positive parity ND states (except for $I_b = 3^-$) together with the yrast SD states are plotted in Fig. 4(a), whereas negative parity ND states along with the yrast SD states are shown in Fig. 4(b). The positive parity ND states beginning with band-head $I_b = 8\hbar$ attains the plateau behavior and completely merge with its yrast SD states at angular momentum I = 30ℏ. Following the above discussion, this identicity fixes the positive parity to its yrast SD band-head with threshold excitation energy ~9.5 MeV and is fairly consistent with the observation (Lauritsen *et al.*, 2002, Lauritsen *et al.*, 2003). On the other-hand, no such similarity is visible in any one of the negative parity ND states.

(iv) Finally, in ^{131}Ce (as shown in Fig. 5), the positive parity ND states beginning with band-head $I_b = 23/2\ \hbar$ attains the plateau behavior and completely merge with its yrast SD states at angular momentum I = 51/2 ℏ. Therefore, this identicity fixes the positive parity with excitation energy ~6.7 MeV of its yrast SD band-head and is first time predicted within our systematics. All negative parity ND states do not show similar behavior near their termination points.

This empirical study is highly useful in getting the firsthand information of spin, parity and excitation energy of the yrast SD bands. The above Table shows that the systematically predicted band-head features of ^{194}Hg and ^{152}Dy compare reasonably well with their corresponding experimental values. Therefore, the predicted band-head features of ^{131}Ce are considered to be reasonably correct and deserve a detailed experimental test in near future. Further, these extracted features are authenticated by our Cranking model calculations, which are discussed below.

CRANKED-SHELL MODEL CALCULATIONS FOR YRAST SD STATES

A complete cranking model was developed by Frauendorf (2000). This model has already been used by us for explaining the observed features of the various types of rotational spectra (Lakshmi *et al.*, 2002;, Lakshmi *et al.*, 2004;, Malik, Agarwal and Jain, 2004). Here, we present a brief account of this model for completeness. The main advantage of using this formalism is that if the axis of rotation coincides with one of the principal axes then it reduces to the principal-axis cranking (PAC) with tilt-angle θ = 90°. Within the pairing plus quadrupole-quadrupole interaction, the quasi-particle Routhian is given by

$$h' = h_{sp} - \hbar\omega_0\beta\left(cos\gamma q_0 - \frac{sin\gamma}{\sqrt{2}}\,(q_2 + q_{-2})\right) - \Delta(P^+ + P) - \lambda\vec{\omega}.\vec{j} \qquad (2)$$

With $\vec{\omega}.\vec{j} = \omega(j_1 \sin\theta\cos\varphi + j^2 \sin\theta\sin\varphi + j_3\cos\theta)$. Here, h_{sp} is the single particle Hamiltonian of a deformed field (deformed Woods-Saxon potential); **ω** is the cranking frequency; θ and φ are the tilt-angles of the resultant angular momentum with respect to the principal-axes and j_i (i = 1 to 3) are the components of particle angular momentum **j** along the three-axes, where 3-axis is the symmetry axis. In the present calculations, we have considered φ = 0 and θ = 90° because our rotational angular momentum lies perpendicular to the symmetry axis. Further, $\hbar\omega_0 = 41/A^{-1/3}$ MeV, β and γ are the usual deformation parameters. q_0, q_2 and q_{-2} are the expectation values of the respective components of the quadrupole tensor Q. The operator P^+ creates the pair field, the strength of which is fixed by the gap parameter Δ. The Fermi level is fixed to give correct particle number for each cranking frequency ω.

The total Routhian E′(ω) is calculated by using the Strutinsky re-normalization technique (Strutinsky, 1967),

$$E'(\omega) = E_{LD} - E_{smooth} + \langle\omega|h'|\omega\rangle \qquad (3)$$

Here, E_{LD} is the liquid drop energy and the smooth part of the energy, E_{smooth}, is calculated by the Strutinsky averaging method. The deformation parameters (ε_2, ε_4, γ) are found self-consistently by minimizing the total Routhian E′(ω) for a given frequency and a chosen configuration.

Firstly, we discuss in detail the result of yrast SD band of ^{194}Hg and the results for remaining nuclei will be presented thereafter. For this nucleus, the observed γ-ray energies (Riley *et al.*, 1990; Cederwall *et al.* 1994; Sonzogni, 2008), the transition quadrupole moments (Hughes *et al.*, 1994) and linking transitions between the SD and ND states (Khoo *et al.*, 1996; Brinkman *et al.*, 1996) are very well known. Since the rotational spectrum of a nucleus is governed by pairing correlations, deformation parameters, n-p interaction and quasi-particle alignment. It is a general observation as well as the conclusion also drawn by our ratio E_γ(I)/E_γ (I+2) plots that pairing contribution is quite small but not negligible in yrast SD bands. In order to extract a quantitative information of pairing correlations among the nucleons, we have again taken the help of equation (1). Since this non-linear equation involves two parameters a and b just after fixing the band-head angular momentum I_b. Using Newton-Raphson method taking two experimental values of E_γ's at a time, we have extracted these two parameters for a given angular momentum and are shown, respectively, in Fig. 6(a) and Fig. 6(b). It is quite evident from Fig. 6(a) that inertia equivalent parameter a is not constant, it increases slowly with an increase in angular momentum I. Also, the softness parameter b (as shown in Fig. 6(b)) shows a slow decrease and approaches close to zero value with an increase in angular momentum I. The calculated moments of inertia, by using these varied parameters a and b, is shown in Fig. 6(c). Its variation with angular momentum I shows the rigid rotor value near the band termination and the band-head moment of inertia is about 20% less than that of rigid rotor value. Further, it has already been noticed above that the positive parity ND states beginning with band-heads $I_b = 8\hbar$ and $I_b = 14\hbar$ follow a trend similar to that of yrast SD states near their (i.e., ND states) terminating angular momenta. Their average moment of inertia is about ~50% less than that of SD band. Thus an inequality in moment of inertia, i.e., $\Theta_{ND} < \Theta_{SD} < \Theta_{Rigid\text{-}rotor}$, supports that that pairing is not negligible near the band-head of yrast SD states. Further, a comparison of b-values near the band-heads of SD and ND bands reveals that the ND state with band-head $I_b = 8\ \hbar$ is ~50% more soft as compare to that of SD state.

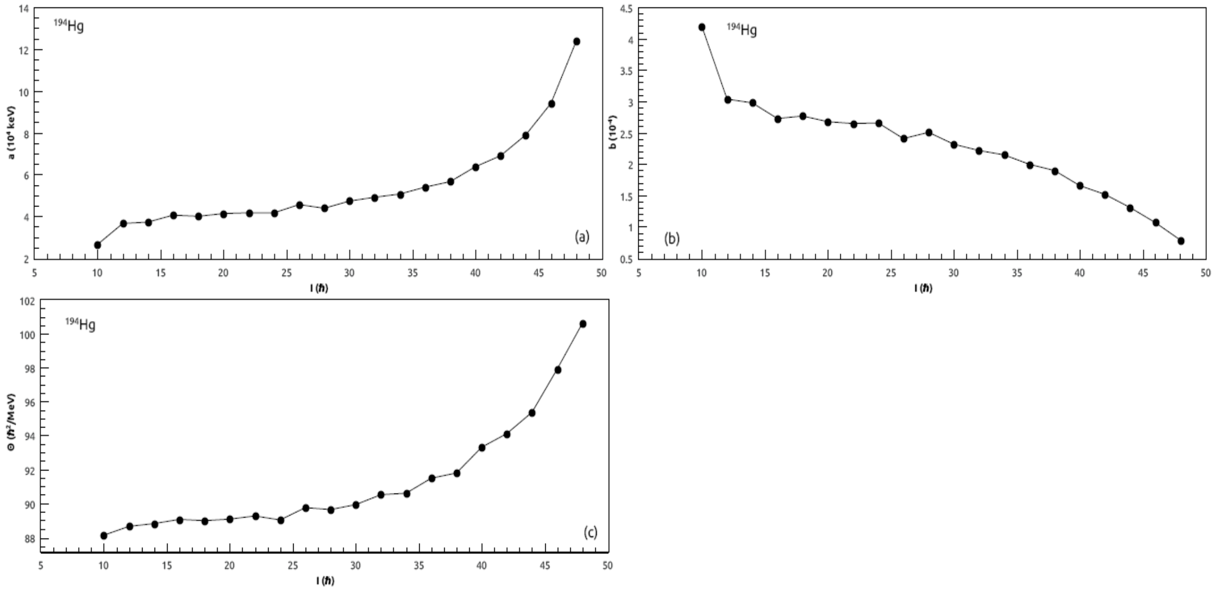

Fig. 6. The top left-panel shows the inertia equivalent parameter a, top right-panel shows the softness parameter b and the lowest panel shows the moment of inertia $\theta = \hbar^2/ab$ vs the angular momentum I for the yrast SD band of ^{194}Hg.

Therefore, we have reduced the pairing strength parameters for proton, Δ_p, and for neutron, Δ_n, by 50% with respect to their corresponding values used for ND state calculations. Using the experimental binding energies (Sonzogni, 2008), the neutron and proton pairing gaps for nuclei are given by

$$\Delta_p = \frac{1}{4}[B(Z-2,N) - 3B(Z-1,N) + 3B(Z,N) - B(Z+1,N)] \quad (4)$$

$$\Delta_n = \frac{1}{4}[B(Z,N-2) - 3B(Z,N-1) + 3B(Z,N) - B(Z,N+1)] \quad (5)$$

Here, we reduce it by 50% (*i.e.*, $\Delta_p = 0.5588$ MeV and $\Delta_n = 0.5454$ MeV) for its yrast SD band calculations.

For a given cranking frequency 0.1 MeV and the positive parity configuration $\pi 6^4 \otimes \nu 7^4$, the parameters $\varepsilon_2 = 0.468$, $\varepsilon_4 = 0.017$, $\gamma = 0$ are determined self-consistently by minimizing the total energy. The calculated excitation energy vs the angular moment I is shown in Fig. 7(a). The experimental data (Sonzogni, 2008) is also shown in this plot. A comparison with the experimental data reveals that (i) the band-head spin ($I_b = 8.3^+\ \hbar$) is nicely reproduced (ii) except for minor deviations, the overall behavior resembles with the observed spectrum. These deviations might be improved further by minimizing in the pairing correlations among the nucleons. The minimization of energy in Δ_p and Δ_n is not considered in this work because our motive is just to obtain the band-head of SD spectrum. Fig. 7(b) shows the plot of angular momentum I vs the rotational frequency $\hbar\omega$. Its comparison with the experimental data illustrates that the experimental data of transitional energies is nicely reproduced at higher rotational frequencies (i.e., $\hbar\omega \sim 0.25$ MeV) by the PAC calculations.

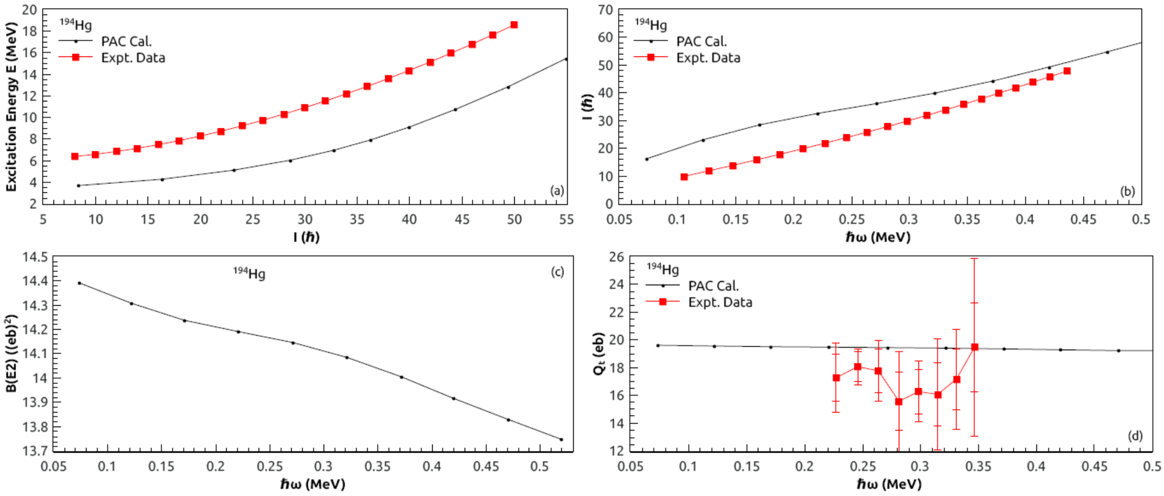

Fig. 7. The top left-panel shows the calculated excitation energy vs the angular momentum, top right-panel shows the angular momentum, the lower panel shows the B(E2) values and the Q_t-values for ^{194}Hg along with the available experimental data.

Finally, the B(E2)-values

$$B(E2, \Delta I = 2) = \frac{15}{128\pi}\left(Q_0' \sin^2\theta + \sqrt{\frac{2}{3}}\, Q_2'(1+\cos^2\theta)\right)^2 \qquad (6)$$

and the corresponding extracted quadrupole moment Q_t are plotted, respectively, in Fig. 7(c) and Fig. 7(d). In Fig. 7(c), a slight decrease in B(E2)-values with increasing rotational frequency ℏω is seen but the overall trend is constant. This constant behavior is more vivid from the Q_t plot shown in Fig. 7(d). The experimental data of Q_t (Hughes *et al.*, 1994) is also shown in Fig. 7(d). The observed Q_t-values within the error bars show a nearly constant behavior over a considerable range of rotational frequency and are fully consistent with our PAC calculations.

Following similar steps, we have carried out the PAC calculations for yrast SD band of ^{152}Dy and obtained a set of parameters $\varepsilon_2 = 0.605$, $\varepsilon_4 = 0.003$, $\gamma = 0$ by using $\Delta_p = 0.7794$ MeV and $\Delta_n = 0.5328$ MeV for the positive parity configuration $\pi 6^4 \otimes \nu 7^2$ at a given cranking frequency ω = 0.3 MeV. The PAC results for angular momentum I vs the rotational frequency ℏω together with the experimental data (Sonzogni, 2008) are shown in Fig. 8(a). A comparison between the calculated and observed values reveals that the calculated spin is just two-units less than that of the corresponding observed value at rotational frequency ℏω~ 0.3 MeV. Thus, our PAC calculations not only reproduce the band-head spin within two-units but also the overall trend of the observed rotational spectrum of ^{152}Dy is nicely obtained. Further, the right-panel of this plot (Fig. 8(b)) shows the B(E2)-values, which slightly increase with increasing rotational frequency ℏω. Also, the Q_t-values along with available experimental value (Savajols *et al.*, 1996) vs the rotational frequency ℏω are shown in the lower-panel of this plot (Fig.8(c)). Again the observed and calculated results are fairly in agreement.

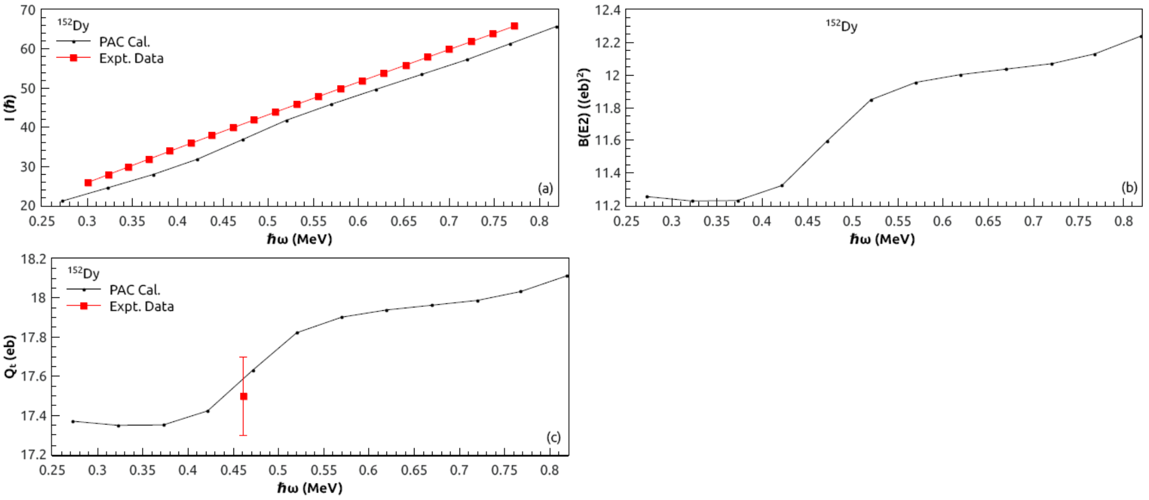

Fig. 8. The panel shows the angular momentum, the right- panel shows the B(E2) values and the lower panel Q_t-values for ^{152}Dy along with the available experimental data.

Finally, the PAC calculations for yrast SD band of ^{131}Ce are performed. This is an odd-A nucleus and also a single neutron together with a pair of protons contribute in the spectrum. So, the pairing correlations among the neutrons are considered to be negligible whereas that among the protons is 50% as compare to ND band calculations. Therefore, in these calculations, a set of parameters $\varepsilon_2 = 0.348$, $\varepsilon_4 = 0.024$, $\gamma = 0$ by using $\Delta_p = 0.5099$ MeV and $\Delta_n = 0.0$ MeV for the positive parity configuration $\pi 5^2 \otimes \nu 6^1$ at a given cranking frequency $\omega = 0.3$ MeV are obtained. The PAC results for angular momentum I vs the rotational frequency $\hbar\omega$ are plotted in Fig. 9(a). The variation of assigned angular momentum (i.e., extracted from our systematic calculations) as a function of observed rotational frequency $\hbar\omega$ are also shown in this plot (i.e., Fig. 9(a)). A comparison between these plots reveals that the PAC calculated spin is nearly three-units higher than that of the corresponding empirically assigned value at rotational frequency $\hbar\omega \sim 0.3$ MeV. The right-panel of this plot (Fig. 9(b)) shows the Q_t-values. The experimental data for its Q_t-value is not known. These Q_t-values decrease slightly with increasing rotational frequencies $\hbar\omega$ but the overall trend is found to be constant.

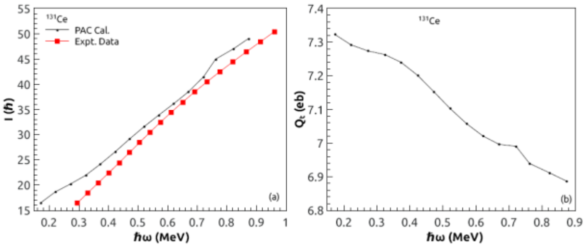

Fig. 9. The panel shows the angular momentum, the right- panel shows the B(E2) values and the lower panel Q_t-values for ^{131}Dy along with the available experimental data.

Thus, our PAC calculations, of all the three nuclei (^{194}Hg, ^{152}Dy and ^{131}Ce), not only reproduce their band-head spins within ~±2 $\hbar$ from their observed and/or predicted values, but also explain nicely the overall trends of their observed rotational spectra together with their electric transition probabilities.

Next, the shape dependent macroscopic-microscopic formalisms (Scharnweber, Greiner and Model, 1971; Brack *et al.*, 1972) based on the Strutinsky shell correction technique (Strutinsky, 1967; Strutinsky, 1968) are found to be quite successful in defining the deformation energy surfaces of nuclei. These deformation energy surfaces generate two stable minima, which correspond to ND state and SD state in a given nucleus. The energy difference between these minima helps in fixing the excitation energy of SD band-head with respect to the ND state. Here, we preferably use the TCSM formalism for obtaining the band-head excitation energy of the yrast SD band with respect to the ND state in a given nucleus and is discussed below.

TCSM APPROACH FOR OBTAINING THE EXCITATION ENERGY OF SD BAND-HEAD

The TCSM was developed by the Frankfurt group (Scharnweber *et al.*, 1971; Maruhn and Greiner, 1972) and whose success has already been tested both in nuclear fission and heavy ion reactions (see e.g., Refs. Maruhn *et al.*, 1980; Gherghescu *et al.*, 2003; Malik and Mazumdar, 2019 and references therein). Within this approach system evolves from a spherical shape to a highly deformed configuration. Such shapes are generally defined by $R = R_0(1 + \sum_l \alpha_{l0}^* Y_l^0)$ with α_{l0} and Y_l^0 are, respectively, the deformation degrees of freedom (i.e., β) and spherical harmonics.

An impact of these degrees of freedom is quite vivid in the TCSM developed by Maruhn and Greiner (1972), which involves three degrees of freedom, viz. the relative center separation R (or equivalently, the elongation parameter $\lambda = (l/(2R_0))$, with l the total length of the system and R_0 the radius of the corresponding spherical nucleus), the deformation β, the neck diameter ε. Using these degrees of freedom, the collective Hamiltonian of the symmetrically elongated shape is written as

$$\mathrm{H} = \mathrm{T}(R, \beta, \varepsilon;\ \dot{R}, \dot{\beta}, \dot{\varepsilon}) + V(R, \beta, \varepsilon), \qquad (7)$$

where a dot on a respective coordinate refers to its velocity. The collective potential energy V(R,β,ε) is obtained within the Strutinsky's method (Strutinsky, 1968) from single particle energies e_n (R,β,ε) of the TCSM and the appropriate liquid drop model of Myers and Swiatecki (1966), with a modified surface asymmetry constant (Johansson *et al.*, 1970). Thus,

$$V = V_{LDM} + \delta U + \delta P \qquad (8)$$

with δU and δP are the shell corrections and pairing contributions, respectively. These contributions involve the summation over the protons (p) and neutrons (n) states. For the interaction region, this potential energy is minimized in a self consistent manner in these shape degrees of freedom.

The shape of a nuclear system evolves continuously from a single mono-nuclear configuration to a highly deformed structure through the saddle-configuration. Each stage of evolution is determined by using self-consistent minimization of the total potential energy (equation (8)) in a three dimensional shape parameters (= R, β, ε). Because the three-dimensional self-consistent minimization is a time consuming process, so we have carried out these calculations only for ^{194}Hg in this paper.

The self-consistent minimized potential energy surface is drawn in Fig.10(a). Two minima appear in this curve, respectively, at an elongation parameters λ = 1.40 and λ = 1.65. In this curve, the first minimum corresponds to the ND state whereas the second represents the SD state. Since, the elongation parameter, λ, plays the role of an axes-ratio, *i.e.*, the ratio of semi-major to semi-minor axis. Therefore, λ-values ~1.40 and 1.65 are equivalent to deformations β~0.24 and 0.46 of the ND shape and SD shape, respectively. We would like to mention here that the ground state of ^{194}Hg is generally oblate in character. In our present calculations, the triaxial parameter γ is excluded just to preserve the axial symmetry, therefore, the quadrupole deformation of ND state (*i.e.*, β = 0.24) is different from the value reported in Ref. (Hubel *et al.*, 1986) (*i.e.*, β~0.13). On the other-hand, SD state β (= 0.46) is same as that of Sun and co-workers (1997) and also deduced from our cranking model calculations. The potential difference between the ND and SD states minima represents appropriate excitation energy of yrast SD band-head with respect to ND state. The SD band-head excitation energy represented by this potential energy difference is ~6.5 MeV and it is in good agreement with the observed value of 6.4 MeV (Sonzogni, 2008). This consistency in the observed and calculated values concludes that both pairing and shell effects play an important role in fixing the stable points of ND and SD structures in the journey of the nucleus from mono-nuclear to highly deformed configurations.

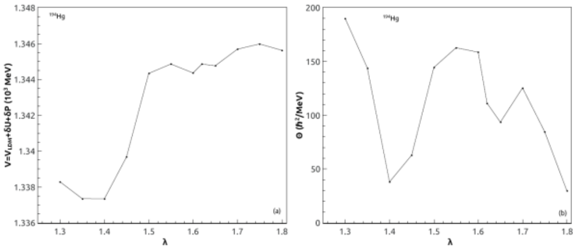

Fig. 10 Left-panel shows the interaction barrier whereas the right-panel shows the moment of inertia vs the elongation parameter λ.

In a SD system, the compound nucleus shape varies continuously from mono-nuclear configuration to a significantly deformed configuration with increasing elongation parameter λ and these shapes are well defined by the transfer of nucleons across the dividing plane through the neck of evoluting system. The single particle levels of these nucleons are responsible for determining the moment of inertia of the system. By using the TCSM states in the cranking formula based on the BCS formalism (see Refs. (Inglis, 1954; Balyaev, 1959 for details), it is given by the following expression

$$\Theta = \hbar^2 \sum_{\mu,\nu>0} \frac{\left\langle \mu \middle| \frac{\partial H}{\partial q_i} \middle| \nu \right\rangle \left\langle \nu \middle| \frac{\partial H}{\partial q_j} \middle| \mu \right\rangle}{(\widetilde{\varepsilon_\mu}+\widetilde{\varepsilon_\mu})^3} \left(u_\mu v_\nu + u_\nu v_\mu\right)^2 \quad (9)$$

In equation (9), |μ> and |ν> denote the single particle states of the TCSM and q_{ij} refers to the collective degrees of freedom like the relative separation R. Here, u_μ and v_μ correspond to the BCS-occupation numbers, and ε_μ and ε_ν represent the quasi-particle energies.

The calculated moment of inertia, as shown in Fig. 10(b), is mainly influenced by the shell structure and it varies with the elongation parameter. A significantly large value of moment of inertia at small center-separation may arise due to diabatic crossing of the single particle levels and it can, therefore, be excluded from the discussion. Following interesting points emerge from this plot.

(a) The moment of inertia of SD state corresponding to deformation, λ = 1.65 is nearly twice as large as compared to that of ND state corresponding to deformation, λ = 1.40. This conclusion is in favor of our systematic calculations.
(b) The calculated moment of inertia of SD state comes out to be ~88 ℏ²/MeV and is fully consistent with our systematic calculations carried out in section II. Since this calculated value (*i.e.*, by using TCSM) depends on the shell structure as well as pairing correlations among the nucleons. Therefore, it fully confirms that pairing is not negligible in the SD bands near their band-heads.

Thus, the predictions made on the basis of our systematic study are fully supported by the quantum mechanical calculations using cranking model together with the TCSM.

CONCLUSION

A more concrete formalism based on available experimental data plus the quantum mechanical models is discussed for the first time for obtaining the band-head characteristics of yrast SD band. The systematic study based on the experimental data is not only useful in obtaining the spin, parity and excitation energy of SD bands; but also supports a gradual increase of moment of inertia with angular momentum in a SD band. The spin-parity of the SD bands extracted from our systematic calculations are well reproduced within the principal axis cranking model. On the other hand, the two-center-shell model not only reproduces the excitation of the band-head with respect to the ND states but also gives an estimate of its (SD-band) moment of inertia which is in agreement with that obtained in our systematic study and hence, supports a finite contribution of pairing correlations among the nucleons. Thus, this determination of moment of inertia of SD bands may resolve in near future the anomalies like identical band phenomena among the neighboring SD nuclei, and the presence of ΔI = 2 staggering in the transitions among the SD states of a given nucleus.

ACKNOWLEDGEMENTS

The author (SSM) is presently working as Guest faculty at Department of Physics, Panjab University, Chandigarh. SSM thanks Panjab University for providing necessary facilities during the course of this work.

REFERENCES

Ahmad, I., M. P. Carpenter, R. R. Chasman, R. V. F. Janssens, and T. L. Khoo. 1991. Rotational bands with identical transition energies in actinide nuclei. Phys. Rev. C44: 1204.

Baktash, C., J. D. Garrett, D. F. Winchell, and A. Smith. 1992. Low-spin indentical bands in neighboring odd-A and even-even nuclei: A challenge to mean-field theories. Phys. Rev. Lett. 69: 1500.

Baktash, C., B Haas, and , and W Nazarewicz. 1995. Annu. Rev. Nucl. Part. Sci. 45: 485.

Balyaev, S.T. 1959, Kgl. Dansk. Vidensk. Sels. Mat.-Fys. Medd. 31: No. 11.

Bohr, A. and B. R. Mottelson, Nuclear structure (Benjamin, New York, 1975) Vol. II Chap. 4.

Brack, M., J. Damgaard, A. S. Jensen, H. C. Pauli, V. M. Strutinsky and C. Y. Wond. 1972. Funny Hills: The Shell-Correction Approach to Nuclear Shell Effects and Its Applications to the Fission Process. Rev. Mod. Phys. 44: 320.

Brinkman, M.J., J. A. Becker, I. Y. Lee *et al.* 1996. Decay from a superdeformed band in ^{194}Pb. Phys. Rev. C 53, R1461(R).

Byrski, T., F. A. Beck, D. Curien *et al.* 1990. Observation of identical superdeformed bands in N = 86 nuclei. Phys. Rev. Lett. 64: 1650.

Casten, R. F., N. V. Zamfir, P. von Brentano, and W.-T. Chou. 1992. Identical bands in widely dispersed nuclei. Phys. Rev. C45, R1413.

Cederwall, B., *et al.* 1994. New features of superdeformed bands in ^{194}Hg. Phys. Rev. Lett. 72: 3150.

Frauendorf, S. 2000. Symmetries in nuclear structure. Nucl. Phys. A677: 115.

Gherghescu, R.A., D. N. Poenaru and W. Greiner, in Proc. of the third Int. Conf. Edited by J. H. Hamilton, R.V. Ramayya and H. K. Carter, Published by World Scientific Publishing Co. (2003) 177.

Hackman, G., T. L. Khoo, M. P. Carpenter *et al.* 1997. Spins, Parity, Excitation Energies, and Octupole Structure of an Excited Superdeformed Band in ^{194}Hg and Implications for Identical Bands. Phys. Rev. Lett. 79: 4100.

Harris, S. M. 1964. Large-Spin Rotational States of Deformed Nuclei. Phys. Rev. Lett. 13: 663.

Hauschild, K., L. A. Bernstein, J. A. Becker et al. 1997. Yrast superdeformed band in ^{194}Pb: Jπ and Ex. Phys. Rev. C55: 2819.

Holmberg, P., and P. O. Lipas. 1968. A new formula for rotational energies. Nucl. Phys. A 117: 552.

Hubel, H., A. P. Byrne, S. Ogaza, A. E. Stuchbery, G. D. Dracoulis and M. Guttormsen. 1986. High-spin structure of $^{190–194}$Hg and the cranked shell model. Nucl. Phys. A453: 316.

Hughes, J. R., I. Ahmad, J. A. Becker et al. 1994. Lifetime measurement in excited and yrast superdeformed bands in ^{194}Hg. Phys. Rev. Lett. 72: 824.

Inglis, D. R. 1954. Particle Derivation of Nuclear Rotation Properties Associated with a Surface Wave. Phys. Rev. 96: 1059.

Johansson, T., S. G. Nilsson and Z. Szymanski. 1970. Theoretical predictions concerning superheavy elements. Ann. Phys. (Paris) 5: 377.

Khoo, T. L., M. P. Carpenter, T. Lauritsen et al. 1996. Excitation Energies and Spins of a Superdeformed Band in ^{194}Hg from One-Step Discrete Decays to the Yrast Line. Phys. Rev. Lett. 76: 1583.

Lakshmi, S., H. C. Jain, P. K. Joshi, Amita, P. Agarwal, A. K. Jain, and S. S. Malik. 2002. Shape transition and tilted axis rotation in ^{136}Ce. Phys. Rev. C66: 041303(R).

Lakshmi, S., H. C. Jain, P. K. Joshi, A. K. Jain, and S. S. Malik. 2004. Magnetic rotation and shape mixing in ^{134}Ce. Phys. Rev. C69: 014319.

Lauritsen, T., M. P. Carpenter, T. Dossing, P. Fallon, B. Herskind, R. V. F. Janssens *et al.* 2002. Direct Decay from the Superdeformed Band to the Yrast Line in ^{152}Dy$_{86}$. Phys. Rev. Lett. 88: 042501.

Lauritsen, T., M.P. Carpenter, R.V.F. Janssens et al. 2003. Linking Of Yrast And Excited Superdeformed Bands In ^{152}Dy. AIP Conference Proceedings 656: 9.

Liu, Yu-Xin., Jian-Gang Song, Hong-Zhou Sun and En-Guang Zhao. 1997. Description of superdeformed nuclear states in the interacting boson model. Phys. Rev. C 56: 1370.

Liu, Yu-Xin. 1998. Superdeformed bands in ^{148}Gd in the interacting boson model. Phys. Rev. C 58: 237.

Liu, Yu-Xin., 1998a. Superdeformed identical bands ^{152}Dy and ^{151}Tb in supersymmetry with a many-body interaction. Phys. Rev. C 58: 900.

Liu, Yu-Xin, Di Sun and En-Guang Zhao. 1999. Systematic description of the superdeformed bands of the odd-A nuclei in the A = 150 region. Phys. Rev. C 59: 2511.

Liu, Yu-Xin, and Dong-Feng Gao. 2001. Description of identical superdeformed bands with ΔI = 4 bifurcation. Phys. Rev. C 63: 044317.

Liu, Yu-Xin, Di Sun, Jia-Jun Wang and En-Guang Zhao. 2001a. Description of superdeformed identical bands of odd-A nuclei in the A∼190 mass region. Phys. Rev. C 63: 054314.

Liu, Yu-Xin, Jia-Jun Wang and Qi-Zhi Han. 2001b. Description of the identical superdeformed bands and ΔI = 4 bifurcation in the A∼130 region. Phys. Rev. C 64: 064320.

Malik, S. S., P. Agarwal, and A. K. Jain. 2004. Magnetic Rotation based on Oblate Shape in Odd Kr-Isotopes . Nucl. Phys. A732: 13.

Malik, S. S., and I. Mazumdar. 2019. Role of *F*-spin multiplets in identical band phenomena in normal deformed nuclei. Nucl. Phys. A 987: 274.

Malik, S.S. and I. Mazumdar. 2019. Role of quantum phase transition in spontaneous fission. Nucl. Phys. A990: 220.

Maruhn, J.A. and W. Greiner. 1972. The asymmetrie two center shell model. Z. Phys. 251: 431.

Maruhn, J.A., W. Greiner and W. Scheid, 1980. Heavy Ion Collisions, edited by R. Bock (North Holland, Amsterdam) Vol. 2, Chap. 6.

Myers, W. D. and W. J. Swiatecki. 1966. Nuclear masses and deformations. Nucl. Phys. 81: 1.

Riley, M.A., *et al*. 1990. Multiple superdeformed bands in ^{194}Hg and their dynamical moments of inertia. Nucl. Phys. A512: 178.

Savajols, H., *et al*. 1996. Lifetime Measurements of Superdeformed Bands in $^{148\text{-}149}$Gd and ^{152}Dy: Evidence for Structure-Dependent Elongations. Phys. Rev. Lett.76: 4480.

Scharnweber, D., W. Greiner and U. Mosel. 1971. Two-center shell model. Nucl. Phys. A164, 257.

Shalaby, A. S. 2004. Identification of bandhead spin and identical bands for odd-A nuclei in A ~ 190 Superdeformed Mass Region. Commun. Theor. Phys. 41: 454.

Shalaby, A. S. 2006. Acta Phys. Hung. A 25: 117.

Singh, B. R Zywine and R B Firestone. 2002. Nucl. Data Sheets 97: 241.

Sonzogni, A. 2008. Nuclear structure and decay data, https://doi.org/10.1051/ndata:07530.

Strutinsky, V. M. 1967. Shell effects in nuclear masses and deformation energies. Nucl. Phys. A95: 420.

Strutinsky, V. M. 1968. “Shells” in deformed nuclei. Nucl. Phys. A122: 1.

Sun, Y., J. Y. Zhang and M. Guidry. 1997. Systematic Description of Yrast Superdeformed Bands in Even-Even Nuclei of the Mass-190 Region. Phys. Rev. Lett. 78: 2321.

Twin, P. J., B. M. Nyako, A. H. Nelson et al. 1986. Observation of a Discrete-Line Superdeformed Band up to 60$\hbar$ in ^{152}Dy. Phys. Rev. Lett. 57: 811.

Wu, C. S. and J. Y. Zeng. 1987. Commun. Theor. Phys. (Beijing) 8: 51.

Wu, C. S., J. Y. Zeng, Z. Xing, X. Q. Chen, and J. Meng. 1992. Spin determination and calculation of nuclear superdeformed bands in A∼190 region. Phys. Rev. C 45: 261.

Wu, C. S. and Z. N. Zhou. 1997. ΔI = 1 staggering in odd superdeformed nuclei. Phys. Rev. C 56: 1814.

Pb. Univ. Res. J (Sci.) Vol. 70, 2020, pp 25-34

EXACT SOLITARY WAVE SOLUTIONS FOR A VARIABLE COEFFICIENT REACTION-DIFFUSION-CONVECTION MODEL

Amit Goyal[*]
Department of Physics, GGDSD College, Chandigarh 160030, India

ABSTRACT

A prototype inhomogeneous model is studied which describes the interaction between reaction mechanism, convection effect and diffusion process. The reaction-diffusion equations arises in many areas, such as flow in porous media, heat conduction in plasma, combustion problems, liquid evaporation, population genetics etc. The most of nonlinear physical phenomena are described by non- linear reaction-diffusion (NLRD) equations with variable coefficients because external factors make the density and/or temperature change in time. The exact solitary wave solutions have been obtained for NLRD equations with time-dependent coefficients of convection and reaction terms using auxiliary equation method. The effect of variable coefficients is studied on physical parameters (amplitude and velocity) of solitary wave solutions

Keywords: Interaction between reaction mechanism, convection effect and diffusion process, reaction-diffusion equations, solitary wave solutions

INTRODUCTION

Reaction diffusion (RD) equations appear in many branches of science and engineering. These equations have attracted considerable attention, as it can be used to model the evolution systems in real world. So far, a lot of studies like travelling eaves, chaotic dynamics, pattern formation etc., has been done on RD systems both theoretically and experimentally. Exact travelling wave solutions, specially solitary wave-type solutions, to nonlinear reaction diffusion (NLRD) equations plays an important role in the qualitative description of many phenomena such as flow in porous media (Pamuk, 2005), heat conduction in plasma (Wilhelmsson, 1988), chemical reactions (Yun-Quan & Jun, 2005), population genetics (Murray, 2002), image processing (Kriv´a & Mikula, 2002) and liquid evaporation (Okrasin´ski *et al.* 2001). The solitary wave solutions to NLRD equations are particularly interesting because experimental findings suggest that reaction diffusion systems may carry spatially well localized solitary patterns that behave like particles and retain their identity while interacting (Bode *et al.*, 2002; Lv & Wang, 2012).

RD equation describes the evolution of a system under the influence of diffusion and reaction. In the assembly of particles, for example cells, bacteria, chemicals, animals and so on, each particle moves in random way. This microscopic irregular movement results in some macroscopic regular motion of the group of particles which is called diffusion process. The gross movement is not a simple diffusion, but one have to consider the interaction between the particles and environment, which results the production of new particles. This constitutes the reaction process. Time evolution of a system under these two effects can be written as

$$q_t = Dq_{xx} + R(x), \tag{1}$$

where $q(x,t)$ represents the concentration of the substance, D is diffusion coefficient, $R(x)$ represents the reaction term. The study of these equations becomes even more interesting for nonlinear reaction term, because the balance between diffusion and nonlinear reaction term may results to the existence of solitary wave solutions.

It is very hard to get a macroscopic behavior from the knowledge of individual microscopic behavior, so we drive a continuum model equation for the global behavior in terms of the particle density, concentration or population. Assuming $c(x, t)$ as number of particles at time t per unit spatial dimension (area, volume, length according to the dimension which we are using), the total concentration at the spatial position x of the system is given by $x\ c(x, t)dx$. Here the functional form $c(x,t)$ is well behaved i.e. evolution of system is continuous and differentiable. This assumption seems to be quite reasonable for the system with large concentration. The diffusion equation can be obtained easily from this when combined with the phenomenological Fick's first law. This law states that the magnitude of flux flow from the regions of the high concentration to the regions of the low concentration is proportional to the concentration gradient, that is

$$j\ (x,t) = -\ D(x)\frac{\partial c}{\partial x} \tag{2}$$

where J $(x,\ t)$ is the diffusion flux which gives the

---

[*] Corresponding author: amit.goyal@ggdsd.ac.in

MS Received: May 20, 2020, Accepted: August, 2020

amount of the substance that will flow through a small area during a small time interval. *D* is the diffusion coefficient and *c* represents the concentration. Now, if the rate of change of the number of particles due to physical or chemical reasons is given by *f* (*x*, *t*, *c*), then according to the Balance law

$$\frac{\partial}{\partial t}\int_x c(x,t)\,dx = \int_s J.ds + \int_x f\big(x,t,c(x,t)\big)\,dx, \tag{3}$$

where the term on left hand side represents the rate of change of total concentration, the first term on right hand side gives the total flux and the second term represents the net growth of concentration inside the region *x*. Applying the Divergence theorem to the surface integral in Eq. (3), one obtains

$$\int_s J.ds = \int_x \partial\nabla.J(x,t)dx. \tag{4}$$

Now using Eqs. (2) and (4) in Eq. (3), it reads

$$\int_x \frac{\partial}{\partial t}c(x,t)\,dx = \int_x D(x)\frac{\partial^2}{\partial x^2}c(x,t) + \int_x f\big(x,t,c(x,t)\big). \tag{5}$$

Since the choice of region is arbitrary, it can be written as

$$\int_x \frac{\partial}{\partial t}c(x,t)\,dx = D(x)\frac{\partial^2}{\partial x^2}c(x,t) + f\big(x,t,c(x,t)\big). \tag{6}$$

This equation is known as the RD equation. Here first term on right side is the diffusion term which describes the movement of the particles and *f* (*x*, *t*, *c*(*x*, *t*)) is the reaction term which describes the various reactions occurring in the system. The diffusion coefficient *D*(*x*) is not constant in general but considering approximately homogeneous system, one can assume *D*(*x*) = *D*, and rewriting *c*(*x*, *t*) as *u*(*x*, *t*) Eq. (6) reads

$$\frac{\partial u}{\partial t} = D\frac{\partial^2 u}{\partial x^2} + f(u). \tag{7}$$

Now, the reaction term would be either linear or nonlinear depending upon the system. If it is a linear term then it can be solved easily using variable separable method. But, if reaction term is nonlinear then these nonlinear reaction diffusion (NLRD) equations can not be solved using direct methods. The two well known examples of the nonlinear reaction terms are the quadratic and cubic nonlinearity.

(i) Reaction terms with quadratic nonlinearity as

$$f(u) = k_1 u(1-u). \tag{8}$$

Hence Eq. (7) reads

$$u_t = Du_{xx} + k_1 u(1-u). \tag{9}$$

This equation models the propagation of a mutant gene with $u(x,\ t)$ denoting the density of advantageous. It is also appeared in chemical kinetics, population dynamics, flame propagation, autocatalytic chemical reactions and brownian motion process. In the past century, this equation has become a basis for a variety of equations of spatial spread. For example, the reaction term in an ecological context may represent the birth-death process, with u as the population density, with logistic population growth

$$f = ru\left(1-\frac{u}{k}\right), \tag{10}$$

where r is the linear reproduction rate and k is the carrying capacity of the environment. The resulting NLRD equation will be

$$\frac{\partial u}{\partial t} = \frac{\partial^2 u}{\partial x^2} + ru\left(1-\frac{u}{k}\right). \tag{11}$$

This equation is known as the Fisher equation after Fisher (1937) who proposed the one dimensional model for the spread of a advantageous gene in a population.

(ii) Reaction terms with cubic nonlinearity:

(iii) $f(u) = k_2 u(1-u^2)$ (12)

The corresponding NLRD equation is known as Fisher-Kolmogorov (FK) equation (Benguria & Depassier, 2005), which arises in the study of pattern formation in bistable systems (Peletier & Troy, 1997).

INLRD EQUATIONS WITH CONVECTION TERM

In a reaction diffusion system, generally, it is assumed that field is fixed i.e. spatial transport is only through diffusion. But, in a real world phenomena, the field itself usually moves. Hence, in many processes, in addition to diffusion, motion can also be due to advection or convection with some kind of back reaction, such as the spread of a favored gene, ecological competition, and so on (Nelson & Shnerb, 1998). Nonlinear convection terms arise naturally, for example, in the motion of chemotactic cells (Benguria & Depassier, 2004). From a physical point of view convection, diffusion and reaction processes are quite fundamental to describe a wide variety of problems in physical, chemical, biological sciences (Debnath, 2012). A general form of such NLRD equation with convection term is

$$u_t + vu^m u_x = Du_{xx} + f(u), \tag{13}$$

where v is convection coefficient and m is a real number. The few examples of the nonlinear equations involving the convection term are given below.

Burgers equation

It is one of the simplest nonlinear equation representing the theory of turbulence described by the interaction of convection and diffusion (Burgers, 1948)

$$u_t + v\,uu_x = Du_{xx}, \tag{14}$$

It appears in various areas of applied mathematics such as modeling of fluid dynamics, turbulence, boundary layer behavior, shock wave formation and traffic flow.

Burgers-Fisher equation

Combining Burgers and Fisher equation, the resulting equation is known as Burger-Fisher equation (Chen & Zhang, 2004), which describes the interaction of reaction mechanisms, convection effects and diffusion processes. The equation is

$$u_t + v\,uu_x = Du_{xx} + k_3 u(1-u). \tag{15}$$

The Burger-Fisher equation has a wide range of applications in plasma physics, fluid physics, capillary-gravity waves, nonlinear optics and chemical physics.

Newell-Whitehead-Segel equation

$$u_t + v\,u_x = Du_{xx} + k_3 u(1-u^2). \tag{16}$$

This equation describes the slow spatial modulation of the stripe patterns in usual pattern forming systems (Newell & Whitehead, 1969) and optical systems (Staliunas & Tlidi, 2005).

MODEL EQUATION

The literature discussing the NLRD equations is massive, but these results assume that the environment is temporally and spatially homogenous. However, this may be a rough approximation to many systems, because most of physical and biological systems are inhomogeneous due to fluctuations in environmental conditions and non-uniform media. Hence, most of real nonlinear physical equations possess variable coefficients, both in space and over time (Sophocleous, 2005; Lai *et al*. 2008; Kui *et al*. 2010). The effect of spatial inhomogeneities on NLRD systems (Nelson & Shnerb, 1998; Nakamura *et al*., 1999; Nobury & Yeh, 2001) has been discussed by many authors, but the effect of temporal inhomogeneities has not been much explored. We shall work on this problem here. There are many NLRD systems where the relevant parameters are time dependent (Neubert *et al*.; Fort & Mendez, 2002) because external factors make the density and/or temperature change in time. For example, in biological applications, such as population range expansion, for which reproductive (reactive) and mobility (diffusive) parameters change in time driven by climatic changes. The dimensionless form of the variable coefficient NLRD equation, studied here, is

$$u_t + v(t)\,u^m u_x = Du_{xx} + \alpha(t)u - \beta(t)\,u^n, \tag{17}$$

where $u = u(x, t)$, is the concentration or density variable depending on the phenomena under study; D is diffusion coefficient; v is convection term coefficient; α, β are reaction term coefficients and m, n are real numbers.

In this work, we have considered Eq. (17) for different values of m and n, and obtained propagating kink-type solitary wave solutions by using the auxiliary equation method (Sirendaoreji & Sun, 2003). For $m = 0$ and $n = 3$, Eq. (17) represents the Newell-Whitehead-Segel equation with variable coefficients. This model has been solved for bell-type solitary wave solutions with constant reaction coefficients (Kumar *et al*., 2008a; Bekir *et al*., 2012). For the same model, we have obtained kink-type solitary wave solutions and extend the formalism to obtain solitary wave solutions with inhomogeneous reaction terms. Further, we extend the analysis for inhomogeneous nonlinear convection term, i.e. for $m = 1$. For $m = 1$ and $n = 3$, Eq. (17) with constant coefficients describes the various biological and physical phenomena (Benguria *et al*., 2004 and references therein). In last, we have considered the case $m = 1$ and $n = 2$, for which Eq. (17) represents the Burger-Fisher equation with variable coefficients, and explored kink-type solutions. We have found that variable coefficients have significant effect on the amplitude and velocity of propagating kink solutions. First, we shall explain auxiliary equation method and then use it to solve variable coefficient NLRD equation for different cases.

AUXILIARY EQUATION METHOD

Sirendaoreji and Sun (2003) proposed auxiliary equation method to solve nonlinear partial differential equations (PDE's) with constant coefficients. Suppose, for a given nonlinear evolution equation with independent variables *x* and *t*, and dependent variable *u*:

$$F(u, u_x, u_t, u_{xx}, u_{tt}, u_{xt}, \ldots\ldots) = 0. \quad (18)$$

By using Galilean transformation, we can write Eq. (18) in travelling wave frame as

$$G(u, u_\xi, u_{\xi\xi}, u_{\xi\xi\xi}, \ldots.\ldots\ldots) = 0, \quad (19)$$

where $\xi = kx - \omega t$, *k* and ω are constants. Let us assume that the solution of Eq. (19) is of the following form

$$u(\xi) = \sum_{i=0}^{n} a_i z^i(\xi), \quad (20)$$

where a_i (i = 0, 1, 2, ...) are real constants to be determined, *n* is a positive integer and $z(\xi)$ represents the solutions of the following auxiliary ordinary differential equation, viz.

$$z_\xi = az(\xi) + z^2(\xi) \quad (21)$$

where *a, b, c* are constants. To determine *u* explicitly, take the following four steps.

Step 1 Substitute Eq. (20) along with Eq. (21) into Eq. (19) and balancing the highest order derivative terms with the highest power nonlinear terms in Eq. (19), to find the value of *n*.

Step 2 Again substitute Eq. (20), with the value of *n* found in Step 1, along with Eq. (21)into Eq. (19), collecting coefficients of

$$z^i z_\xi^j \ (j = 0,1; i = 0,1,2, \ldots..)$$

and then setting each coefficient to zero, to get a set of over-determined partial differential equations for a_i (i = 0, 1, 2…………), *k* and ω.

Step 3 By solving the equations obtained in Step 2, get the explicit expressions for a_i(i = 0, 1, 2………), *k* and ω.

Step 4 By using the results obtained in previous steps, obtain the exact travelling wave solution of Eq. (18) from Eq. (20) depending on the solution $z(\xi)$ of Eq. (21).

This method can also be used to solve nonlinear PDE's with variable coefficients by converting these equations into ODE's in accelerated travelling wave frame with the help of extended Galilean transformation (Greenberger, 1979). Yomba (2004) follow this procedure to solve KdV equation with variable coefficients using auxiliary equation method and Bekir *et al.* (2010) used it to solve Zakharov-Kuznetsov equation with variable coefficients using exp. function method.

$z^i z_\xi^j \ (j = 0,1; i = 0,1,2, \ldots..) a_i \ (i = 0,1,2 \ldots..), k$

V. SOLITARY WAVE SOLUTIONS

(1) Exact solutions of Eq. (17) for *m* = 0 and *n* = 3

Case (a): ***Only v is time dependent***

For this case, Eq. (17) reads

$$u_t + v(t)u_x = Du_{xx} + \alpha u - \beta u^3. \quad (22)$$

To begin with, one can assume the solution of Eq. (22) in extended Galilean frame of reference (Greenberger, 1979), $\xi = kx + \eta(t)$, *k* is constant, as

$$u(\xi) = a(t) + b(t)\ \phi(\xi), \quad (23)$$

where $\phi(\xi)$ satisfies an ordinary differential equation, viz.

$$\phi_\xi = p\phi + \phi^2, \quad (24)$$

where *p* is constant. Substituting Eqs. (23) and (24) in Eq. (22), and equating the coefficients of ϕ^i's (i = 0, 1, 2, 3) to zero, a set of equations can be found as

$$\begin{aligned}
\phi^3 &: \quad -2bDk^2 + \beta b^3 = 0, \\
\phi^2 &: \quad b\eta_t + bkv - 3pbDk^2 + 3ab^2\beta = 0, \\
\phi^1 &: \quad b_t - p^2 bDk^2 + 3a^2 b\beta - \alpha b + pb\eta_t + pbkv = 0, \\
\phi^0 &: \quad a_t + \beta a^3 - \alpha a = 0, \qquad (25)
\end{aligned}$$

Solving these equations consistently, the various unknown parameters, *a*, *b*, *k* and $\eta(t)$, found to be

$$a = \frac{p}{2} b = \sqrt{\frac{\alpha}{\beta}}$$

$$k^2 = \frac{2\alpha}{p^2 D}, \eta(t) = -k \int v(t)\, dt. \quad (26)$$

It indicates that *a* and *b* are constants. Integrating Eq. (24), the solution for $\phi(\xi)$ is found as

$$\phi(\xi) = -\frac{p}{2}\left[1 + \tanh\left(\frac{p}{2}\xi\right)\right], \quad (27)$$

Using Eqs. (23), (26) and (27), the solution for Eq. (22) reads

$$u(\xi) = -\sqrt{\frac{\alpha}{\beta}\tanh\left(\frac{p}{2}\,\xi\right)}, \tag{28}$$

where $\xi = k\ \ x - \ \ v(t)\ dt$. This implies that non-trivial time dependence of ξ can be expressed only in terms of function of $v(t)$. Here, $v(t)$ can be assumed as an arbitrary function of time which effects the velocity of wave. Typical amplitude profile of Eq. (28) is shown in Fig. 1, for $\alpha = 1$, $\beta = 1$, $D = 2$, $p = -1$, $k = 1$ and $v(t) = \cos(2t)$. It is a kink-type solitary wave solution. It is interesting to note that for small magnitude of x the function $u(x, t)$ has periodic structure in time but as magnitude of x increases, $u(x, t)$ approaches a constant value, i.e. amplitude of wave becomes constant.

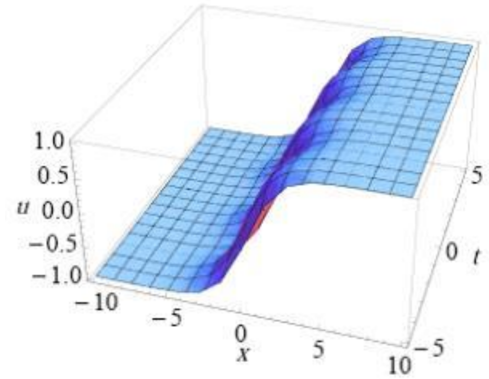

Fig. 1: Amplitude profile of $u(x, t)$, Eq. (28) for values mentioned in the text.

If it is assumed that $v(t)$ is also a constant, then the solution for Eq. (22) reads

$$u(\xi) = -\sqrt{\frac{\alpha}{\beta}}\tanh\beta\left(\sqrt{\frac{\alpha}{2D}}(x2 - vt)\right), \tag{29}$$

which is same as obtained by Kumar *et al*. (2008b).

Case (b): ***v*, *α* and *β*, all are time dependent**

In order to solve Eq. (22) for the case when v, α and β all are time dependent, following the same procedure as in last section, one will get the same set of equations as Eq. (25) with $v(t)$, $\alpha(t)$ and $\beta(t)$. Solving these equations consistently, the following relations can be found,

$$b(t) = e^{\left((\int \alpha(t))\,dt - 2p^2Dk^2t\right)},$$

$$a(t) = p\,b(t)\,, \beta(t) = \frac{2Dk^2}{b^2(t)},$$

$$\eta(t) = (-3pDk^2t - k\int v(t)dt). \tag{30}$$

The complete solution for $u(\xi)$, Eq. (17) for $m = 0$ and $n = 3$, comes out to be

$$u(\xi) = \frac{p}{2}\,e^{\left(\int 2\alpha(t)dt - 2p^2Dk^2t\right)}\left[1 - tanh\left(\frac{p}{2}\,\xi\right)2\right]. \tag{31}$$

Here, $\beta(t)$ is fixed, but $v(t)$ and $\alpha(t)$ can be chosen arbitrary functions of time. From solution, it is clear that convection coefficient effects the velocity of wave and reaction coefficient effects the amplitude of wave exponentially. Amplitude profile of Eq. (31) is shown in Fig. 2, for $D = 1$, $p = 2$, $k = 1$, $\alpha(t) = \cos(t)$ and $v(t) = \tanh(t)$. Here, the amplitude of profile is varying exponentially due to inhomogeneous reaction coefficient.

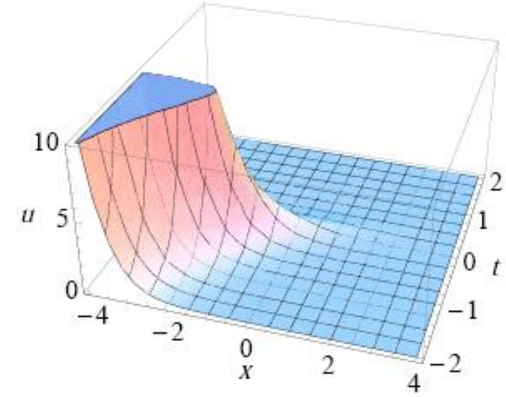

Fig. 2: Amplitude profile of $u(x, t)$, Eq. (31) for values mentioned in the text.

(2) Exact solutions of Eq. (17) for *m* = 1 and *n* = 3

Case (a): ***Only* v *is time dependent***

For this case, Eq. (17) reads

$$u_t + v(t)\,uu_x = Du_{xx} + \alpha u - \beta u^3. \tag{32}$$

Again, substituting Eqs. (23) and (24) in Eq. (32), and equating the coefficients of ϕ^i's ($i = 0, 1, 2, 3$) to zero, the following set of equations can be found

$$\begin{aligned}
&\phi^3: \quad -2bDk^2 + \beta b^3 - b^2kv = 0,\\
&\phi^2: \quad 3pbDk^2 - 3\beta ab^2 - pb^2kv - abkv - b\eta_t = 0,\\
&\phi^1: \quad p^2bDk^2 + \alpha b - 3\beta a^2b - b_t - pb\eta_t - pbkv = 0,\\
&\phi^0: \quad a_t - \alpha a + \beta a^3 = 0,
\end{aligned} \tag{33}$$

These equations can be solved only for α & $\beta < 0$. Assume $\alpha = -\alpha_1$ and $\beta = -\beta_1$, such that α_1 & $\beta_1 > 0$, and solve these equations consistently, to obtain the following relations

$$a(t) = p\,b(t) = p\sqrt{\frac{\alpha_1}{p^2\beta_1 + e^{2\alpha_1 t}}},$$

$$v(t) = \frac{2Dk}{b(t)} + \frac{\beta_1 b(t)}{k},$$
$$\eta(t) = -Dpk^2 t - \tfrac{1}{2p}\ln[p^2\beta_1 e^{-2\alpha_1 t} + 1]. \quad (34)$$

The solution for Eq. (32) using Eq. (23) and (27) becomes

$$u(\xi) = \tfrac{p}{2}\sqrt{\tfrac{\alpha_1}{p^2\beta_1 + e^{2\alpha_1 t}}}\left[1 - tanh\left(\tfrac{p}{2}\xi\right)\right]. \quad (35)$$

Typical profile of Eq. (35) is shown in Fig. 3, for $\alpha_1 = 1$, $\beta_1 = 1$, $D = 1$, $p = 1$ and $k = 1$. It is also a kink-type solitary wave solution, whose amplitude and velocity are changing with time due to time-dependent coefficient of convection term.

Case (b): ***v*, *α* and *β*, all are time dependent**

In order to solve Eq. (32) for the case when *v*, *α* and *β* all are time dependent, we considered the same set of equations as Eq. (33) with *v*(*t*), *α*(*t*) and *β*(*t*). Solving these equations consistently one can obtain the following relations,

$$a(t) = p\,b(t) = \frac{p}{\sqrt{p^2 + e^{-2\int \alpha(t)dt}}},$$
$$v(t) = \frac{2Dk}{b(t)} + \frac{\beta(t)b(t)}{k}, \qquad \beta(t) = \alpha(t)$$
$$\eta(t) = -Dpk^2 t - \tfrac{1}{2p}\ln[p^2\beta_1 e^{-2\alpha_1 t} + 1]. \quad (36)$$

The complete solution for *u*(*ξ*), Eq. (17) for *m* = 1 and *n* = 3, reads

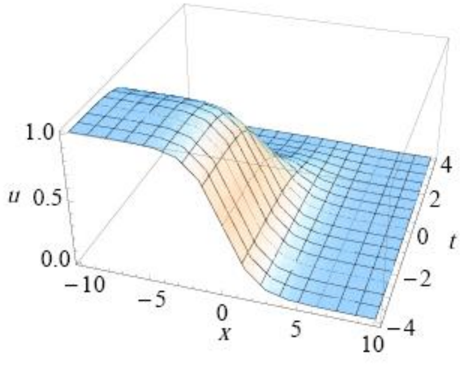

Fig. 3: Amplitude profile of *u*(*x*, *t*), Eq. (35) for values mentioned in the text.

$$u(\xi) = \frac{p}{2\sqrt{p^2 + e^{-2\int \alpha(t)dt}}}\left[1 - tanh\left(\tfrac{p}{2}\xi\right)\right]. \quad (37)$$

Here, *v*(*t*) is fixed but *α*(*t*) can be chosen arbitrarily which effects the both parameters, amplitude and velocity, of wave. Amplitude profile of Eq. (37) is shown in Figure 4, for *D* = 1, *p* = 2, *k* = 1 and *α*(*t*) = sech(*t*).

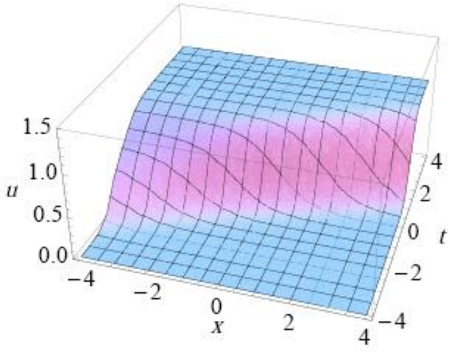

Fig. 4: Amplitude profile of *u*(*x*, *t*), Eq. (37) for values mentioned in the text.

(3) Exact solutions of Eq. (17) for *m* = 1 and *n* = 2

Case (a): ***Only* v *is time dependent***

For this case, Eq. (17) reads

$$u_t + v(t)\,uu_x = Du_{xx} + \alpha u - \beta u^2. \quad (38)$$

Substituting Eqs. (23) and (24) in Eq. (38), and equating the coefficients of ϕ^i's (*i* = 0, 1, 2, 3) to zero, a set of equations can be found as

$$\phi^3: \quad b^2kv - 2bDk^2 = 0,$$
$$\phi^2: \quad \beta b^2 + abkv + pb^2kv - 3pbDk^2 + b\eta_t = 0,$$
$$\phi^1: \quad -\alpha b + 2\beta ab + pbkv - p^2bDk^2 + b_t + pb\eta_t = 0,$$
$$\phi^0: \quad -\alpha a + \beta a^2 + a_t = 0, \quad (39)$$

Solving these equations consistently, the various unknown parameters can be obtained as

$$\beta = \alpha, a(t) = pb(t),$$
$$b(t) = \frac{1}{2p}\left[1 - tanh\left(\frac{-\alpha t}{2}\right)\right] = \frac{1}{p(1 + e^{-\alpha t}},$$
$$\upsilon(t) = \frac{2Dk}{b(t)} = 2pDk\,(1 + e^{-\alpha t}),$$
$$n(t) = \int -\left(pDk^2 + \alpha\,b(t)\right)dt$$
$$= -\left(pDk^2 + \tfrac{\alpha}{2p}\right)t - \tfrac{1}{p}\,In\,cosh\left(\tfrac{-\alpha t}{2}\right) \quad (40)$$

Using Eqs. (23), (27) and (40), the solution for Eq. (38) will take the form as

$$u(\xi) = \tfrac{1}{4}\left[1 - tanh\left(\tfrac{-\alpha t}{2}\right)\right]\left[1 - tanh\left(\tfrac{p}{2}\xi\right)\right]. \quad (41)$$

Typical amplitude profile of Eq. (41) is shown in Figure 5, for $\alpha = 1$, $D = 1$, $p = 1$ and $k = 1$. It is a kink-type solitary wave solution, whose amplitude and velocity are changing with time due to time- dependent coefficient of convection term.

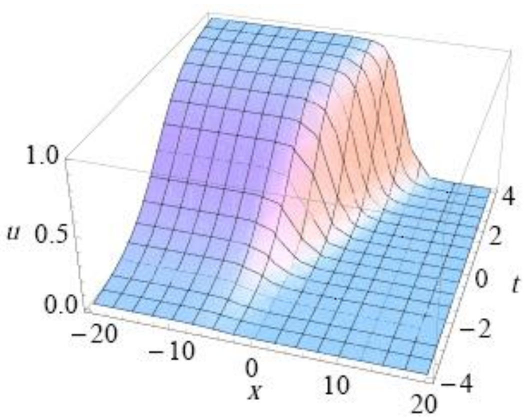

Fig. 5: Amplitude profile of $u(x, t)$, Eq. (41) for values mentioned in the text.

Case (b): ***v*, *α* and *β*, all are time dependent**

In order to solve Eq. (38) for the case when v, α and β all are time dependent, following the same procedure, the same set of equations can be found as Eq. (39) with time dependent coefficients. Solving these equations the unknown parameters are

$$\beta(t) = \alpha(t), \qquad a(t) = p\,b(t),$$
$$v(t) = \frac{2Dk}{b(t)} = 2pDk\left(1 + e^{-\int \alpha(t)dt}\right),$$
$$\eta(t) = \int -\left(pDk^2 + \alpha(t)b(t)\right)dt.$$
$$= -pDk^2 t - \frac{1}{2p}\int \alpha(t)dt - \frac{1}{p}\ln\cosh\left(-\frac{1}{2}\int \alpha(t)\,dt\right).$$

The complete solution for $u(\xi)$, Eq. (17) for $m = 1$ and $n = 2$, comes out to be

$$u(\xi) = \frac{1}{4}\left[1 - \tanh\left(\frac{\int -\alpha(t)dt}{2}\right)\right]\left[1 - \tanh\left(\frac{p}{2}\xi\right)\right]. \qquad (42)$$

Here, $v(t)$ is fixed but $\alpha(t)$ can be chosen arbitrarily which effects the both parameters, amplitude and velocity, of wave. Typical amplitude profile of Eq. (42) is shown in Figure 6, for $p = 1$, $D = 1$, $k = 1$, and $\alpha(t) = \cos(t)$.

Special case

If we assume Eq. (38) for the case when v, α and β all are constant, then by following the same procedure, one can obtain the various parameters as

$$a = 1, b = \frac{1}{p}, \; v = 2pDk,$$
$$\eta(t) = \left(pDk^2 - \frac{\alpha}{p}\right)t. \qquad (43)$$

Hence, the solution for constant coefficient equation becomes

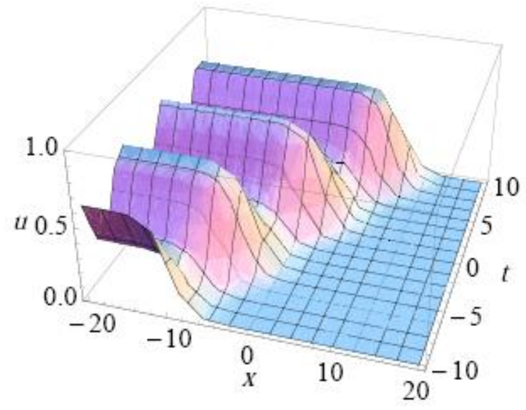

Fig. 6: Amplitude profile of $u(x, t)$, Eq. (42) for values mentioned in the text.

$$u(\xi) = \frac{1}{2}\left[1 - \tanh\left(\frac{p}{2}\xi\right)\right]. \qquad (44)$$

which is of same form as obtained by Chen and Zhang (2004).

CONCLUSION

We have studied a prototype model for the reaction, diffusion and convection processes with inhomogeneous coefficients. Employing auxiliary equation method, the kink-type solitary wave solutions have been found for variable coefficient Burgers-Fisher and Newell-Whitehead-Segel (NWS) equation. It is observed that time dependent reaction and convection coefficients will effect the wave parameters, like amplitude and velocity. It is found that for linear convection term and cubic nonlinear reaction term, that is NWS equation for $m = 0$ and $n = 3$, the convection coefficient $v(t)$ and one of the reaction coefficient $\alpha(t)$ can be chosen arbitrary functions of time whereas other reaction coefficient $\beta(t)$ is fixed. Here, the convection coefficient effects the velocity of wave whereas reaction coefficient effects the amplitude of wave exponentially. For $m = 1$ and $n = 3$ case, only reaction term coefficient can be chosen arbitrarily which effects the both parameters of wave. For Burgers-Fisher equation, that is $m = 1$ and $n = 2$ case, again reaction term coefficient can be chosen arbitrarily. For constant coefficients, the results are same as the previous results. Hence, the variable coefficients help us to control the properties of solitary wave solutions in RD system. The variation of amplitude of waves has been shown for different functional form of the variable coefficients. The results obtained here may be useful for the one who is working on specific phenomena based on RD type equations. The approach applied in this work is general and can be employed in further works to obtain exact solutions for other types of nonlinear equations with variable coefficients.

REFERENCES

Bekir A. and E. Aksoy. 2010. Exact solutions of nonlinear evolution equations with variable coefficients using exp-function method. *Applied Mathematics and Computation*, 217(1):430–436.

Bekir A., E. Aksoy, and O¨. Gu¨ner. 2012. Bright and dark soliton solutions for variable-coefficient diffusion–reaction and modified Korteweg–de Vries equations. *Physica Scripta*, 85(3): 035009.

Benguria R. D. and M. C. Depassier. 2005. On the transition from pulled to pushed monotonic fronts of the extended Fisher–Kolmogorov equation. *Physica A: Statistical Mechanics and its Applications*, 356(1):61–65.

Benguria R. D., M. C. Depassier, and V. M´endez. 2004. Minimal speed of fronts of reaction-convection-diffusion equa- tions. *Physical Review E*, 69(3):031106.

Bode M., A. W. Liehr, C. P. Schenk, and H. G. Purwins. 2002. Interaction of dissipative solitons: particle-like behaviour of localized structures in a three-component reaction-diffusion system. *Physica D: Nonlinear Phenomena*, 161(1):45–66.

Burgers J. M. 1948. A mathematical model illustrating the theory of turbulence. *Advances in Applied Mechanics*, 1:171–199.

Chen H. and H. Zhang. 2004. New multiple soliton solutions to the general Burgers–Fisher equation and the Kuramoto–Sivashinsky equation. *Chaos Solitons and Fractals*, 19(1):71–76.

Debnath L. 2012. *Nonlinear partial differential equations for scientists and engineers*. Springer.

Fisher R. A. 1937. The wave of advance of advantageous genes. *Annals of Eugenics*, 7(4):355–369.

Fort J. and V. M´endez. 2002. Wavefronts in time-delayed reaction-diffusion systems. Theory and comparison to experiment. *Reports on Progress in Physics*, 65(6):895.

Greenberger D. M. 1979. Some remarks on the extended Galilean transformation. *American Journal of Physics*, 47:35–38.

Kriv´a Z. and K. Mikula. 2002. An adaptive finite volume scheme for solving nonlinear diffusion equations in image processing. *Journal of Visual Communication and Image Representation*, 13(1):22–35.

Kui C. B., MS Qiang, and WB. Hong. 2010. Exact solutions of generalized Burgers–Fisher equation with variable coefficients. *Communications in Theoretical Physics*, 53(3):443.

Kumar R., R. S. Kaushal, and A. Prasad. 2008a. Soliton-like solutions of certain types of nonlinear diffusion–reaction equations with variable coefficient. *Physics Letters A*, 372(11):1862–1866.

Kumar R., R. S. Kaushal, and A. Prasad. 2008b. Some new solitary and travelling wave solutions of certain nonlinear diffusion–reaction equations using auxiliary equation method. *Physics Letters A*, 372(19):3395–3399.

Lai S., X. Lv, and Y. Wu. 2008. Explicit solutions of two nonlinear dispersive equations with variable coefficients. *Physics Letters A*, 372(47):7001–7006.

Lv G. and M. Wang. 2012. Nonlinear stability of traveling wave fronts for delayed reaction diffusion systems. *Nonlinear Analysis: Real World Applications*, 13(4):1854–1865.

Murray J. D. 2002. *Mathematical biology I: an introduction*. Springer.

Nakamura K. I., H. Matano, D. Hilhorst, and R. Sch¨atzle. 1999. Singular limit of a reaction-diffusion equation with a spatially inhomogeneous reaction term. *Journal of Statistical Physics*, 95(5-6):1165–1185.

Nelson D. R. and N. M. Shnerb. 1998. Non-Hermitian localization and population biology. *Physical Review E*, 58(2):1383.

Neubert M. G., M. Kot, and MA Lewis. 2000. Invasion speeds in fluctuating environments. *Proceedings of the Royal Society of London, Series B: Biological Sciences*, 267(1453):1603–1610.

Newell A. C. and J. A. Whitehead. 1969. Finite bandwidth, finite amplitude convection. *Journal of Fluid Mechanics*, 38(02):279–303.

Norbury J. and L. C. Yeh. 2001. Inhomogeneous fast reaction, slow diffusion and weighted curve shortening. *Nonlin- earity*, 14(4):849.

Okrasin´ski W., M. I. Parra and F. Cuadros, 2001. Modeling evaporation using a nonlinear diffusion equation. *Journal of Mathematical Chemistry*, 30(2):195–202.

Pamuk S. 2005. Solution of the porous media equation by Adomian's decomposition method. *Physics Letters A*, 344(2):184–188.

Peletier L. A. and W. C. Troy. 1997. Spatial patterns described by the extended Fisher–Kolmogorov equation: periodic solutions. *SIAM Journal on Mathematical Analysis*, 28(6):1317–1353.

Sirendaoreji and J. Sun. 2003. Auxiliary equation method for solving nonlinear partial differential equations. *Physics Letters A*, 309(5-6):387–396.

Sophocleous C. 2005. Further transformation properties of generalised inhomogeneous nonlinear diffusion equations with variable coefficients. *Physica A: Statistical Mechanics and its Applications*, 345(3):457–471.Yomba E. 2004. Construction of new soliton-like solutions for the (2 + 1) dimensional KdV equation with variable coefficients. *Chaos Solitons and Fractals*, 21(1):75–79.

Staliunas K. and M. Tlidi. 2005. Hyperbolic transverse patterns in nonlinear optical resonators. *Physical Review Letters*, 94(13):133902.

Wilhelmsson H. 1988. Simultaneous diffusion and reaction processes in plasma dynamics. *Physical Review A*, 38(3):1482.

Yun-Quan K. E. and Y. U. Jun. 2005. The first integral method to study a class of reaction-diffusion equations. *Communications in Theoretical Physics*, 43(4):597.

Pb. Univ. Res. J (Sci.) Vol. 70, 2020, pp 35-52

THEORETICAL INTERPRETATION OF HEAVY-ION REACTIONS AT LOW ENERGIES

Pooja Kaushal
Department of Physics, Panjab University, Chandigarh-160014

ABSTRACT

A number of emission processes are possible from the ground state of parent nucleus and from the excited compound nuclear systems formed in heavy-ion induced reactions at low energies. Relevant theoretical models mainly fall under two main categories, viz., (i) the cluster models, where the preformation probability, $P_0 \neq 1$, and (ii) the fission models, where $P_0 \approx 1$. These models are developed broadly in the framework of Quantum Mechanical Fragmentation Theory (QMFT) and are mainly distinguished by the inclusion or non-inclusion of the concept of cluster preformation probability, P_0. The inclusion of P0 in the cluster models refers to the incorporation of nuclear structure effects in the decaying nucleus, which are completely ignored in fission models. Finally, a theory for cluster formation in nuclei and in heavy-ion collisions has been worked out in terms of QMFT wherein the Dynamical Cluster-decay Model (DCM) is introduced. The article reviews the progress made in DCM and its applications in studying the compound nucleus formation probabilities in the low-energy heavy-ion reactions at various center-of-mass energies and the decay mechanism of the compound nuclei.

Keywords: Heavy-ions nuclear reactions, compound nucleus formation and decay mechanism, Quantum mechanical fragmentation theory, Dynamical Cluster-decay Model.

INTRODUCTION

In case of heavy-ion collisions, the interaction potential comprises of not only the repulsive Coulomb force, but also the attractive nuclear force, though short-ranged, but it is this force that plays a crucial role in compound nucleus formation process. In order to form a compound nucleus, the kinetic energy associated with the entrance channel should be sufficient enough to overcome the Coulomb barrier and come well into the nuclear attraction range. Depending upon the kinetic energy possessed by the colliding nuclei, the Coulomb barrier could either be crossed over or quantum mechanical tunneling of the barrier may occur. A new possibility arises when the associated kinetic energy is not enough that the Coulomb barrier could be crossed following which the composite system might not form a true compound nucleus, but decays via some competing non-compound nuclear processes, reseparating prematurely. It has been observed experimentally that on the basis of excitation energy, angular momentum and mass asymmetry of the entrance channel, the composite system produced as a result of heavy-ion collision, may either form an equilibrated compound nucleus or the projectile gets captured by the target for a short period of time and reseparates much earlier than the evolution of final equilibrated compound nucleus. The heavy-ion reactions also contribute towards synthesis of super-heavy nuclei, which further paved way for the discovery of these non-compound nucleus processes like quasi-fission, fast fission; deep inelastic collision (DIC), incomplete fusion (ICF). In heavy ion collisions, forming of evaporation residues (ER) is profoundly repressed by fission and quasi-fission-like non-compound nucleus (nCN) processes (Swiatecki, 1981; Bjornholm *et al*., 1982; Blocki *et al*., 1986) (see, Fig. 1.1). The sticking time is one of the major factors determining the future of composite system after collision of target and projectile. It is anticipated that the sticking time is associated with compound nucleus formation probability, P_{CN}. For the case of fission following fusion, the projectile-target system sticks together for additional period (10^{-18}–10^{-16} sec) and typically completes several collisions/rotations. However, if the time of interaction is short (~ 10^{-20} sec), the system splits into fragments before a complete equilibration. Charge product Z_pZ_t (projectile and target proton numbers, respectively) is another major factor playing a decisive role in dynamical evolution of trajectories of heavy-ion reactions. Entrance channel mass asymmetry, $\eta = A_1 - A_2/A_1 + A_2$ (A_1, A_2 being mass numbers of the heavy and corresponding lighter nuclei, respectively) is another important quantity for understanding of saddle point behaviour and its stability with respect to the Businaro-Gallone mass asymmetry, α_{BG} (Businaro *et al*.,1957). For $\eta < \alpha_{BG}$, mass transfer takes place from projectile to target nucleus resulting into dinuclear system that reseparates prior to is equilibration in all degrees of freedom, favoring more asymmetric shapes leading to quasi-fission. On the

---

* Corresponding author e-mail: poojaphysics7@gmail.com
MS Received: September 16, 2020, Accepted: November 15, 2020

other hand, for $\eta > \alpha_{BG}$, the direction of mass drift is preferably in reverse order that leads to compound nucleus formation (Pant *et al*., 1996). Theoretical explanation of asymmetric shape, taking into account the fragment shell properties, was given by Meitner as early in 1950 (Meitner, 1950). In addition to this, the orientation of the projectile with respect to the target nucleus at the time of collision, also plays an important role in deciding the final outcome of such a collision. The lateral or sideways contact (analogous to high capture barrier) of the projectile with target fosters the formation of compound nucleus, whereas an elongated contact (analogous to a lower barrier) enhances the quasi-fission probability (Hinde *et al*., 2002; Denisov *et al*. 2002; Hinde *et al*. 1995; Hinde *et al*. 1996). The fission dynamics of different isotopes of a nucleus, neutron to proton ratio and contributions from near scission configurations are other factors that affect the fusion-fission dynamics. These low energy heavy-ion reactions can be categorized as fusion reactions and fusion-fission processes.

Fusion reactions are pure compound nucleus processes where absolute transmittal of mass, kinetic energy, and angular momentum between the entrance channel takes place. The complete rotation of the composite system leads to the formation of a fully equilibrated compound nucleus followed by complete identity loss of the interacting entities. The compound nucleus, so formed decays via (a) light particles (n, p, α) and/ or γ rays that are collectively known as evaporation residues, (b) intermediate mass fragments or group of nuclei in the window of $5 \leq A \leq 20$ and $2 \leq Z \leq 10$, and (c) symmetric or near symmetric fission fragments. It is to be noted that amalgamation of the above referenced processes, (a)−(c), or predominantly a particular one out of them is possible for different compound nuclei belonging to distinct mass regions. For instance, lighter compound systems such as ^{105}Ag$*$ (Chopra *et al*.; 2013), ^{117}Sb$*$ (Kaushal, 2020), ^{120}Te$*$ (Kaushal, 2020), and ^{124}Ce$*$ (Kaur *et al*., 2014) have evaporation residues as the predominant decay mode with a small contribution from Intermediate mass fragments. In case of medium mass systems like ^{202}Po$*$ formed via various entrance channels, for eg., $^{16}O+^{186}Os\rightarrow^{202}Po*$ and $^{34}S+^{168}Er\rightarrow^{202}Po*$ (Morton *et al*., 2000; Rafiei *et al*., 2008), both evaporation residue and fission processes compete. In this process, the decaying nucleus may go to ground state or to both ground state and excited state(s), including the isomeric, metastable state(s) of the daughter nucleus.

Fusion-fission reactions are the reactions where the pure compound nucleus-content is small, comprising primarily of fusion-fission (ff) and quasi-fission (qf) or qf-like, nCN processes that include Deep Inelastic Collision (DIC) and Incomplete Fusion (ICF). The beam energy and mass-asymmetry [associated with the product (ZpZt) of the atomic numbers of the projectile (Zp) and target (Zt)] associated with the entrance channel nuclei play a decisive role in differentiating these nCN processes from each other.

(a) Quasi-fission (qf): In this process, there is partial transfer of kinetic energy and angular momentum that leads to exchange of only a few nucleons with surfaces of interacting nuclei overlapping for a very short duration of time, resulting in restricted rotation of the composite system. This happens due to fast breakup of partially fused composite system. The identities of the interacting partners do not get destroyed and the interaction time ($10^{-21}-10^{-18}$ sec), lies halfway between deep-inelastic collisions and compound nucleus reactions. In quasi-fission, the dinuclear composite system enters into the fission valley during the time of descent from saddle-to-scission point. The composite system breaks into fragments prior to complete mass equilibrium, and have strong mass-angle correlation that consequently inhibits evaporation residue production. In this case, a leading role is played by the properties of the colliding nuclei that include their mass-asymmetry (the product Z_pZ_t) and deformations (Swiatecki, 1981; Bjornholm *et al*., 1982; Blocki *et al*., 1986; Back *et al*., 1996; Hinde *et al*., 2002). It is to be added here that onset of quasi-fission is governed by a critical Z_pZ_t value. While the earlier experiments predict this value to be around 1600 (Swiatecki, 1981; Bjornholm *et al*., 1982; Blocki *et al*., 1986) the latest research in this particular area suggests that quasi-fission begins around $Z_pZ_t = 1000$ (Rafiei *et al*., 2008). Also, further enhancement of quasi-fission occurs, when the target nuclei are sufficiently deformed (Hinde *et al*., 1996).

(b) Fast fission: The phenomenon of fast fission has properties that are intermediate between deep inelastic and compound nucleus reactions. In this process, the composite system becomes unstable and hinders compound nucleus formation due to negligibly small fission barrier. As a result, the system undergoes re-separation much earlier than the forming of compound nucleus and fission occurs prior to the equilibration stage. Such a reaction process occurs at high bombarding energies and for systems having larger fissility and smaller fission barrier. Fast fission is further probable when the configuration attained during capture phase is in between saddle and scission point regions (Grégoire *et al*., 1982).

(c) Deep Inelastic Collision (DIC): Dissipation of enormous amounts of kinetic energy and angular momentum, followed by exchange of nucleons in significant numbers, occurs in case when the target and projectile cling together for a comparatively protracted period of time. This is the case of DIC, where the target-projectile (t-p) mass-asymmetry is conserved (Schröder *et al*., 1984). This is the predominant mode when the entrance channel comprises of symmetric t-p combinations meaning, thereby, that such a nuclear system is also characterized by large Coulomb repulsions. Note that the reaction time scale for DIC is lesser than that of quasi-fission.

(d) In-Complete Fusion (ICF): In ICF reactions, only some portion of the projectile gets fused to the target nucleus resulting in formation of an incompletely fused, excited composite system, which has lower mass and charge than the compound nucleus (Siemsen, 1983). Due to partial transfer of the projectile's angular momentum, the remaining part of the projectile escapes in forward cone with nearly the same beam velocity. ICF occurs predominantly, where the target-projectile combinations are more asymmetric. Also, the ICF starts becoming more dominant with increase of the energy of the projectile (Corsi *et al*., 2009; Gupta *et al*., 2008).

COLD VERSUS HOT FUSION

Further, if such a compound nucleus with excitation energy ranging 10−20 MeV, de-excites by emitting 1−2 neutrons, it is known as "cold fusion" phenomena. On the other hand, "hot fusion" reaction occurs, if this range is 40−50 MeV and the emitted number of neutrons are more than 2. The idea of "cold fusion" in terms of Quantum Mechanical Fragmentation Theory (QMFT) was for the first time given by Gupta and Greiner along with their collaborators (Maruhn *et al*., 1974; Gupta *et al*., 1975; Gupta *et al*., 1999) in 1974−75. Cold fusion reactions corresponding to the minimas are characterized by lowest interaction barrier accompanied by largest interaction radius with elongated, "non-compact" nuclear shape, while hot fusion reactions are the ones with largest interaction barrier and smallest (most compact) interaction radius corresponding to "compact" nuclear shape. Quantum-mechanically, the fusion process refers to tunneling through the 1-d barrier comprising of the Coulomb, centrifugal and nuclear potentials. Thus, the understanding of the nucleus-nucleus interaction potential is essential in order to study various aspects of nuclear reaction dynamics.

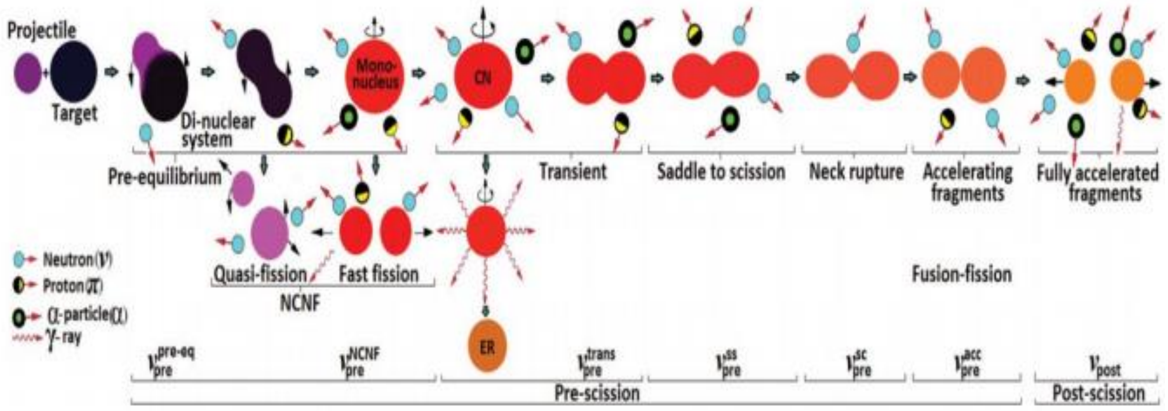

Fig. 1.1: Schematic representation of various decay processes in low energy heavy-ion reactions, from (Banerjee *et al*., 2019).

Frequently employed probes used to analyze the heavy-ion induced fusion-fission reaction mechanism include pre-scission neutrons, pre-scission γ-rays, evaporation residue measurements, pre-scission charged particles, measurements of fission fragment mass-energy correlations, measurements of fission fragment angular distribution, K-shell ionization and crystal blocking. The dissipation and the fission survival time for fusion-fission reactions can be calculated using these probes. Out of all the above-mentioned probes, the pre-scission neutrons are extensively used to comprehend the fission dynamics.

During fission process, many neutrons are emitted, before and after the scission. Neutrons that are emitted prior to the fission process are termed the pre-scission neutrons. The major advantage of using this probe is the absence of the Coulomb barrier. Neutron emission serves as a clock for measuring fission time scale and has proved to be quite useful in investigation of the nuclear fission mechanism. This is so because neutrons from a hot compound nucleus are emitted in succession until it fissions and thus the pre-scission neutron multiplicity acts as a measure of the fission time scale (Ramachandran *et al*., 2015). Neutron multiplicity is defined as the average number of neutrons emitted per fission event. The multiplicity of neutrons for quasi-fission process is lower than that for the fusion-fission process. In theoretical description, the emission of neutrons in fusion-fission reactions can occur at different phases of the reaction process such as (i) the compound nucleus formation stage, (ii) pre-saddle, and (iii) saddle-to scission stage. Fig. 1.1 shows the classification of neutrons emitted during various stages from equilibrium to scission point. In heavy-ion reactions, equilibration of energy occurs prior to other degrees of freedom. Neutrons may be emitted from the di-nuclear complex as it evolves towards formation of an equilibrated compound nucleus. So, neutron emission during the compound nucleus formation phase provides a crucial contribution towards the pre-scission neutron yield. The emission of neutrons can also take place during pre-saddle stage but this is accompanied by complete hinderance of the fission process. During this time, the neutrons emitted cannot contribute much towards the pre-scission neutron multiplicity. Once the saddle point is reached, the compound nuclear system is committed to fission as per Bohr-Wheeler nuclear fission model (Bohr and Wheeler, 1939), but it takes finite time to attain the scission stage (due to viscous characteristic of nuclear matter). Further, Hoffman and Nix (Hoffmann and Nix, 1983) showed that saddle-to-scission time increases with increase in fissility of the fissioning nucleus. This is because the difference of potential energy between the saddle and scission points increases with fissility. Thus, neutrons emitted during saddle-to-scission transition may also make a contribution to the pre-scission neutrons.

THEORETICAL FRAMEWORK

The relevant theoretical models are developed broadly in the framework of Quantum Mechanical Fragmentation Theory (QMFT). This methodology establishes a quantum concept of probability along with role of the shell effects for evaporation residue, fusion-fission, spontaneous fission and cluster radioactivity etc.

Quantum Mechanical Fragmentation Theory (QMFT): In QMFT, the quantum mechanical concept of probability is used to investigate the role of shell effects in fusion, fission and cluster radioactivity. QMFT is worked out in terms of the following collective variables:

(i) Relative separation, R, of the two interacting/ decaying fragments.

(ii) Multiple parameters $\beta\lambda i$ (λ = 2,3, 4... and i = 1,2), i.e., deformations of the two fragments; corresponding orientation degrees-of-freedom θi , i = 1,2 and Azimuthal angle Φ between the principal planes of deformed nuclei, illustrated in Fig. 1.2.

(iii) Neck-length or the barrier lowering parameter ΔR between the two interacting nuclei, following the relation $R = R1+R2+\Delta R$.

(iv) Mass (and charge) asymmetries, expressed as:

$$\eta = A_1 - A_2 /A \; ; \; \eta_Z = Z_1 - Z_2 /Z \tag{1}$$

Similarly,

$$\eta_N = N_1 - N_2/N \tag{2}$$

represents the neutron asymmetry. These are further associated as

$$\eta = \frac{Z}{A}\eta Z + \frac{N}{A}\eta N \tag{3}$$

wherein $A = A_1 + A_2$, $Z = Z_1 + Z_2$ and $N = N_1 + N_2$. A_i, Z_i and N_i (i = 1, 2) are the mass, charge and neutron number of two nuclei, respectively. The constraining values of η are $0 \leq |\eta| \leq 1$, accounting for an integrated interpretation for transfer of few-nucleons, cluster (multi-nucleon) transfer, complete fusion of nuclei ($|\eta| = 1$) and fission of compound nucleus that could either be symmetric ($\eta = 0$), asymmetric or super-asymmetric. Similarly, η_Z coordinate represents the associated charge distribution effects. Nuclear structure effects, which take into account the deformations of the fragments, strongly influence the heavy-ion reaction dynamics. The higher order multipole deformations of the nuclei, $\beta_{\lambda i}$ ($\lambda = 2,3,4$), correspond to deviation from spherical nuclear shape. It is important to note that while considering deformed configuration of a nuclear system, their corresponding orientations *w.r.t.* each other cannot be ignored. Therefore, along with deformations, appropriate choice of orientations of nuclei is equally important to understand the dynamics of heavy-ion reactions under extreme conditions. Further, it has been shown by Gupta and collaborators on the basis of QMFT collaborators (Maruhn *et al.*, 1974; Gupta *et al.*, 1975; Gupta *et al.*, 1999) that in collisions of deformed oriented nuclei, the barrier height and interaction radius, *i.e.*, the shape of nuclear interaction potential gets affected which leads to enhancement of fusion cross sections. For β_{2i} deformations, optimum orientations are assigned to hot fusion and cold fusion reactions characterized by "hot (compact)" and "cold (elongated)" configurations, respectively, corresponding to highest interaction barrier (or smallest, most compact interaction radius) and lowest interaction barrier (or largest interaction radius). Unaffected by signs of β_{4i} deformations, the θ_i^{opt} orientations are uniquely fixed or optimized according to the signs (i.e., +, - or zero) of β_{2i} deformations. The compact orientations, θ_{ci}, however refer to collisions occurring at smallest interaction radius (Gupta *et al.*, 2005; Gupta *et al.* 2006). Therefore, for proper understanding of nuclear reaction dynamics, an explicit inclusion of deformation and orientation effects becomes extremely important. In QMFT based DCM (Gupta *et al.* 2005; Singh *et al.* 2008; Sharma *et al.* 2011), along with inclusion of temperature and angular momentum, the deformations and orientation effects of the reaction partners/decay fragments are taken care. In nature, deformed nuclei can however be oriented either in same plane ($\Phi = 0^0$) or different planes ($\Phi_c \neq 0^0$). A detailed analysis of various orientations associated with nuclei deformed upto hexadecapole parameters, can be studied from (Gupta *et al.*, 2006). The application of including these additional degrees of freedom, especially the higher multipole deformations and non-coplanarity, has been studied for different radioactive and non-radioactive compound nuclear systems like ^{202}Po*, ^{246}Bk*, ^{220}Th*, ^{105}Ag*, ^{196}Pt* and ^{164}Yb* (Chopra *et al.*, 2018). This calls for a theory or model that deals with all the aspects of compound nucleus decay and can efficiently analyze different channels through which the compound nucleus decays/formed.

Based on the above discussed Quantum mechanical fragmentation theory, the theoretical models are broadly classified as (i) the cluster models, where the preformation probability, $P_0 \neq 1$, and (ii) the fission models, where $P_0 \approx 1$. Fission and cluster decay include two distinct physical approaches theoretically. In case of cluster decay, it is assumed that the cluster gets pre-formed in the mother/decaying nucleus prior to its penetration into the nuclear interaction barrier. Whereas, in fission, there is a continuous deformation of nucleus as it penetrates the interaction barrier. As the system reaches the saddle configuration, the charge as well as mass of fission fragments remain fixed. The system finally attains the scission configuration simply by running down the Coulomb barrier. Various theoretical models on the basis of such concepts have been proposed for both cluster decay and fission processes by numerous theoretical groups (Santhosh *et al.*, 2012). These models are briefly discussed as follows:

A. The Unified Fission Models (UFM)

In case of fission process, two approaches are followed. In the first approach, without caring for cluster getting pre-formed or not in the parent nucleus, the quantum mechanical penetration of barrier as proposed by Gamow (Gamow, 1928) is used. In Unified Fission Models (UFMs), the three processes, viz., α decay, cluster decay and fission, cannot be distinguished from each other. Alternately, in other fission approaches, there is continuous deformation of the parent nucleus, thus reaching the saddle or scission shape. The basis of all fission models involve the concept of barrier penetration, so these approaches can also be applied to cluster decay process. The central idea involved in UFMs is that the α particle and the heavy cluster(s) have equally probable preformation probabilities, i.e., $P_0 = 1$. Thus, UFMs do not contain the necessary structural information. Various variants of UFMs include the Saddle point fission model, Cubic plus quadratic parabolic nuclear potential model, Cubic plus Yukawa-plus exponential potential model, Analytical super asymmetric fission model, Nuclear proximity potential model, Coulomb and proximity potential model and Coulomb and proximity potential model for deformed nuclei (Santhosh *et al.*, 2012). Săndulescu, Poenaru and Greiner (Sandulescu *et al.*, 1980) performed a theoretical calculation involving cluster decay using such a theoretical unified fission model named the Analytical Super Asymmetric Fission Model (ASAFM). It is basically a fission model for α decay further adapted to include heavy cluster decays, taking angular momentum and excitation effects into account. ASAFM can be applied for α decay studies and emissions from excited states of parent nucleus. The realistic calculations were carried out for the first by Shi and Swiatecki (Shi and Swiatecki, 1985) by including proximity and Coulomb interaction. Hence, Nuclear proximity potential model was developed, wherein the energy barrier corresponding to touching and separated configuration comprises of the Coulomb repulsion among the colliding nuclei and the nuclear proximity potential of Blocki *et al.* (Blocki *et al.*, 1977), (Blocki's pocket formula), came into existence. The Blocki formula is based on proximity theorem which states that the force of interaction amid two arched entities in close proximity is directly proportional to the interaction potential/unit area or the product of geometrical factor and a universal function (associated with surface energy coefficient), and is independent of the masses of the interacting nuclei. The Coulomb barrier height and width of the interaction potential gets significantly reduced via incorporation of nuclear proximity. The model was further refined to include the ground state deformations corresponding to parent/daughter nuclei along with attenuation of shell effects due to nuclear interactions between the fragments concerned. It is a difficult task to ascribe a unique nuclear potential, which can be extensively employed for probing and analyzing distinct reaction mechanisms on one single platform. The role of colliding nuclei in the expression for nuclear potential can be analyzed in terms of geometrical factor (that is proportional to the reduced radii of colliding nuclei) and a universal function (which depends on minimum separation distance between interacting nuclei and is independent of shapes and geometry of nuclear system). Thus, free of any adjustable parameters, the proximity potential of Blocki *et al.* (Blocki *et al.*, 1977) uses the measured nuclear surface tension values and surface diffuseness, thereby providing an easy formula for calculation of nucleus-nucleus interaction energy as functions of separation distance between surfaces of approaching nuclei. Coulomb and proximity potential model (CPPM) (Santhosh and Joseph, 2002) involves one such form of the proximity potential. The total potential is calculated as the sum of Coulomb, proximity and centrifugal potentials for touching configuration and separated fragments. At present, various versions of proximity potential are in use by different theoretical groups, viz., Proximity 1977, Proximity 1988, Modified Proximity 1988, Proximity 2000, Proximity 2000 DP and Proximity 2010. These potentials differ in chosen expressions for specific nuclear surface tension (incorporated via surface energy constant or surface asymmetry constant), universal function, the mean curvature radius of the interacting nuclei etc. (Kumari and Toshiwal, 2015; Kumar and Sharma, 2012). Further, a modified version of CPPM has been proposed (Santhosh *et al.*, 2011) for deformed nuclei, CPPMDN, wherein the emitted cluster is assumed to be spherical. The parent and daughter nuclei may, however, have axially symmetric deformation. The potential energy barrier depends upon the angle between the symmetry axis of parent or daughter as well as the direction of cluster emission. In CPPMDN, the interaction potential between two nuclei is sum of the deformed Coulomb, deformed proximity and centrifugal potentials corresponding to touching configuration and separated fragment configuration.

B. The Cluster Models

The cluster models are based on the assumption that the heavy clusters are assumed to be pre-born inside the parent nucleus prior to their penetration across the interaction potential barrier with respective Q value. The probabilities of pre-formation inside the parent cluster vary for clusters of different size/mass. Also, the barrier assault frequencies differ minutely for distinct clusters. So, in cluster models, the decay is supposed to be a non-adiabatic and sudden process that occurs in two steps: (i) the cluster formation inside the parent nucleus and (ii) penetration of these preformed clusters through their respective interaction potential barriers. The basic approach in cluster models is that the emitted cluster(s) are preborn/pre-formed in the parent nucleus with certain probability, which decreases as the size of cluster increases, thereby, suggesting that the cluster-decay process will somewhere stop and that the fission process will take over. Since for cluster models, the preformation probability, $P_o \neq 1$, the nuclear structure aspect is taken care of in these models. The barrier penetration probability, P, is calculated via WentzelKramers-Brillouin (WKB) approximation, employing different potential forms. Various approaches that fall under the class of cluster models include the Microscopic Model (Blendowske and Walliser, 1988), (M3Y)- Double folded Michigan-3 Yukawa Potential Model (Khoa and Oertzen, 1993), the Cosh Potential Model (Buck *et al.*, 1992; Buck *et al.*, 1993) and the Preformed Cluster Model (PCM) (Malik and Gupta, 1989; Kumar and Gupta, 1997). The Microscopic description enters via shell model and helps to estimate cluster preformation probability. The microscopic model was employed by Blendowske et al. (Blendowske and Walliser, 1988) for explaining the ^{14}C cluster emission from Ra nuclei. The probability of finding ^{14}C cluster in Ra nucleus was determined via microscopic wave function along with a phenomenological nuclear potential. In phenomenological approach, the available experimental data was fitted via systematic variation of the parameters corresponding to the assumed form of potential. Another model in this category is the Preformed Cluster Model (PCM) (Malik and Gupta, 1989; Kumar and Gupta, 1997) that is essentially based on collective clusterization criteria. PCM is used to study the ground state process like cluster emission and spontaneous fission etc. Gupta *et al.* 2002; Gupta *et al.* 2003 have modified this model by incorporating deformation effects of decaying fragments. The PCM was further reformulated by Gupta *et al.* 2002; Gupta *et al.* 2003 to analyze decays of hot and rotating compound nuclear systems formed in the heavy-ion reactions, and it was termed as the Dynamical Cluster-decay Model (DCM) (Gupta *et al.* 2005; Singh *et al.* 2008; Sharma et al. 2011). Both PCM and DCM are based on well-known quantum mechanical fragmentation theory, QMFT (Maruhn *et al.*, 1974; Gupta *et al.*, 1975; Gupta *et al.*, 1999).

C. Dynamical Cluster-decay Model

DCM is a nonstatistical model used to understand the decay of hot and rotating CN formed in low-energy heavy-ion reactions. In DCM, the emissions of light particles, intermediate-mass fragments, as well as fusion-fission fragments are treated on equal footings as collective mass motion of the pre-formed/pre-born clusters through the interaction potential barrier. DCM can be applied to both positive and negative Q-value systems with appropriate inclusion of angular momentum and charge dispersion effects. DCM involves the use of a single neck-length parameter that attributes characteristic in-built barrier modification. For a given compound nucleus, the neck-length parameter in DCM is associated with the total kinetic energy. This effective Q-value is determined with regard to compound nucleus binding energy and the ground state binding energies of the emitted clusters/fragments (Gupta *et al.*, 2002).

The model is based on the dynamical or quantum mechanical fragmentation theory collaborators (Maruhn *et al.*, 1974; Gupta *et al.*, 1975; Gupta *et al.*, 1999) in which the decay of a hot CN with temperature T and angular momentum ℓ, is worked out in terms of the collective coordinates of mass (and charge) asymmetries $\eta = (A_1 - A_2)/(A_1 + A_2)$ [and $\eta_Z = (Z_1 - Z_2)/(Z_1 + Z_2)$] and relative separation coordinate R, multipole deformations $\beta\lambda i$ ($\lambda = 2,3,4$; $i = 1,2$), orientations θ_i, and the azimuthal angle ϕ ($= 0^\circ$ for two nuclei lying in the same plane, as shown in Fig. 1.2).

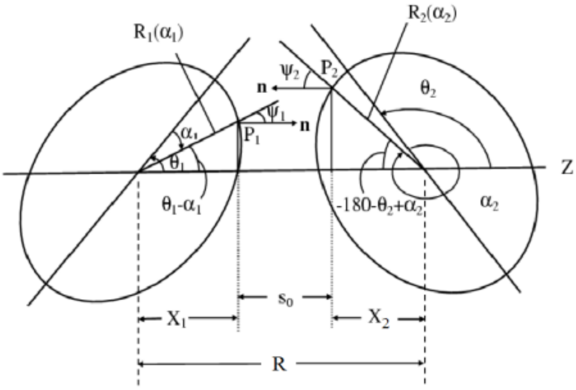

Fig. 1.2: Schematic representation of two equal or unequal axially symmetric deformed, oriented nuclei, (coplanar nuclei) both lying in the same plane, for various θ_1 and θ_2 values lying in the range 0^0 to 180^0 (Gupta et al., 2004).

In terms of these coordinates, for partial waves, we define for each fragmentation (A_1, A_2), the CN decay or formation cross section is given by,

$$\sigma = \frac{\pi}{k^2}\sum_{\ell=0}^{\ell_c}(2\ell+1)P_0P; \qquad k = \sqrt{\frac{2\mu E_{c.m.}}{\hbar^2}} \tag{4}$$

where P_0 is the preformation probability referring to η motion at a fixed R value and P, the penetrability, to R motion for each η, both dependent on angular momentum and temperature T. μ is the reduced mass. ℓ_{max} is the maximum angular momentum, defined for light-particles evaporation residue cross section $\sigma_{ER} \rightarrow 0$.

The same formula as above is applicable to the noncompound, quasifission (qf) decay process, where P_0=1 for the incoming channel since for qf process the target and projectile nuclei can be considered to have not yet lost their identity. Then, for P calculated as for the incoming channel η_{ic},

$$\sigma = \frac{\pi}{k^2}\sum_{\ell=0}^{\ell_c}(2\ell+1)P_{\eta ic} \tag{5}$$

Thus, in DCM, the cross section for each (pair of) decay product is calculated as emission of preformed cluster(s) through their interaction barrier. Noting that Eq. (1) is defined in terms of the exit or decay channels alone, i.e., both the formation P_0 and then their emission via barrier penetration P are calculated only for decay channels (A_1, A_2), it follows from Eq. (1) that

$$\sigma_{ER} = \frac{\pi}{k^2}\sum_{x=1}^{4or5}\sigma_{xn} \quad , \qquad (6)$$

and

$$\sigma_{ff} = 2\sum_{A/2-x}^{A/2}\sigma_{(A_1,\, A_2)} \qquad (7)$$

giving σCN = σER + σff, and σfusion = σCN + σqf. Then, for each ℓ, the preformation yields $P_0(A_i)$ of fragments A_i are given by the solution of the stationary Schrödinger equation in η, at a fixed R = R_a,

$$\left\{-\frac{\hbar^2}{2\sqrt{B_{\eta\eta}}}\frac{\partial}{\partial\eta}\frac{1}{\sqrt{B_{\eta\eta}}}\frac{\partial}{\partial\eta}+V(R,\eta,T)\right\}\psi^{\nu}(\eta)=E^{\nu}\psi^{\nu}(\eta) \qquad (8)$$

with ν = 0,1,2,3,... referring to ground-state (ν = 0) and excited-state solutions. The mass parameters, $B_{\eta\eta}$, are the smooth classical hydrodynamical masses, since at large T values the shell effects are almost completely washed out. The preformation probability is $P_0(A_i)=|\psi_R(\eta(A_i))|^2\sqrt{B_{\eta\eta}}\frac{2}{A}$. The collective fragmentation potential V(R,η,T) in Eq. (8), which brings in the structure effects of the CN in to the formalism, is calculated according to the Strutinsky renormalization procedure (B = V_{LDM} + δU; B is binding energy), as

$$V_R(\eta,T)=-\sum_{i=1}^{2}\left[V_{LDM}(A_i,Z_i,T)+\delta U_i\exp\left(-\frac{T^2}{T_0^2}\right)\right]+V_P(R,A_i,\beta_{\lambda i},\theta_i,\phi,T)$$
$$+V_C(R,Z_i,\beta_{\lambda i},\theta_i,\phi,T)+V_\ell(R,A_i,\beta_{\lambda i},\theta_i,\phi,T), \qquad (9)$$

where V_C, V_P, and V_ℓ are the temperature and orientation-dependent Coulomb, nuclear proximity and angular-momentum-dependent potentials, respectively (Gupta *et al.*, 2005). δU are the empirical shell corrections, made T dependent to vanish exponentially with T_0 = 1.5 MeV (Jensen and Damgaard, 1973) and V_{LDM} is T -dependent liquid drop energy. The experimental binding energies split into V_{LDM} and δU components, incorporates the deformation effects of nuclei.

The scattering potential V(R) is determined as the sum of deformations-orientations-and temperature-dependent Coulomb, nuclear proximity and angular momentum-dependent potentials, as

$$V(R,\ell,T) = V_c(R, Z_i, \beta_{\lambda i}, \theta_i, \Phi, T) + V_p(R, A_i, \beta_{\lambda i}, \theta_i, \Phi, T) + V_\ell(R, A_i, \beta_{\lambda i}, \theta_i, \Phi, T) \qquad (10)$$

The scattering potential V (R) for a fixed η value is illustrated in Fig. 1.3(a) for decay of ^{117}Sb∗ compound nucleus formed via 4He +113In reaction to (a) ground state of 116Sb, and (b) metastable state 116mSb via 1n-emission. The penetrability P in Eq. (4) or Eq. (5) is the WKB integral,

$$P=\exp\left[-\frac{2}{\hbar}\int_{R_a}^{R_b}\{2\mu[V(R,T)-Q_{eff}]\}dR\right] \qquad (11)$$

solved analytically (Malik and Gupta, 1989), with the second turning point R_b [see Fig. 1.3(a)] satisfying

$$V(R_a) = V(R_b) = Q_{eff}, \qquad (12)$$

Q_{eff} being the effective Q value for the ground state decay. For decay of the compound nucleus to the metastable state, the Q-value in Eq. (12) changes to the Q-value for decay to ground state plus ε, the excitation energy, i.e., the metastable state's energy difference with respect to w.r.t. its ground state. The Q_{eff} -value in Eq. (12) is thus replaced by (Gupta *et al.*, 1993),

$$Q^{*}_{eff} = Q_{eff}+\varepsilon, \qquad (13)$$

for the (excited) metastable state lying above its respective ground state, as illustrated in Fig. 1.3(b). For the decay of hot CN, the first turning point R_a, defining the point of fragment or cluster preformation P0, and the penetration path for calculating penetrability P, is postulated by Gupta *et al.* (Gupta *et al.*, 2005; Gupta *et al.* 2006) as,

$$R_a(T) = R_1(\alpha_1,T) + R_2(\alpha_2,T) + \Delta R(\eta,T), = R_t(\alpha,\eta,T) + \Delta R(\eta,T) \qquad (14)$$

Thus, the only parameter of the model is the T -dependent ΔR(T), the neck-length [or barrier-lowering ΔV_B, refer to Eq. (17)] parameter, which assimilates the deformation and neck formation effects between two nuclei, introduced within the extended orbiting cluster model of Gupta and collaborators (Khosla *et al.*, 1990; Kumar and Gupta, 1997; Gupta *et al.* 1997). This method of introducing a neck-length parameter R is similar to that used in both the scission-point (Matuse *et al.*, 1997) and saddle-point (Sanders *et al.*, 1999; Sanders, 1991) statistical fission models. The R_i in Eq. (14) are the radius vectors given by

$$R_i(\alpha_i,T)=R_{0i}(T)\left[1+\sum_{\lambda}\beta_{\lambda i}Y_{\lambda}^{(0)}(\alpha_i)\right] \qquad (15)$$

and T-dependent radii $R_{0i}(T)$ for the equivalent spherical nuclei (Royer and Mignen, 1992),

$$R_{0i}(T) = \left[1.28A_i^{1/3} - 0.76 + 0.8A_i^{-1/3}\right]\left(1 + 0.0007T^2\right) \qquad (16)$$

The angles α_i of radius vectors are measured in the clockwise direction from the nuclear symmetry axis and the orientation angles θ_i are measured anticlockwise from the collision Z axis (see Fig. 1.2). Next, the potential at first turning point V (R_a,) is related to the top of the barrier $V_B(\ell)$ for each value, by defining their difference $\Delta V_B(\ell)$ as the effective lowering of the barrier

$$\Delta V_B(\ell)=V(R_a, \ell) - V_B(\ell) \qquad (17)$$

Note, $\Delta V_B(\ell)$ for each is defined as a negative quantity since the actually used barrier is effectively lowered. The ΔR(T), the barrier lowering parameter, is generally positive but it can take negative values as well. The negative ΔR(T) value occurs as R_a (the first turning point of the penetration path) can always be chosen to start from $R_0(T)$ (radius for the equivalent spherical compound nucleus). Thus, the fitting parameter ΔR controls the barrier lowering and can take values such that $R_0 \leq R_a \leq R_B$, the interaction barrier RB. This is illustrated in Fig. 1.3. A semi-empirical statistical relation relates the nuclear temperature T (in MeV) to the CN excitation energy, E^*_{CN} (in units of MeV), as:

$$E^*_{CN}=Ec.m.+Qin=(A/a)T2-T \qquad (18)$$

The parameter A/a is proportional to the nucleon number of the nucleus (LeCourteur and Lang, 1959; Okuducu, 2006), where the empirical constant a can take values from 9-11 depending upon the compound nucleus mass, A. Q_{in} is the entrance or incoming channel Q value.

The compound nucleus fusion/ formation probability P_{CN} (Kaur *et al.*, 2014) is defined as

$$P_{CN} = \frac{\sigma_{CN}}{\sigma_{fusion}} = 1 - \frac{\sigma_{nCN}}{\sigma_{fusion}} \qquad (19)$$

and the compound nucleus survival probability P_{surv} (Chopra *et al.*, 2015), the probability that the fused system will de-excite by emission of neutrons or light particles (equivalently, the Evaporation Residue) rather than fission, as

$$P_{surv} = \frac{\sigma_{ER}}{\sigma_{CN}} = \frac{\sigma_{ER}}{(\sigma_{ER} + \sigma_{ff})} \qquad (20)$$

where the (total) fusion cross section $\sigma_{fusion} = \sigma_{CN} + \sigma_{qf}$ with σ_{CN} as the CN formation cross section (sum of ER and ff cross sections, $\sigma_{CN} = \sigma_{ER} + {}_{\sigma ff}$), and σ_{qf} as the noncompound (nCN), quasifission cross section.

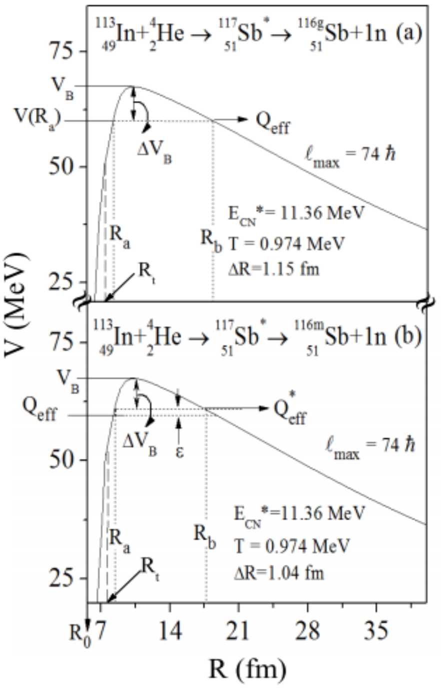

Fig. 1.3: The scattering potential V (R), dependent on temperature (T) and ℓ-values, for decay of $^{117}Sb^*$ to (a) ground state of ^{116}Sb, and (b) metastable state ^{116m}Sb via 1n-emission, at E^*_{CN} = 11.360 MeV (T = 0.974 MeV) at their ℓ_{max} values. R_a and R_b, respectively, the first and second turning points, and ΔV_B = V $(R_a)-V_B$, the barrier lowering parameter are also marked. The decay path for ground and metastable decays are defined respectively by V (R_a, ℓ)=Q_{eff} and V (R_a, ℓ)= Q^*_{eff}, beginning at their respective R_a (=R_t+ΔR) in each case.

EVOLUTION OF DCM AND CURRENT STATUS

Going back to early 1970’s, the very fundamental quantum mechanical fragementaton theory (QMFT), that forms the basis for both the PCM and DCM is reviewed in many articles in (Greiner and Gupta, 1999) and in reviews: (Beck, 2010; Singh *et al.*, 2014).

In DCM, a dynamical collective clusterization process is proposed as a possible alternative of the Hauser-Feshbach (HF) analysis and statistical fission models. The proposed dynamical cluster-decay model treats all the three processes of light-particle, intermediate-mass fragments and fusion-fission emission on equal footings as dynamical collective mass motions of preformed fragments or clusters through the barrier. DCM involves the use of a single neck-length parameter that attributes characteristic in-built barrier modification. It is important to note that, in terms of the barrier picture, a cluster-decay process is in fact a fission process with structure effects of the compound nucleus also included via the preformation probabilities of the fragments, but without any phase space arguments, i.e., without any level density calculations. A special case of DCM, where preformation probability is unity, $P_0=1$ (Kumar *et al.*, 2009) is the Wong formula (Wong, 1973). The idea of preformation concept was introduced and the role of temperature dependence in the fragmentation potential was developed. For the nuclear interaction potential, the well known T-dependent nuclear proximity pocket formula due to Blocki *et al.* (Blocki *et al.*, 1977) is used. Alternately, one may also use Skryme Energy Density Formalism (SEDF) (Puri *et al.*, 1991), which is more of a microscopic approach. The concept of oriented collision of deformed reaction partners and predictions of many reactions are the outcomes of this successful model (Gupta *et al.*, 2003; Balasubraniam *et al.*, 2003; Gupta *et al.*, 2004; Gupta *et al.*, 2005; Manhas and Gupta, 2005).

Dynamical cluster-decay model (DCM) is developed for the decay of a hot and rotating compound nucleus (CN) formed in heavy-ion reactions, which contains the spontaneous (temperature, $T=0$, angular momentum, $\ell=0$) ground-state decay (the cluster radioactivity) and decay of non-rotating ($\ell=0$) recoiled ($T\neq0$) superheavy nuclei as its special cases. The DCM introduces the concept of preformed clusters for the first time, thereby including nuclear structure effects explicitly, which then penetrate the confining nucleus- nucleus interaction barrier, advanced first as a preformed cluster model [PCM with ($T=0$)] for exotic cluster radioactivity, observed at $T=0$, $\ell=0$. Then, over the years, the temperature T was introduced within the model. More recently, the model is applied as PCM with ($T\neq0$) to the observed α-decay chains and the predicted heavy particle/cluster radioactivity (HPR) of recoiled superheavy nuclei (SHN) carrying a recoil energy E_R, without ℓ effects ($\ell=0$). The model with both T and ℓ effects, the DCM, has been used for a large number of reactions from light, medium, heavy and superheavy mass regions of compound systems. The very basic work of ground-state cluster-decay process, the exotic cluster radioactivity, has been worked upon for many years, and the DCM is a re-formulation of the preformed cluster decay model (PCM) (Malik and Gupta, 1989; Kumar and Gupta, 1997; Arun *et al.*, 2009; Sawhney *et al.*, 2011; Kumar and Sharma, 2012), whose temperature-dependent version PCM($T\neq0$) has been shown to be nicely working for α-decay half-lives and possibly heavier cluster decays of hot ($T\neq0$), but non-rotating ($\ell=0$) recoiled superheavy nuclei. Some of the reviews are: (Gupta and Greiner, 1994; Greiner and Gupta, 1999).

In heavy-ion collisions at below and near barrier energies, the projectile loses all its energy to target and forms a compound nucleus which is highly excited, i.e., with temperature, T that carry angular momentum, ℓ. The two possible decay modes of the compound nucleus are shown in Figure 1.4 schematically.

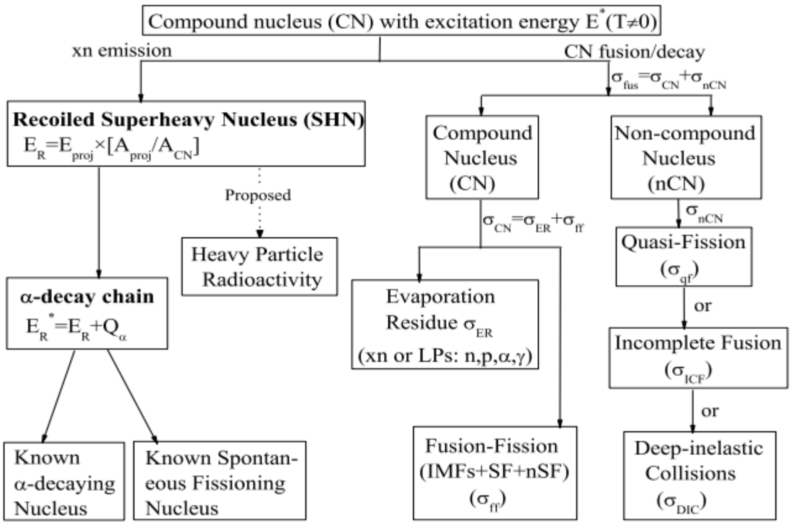

Fig. 1.4: An illustrative decay of excited compound-nucleus (Hemdeep; 2018).

The first decay mode demonstrates the existence of formation of Superheavy nucleus after the emission of few neutrons and then this recoiled Superheavy Nucleus (SHN) decays by the different α-decay chains and further SHN is controlled by the competing known spontaneous fission and the known α-decaying nucleus as the end product. In addition to the α-decay chains, the Heavy particle radioactivity has also been proposed as one of the competing process with α-decay and spontaneous fission of recoiled SHN after xn emissin from the recoiled superheavy nucleus.

In the other mode, the hot ($T\neq0$) and rotating ($\ell\neq0$) CN formed de-excites or decays by emitting light particle, i.e., n, p, α, γ with their heavier counterparts termed as Evaporation Residue (ER) and fusion-fission (ff) part consisting of Intermediate mass fragments (IMFs) with the near-symmetric (nSF) and symmetric fission (SF) fragments comprising the CN cross section σ_{CN}, i.e., $\sigma_{CN} = \sigma_{ER}+\sigma_{ff}$. In addition to the CN processes there are some non-compound nucleus (nCN) decay processes like Quasi-fission (QF), Deep-inelastic collisions (DIC) and In-complete fusion (ICF), etc., which contribute to the (total) fusion cross section $\sigma_{fus}(=\sigma_{CN}+\sigma_{nCN})$, observed in experiments.

The DCM is now developed with all the effects of temperature and angular momentum included, together with the deformations and orientations of both the incoming and outgoing nuclei (treated as clusters) in the same plane (co-planar) or in different planes (non-coplanar). See, e.g., the reviews in (Gupta *et al.*, 2008; Beck, 2010).

Recently, a systematic study of a large number of reactions from different mass regions, and formed via different entrance channels has been done. Reactions with measured or empirically predicted nCN cross-section σ_{nCN} for co-planar nuclei were chosen and calculations were carried out with non-coplanarity aspect included (Chopra *et al.*, 2018). Within the DCM, various radioactive (^{246}Bk∗, ^{220}Th∗, ^{202}Po*) and non-radioactive (^{105}Ag∗, ^{164}Yb∗, ^{196}Pt∗) compound systems have been studied, where it is shown that both higher-multipole deformations and noncoplanarity play different roles for different compound nuclei, i.e., are CN-specific, and hence act as essential, additional good degrees-of-freedom, which must be included while characterizing a CN formed in any low-energy HIR. For ^{246}Bk∗ and ^{196}Pt∗ formed via different reaction channels, the empirically determined, non-zero nCN contribution σ^{emp}_{nCN}, for both quadrupole deformed-optimum oriented configuration and then for the inclusion of higher multipole deformations with corresponding compact orientations, with planar configurations, gets reduced to zero on inclusion of noncoplanarity degree-of-freedom. In case of ^{164}Yb∗, the DCM calculation fits the measured data nearly exactly for higher multipole deformation case, with a strongly reduced (almost zero) nCN contribution in going from planar to non-coplanar configurations. For CN ^{105}Ag∗, an enhanced nCN contribution is observed, whereas in ^{220}Th∗ and ^{202}Po* the 4n decay has an nCN content, which remains nearly the same for adding or not adding higher multipole deformations in coplanar or non-coplanar configurations. Thus, in order to obtain a true/ real outcome of a CN fusion reaction, analyzing a compound nuclear system with higher-multipole deformations and non-coplanar configurations is almost essential. Thus, more such possible cases of non-zero nCN contribution in total fusion cross-section for coplanar collisions could possibly be explained by adding non-coplanarity degree of freedom or else establish fusion hindrance phenomenon. The idea is to establish non-coplanarity as a free degree of freedom like deformations and orientations.

Similarly, the observed α-decay chain(s) of recoiled residue product, the SHN, after xn emission, could end in a known spontaneous fissioning nucleus or the recoiled residue product SHN itself as a known spontaneous fissioning nucleus without any α (Utyonkov *et al.*, 2015) or heavyparticle decay (Sawhney *et al.*, 2014). This spontaneous α-decay process, when calculated on PCM at T=0 result in a factor of the order of 10^4 disagreement with measured α-decay half-life, which, however, is completly removed within the PCM($T\neq0$) itself with T-dependence determined and included in respect of the measured recoil energy E_R of SHN. The heavyparticle radioactivity (HPR) and spontaneous fissioning of the recoiled product are still open questions. Furthermore, like for α-decay chain ending in a known α-decaying nucleus, the alternative is a spontaneous fissioning nucleus. This phenomenon which is a reverse of α-decay is explained/worked out in the sense that instead of α-decay, it is a case of nucleus formation by adding an α-particle. Recently, the temperature-dependent preformed cluster model [PCM(T)] has been employed (Kaur *et al.*, 2018) to extend the work (Niyti *et al.*, 2015) on α-decay chains of various isotopes of Z = 113–118 superheavy nuclei (SHN), to spontaneous fissioning nuclei ^{266}Lr, ^{267}Rf, $^{266-268}$Db, ^{281}Rg, and

^{282}Cn occurring as end products of these α-decay chains. The behavior of fragment mass distribution and competitive emergence of the dominant decay mode, i.e., the α-emission versus spontaneous fission (SF), are studied for identifying the most probable heavy fission fragments, along with the estimation of SF half-life times $T^{SF}1/2$ and total kinetic energy (TKE) of the above noted isotopes of Z = 103–112 nuclei decaying via the SF process. Similar theoretical analysis of the available experimental data for α-decay chains of hot ($T\neq0$) but non-rotating ($\ell=0$), i.e., recoiling residual superheavy nuclei, together with their ending in a known fissioning nucleus or in a spontaneous fissioning nucleus without any α-decay can be worked upon.

The study of hot ($T\neq0$) and rotating ($\ell\neq0$) complex systems formed in heavy ion reactions is further extended to many more reactions, which decay via light particles (n, p, α) and γ-ray emission, constituting the evaporation residue (ER) cross section, the intermediate mass fragments, and the symmetric or near symmetric fusion-fission (ff). Combination of the above mentioned processes or predominantly a particular one out of the remaining is possible for different compound nuclei belonging to distinct mass regions. For instance, lighter compound systems such as ^{105}Ag∗ (Chopra *et al.*, 2013), ^{117}Sb∗ (Kaushal, 2020), ^{120}Te∗ (Kaushal, 2020) and ^{124}Ce∗ (Kaur *et al.*, 2014) have evaporation residues as the predominant decay mode with a small contribution from Intermediate mass fragments. In case of medium mass systems like ^{202}Po∗ formed via various entrance channels, for e.g., $^{16}O+^{186}Os\rightarrow^{202}Po*$ and $^{34}S+^{168}Er\rightarrow^{202}Po*$ (Morton *et al.*, 2000; Rafiei *et al.*, 2008), both evaporation residue and fission processes compete.

Very recently, thus the decay cross-sections of this hot and rotating ^{88}Mo∗ compound system are calculated for both the experimentally observed Fusion-Evaporation (FE) and Fusion-Fission (FF) channels. In FF decay mode, the explicit contribution of Intermediate Mass Fragments (IMF), Heavy Mass Fragments (HMF) and fission fragments (symmetric/asymmetric) is detected within DCM framework (Grover *et al.*, 2020).

Then, there is also the competing non-compound nucleus (nCN) process, the quasi-fission (qf)-like process, which is of particular interest since (non-zero) nCN component in fusion cross-section refers to ‘barrier lowering’ effect due to fusion hindrance phenomenon. The formation and decay of the ^{220}Th∗ compound nucleus formed via some entrance channels ($^{16}O+^{204}Pb, ^{40}Ar+^{180}Hf, ^{48}Ca+^{172}Yb, ^{82}Se+^{138}Ba$) at near barrier energies has been studied within the DCM (Hemdeep *et al.*, 2018). Herein, for best fitting of the measured evaporation residue cross sections, with quasifission (qf) content, if any, the fusion-fission (ff) component is predicted. More recently, a systematic study of dynamical aspects associated with heavy-ion-induced ^{16}O + ^{89}Y reaction is carried out at center-of-mass energy $E_{c.m.}$ = 89 MeV (Sharma and Sharma, 2020). The complete fusion (CF) and incomplete fusion (ICF) contributions are estimated by using DCM. The incomplete fusion component is examined by normalizing the incident beam energy for each of the breakup fragment. The fusion evaporation cross-sections that emerged from CF and ICF channels are duly addressed using the optimized value of neck-length parameter ΔR. Further, the mass yield of compound nuclei (CN) formed in the CF and ICF processes is analyzed with respect to angular momentum values. The DCM-based calculations indicate the possible contribution of deep inelastic collision (DIC) in the decay of ^{105}Ag∗ at higher values, and DIC cross-sections are predicted which call for future validation.

The decay mechanism of ^{217}At∗ formed in ^{9}Li + ^{208}Pb reaction is studied within the dynamical cluster decay model (DCM) at various center-of-mass energies (Kaur *et al.*, 2017). The aim is to see the behavior of a light neutron-rich radioactive beam on a doubly-magic target nucleus for the (total) fusion cross section σ_{fus} and the individual decay channel cross sections. The ^{9}Li induced reaction on doubly-magic ^{208}Pb is more of a quasi-fission-like nCN decay, which is further analyzed in terms of the statistical CN formation probability P_{CN} and CN survival probability P_{surv}. In (Kaur *et al.*, 2018), the decay mechanism of compound nuclei formed in reactions induced by neutron-rich ^{9}Li nucleus on doubly magic shell nucleus ^{208}Pb and various other targets such as ^{27}Al, ^{67}Cu, ^{70}Zn and ^{120}Sn, is studied within the DCM for a fixed single value of the only parameter of the model, the neck-length parameter ΔR, at a fixed laboratory energy E_{Lab}. The role of light neutron-rich projectile like ^{9}Li is investigated on (total) fusion cross section σ_{fus}, showing that σ_{fus} decreases with target mass only for the most abundant isotope, and that σ_{fus} is largest for a target with magic neutron number. Another important result confirmed here again is that an almost same amount of modification in the barrier takes place in reactions induced by the same projectile having the same incident energy (Kaur *et al*., 2015). Furthermore, the synthesis of ^{217}At$*$ via various target-projectile combinations, for "hot" compact configurations is carried out.

DCM is further employed to analyze decays of compound nuclei to ground and metastable state(s) of the decay-fragments. The decay mechanism of ^{202}Po$*$, formed in ^{48}Ca+^{154}Gd reaction, is studied within the DCM at various excitation energies E^*_{CN} wherein neutron emission xn, x = 3−5, are the predominant decay modes. ^{202}Po$*$ decays to the ground state of ^{198}Po by emission of 4n and the metastable states ^{199m}Po and ^{197m}Po via 3n and 5n emissions, respectively. Both type of decays are analyzed separately, using neck-length ΔR (equivalently, 'barrier lowering') parameter, to best fit the evaporation residue (ER) or channel cross section (σ_{xn}) data and predict the quasi-fission (qf)-like non-compound (σ_{qf}) cross sections. This study is done by inclusion of deformation effects up to quadrupole deformations, and "optimum" orientations, for coplanar nuclei using "hot (compact)" configurations (Kaushal *et al*., 2018). As an extension of this work, wherein, the effects of inclusion of additional degrees-of-freedom, i.e., the higher multipole deformations, the octupole (β_{3i}) and hexadecapole (β_{4i}), the corresponding compact angles in the decay of ^{202}Po$*$ are investigated (Kaushal and Sharma, 2019). Possible target-projectile combinations are identified for the synthesis of ^{202}Po$*$. Following the study of "hot" fusion reactions, (Kaushal, 2020) presents the DCM analysis of ^{117}Sb$*$ formed in ^{4}He+^{113}In reaction. Analysis is done at some astrophysical energies, where ^{117}Sb$*$ decays via 1n-emission to ground state and metastable state of ^{116}Sb. The DCM cross sections, σ_{1n}, are calculated at various energies, center-of-mass range ($E_{c.m.}$=9.66−13.64 MeV), corresponding to available experimental data for α-induced reaction with the odd-Z, proton-rich nuclide ^{113}In. The only parameter of DCM is the neck-length parameter, ΔR, that is optimized to best fit the experimental data and used for making predictions over a wider energy spread. Possible synthesis via probable target-projectile combinations is also worked out for this medically important radionuclide. In (Kaushal, 2020), another "cold fusion" reaction is analyzed. Herein, the dynamics of one out of thirty-five known rare p-nuclei, i.e., ^{120}Te$*$ compound nucleus is worked out over an incident α-beam energy, $E_\alpha \sim$ 10.3−30 MeV, constituting energies below, around and above the Coulomb barrier. The experimental data is available for the decay of ^{120}Te$*$ (formed in α+^{116}Sn reaction) to both ground and metastable states, where the predominant decay mode is neutron emission, xn, (x = 1,2). Both kinds of decays are independently addressed within the DCM to best fit the data for observed xn, x = 1 or 2 channel cross sections. An attempt is made to make some possible predictions for future validations.

These are the possible cases of applications of both the DCM and PCM, whose systematic study is likely to reveal many new significant results for heavy ion physics. The importance of such theoretical analysis pertains to the fact that not only a better understanding of the observed experimental data is needed but also theoretical predictions are required for planning new experiments.

SUMMARY

The possibility of large variations in the experimental conditions make the heavy-ion reaction studies engrossing and highly interesting area of research. Heavy-ion collisions provide the opportunity of probing variety of remarkably contrasting collective phenomena. Each of these phenomena pose a new challenge to theoretical nuclear models governing nuclear reactions. The relevant theoretical models are developed within the Quantum Mechanical Fragmentation Theory (QMFT) and are mainly categorized as the cluster models and the fission models. QMFT is based on the notion of fragments being pre-born or pre-formed inside the compound nucleus, wherein, the kinetic energy of a nuclear system is taken into account by the mass parameter and potential energy surfaces, while the potential energy determines the static nuclear properties. The inclusion of P0 in the cluster models refers to the incorporation of nuclear structure effects in the decaying nucleus, which are completely ignored in fission models. The Dynamical Cluster-decay Model (DCM), a non-statistical approach, is used extensively to analyze the decay of hot and rotating compound nuclei formed in low-energy heavy-ion reactions. DCM provides the advantage of calculating relative probabilities of binary decay fragments produced in the decay of excited compound nucleus. QMFT forms the basis of DCM, wherein compound nucleus decay is governed via collective coordinate approach involving a two step mechanism for analyzing the compound nucleus decay dynamics. Firstly, the preformation probability (P_0) of the fragments within the parent compound nucleus and then, the penetration probability (P) of the preformed fragments/clusters across the Coulomb barrier. In step one, the possible decay fragments of a particular compound nucleus are considered to be pre-born inside the mother compound nucleus with relative preformation probabilities P_0, providing convincing knowledge regarding nuclear structure effects. Step two deals with the penetration, as per the quantum concept of Gamow's α-decay theory, of these already preformed clusters through their respective potential barriers with a tunneling probability, P, obtained in R-motion using WKB-approximation. DCM has evolved over the years and incorporates the effects of temperature, angular momentum along with additional degrees-of-freedom, namely the deformations and orientations. The fact that there is no 'final' theory in science and no unquestioned authority among scientists necessitates the interplay of theory and experiments fundamental to the progress of science.

REFERENCES

Arun, S. K., R. K. Gupta, B. B. Singh, S. Kanwar and M. K. Sharma. 2009. ^{208}Pb-daughter cluster radioactivity and the deformations and orientations of nuclei. Phys. Rev. C 79: 064616.

Back, B. B. and P.B. Fernandez, *et al*. 1996. Entrance-channel effects in quasifission reactions. Phys. Rev. C 53: 1734.

Balasubraniam, M., R. Kumar, R. K. Gupta, C. Beck and W. Scheid. 2003. Emission of intermediate mass fragments from hot ^{116}Ba* formed in low-energy ^{58}Ni +^{58}Ni reaction. J. Phys. G 29: 2703.

Banerjee,T., S. Nath, and S. Pal. 2019. Detailed statistical model analysis of observables from fusion-fission reactions. Phys. Rev. C 99: 024610.

Beck, C. 2010. Lecture Notes in Physics, 818, "Clusters in Nuclei". Springer Vol. I: 223-264.

Blendowske, R. and H. Walliser. 1988. Systematics of cluster-radioactivity-decay constants as suggested by microscopic calculations. Physical review letters 61: 1930.

Blocki, J., J. Randrup, W.J. Swiatecki and C.F. Tsang. 1977. Proximity forces.Ann. Phys. (N.Y.) 105: 427.

Blocki, J. P., H. Feldmeier and W.J. Swiatecki. 1986. Dynamical hindrance to compound-nucleus formation in heavy-ion reactions. Nucl. Phys. A 459: 145.

Bjornholm, S. and W. J. Swiatecki. 1982. Dynamical Aspects of Nucleus-Nucleus Collisions. Nucl. Phys. A 391: 471.

Bohr, N. and J. A. Wheeler. 1939. The Mechanism of Nuclear Fission. Phys. Rev. 56: 426.

Buck, B., A.C. Merchant and S.M. Perez. 1992. α decay calculations with a realistic potential. Phys. Rev. C 45: 2247.

Buck, B., A.C. Merchant and S.M. Perez. 1993. Half-lives of favored alpha decays from nuclear ground states. At. Data Nucl. Data Tables 54: 53.

Businaro, U. L. and S. Gallone. 1957. Asymmetric equilibrium shapes in the liquid drop model. Nuovo Cimento 5: 315.

Chopra, S., M. Bansal, M. K. Sharma and R. K. Gupta. 2013. One-neutron and noncompound-nucleus decay contributions in the ^{12}C+^{93}Nb reaction at energies near and below the fusion barrier. Phys. Rev. C 88: 014615.

Chopra, S., A. Kaur and R. K. Gupta. 2015. Determination of the compound nucleus survival probability P_{surv} for various "hot" fusion reactions based on the dynamical cluster-decay model. Phys. Rev. C 91: 034613.

Chopra, S., Hemdeep, P. Kaushal and R. K. Gupta. 2018. Signatures of higher-multipole deformations and noncoplanarity as essential, additional degrees-of-freedom in heavy-ion reactions. Physical Review C 98: 041603(R).

Corsi, A. and O.Wieland, et al. 2009. Excitation of the dynamical dipole in the charge asymmetric reaction ^{16}O+^{116}Sn. Phys. Lett. B 679: 197.

Denisov, V. Yu. and W.Norenberg. 2002. Entrance channel potentials in the synthesis of the heaviest nuclei. Eur. Phys. J. A 15: 375.

Gamow, G. 1928. Zur Quantentheorie des Atomkernes. Z. Phys. 51: 204.

Grégoire, C., C. Ngô and B. Remaud. 1982. Fast fission phenomenon, deep inelastic reactions and compound nucleus formation described within a dynamical macroscopic model. Nucl. Phys. A 383: 392.

Greiner, W. and R.K. Gupta. 1999. Heavy Elements and Related New Phenomena. World Sc. Publication Vols. I and II.

Greiner, W. and R.K. Gupta. 1999. Heavy Elements and Related New Phenomena. World Sc. Publication Vol. II: 730.

Grover, N., B. Thakur and M. K. Sharma. 2020. Fragmentation analysis of ^{88}Mo* compound nucleus in view of different decay mechanisms. EPJ Web of Conferences 232: 03004.

Gupta, R. K., W. Scheid and W. Greiner. 1975. Theory of Charge Dispersion in Nuclear Fission. Phys. Rev. Lett. 35: 353.

Gupta, R. K., M. Horio, A. Săndulescu, M. Greiner and W. Scheid. 1993. Cluster preformation probabilities and fine-structure effects in heavy-cluster decays using folding potentials. J. Phys. G: Nucl. Part. Phys. 19: 2063.

Gupta, R.K. and W. Greiner. 1994. Cluster Radioactivity. Int. J. Mod. Phys. E 3: 335.

Gupta, R. K., S. Kumar and W. Scheid. 1997. Structural Configurations in an Extended Orbiting Cluster Model for Molecular Resonance States. Int. J Mod. Phys. E 6: 259.

Gupta, R. K. and W. Greiner. 1999. Heavy Elements and Related New Phenomenon, edited by W. Greiner and R. K. Gupta, (World Scientific, Singapore) I: 397; ibid I: 536.

Gupta, R. K., M. Balasubramaniam, C. Mazzocchi, M. La Commara and W. Scheid. 2002. Decay of excited ^{116}Ba* formed in the ^{58}Ni+^{58}Ni reaction via the emission of intermediate mass fragments. Phys. Rev. C 65: 024601.

Gupta, R. K., R. Kumar, N. K. Dhiman, M. Balasubraniam, W. Scheid and C. Beck. 2003. Cluster decay of hot ^{56}Ni * formed in the ^{32}S + 24 Mg reaction. Phys. Rev. C 68: 014610.

Gupta, R. K., M. Balasubraniam, R. Kumar, D. Singh and C. Beck. 2004. Collective clusterization effects in light heavy ion reactions. Nucl. Phys. A 738: 479c.

Gupta, R. K., N. Singh and M. Manhas. 2004. Generalized proximity potential for deformed, oriented nuclei. Phys. Rev. C 70: 034608.

Gupta, R. K., M. Balasubramaniam, R. Kumar, D. Singh, C. Beck and W. Greiner. 2005. Dynamical cluster-decay model for hot and rotating light-mass nuclear systems, applied to low-energy ^{32}S+^{24}Mg→^{56}Ni∗ reaction. Phys. Rev. C 71: 014601.

Gupta, R. K., M. Balasubramaniam, R. Kumar, N. Singh, M. Manhas and W. Greiner. 2005. Optimum orientations of deformed nuclei for cold synthesis of superheavy elements and the role of higher multipole deformations. J. Phys. G: Nucl. Part. Phys. C 31: 631.

Gupta, R. K., M. Manhas and W. Greiner. 2006. Compactness of the ^{48}Ca induced hot fusion reactions and the magnitudes of quadrupole and hexadecapole deformations. Phys. Rev. C 73: 054307.

Gupta, R. K., S. K. Arun, R. Kumar and Niyti. 2008. Int. Rev. Phys. (IREPHY) 2: 369.

Gupta, U., P. P. Singh, D. P. Singh, M. K. Sharma, A. Yadav, R. Kumar, B. P. Singh and R. Prasad. 2008. Observation of large incomplete fusion in ^{16}O+^{103}Rh system at ≈ 3-5 MeV/nucleon. Nucl. Phys. A 811: 77.

Hemdeep, S. Chopra, A. Kaur, P. Kaushal, and R. K. Gupta. 2018. Role of higher-multipole deformations and noncoplanarity in the decay of the compound nucleus ^{220}Th∗ within the dynamical cluster-decay model. Phys. Rev. C 97: 044623.

Hemdeep. 2018. Role of multipole deformations and coplanar or noncoplanar collisions in the decay of hot and rotating compound nuclei. Thesis: Panjab University, Department of Physics, India.

Hinde, D. J. and M. Dasgupta, *et al*. 1995. Fusion-Fission versus Quasifission: Effect of Nuclear Orientation. Phys. Rev. Lett. 74: 1295.

Hinde, D. J., M. Dasgupta, J. R. Leigh, J. C. Mein, C. R. Morton, J. O. Newton and H. Timmers. 1996. Conclusive evidence for the influence of nuclear orientation on quasifission. Phys. Rev. C 53: 1290.

Hinde, D. J. and A.C. Berriman, et al. 2002. Role of Entrance-channel Dynamics in Heavy Element Synthesis. J. Nucl. Radiochem. Sci. 3: 31.

Hinde, D. J., M. Dasgupta and A. Mukherjee. 2002. Severe Inhibition of Fusion by Quasifission in Reactions Forming ^{220}Th. Phys. Rev. Lett. 89: 282701.

Hoffmann, H. and J.R. Nix. 1983. Fission dynamics simplified. Phys. Lett. B 122: 117.

Jensen, A. S. and J. Damgaard. 1973. Shell effects in a paired nucleus for finite excitation energies. Nucl. Phys. A 203: 578.

Kaur, A., S. Chopra, and R. K. Gupta. 2014. α-cluster versus non-α-cluster decay of the excited compound nucleus ^{124}Ce∗ using the dynamical cluster-decay model. Phys. Rev. C 89: 034602.

Kaur, A., S. Chopra and R. K. Gupta. 2014. Compound nucleus formation probability P_{CN} determined within the dynamical cluster-decay model for various “hot” fusion reactions. Phys. Rev. C 90: 024619.

Kaur, M., B. B. Singh, M. K. Sharma and R. K. Gupta. 2015. Decay analysis of compound nuclei with masses A ≈ 30– 200 formed in reactions involving loosely bound projectiles. Phys. Rev. C 92: 024623.

Kaur, A. , Hemdeep, P. Kaushal, B. R. Behera, R. K. Gupta. 2017. Dynamical Cluster-decay Model (DCM) applied to ^{9}Li+^{208}Pb reaction. Nuclear Physics A 966: 306-323.

Kaur, A., P. Kaushal, Hemdeep, R. K. Gupta. 2018. Decay analysis of compound nuclei formed in reactions with exotic neutron-rich ^{9}Li projectile and the synthesis of ^{217}At* within the dynamical cluster-decay model. Nuclear Physics A 969: 184-195.

Kaur, A., G. Sawhney, M. K. Sharma and R. K. Gupta. 2018. Spontaneous fission of the end product in α-decay chain of recoiled superheavy nucleus: A theoretical study. International Journal of Modern Physics E Vol. 27: 1850043.

Kaushal, P., A. Kaur, Hemdeep, S. Chopra and R. K. Gupta. 2018. ^{48}Ca-induced reaction on the lanthanide target ^{154}Gd and its decay to ground and metastable states within the dynamical cluster-decay model. Phys. Rev. C 98: 014602.

Kaushal, P. and M. K. Sharma. 2019. Systematic decay analysis of ^{202}Po* compound nucleus using Dynamical Cluster-decay Model. Int. J. Mod. Phys. E 28: 1950105(1-25).

Kaushal, P. 2020. Analysis of the decay of the rare p nucleus ^{120}Te* within a collective clusterization approach. Phys. Rev. C 101: 014615.

Kaushal, P. 2020. Analysis of ^{113}In (α,n) $^{116g/(or)m}$Sb reaction at astrophysically interesting center-of-mass energies and synthesis of ^{117}Sb* within the Dynamical Cluster-decay Model. Nucl. Phys. A 994: 121677.

Khoa, D. T. and W. von Oertzen. 1993. A nuclear matter study using the density dependent M3Y interaction. Phys. Lett. B 304: 8.

Khosla, H. S., S. S. Malik and R. K. Gupta. 1990. Two-centre shell model description of quasi-molecular resonance states in heavy-ion collisions. Nucl. Phys. A 513: 115.

Kumar, S. and R.K. Gupta.1997. Neck formation and deformation effects in a preformed cluster model of exotic cluster decays. Phys. Rev. C 55: 218.

Kumar, R., M. Bansal, S. K. Arun and R. K. Gupta. 2009. Angular momentum effects and barrier modification in sub-barrier fusion reactions using the proximity potential in the Wong formula. Phys. Rev. C 80: 034618.

Kumar, R. and M.K. Sharma. 2012. Systematic study of various proximity potentials in Pb-daughter cluster radioactivity. Phys. Rev. C 85: 054612.

Kumari, R. and A. Toshniwal. 2015. A new technique to determine fusion barrier heights using proximity potentials. EPJ Web of Conferences 86:00022.

LeCouteur, K. J. and D. W. Lang. 1959. Neutron evaporation and level densities in excited nuclei. Nucl. Phys. 13: 32.

Malik, S. S. and R. K. Gupta. 1989. Theory of cluster radioactive decay and of cluster formation in nuclei. Phys. Rev. C 39: 1992.

Manhas, M. and R. K. Gupta. 2005. Proximity potential for deformed, oriented nuclei: “Gentle” fusion and “hugging” fusion. Phys. Rev. C 72: 024606.

Maruhn, J. and W. Greiner. 1974. Theory of Fission-Mass Distributions Demonstrated for ^{226}Ra, ^{236}U, ^{258}Fm. Phys. Rev. Lett. 32: 548.

Matsuse, T., C. Beck, R. Nouicer and D. Mahboub. 1997. Extended Hauser-Feshbach Method for Statistical Binary-Decay of Light-Mass Systems. Phys. Rev. C 55: 1380.

Meitner, L. 1950. Fission and nuclear shell model. Nature 165: 561.

Morton, C. R., A. C. Berriman, R. D. Butt, M. Dasgupta, A. Godley, D. J. Hinde and J. O. Newton. 2000. Memory of the entrance-channel K distribution observed in fission at high angular momentum. Phys. Rev. C 62: 024607.

Niyti, G. Sawhney, M. K. Sharma and R. K. Gupta. 2015. α-decay chains of recoiled superheavy nuclei: A theoretical study. Phys. Rev. C 91 : 054606.

Okuducu, S., S. Sönmezoğlu and E. Eser. 2006. Calculation of nuclear level density parameters of some deformed light nuclei using collective excitation modes. Phys. Rev. C 74: 034317.

Pant, L. M., A. Saxena, R. K. Choudhury and D. M. Nadkarni. 1996. Mass dependence of fragment anisotropy in the fission of ^{11}B+^{237}Np and ^{16}O+^{209}Bi systems. Phys. Rev. C 54: 4.

Puri, R. K., P. Chattopadhyay and R. K. Gupta. 1991. Spin density contribution in heavy-ion interaction potentials using energy density formalism. Phys. Rev. C 43: 315.

Rafiei, R., R. G. Thomas, D. J. Hinde, M. Dasgupta, C. R. Morton, L. R. Gasques, M. L. Brown and M. D. Rodriguez. 2008. Strong evidence for quasifission in asymmetric reactions forming ^{202}Po*. Phys. Rev. C 77: 024606.

Ramachandran, K. and A. Chatterjee, *et al*. 2015. Fission time-scale from the measurement of pre-scission light particles and γ-ray multiplicities. Pramana 85, No. 2: 335.

Royer, G. and J. Mignen. 1992. Binary and ternary fission of hot and rotating nuclei. J. Phys. G: Nucl. Part. Phys. 18: 1781.

Sanders, S. J. 1991. Fusion-fission in nuclear systems with 40≤ACN≤80. Phys. Rev. C 44: 2676.

Sanders, S. J., A. Szanto de Toledo and C. Beck. 1999. Binary Decay of Light Nuclear Systems. Phys. Rep. 311: 487.

Sandulescu, A., D. N. Poenaru and W. Greiner. 1980. New type of decay of heavy nuclei intermediate between fission and. cap alpha. decay. Sov. J. Part. Nucl. 11: 528.

Santhosh, K. P. and A. Joseph. 2002. Exotic decay in cerium isotopes. Pramana 58:611.

Santhosh, K. P., S. Sahadevan, J. G. Joseph.2011. Alpha decay of even–even nuclei in the region 78⩽ Z⩽ 102 to the ground state and excited states of daughter nuclei. Nucl. Phys. A 850: 34.

Santhosh, K. P., S. Sahadevan, B. Priyanka, M.S. Unnikrishnan. 2012. Systematic study of heavy cluster emission from $^{210\text{-}226}$Ra istopes. Nucl. Phys. A 882: 49.

Sawhney, G., M. K. Sharma and R. K. Gupta. 2011. Role of higher-multipole deformations in exotic ^{14}C cluster radioactivity. Phys. Rev. C 83: 064610.

Sawhney, G., K. Sindhu, M. K. Sharma and R. K. Gupta. 2014. Role of nuclear deformations and proximity interactions in heavy particle radioactivity. Eur. Phys. J. A 50: 175.

Schröder, W. U. and J. R. Huizenga. 1984. Treatise on Heavy-ion Science edited by D. A. Bromley (Plenum Press, New York) 2: 115.

Sharma, M. K., G. Sawhney, R. K. Gupta and W. Greiner. 2011. The decay of the compound nucleus ^{215}Fr* formed in the ^{11}B+^{204}Pb and ^{18}O+^{197}Au reaction channels using the dynamical cluster-decay model. J. Phys. G: Nucl. Part. Phys. 38: 105101.

Sharma, I., and M. K. Sharma. 2020. Fragmentation analysis of ^{105}Ag$*$ nucleus governed via complete and incomplete fusion channels at $E_{c.m.}$ = 89 MeV. Modern Physics Letters A 35: 2050084.

Shi, Y. J. and W. J. Swiatecki. 1985. Estimates of radioactive decay by the emission of nuclei heavier than α-particles. Nucl. Phys. A 438: 450.

Siemsen, R. S. 1983. Incomplete fusion reactions as binary λ-matched reactions. Nucl. Phys. A 400: 245.

Singh, B. B., M. K. Sharma, and R. K. Gupta. 2008. Decay of ^{246}Bk$*$ formed in similar entrance channel reactions of ^{11}B+^{235}U and N+^{232}Th at low energies using the dynamical cluster-decay model. Phys. Rev. C 77: 054613.

Singh, B. B., S. Kumar, M. K. Sharma and S. K. Patra. 2014. Extensions of Natural Radioactivity to 4th-Type and of the Periodic Table to Super-heavy Nuclei: Contribution of Raj K Gupta to Cold Nuclear Phenomena. Journal of Nuclear Physics, Material Sciences, Radiation and Applications 1: 133-143.

Swiatecki, W. J. 1981. The dynamics of nuclear coalescence or reseparation. Phys. Scr. 24: 113.

Utyonkov, V. K. *et al.* 2015. Experiments on the synthesis of superheavy nuclei ^{284}Fl and ^{285}Fl. Phys. Rev. C 92: 034609.

Wong, C. Y. 1973. Interaction Barrier in Charged-Particle Nuclear Reactions. Phys. Rev. Lett. 31: 766.

Pb. Univ. Res. J (Sci.) Vol. 70, 2020, pp 53-62

POSTBIOTICS AND ANTIBIOTIC CIPROFLOXACIN TOGETHER ATTENUATES *P. AERUGINOSA* PAO1 BIOFILM FORMATION

Vivek Sharma, Swati Chandla, Kusum Harjai and Geeta Shukla*
Department of Microbiology, Basic Medical Sciences (Block-1),
Panjab University, Chandigarh 160014, India

ABSTRACT

The study was designed to compare the antibiofilm potential of purified postbiotics (bacteriocin and EPS) isolated from probiotic *Lactobacillus fermentum* PUM alone as well as in combination with antibiotic ciprofloxacin against the most prevalent biofilm forming and antibiotic resistant *Pseudomonas aeruginosa* PAO1. Experimentally, it was observed that precoating of foley catheters with purified postbiotics in combination with ciprofloxacin dwindled the biofilm formation maximally compared with individual counterparts. More specifically, flow cytometery, confocal laser scanning microscopy and scanning electron microscopy showed that the combination of bacteriocin and EPS with ciprofloxacin resulted in 85.3% dead cells, followed by bacteriocin with ciprofloxacin and bacteriocin with EPS with 78.2% dead cells compared with 62.8% and 59.7% dead cells with EPS together with ciprofloxacin and ciprofloxacin alone respectively. Taken together, the study demonstrates that postbiotics of indigenous probiotic *L. fermentum* PUM can be used as an alternate strategy to combat *P. aeruginosa* PAO1 biofilm related infections in combination with antibiotic.

Keywords: Postbiotics, Antibiotics, Biofilm, Bacteriocin

INTRODUCTION

Biofilms are the three-dimensional consortia of microbes that accumulate and establish at the surfaces as an extracellular polymer with intermixed water channels (Vasudevan, 2014). Biofilm formation is expressed as an adjustment of microorganisms to hostile environment where bacteria adhere irreversibly to a surface by giving more different adhesion sites to the substrates. Of all human bacterial infections, about 75 per cent are biofilm-related including both device and non-device associated infections (Miguel et al., 2016). The most common surfaces for the biofilm related infections are implanted medical devices such as catheters and artificial heart valves which poses high health risk to human beings (Bors and Horswill, 2011). The nature of microorganisms forming biofilm is responsible for up to 1000-fold increase in resistance to antibiotics and host defence mechanism leading to highly recalcitrant, chronic and non-healing infections compared with their planktonic counterparts making it difficult to treat and eradicate the infections (Wu et al., 2015; Hall and Mah, 2017). Therefore, mismatch between existing antibiotics and their anti-biofilm activity has led scientists to formulate the optimal approach to combat chronic biofilm related infections vis-a-vis new antimicrobial agents as formation of biofilm leads to the bacterial pathogenicity and resistance. Hence, attempts are being made either to reduce or eliminate the biofilm formation using various natural bio-interventions such as matrix degrading enzymes, phytochemicals, bacteriophages and probiotics (Chhibber et al., 2013; Kumar et al., 2013). Among these, postbiotics have been found to exhibit inhibitory potential against numerous species of pathogens such as *L. monocytogenes*, *C. perfringens*, *S. enterica* and *E. coli* (Thanh et al., 2010).

Postbiotics are defined as the soluble products secreted by live bacteria and are of various types such as peptides, SCFA, enzymes, teichoic acids, peptidoglycan-derived mucopeptides, EPS, bacteriocin and cell surface proteins etc (Tsilingiri and Rescigno, 2013). Bacteriocin, a ribosomally synthesized peptide having antimicrobial potential towards closely related strain and can be of three types i.e. Type1, II and III (Kemperman et al., 2003). Most of the bacteriocins, produced by lactic acid bacteria (LAB) are type II and are small, hydrophilic, cationic or amphiphillic molecules comprising of 20-60 amino acid residues that are stable in wide range of temperature as well as pH and molecular weight varies from < 10kDa to > 30 kDa that may be complexed either with a polysaccharide or lipid moiety which is essential for antibacterial potential (Ammor et al., 2006). Most of the bacteriocins inhibit the species that are closely related to each other representing the narrow

---

* Corresponding author e-mail: geeta_shukla@pu.ac.in
MS Received: July 31, 2020, Accepted: October 15, 2020

inhibitory spectrum while other bacteriocins like Nisin, have a wide inhibitory spectrum. Additionally, many bacterial strains are also known to secrete exopolysaccharide (EPS) playing important role in the cell protection and have been used in industries such as medicine, pharmaceuticals and cosmetics (Lindstrom et al., 2012). EPS produced by LAB have anti-ulcer, antioxidant, cholesterol lowering activity and immune-stimulating potentials due to which it has gained special attraction in human healthcare (Kim et al., 2009).

P.aeruginosa are among several multi-drug resistant (MDR) bacterial species and has been labelled as a global priority pathogen by World Health Organization (WHO) due to its ability to cause various diseases such as respiratory infections, gastrointestinal infections, urinary tract infection, bacteraemia, soft tissue infections, corneal ulceration, endocarditis and biofilm associated infections, prioritizing the development of novel antimicrobial strategies (WHO, 2017). In our earlier studies, we have found that prior coating of surface with both crude and purified postbiotics (bacteriocin and EPS) produced by isolated probiotic *L. fermentum* PUM attenuated the biofilm formation (Sharma et al., 2017; Sharma et al., 2018). Therefore, in the present study attempt was made to compare the antibiofilm potential of purified postbiotics alone and in combination with ciprofloxacin to attenuate the formation of *P. aeruginosa* PAO1 biofilm on clinically used foley catheter.

MATERIALS AND METHODS

Bacterial strains

Probiotic *L. fermentum* PUM was isolated from neonatal fecal sample using deMan Rogosa Sharpe (MRS) agar and is well characterised phenotypically, phylogenetically and for probiotic characteristics (Sharma et al., 2017). *P. aeruginosa* PAO1 strain was grown on Luria-Bertani (LB) agar by incubating at 37°C for 24h and maintained regularly in the laboratory by regular sub-culturing.

Biofilm formation on catheters

To validate the anti-biofilm potential of postbiotics, clinically used foley catheter was used as the preferred surface to form the biofilm of *P. aeruginosa* PAO1. Briefly, *P. aeruginosa* PAO1 (10^6 CFU/mL) was grown overnight and sub-cultured into flasks. With the help of sterile forceps, 3-4 sterile cut pieces of catheter (1cm) were gently transferred into each inoculated media flask and was incubated at 37ºC for seven consecutive days. To monitor the biofilm formation, after each day of incubation, catheter pieces from flask were taken out carefully and washed gently with phosphate buffered saline (PBS; 0.01M, pH 7.2). Non-adherent cells were removed gently by washing catheter with PBS (Fracchia et al., 2010) and adhered cells were scrapped gently, dissolved in PBS and cell viability in the biofilm was assessed by spread plate method. The results were expressed as $\log_{10}$CFU/mL and repeated three times (Murugan et al., 2016).

Effect of ciprofloxacin on biofilm formation

P. aeruginosa PAO1 biofilms were formed on catheter surface in presence of sub-Minimum Inhibitory Concentration (sub-MIC) of ciprofloxacin (Saini et al., 2017) and was monitored daily for seven days. After every 24h of incubation at 37°C, biofilm cells were scrapped off the catheter and enumerated by spread plate method (Murugan et al., 2016).

Determination of fractional inhibitory concentration index (FICI)

FICI was determined by using checkerboard assay as described by Mataraci and Dosle (2012). Briefly, the assay was carried out in a 96 well microtiter plate following a configuration of 8:8 yielding 64 different combinations. Ciprofloxacin and postbiotics were two fold serially diluted and added into each well, followed by inoculation with 6h old *P. aeruginosa* PAO1 culture to give a final concentration of 10^6 CFU/ml. Wells with no antibiotics served as positive control. After incubation at 37°C for 24h, plates were visualized for turbidity, an indicative of bacterial growth. The inhibitory concentration in combination (antibiotic and postbiotics) was derived from the lowest concentration of antibiotic and postbiotics showing no visible growth. FIC was calculated by dividing the MIC of antibiotic in combination of postbiotic by MIC of antibiotic/postbiotic alone (Fratini et al., 2017). FICI was calculated by summing the FIC of ciprofloxacin and postbiotic. The combination is considered synergistic when the ΣFIC is ≤ 0.5, indifferent when the ΣFIC is > 0.5 to < 2, and antagonistic when the ΣFIC is ≥ 2.

Effect of precoating of ciprofloxacin and postbiotics on biofilm formation

Ciprofloxacin and postbiotics (bacteriocin and EPS) were tested individually as well as in combination for their ability to attenuate the biofilm formation of *P. aeruginosa* PAO1 on foley catheter. Briefly, to each well of 12 well polystyrene microtiter plates, catheter piece (1cm) was placed and dipped in ciprofloxacin (0.6µg/mL), bacteriocin (2mg/mL) and EPS (4mg/mL) separately as well as in combination with a final volume of 200 µL for 18h at 4ºC. After that, 20µL of overnight grown *P. aeruginosa* PAO1 was added to microtiter plate containing foley catheter pieces to form biofilm at 37°C subsequently for seven days with regular changing of media every day. Further, to assess the effect of combinations towards the prevention of biofilm formation, biofilms formed on catheter were scraped on each day and dissolved in PBS for qualitative (Confocal laser scanning microscopy and scanning electron microscopy) and quantitative (spread plate method and flow cytometry) enumeration of biofilm cells and results were expressed as $\log_{10}$ CFU/ml.

Confocal Laser Scanning Microscopy

Briefly, cells were washed twice with PBS on day 1 and day 5 and cell viability was determined by incubating biofilm cells with an equal amount of syto9 and propidium iodide (PI; 3µL each). The plate was incubated for 20 minutes at room temperature in the dark and images were acquired in a Nikon TM View FV1000 (Nikon) confocal laser scanning microscope (Cerca et al., 2012).

Scanning Electron Microscopy

To observe the nature of the surface of biofilm on day 1 and day 5, catheter pieces were fixed in 2.5% glutarldehyde in 0.1 M phosphate buffer (pH 7.4) for 1h and then dehydrated in a graded series of aqueous ethanol solutions (50-100 %). Following, the samples were mounted on aluminium stubs, sputtered with gold and examined in SEM JSM-6100 (Saini et al., 2017).

Flow Cytometry

Biofilm cells were harvested on day 1 and day 5 from catheter pieces suspended in 12-well plates and were resuspended in 100 µL of flow cytometry staining buffer in a tube followed by addition of PI (5µL). Each tube was mixed gently and incubated for 1 minute in the dark. PI fluorescence emitted by the dead cells was determined with FACScan™ instrument using the FL-3 channel and then data was acquired (Kerstens et al., 2015).

Mechanism of bacteriocin action

In order to determine the effect of bacteriocin treatment on *P. aeruginosa* PAO1 cells, SEM was performed with sub MIC concentration of purified bacteriocin. Briefly, *P. aeruginosa* PAO1 cells treated with purified bacteriocin for 1h at 37°C, centrifuged at 9000 g for 10 minutes. The pellet obtained was fixed with glutarldehyde (2.5%) for 1h and then dehydrated in increasing concentrations of aqueous ethanol solutions (50-100 %). Thereafter, the samples were air dried in a desiccator and fixed on aluminium stubs prior to coating with gold and examined in SEM JSM-6100 for determining cell surfaces changes.

STATISTICAL ANALYSIS

The data was analysed statistically by student ‘t’ test. All the results were expressed as mean ± standard deviation (SD). A p-value of < 0.05 was considered significant.

RESULTS

Formation of biofilm and determination of fractional inhibitory concentration index

It was observed that biofilm formed by *P. aeruginosa* PAO1 on foley catheter increased from day 1 to day 7 with maximum biofilm cell density on day 5 and thereafter started decreasing (Fig. 1). It was interesting to observe that in vitro interaction of ciprofloxacin (0.06 µg/mL) and purified postbiotics, bacteriocin (0.4 mg/mL) and EPS (1 mg/ml) yielded a FICI of 0.06 (FICI≤0.5) against planktonic cells of *P. aeruginosa* PAO1 thereby, suggesting a synergistic effect.

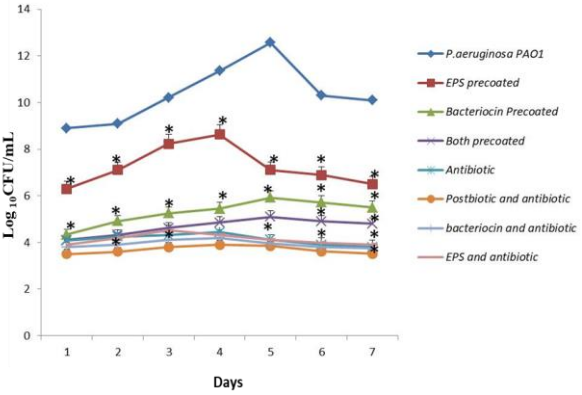

Fig. 1 Inhibitory effect of purified postbiotics and ciprofloxacin precoated on foley catheter alone and in combination on *P. aeruginosa* PAO1 biofilm. Experiment was performed in triplicates. Values are expressed in terms of mean of $\log_{10}$ CFU/mL. *$p<0.05$ v/s *P. aeruginosa* PAO1.

Antibiofilm potential of purified postbiotics and ciprofloxacin on foley catheter

Precoating of clinically used foley catheter either with purified postbiotics (bacteriocin and EPS) or ciprofloxacin alone and combination of both purified postbiotics with ciprofloxacin reduced the biofilm formation significantly ($p<0.05$) at each point of observation compared with biofilm formed by *P.aeruginosa* PAO1 (Fig. 1). More specifically, it was found that biofilm reduction was maximum with postbiotics used in combination with ciprofloxacin than bacteriocin, EPS or ciprofloxacin used alone.

Confocal laser scanning microscopic analysis

Further, confocal laser scanning micrscopy also showed that combination of postbiotics with ciprofloxacin led to enhanced killing of biofilm cells as was evident by the presence of yellow colored clustered cells and more dispersed red (dead) cells along with presence of less number of live (green) cells (Fig. 2).

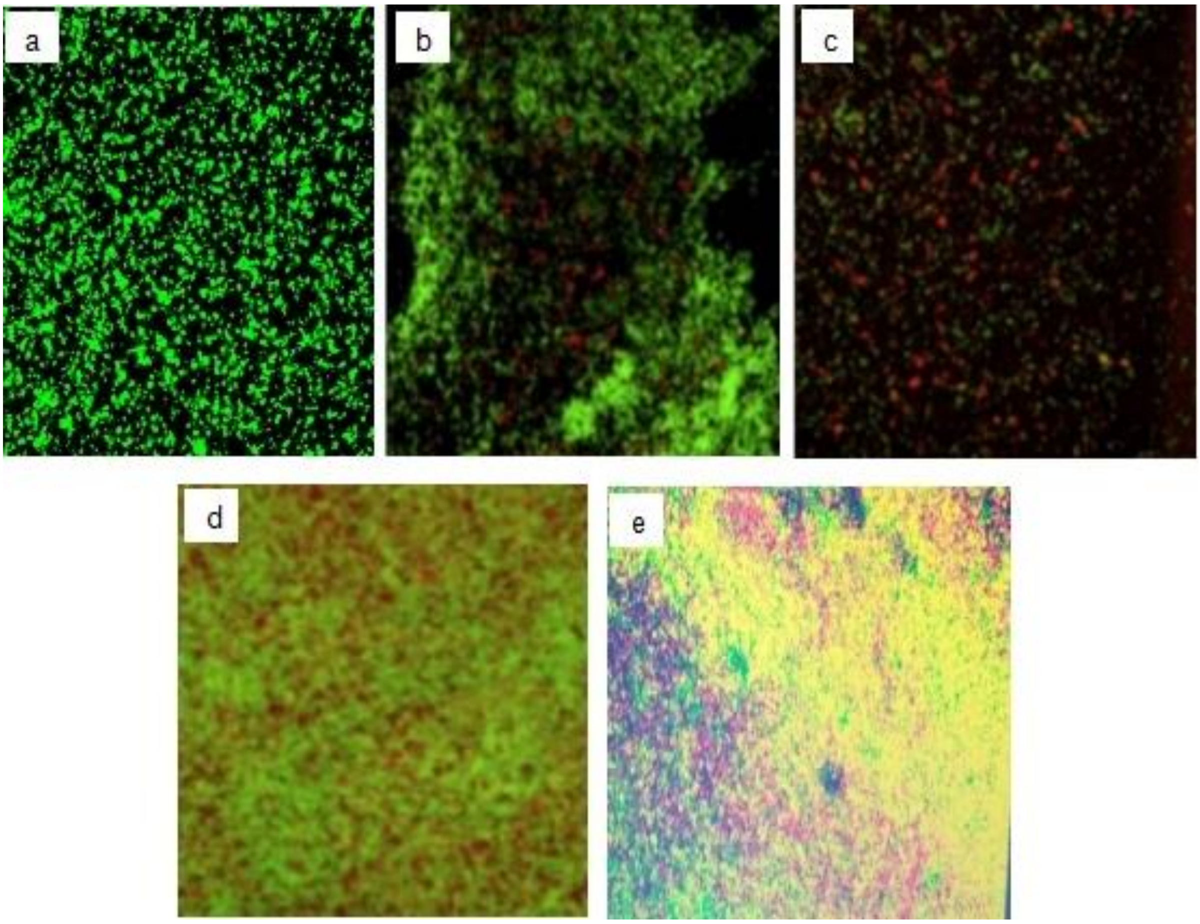

Fig. 2 Confocal laser scanning microscopic analysis showing effect of different treatments on day 5 of *P. aeruginosa* PAO1 biofilm: a) Control; b) Ciprofloxacin; c) Bacteriocin and Ciprofloxacin; d) EPS and Ciprofloxacin; e) Postbiotics and Ciprofloxacin.

Scanning electron microscopic analysis

The antibiofilm potential of postbiotics and ciprofloxacin in combination was further observed with scanning electron microscope which also indicated that postbiotics and ciprofloxacin used together reduced the biofilm cells much more effectively, compared with purified postbiotics and ciprofloxacin alone as number of biofilm forming cells were less on the foley catheter (Fig. 3).

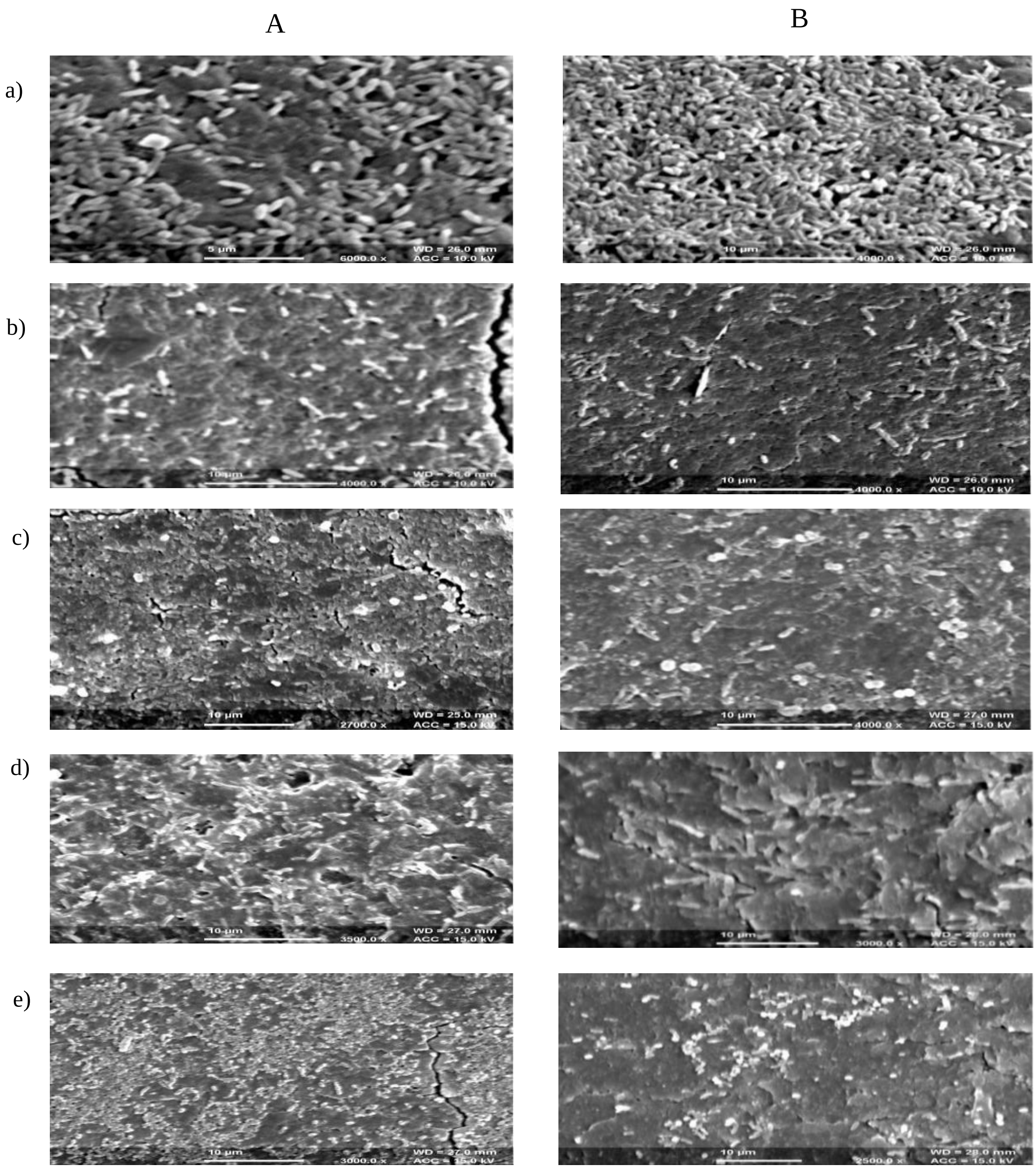

Fig. 3 Scanning electron micrograph showing effect of different treatments on day 1(A) and day 5(B) of *P. aeruginosa* PAO1 biofilm: a) *P. aeruginosa* PAO1; b) Ciprofloxacin; c) Ciprofloxacin and Bacteriocin precoated; d) Ciprofloxacin and EPS precoated; e) Bacteriocin, EPS and Ciprofloxacin.

Flow cytometry analysis

Flow cytometry also showed that combination of postbiotics and ciprofloxacin had significantly ($p<0.05$) reduced number of viable biofilm forming cells as 50.1% of cells were dead on day 1 compared with 38.2% dead cells with both postbiotics and 37.1% with ciprofloxacin alone (Fig. 4). However, on day 5, percentage of dead cells increased further with postbiotics and ciprofloxacin (85.3%), compared with bacteriocin and ciprofloxacin (78.3%), both postbiotics (78.2%), bacteriocin alone (65.4%), EPS and ciprofloxacin (62.8%), ciprofloxacin alone (59.7%) and EPS alone (45.3%; Fig. 4; Table 1). It was interesting to observe, that bacteriocin alone as well as in combination with EPS had higher inhibition even than ciprofloxacin alone and the antibiofilm potential of both postbiotics (bacteriocin and EPS) was comparable with bacteriocin and ciprofloxacin.

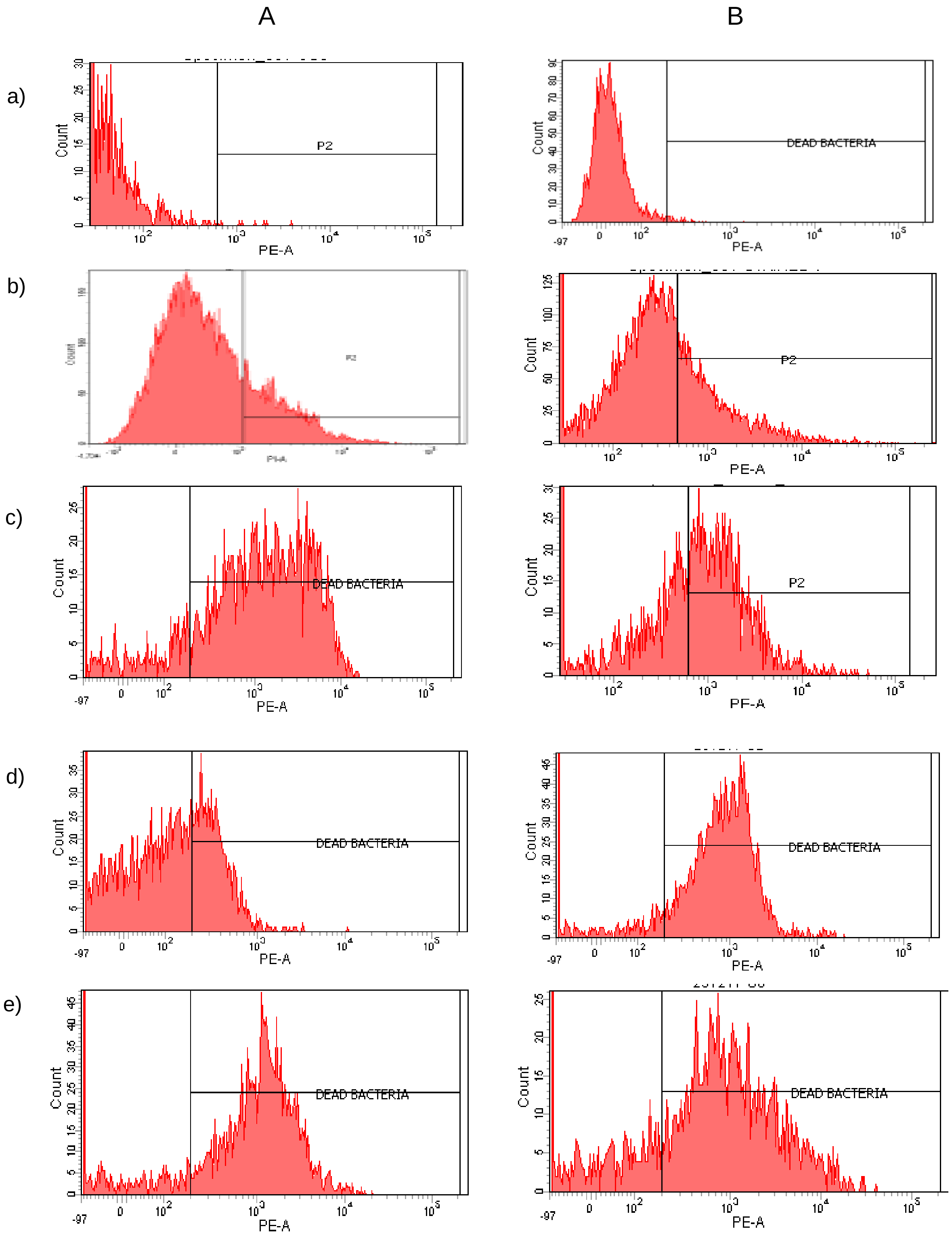

Fig. 4 Representative flow diagram showing bactericidal effect of purified postbiotics alone and in combination with ciprofloxacin precoated on foley cather on day 1(A) and day 5(B) of *P. aeruginosa* PAO1 biofilm: a) Control; b) Ciprofloxacin; c) Bacteriocin and Ciprofloxacin; d) EPS and Ciprofloxacin ; e) Postbiotic and Ciprofloxacin.

Table 1 Quantitative analysis of pre-coating with purified postbiotics and ciprofloxacin alone and in combination on the viability of *P. aeruginosa* PAO1 biofilm as per flow cytometer on day 1 and day 5 post incubation.

Coating on foley catheter	**Percentage of dead cells**	
	Day 1	Day 5
Ciprofloxacin	37.1±0.12	59.7±0.56
Purified bacteriocin	35.3±0.23	65.4*±0.31
Purified EPS	25.2±0.29	45.3±0.45
Bacteriocin and ciprofloxacin	45.4*±0.59	78.3*±0.98
EPS and Ciprofloxacin	39.8*±0.65	62.8*±0.71
Bacteriocin and EPS	38.2*±0.21	78.2*±0.32
Bacteriocin, EPS and Ciprofloxacin	**50.1*±0.23**	**85.3*±0.21**

Values are expressed as mean ± SD. *p<0.05 v/s ciprofloxacin

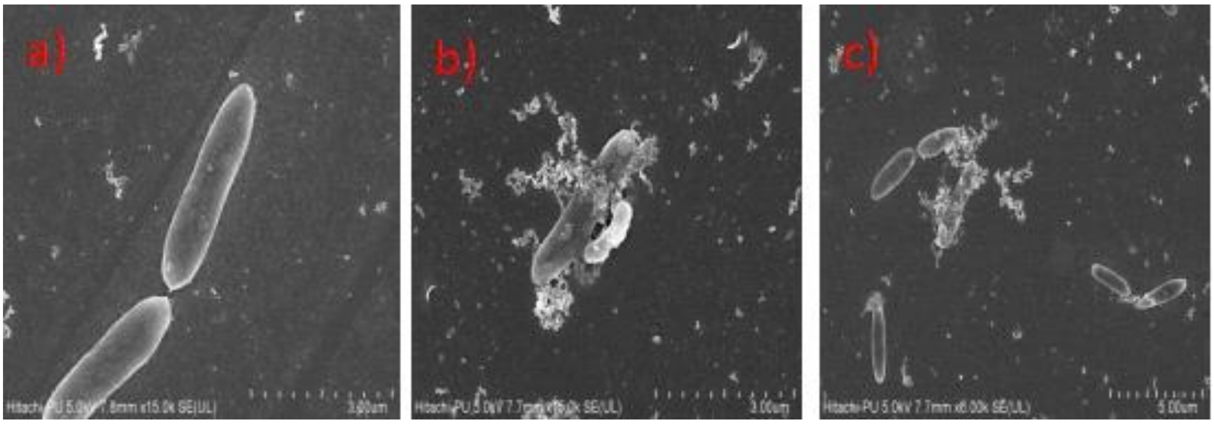

Fig. 5 Scanning electron micrograph showing effect of bacteriocin treatment on *P. aeruginosa* PAO1 planktonic cells: a) Control; b) and c) Bacteriocin treated.

Mechanism of bacteriocin action

It was interesting to observe that purified bacteriocin treated *P. aeruginosa* PAO1 cells had disrupted cell morphology due to damaged cell membrane compared with normal morphology of untreated cells (Fig. 5).

DISCUSSION

Biofilm forming pathogenic bacteria presents a major therapeutic challenge due to enhanced antibiotic resistance thereby posing a great threat to human health. Thus, there is an increasing need to explore new antimicrobial agents that present novel properties to efficiently control and manage the biofilm associated diseases. In this context, we have earlier observed that prior coating of surfaces with both crude and purified postbiotics derived from probiotic *L. fermentum* PUM led to significant reduction in biofilm formation (Sharma et al., 2017; Sharma et al., 2018). Further to elaborate our earlier observations, an attempt was made to compare the antibiofilm potential of most commonly used antibiotic ciprofloxacin alone and in combination with postbiotics (Bacteriocin and EPS) on the formation of *P.aeruginosa* PAO1 biofilm.

It was interesting to observe that though both postbiotics alone as well as in combination with ciprofloxacin inhibited *P. aeruginosa* PAO1 biofilm formed on clinically used foley catheters but the combination of postbiotic and ciprofloxacin was most effective indicating the synergistic effect. This may be due to additive effect of ciprofloxacin that inhibited the bacterial cells mainly by inhibiting bacterial enzyme topoisomerases such as DNA gyrases and topoisomerases IV leading to inhibition of DNA replication (Cirioni et al., 2010). Further, purified bacteriocin inhibited bacterial cells due to membrane permeabilization leading to pore formation while EPS reduced the cell-surface interaction (Park et al., 2011). The antimicrobial action of bacteriocins may be due to either formation of ion channels in the cell membrane or nucleases activity upon gaining access to cell, leading to pore formation in cell membrane, vis-a-vis ion leakage and loss of proton motive force (Gabrielsen et al., 2014). The present observation is in accordance with earlier studies where synergistic effect of phytochemicals and various other antibiotics have been reported (Monte et al., 2014; Jo et al., 2016). These scientists have also shown that phytochemicals in combination with antibiotics (tetracycline, erythromycin and ciprofloxacin) inhibited the growth of *S. aureus* and *E.coli* biofilms by altering their motility and quorum sensing. Similarly, in another study, it was observed that the combination of bacteriophages with cefoxitin, chloramphenicol and polymyxin B improved antimicrobial efficacy against *S. aureus*. Casey et al. and Hockenhull et al. have also observed that coating of vancomycin and other antibiotics on central venous catheters has also reduced the catheter associated bloodstream infections (Casey et al., 2008; Hockenhull et al., 2009).

This is first ever such study indicating that both the postbiotics isolated from probiotic *L. fermentum* PUM have the potential to attenuate the biofilm formation of *P. aeruginosa* PAO1 mainly due to combinatorial effect as bacteriocin led to membrane permeabilization resulting into pore formations while EPS reduced the cell- surface interactions. Additionally, it is suggested that such combinations of postbiotics and antibiotics may represent a promising anti-biofilm strategy that needs to be validated in relevant biofilm model systems that will contribute in translating such combinations into multifunctional anti-biofilm agents.

ACKNOWLEDGMENTS

Financial assistance provided by University Grant Commission-Basic Scientific Research, New Delhi, INDIA, is highly acknowledged. We are thankful to the Central Instrumentation Laboratory, Sophisticated Analytical Instrumentation Facility (SAIF), Chandigarh, Panjab University, India for confocal laser scanning microscope and scanning electron microcope analysis.

REFERENCES

Ammor S., G. Tauveron, E. Dufour, and I. Chevallier. 2006. Antibacterial activity of lactic acid bacteria against spoilage and pathogenic bacteria isolated from the same meat small-scale facility: 1-Screening and characterization of the antimicrobial compounds. Food Control, 17 : 454-61.

Boles B.R. and A.R. Horswill. 2011. Staphylococcal biofilm disassembly. Trends Microbiol., 19 : 449-455.

Casey A.L., L.A. Mermel, P. Nightingale, and T.S. Elliott. 2008. Antimicrobial central venous catheters in adults: A systematic review and meta-analysis. Lancet Infect. Dis., 8 : 763-776.

Cerca N., S. Martins, F. Cerca, K.K. Jefferson, G.B. Pier, R. Oliveira, and J. Azeredo. 2012. Comparative assessment of antibiotic susceptibility of coagulase-negative staphylococci in biofilm versus planktonic culture as assessed by bacterial enumeration or rapid XTT colorimetry. J. Antimicrob. Chemother., 56 : 331-336.

Chhibber S., D. Nag, and S. Bansal. 2013. Inhibiting biofilm formation by *Klebsiella pneumoniae* B5055 using an iron antagonizing molecule and a bacteriophage. BMC Microbiol., 13 : 174-179.

Cirioni O., F. Mocchegiani, R. Ghiselli, C. Silvestri, E. Gabrielli, E. Marchionni, F. Orlando, D. Nicolini, A. Risaliti, and A. Giacometti. 2010. Daptomycin and rifampin alone and in combination prevent vascular graft biofilm formation and emergence of antibiotic resistance in a subcutaneous rat pouch model of staphylococcal infection. Eur. J. Vasc. Endovasc. Surg., 40 : 817-22.

Fracchia L., M. Cavallo, G. Allegrone and M.G. Martinotti. 2010. A *Lactobacillus*-derived biosurfactant inhibits biofilm formation of human pathogenic *Candida albicans* biofilm producers, In: Current research technology and education topics in applied microbiology and microbial biotechnology (Ed. A. Méndez-Vilas) pp. 827-837. Formatex (Spain).

Fratini F., S. Mancini, and B. Turchi. (2017). A novel interpretation of the fractional inhibitory concentration index: the case of *Origanum vulgare* L. and *Leptospermum scoparium* J.R. et *G. Forst* essential oils against *Staphylococcus aureus* starins. Microbiol Res., 195 : 11-17.

Gabrielsen C., D.A. Brede, I.F. Nes and D.B. Diep. 2014. Circular bacteriocins: biosynthesis and mode of action. Appl. Environ. Microbiol., 80 : 6854-6862.

Hall C.W. and T.F. Mah. 2017. Molecular mechanisms of biofilm-based antibiotic resistance and tolerance in pathogenic bacteria. FEMS Microbiol. Rev., 41 : 276-301.

Hockenhull J.C., K.M. Dwan, G.W. Smith, C.L. Gamble, A. Boland, T.J. Walley, and R.C. Dickson. 2009. The clinical effectiveness of central venous catheters treated with anti-infective agents in preventing catheter-related bloodstream infections: A systematic review. Crit. Care Med., 37 : 702-712.

Jo A., T. Ding, and J. Ahn. 2016. Synergistic antimicrobial activity of bacteriophages and antibiotics against *Staphylococcus aureus.* Food Sci. Biotechnol., 25 : 935-940.

Kemperman R., A. Kuipers, H. Karsens, A. Nauta, O. Kuipers, and J. Kok. 2003. Identification and characterization of two novel clostridial bacteriocins, circularin A and closticin. Appl. Environ. Microbiol., 69 : 1589-1597.

Kerstens M., G. Boulet, M. Van kerckhoven, S. Clais, E. Lanckcker, P. Delputte, L. Maes, and P. Cos. 2015. A flow cytometric approach to quantify biofilm. Folia Microbiol., 60 : 335-342.

Kim Y., S. Oh, and S.H. Kim. 2009. Released exopolysaccharide (r-EPS) produced from probiotic bacteria reduce biofilm formation of enterohemorrhagic *Escherichia coli* O157:H7. Biochem. Biophys. Res. Commun., 379 : 324-29.

Kumar L., S. Chibber, and K. Harjai. 2013. Zingerone inhibit biofilm formation and improve antibiofilm efficacy of ciprofloxacin against *Pseudomonas aeruginosa* PAO1. Fitoterapia, 90 : 73-78.

Lindstrom C., O. Holst, L. Nilsson, R. Oste, and K.E. Andersson. 2012. Effects of *Pediococcus parvulus* 2.6 and its exopolysaccharide on plasma cholesterol levels and inflammatory markers in mice. AMB Express, 2 : 66-107.

Mataraci E. and S. Dosle. 2012. *In vitro* activities of antibiotics and antimicrobial cationic peptides alone and in combination against methicillin-resistant *Staphylococcus aureus* biofilms. Antimicrob. Agents Chemother., 56 : 6366-6371.

Miguel S., R. Lagrafeuille, B. Souweine, and C. Forestier. 2016. Anti-biofilm activity as a health issue. Front. Microbiol., 7 : 1-14.

Monte J., A.C. Abreu, A. Borges, L.C. Simoes, and M. Simoes. 2014. Antimicrobial activity of selected phytochemicals against *Escherichia coli* and *Staphylococcus aureus* and their biofilms. Pathogens, 3 : 473-498.

Murugan K., K. Selvanayaki, and S.A. Sohaibani. 2016. Urinary catheter indwelling clinical pathogen biofilm formation, exopolysaccharide characterization and their growth influencing parameters. Saudi J. Biol. Sci., 23 : 150-159.

Park S.C., Y. Park, and K.S. Hahm. 2011. The role of antimicrobial peptides in preventing multidrug-resistant bacterial Infections and biofilm formation. Int. J. Mol. Sci., 12 : 5971-5992.

Saini H., A. Vadekeetil, S. Chhibber, and K. Harjai. 2017. Azithromycin-ciprofloxacin-impregnated urinary catheters avert bacterial colonization, biofilm formation, and inflammation in a murine model of foreign-body associated urinary tract infections caused by *Pseudomonas aeruginosa*. Antimicrob. Agents Chemother., 61 : e0190616.

Sharma V., K. Harjai, and G. Shukla. 2017. Effect of bacteriocin and exopolysaccharide isolated from probiotic on *P. aeruginosa* PAO1 biofilm. Folia Microbiol., 63 : 181-90.

Sharma V., K. Harjai, and G. Shukla. 2018. Purification, characterisation and antibiofilm potential of postbiotics (bacteriocin and

EPS) isolated from *L.fermentum* against *P.aeruginosa* PAO1. British J. Pharma. Med. Res., 3 : 1510-23.

Thanh N.T., L.T. Chwen, H.L. Foo, M. Hair-Bejo, and A.B. Kasim. 2010. Inhibitory activity of metabolites produced by strains of *Lactobacillus plantarum* isolated from Malaysian fermented food. Int. J. Probiotics and Prebiotics, 5 : 37-42.

Tsilingiri K. and M. Rescigno. 2013. Postbiotics: what else?. Benef. Microbes, 4 : 101-107.

Vasudevan R. 2014. Biofilms: microbial cities of scientific significance. J. Microbiol. Exp., 1 : 14-22.

WHO. 2017. Prioritization of pathogens to guide discovery, research and development of new antibiotics for drug-resistant bacterial infections including tuberculosis. Geneva: World Health Organization.

Wu H., C. Moser, H.Z. Wang, N. Høiby, and Z.J. Song. 2015. Strategies for combating bacterial biofilm infections. Int. J. Oral Sci., 7 : 1-7.

Pb. Univ. Res. J (Sci.) Vol. 70, 2020, pp 63-76

SIGNIFICANCE OF DIETARY FACTORS IN SYSTEMIC LUPUS ERYTHEMATOSUS (SLE)

Akhil[1], Jyotsana Kaushal[1], Ankit Tandon[1], Kumari Anupam[2] and Archana Bhatnagar[1]*
[1]Department of Biochemistry, BMS-Block II, South Campus,
Panjab University, Chandigarh - 160014, India.
[2]All India Institute of Medical Sciences (AIIMS), Bilaspur - 174001, Himachal Pradesh, India.

ABSTRACT

Systemic lupus erythematosus (SLE) is an autoimmune disorder of unknown etiology, characterized by multiple organ involvement including kidney, lungs, skin, joints and central nervous system. Despite the many years of scrutiny, a safe targeting approach for SLE is still lacking. In past decades, researchers have demonstrated the potential of nutritional factors in SLE and have suggested treatment options through diet. Proper diet in SLE can modulate the symptoms, preserve the body's homeostasis and improve physical and mental well-being. This review clearly emphasizes the beneficial role of diet in SLE patients and the mentioned information could be used in daily life practice. Based on current literature, it was observed that the diet with high content of fibres, poly-unsaturated fatty acids, vitamins, minerals and nutraceutics can decrease the activity of SLE by modulating the inflammation and other immune functions.

Keywords: Diet, systemic lupus erythematosus (SLE), nutrients, autoimmune diseases.

INTRODUCTION

Systemic lupus erythematosus (SLE) is the prototype of autoimmune diseases, characterised by abnormal inflammatory response due to aberrant innate and adaptive immune responses. With unknown etiology, its mechanisms involve genetic, hormonal, epigenetic and environmental factors. The contribution of life style associated factors is still unclear, however recent studies aimed to investigate the impact of dietary habits and microbiome composition in diseases pathogenesis (Aparicio-Soto, Sánchez-Hidalgo, and Alarcón-de-la-Lastra 2017, (Katz-Agranov and Zandman-Goddard 2017). Indeed, some clinical characteristics of SLE are associated with nutrition (de Medeiros et al. 2019), thus deficiency of vitamins and minerals overlaying by systemic presentation of nephritis, arthritis and heart damage, which contributes to the increase in morbidity and mortality of these patients (Perricone et al. 2013, Teng et al. 2020). In last two decades, various clinical and pre-clinical studies have investigated the impact of diet on SLE pathogenesis and has become a highlighted topic for researchers. Various nutritional therapies including the use of supplements (*i.e.* minerals, vitamins etc.) and restrictions on carbohydrates and proteins has been applied to control the inflammatory responses in SLE (Aparicio-Soto, Sánchez-Hidalgo, and Alarcón-de-la-Lastra 2017, Constantin et al. 2019). Nutritional supplements may have potential effect on diseases activity with fewer or no side effects than those pharmacological therapies and improving the quality of life of SLE patients. Various evidences demonstrate that some nutrients and diet have antioxidant, anti-inflammatory and immune modulatory activity that may potentially regulates the diseases activity. Present review demonstrates the impact of diet and nutrients on SLE pathogenesis.

MACRONUTRIENTS

Macronutrients are the group of environmental substances i.e. widely used by organism for their metabolic processes. Several theories demonstrated the effect of major macronutrients

---

* Correspondence email: *bhatnagar.archana@gmail.com*
MS Received: November 23, 2020, Accepted: December 25, 2020

such as carbohydrates, proteins, fatty acids and fibres on body weight regulation, homeostasis, and the immune response.

CARBOHYDRATES

Carbohydrates provides energy, but when consumed in excess that may lead to weight gain. Although there is no clear evidence for proportion of carbohydrates in diet but there imbalance proportion has been suggested as the risk factor for clinical manifestation of various autoimmune diseases such as arthritis and SLE (dos Santos et al. 2013). As obesity is well known risk factor that is involved in expression of inflammatory cytokines such as tumor necrosis factor-alpha (TNF-α) and Interleukin-6 (IL-6) through several pathways. Activation of these pro-inflammatory pathways are associated with various severe morbidities in SLE patients (Elkan et al. 2012). SLE patients with obesity are characterised by a higher risk for developing insulin resistance and Type 2 diabetes mellitus (T2DM) (Kotyla 2019), which can also be associated with high risk of cardio-vascular morbidities, that may leads to early death in SLE patients (Liu and Kaplan 2018). Several studies demonstrate that up to 35% of SLE patients are overweight and 38% are obese, and these patients are characterized by very high level of C-reactive protein(CRP) (Borges et al. 2012, Oeser et al. 2005). Therefore, SLE patients should maintain a balance diet and avoid excess daily calorie intake, especially in case of obese patients.

Proteins

Several studies in animal model and human has been addressed the restriction on dietary protein. Moderate protein intake of 0.6g/kg/day is useful for decline in glomerular filtration rate in SLE patients (Milovanov et al. 2013). Reduction of protein intake may be successful approach in patients with lupus nephritis as high protein intake may leads to renal infiltrate (Milovanov et al. 2009). A study on mouse demonstrated that a limit consumption of phenylalanine and tyrosine could also have some benefits in lupus nephritis patients and reduced autoantibody production (Brown 2000, Corman 1985).

Not only proteins but some amino acids may also influence the diseases pathogenicity. Serum level of L-canavanine was significantly high in a group of Mexican SLE patients (Agmon-Levin and Shoenfeld 2016). Main source of L-canavanine is alfa-alfa and its sprouts may induced lupus like syndrome in healthy individuals and may reactivate SLE in inactivated patients (Hong et al. 2009). Another study shown that high L-arginine intake may leads to renal fibrosis and shortened life span of MRL/lpr mice (Peters et al. 2003). Main source of L-arginine is nuts, seeds, and dairy products that should be consumed by patients in limited amount as they have some another health benefits too (Tapiero et al. 2002). Major sources of the dietary proteins are mentioned in **Table 1** (given by United State Department of Agriculture (USDA), National Database for Standard References).

Table 1 Nutrients sources involved in Systemic lupus erythematosus.

Nutrients		**Sources**
MACRONUTRIENTS		
Amino acids		Eggs, meat, dairy products, pulses/legumes, whole cereals, royal jelly, and seafoods.
Polyunsaturated fatty acids	Omega-3	Fish oil, krill oil, flaxseed oil, canola oil, soybean oil, olive oil, nuts, margarine, and fishes (i.e., salmon, tuna, sardine, herring, mackerel, sablefish, whitefish).
	Omega-6	Safflower oil, sunflower oil, soybean oil, maize oil, sesame oil, canola oil, corn oil, poppy seed oil, nuts, walnut oil, primrose oil, margarine, ruminant, meat, eggs, and milk.

Fiber		Beans, cereals, pulses/legumes, whole grains, vegetables, fruits, curry powder, cinnamon, dried rosemary, dried oregano, coriander seed, dried basil, chili powder, and cloves.
MICRONUTRIENTS		
Vitamins	Vitamin A	Carrots, sweet potatoes, pumpkins, spinach, shallots, kale, pepper, liver, fish oil, various meats, and tropical fruits.
	Vitamin B complex	Fortified cereals, peanut butter, potatoes, dried peppers, nuts, banana, avocado, eggs, chicken, various red meats, liver, molluscs, salmon, and sardine.
	Vitamin C	Tangerine, orange juice, apple, papaya, guava, litchis, kiwi, broccoli, tomato, carrot, pepper, and whole cereals, green tea, coriander leaf.
	Vitamin D	Sunlight exposure, eggs, liver, fatty fishes (i.e., salmon eel, mackerel, trout sturgeon, swordfish, and sardine), fish oil, cod liver, mushrooms, and supplemented dairy products.
	Vitamin E	Wheat germ, sunflower oil and seeds, canola oil, soybean, whole cereals, nuts, almonds, peanut butter, milk, fish, spinach, pepper, and margarine.
Minerals		
	Calcium	Dairy products, dried basils, dried tofu, kale, soybean, spinach, sardine, and fortified whole cereals.
	Zinc	Molluscs, whole cereals, peanut butter, seeds, white beans, soybean, spinach, milk, beef, turkey, and lamb.
	Sodium	Table salt, soy sauce, salted fishes (i.e., mackerel and salmon), wasabi, salted tofu, chili powder, canned foods, and cheeses with salt.
	Selenium	Pike, carp, rainbow trout, molluscs, wheat germ, whole cereals, sunflower seeds, nuts, fish (tuna, cod, haddock, salmon, crayfish, herring), egg, chicken liver, turkey, lamb, beef, mustard seed, fortified flours and products, and ricotta.
	Iron	Fortified whole cereals, dried basil, dried spearmint, seaweed, cumin seed, fenugreek seed, turmeric, bay leaf, soybeans, kale, pulses/legumes, molluscs, various meats, spinach, and broccoli.
	Copper	Beans, sesame seeds, sunflower seeds, dried basil, lentils, mushrooms, seaweed, nuts, molluscs, various meats, and liver.
Nutraceutics		
Polyphenols	Resveratrol	Grapes, peanut, wine, dark chocolate, tea and berries).
	Curcumin	Turmeric
	Virgin olive oil	
Flavonoids	Lycopene	Red tomatoes and carrots
	Apigenin	Thyme, peppermint, and olives

Fatty acids

Especially poly-unsaturated fatty acids (PUFAs) are the essential and effective diet factors for the SLE patients (Huerta et al. 2016). Omega -3- fatty acids, such as eicosapentanoic acid (EPA) and docosahexanoic acid (DHA), can reduce the level of inflammatory mediators as well as CRP and other inflammatory mediators like T cell mediated cytotoxicity and chemotaxis from monocytes and neutrophils (Borges et al. 2014, Halade et al. 2010). Mechanism behind the anti-inflammatory of EPA was due to inhibition of cyclooxygenase (COX)-1 (Smith 2005). Apart from anti-inflammatory effect, omega-3- fatty acids can also be protect from free radicals and helps in reducing the auto-antibodies and regulates proteinuria and blood pressure in SLE patients (Klack, Bonfa, and Borba Neto 2012).

The dietary intake of saturated fatty acids have association with greater body mass index (BMI) (Van Dam et al. 2002). There is significant association between BMI in SLE patients and presence of lupus nephritis and hypertension (Rizk et al. 2012).Saturated fatty acids increase the sensitivity of receptor to LPS that may increase the inflammation in SLE patients, whereas as PUFS reduce the responsiveness to LPS (Bray et al. 2002). Main sources of saturated fatty acids are coconut, coconut oil, palm oil and palm kernel oil that should be consumed by SLE patients in limited amount.

Major sources of the dietary fatty acids are mentioned in **Table 1**. Fish oil with high amount of DHA reduced the auto-antibody deposition in kidney and lipopolysaccharides (LPS) induced IL-18 production. Omega-3-PUFA from fish oil have been investigated to improve the endothelial function in SLE patients (Wright et al. 2008). Fish oil supplements has also been investigated for improving the conditions of fatigue and depression in SLE patients (Arriens et al. 2015). Another omega-3-PUFA like linoleic acid has been demonstrated to obstruct oxidative stress as well as nuclear factor kappa B (NF-κB), thus improved the SLE activity (Bergamo et al. 2006). Extra virgin olive oil, a main source of unsaturated fatty acid, exerts beneficial effects by involving in various pathways such as JAK-STAT, MAPK and NF-κB pathways (Aparicio-Soto et al. 2016). High dosage of fish oil (18g/day) may be beneficial for reducing the (Tri-glycerides) TG level, while increasing the level of HDL-C (Patavino and Brady 2001).

Fibres

Dietary fibres are the carbohydrate polymers that are resistance to digestive enzymes and thus neither digested or absorbed in the small intestine (Jones 2014). The daily intake of fibres in the form of cereals, vegetables and fruits should be in adequate amount in order to reduces blood pressures and hyperlipidemia and C reactive protein (CRP) (Klack, Bonfa, and Borba Neto 2012). Major sources of the dietary fibres are mentioned in **Table 1**. Exceeding fibre intake should be avoided because it can reduce the absorption of nutrients and adequate water consumption should be considered. Fibres also regulates the gut microbiota that may influence the development of autoimmune and cardiovascular disorders (Makki et al. 2018). Lower availability of fibres can leads to inflammation and imbalance in innate and adaptive immunity (Kim et al. 2016).

MICRONUTRIENTS

Micronutrients are the essential elements that are required in very low quantity and have very important role in various metabolic activities throughout life to maintain good health. Micronutrients are comprised of vitamins and minerals that cannot be synthesized by our body but must be a part of diet (Gernand et al. 2016).

Vitamins

Vitamin A, retinoic acid, have antineoplastic effect and maintain immune system by inhibiting the Th-17 and auto-antibody generation (**Figure 1**), thus should be included in diet of SLE patients (Klack, Bonfa, and Borba Neto 2012).A study on MRL/lpr mice demonstrate that, Vitamin A exerted its effect on development of autoimmunity by decreasing the inflammation (Liao et al. 2015).

Daily intake of 100,000U of Vitamin A produced Natural killer cells, enhanced antibody dependent cellular cytoxicity and IL-2 level in SLE patients (Gergely et al. 1988).

Usually the deficiency of Vitamin B complex has been shown in autoimmunity patients. Several studies also demonstrated the deficiency of Vitamin B complex in SLE patients as compared to healthy controls (Le-dong, Kang, and Qian 2007). Natural sources for Vitamin B complex included red meat, liver, banana, and eggs (**Table 1**) (Klack, Bonfa, and Borba Neto 2012).

Vitamin C, an important anti-oxidant and reduces the inflammation and anti-dsDNA antibody generation (**Figure 1**), therefore, it should be supplemented in SLE patients at a dose of 1g/day or in combination with vitamin E due to its synergic potential (Constantin et al. 2019).

Vitamin D have very important role in mineral metabolism and immune system homeostasis and its deficiency may leads to more severe SLE symptoms, especially in patients with dark skin (Mu, Zhang, and Luo 2015). Vitamin D plays a protective role in SLE patients by reducing the auto-antibody mediated injury of podocytes in kidney (Yu et al. 2019). Deficiency of Vitamin D is correlated with high SLEDAI score with juvenile-onset SLE (El Garf et al. 2015). Very low serum level of Vitamin D found in SLE patients compared with those of healthy controls and Vitamin D supplementation was found to be very helpful in improving the fatigue in SLE patients (Islam et al. 2019, Zheng et al. 2019). Deficiency of vitamin D leads to more severe SLE through higher expression of mTOR mRNA (Zhao et al. 2017). In lupus patients, increased level of IL-17, IL-6 and auto-antibodies (**Figure 1**) has been associated with a Vitamin D deficiency (Souto et al. 2011). Vitamin D show its immunomodulatory effects by downregulating the expression of the toll like receptors-3 (TLR-3) and TLR-9 (Yazdanpanah et al. 2017). Higher level of interferon-alpha (IFN-α) and IFN-ϒ has been observed in SLE patients with vitamin D deficiency (Ritterhouse et al. 2011). Vitamin D also induce the expansion of Treg cells (Piantoni et al. 2015). The $CD4^+/CD8^+$ ratio is very high in SLE patients with Vitamin D deficiency (Zhao et al. 2017). Sunlight is known to initiate the production of vitamin D, but SLE patients have photosensitivity, thus the dietary intake of vitamin should be preferred.

Current understanding regarding the role of Vitamin E in SLE patients is in developing stage. A study demonstrated a low serum level of vitamin E in SLE patients compared with those normal individuals (Comstock et al. 1997). Oral administration of vitamin E in SLE patients inhibits the synthesis of antibodies (**Figure 1**) (Maeshima et al. 2007). Antioxidants enzymes such as Reduced glutathione-S-transferase (GSH) and Superoxide dismutase were significantly increased, when Vitamin E and *Nigella sativa* were supplemented together (Shahba et al. 2015). Major sources of the vitamins are mentioned in **Table 1** (USDA, National Database for Standard References).

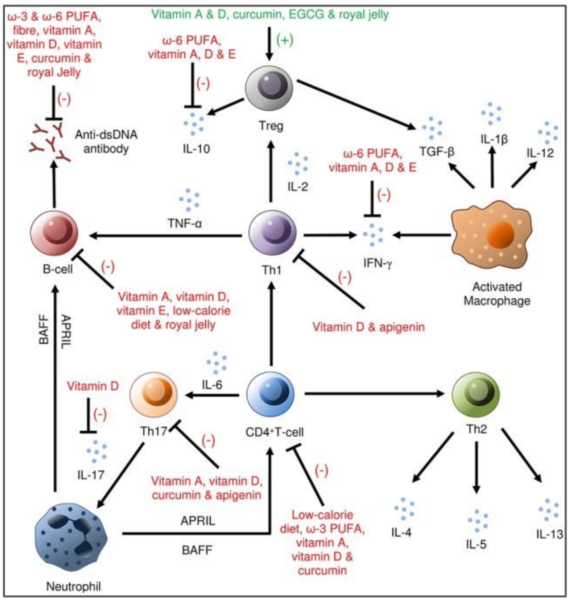

Fig. 1. Immunomodulatory function of vitamins in SLE (Islam et al. 2020). Vitamin A and C inhibits anti-dsDNA antibodies and Th17 cells generation. Vitamin D inhibits IL-6 and IL-17 secretion, and expression of TLR-3 and TLR-9. Vitamin E inhibits secretion of IL-10, IFN-ϒ and anti-dsDNA antibody.

Minerals

Special attention needs to be paid to mineral intake because they generally attenuate SLE via different immunomodulatory mechanisms. Minerals such as calcium, zinc, iron, sodium, copper and selenium play a role in SLE activity by modulating the immune function. It was demonstrated that a decrease in zinc concentration can improve the severe symptoms in SLE patients (Leiba et al. 2001). Major source of zinc is molluscs, milk and soybean (Klack, Bonfa, and Borba Neto 2012). Sodium intake has no benefits in SLE and can also create severe conditions in patients (Țânțu et al. 2014).

Selenium has anti-inflammatory and anti-oxidant activity, and the major sources are nuts, eggs and whole cereals (Klack, Bonfa, and Borba Neto 2012). Calcium level can be elevated by intake of spinach, dairy products and soybean. Iron should be present in diet of anaemic SLE patients and major sources for iron are beans, lentils, tofu and cashew (Klack, Bonfa, and Borba Neto 2012). Due to this, it becomes important to pay attention to the mineral intake in case of SLE patients.

NUTRACEUTICS

Various nutrients were demonstrated in the past that have an additional potential effect on body's metabolism. It has also been shown that nutrients can modify the organ and tissue integrity as well as immune response. The adverse effect i.e. induced due to various chemical therapeutics used in the current treatment regime can be overcome by using these nutraceutics.

Resveratrol, is a phytoalexin molecule belongs to the polyphenol stilbenoids group with a high antioxidant and anti-inflammatory potential (Pannu and Bhatnagar 2019b). It is majorly found in grapes, peanut, wine, dark chocolate, tea and berries (blueberries and bilberries). A study carried out in our lab on pristane induced SLE mice model demonstrated the beneficial effect of resveratrol in morbidities related to lupus nephritis along with reduction in serum levels of various inflammatory markers such as IL-6, IFN-α and TNF-α (Pannu and Bhatnagar 2019a).

Curcumin, a natural polyphenol of turmeric, has been investigated as protective agent in lupus nephritis by reducing serum auto-antibodies level, and inhibiting inflammasome expression (Zhao et al. 2019). Curcumin also enhanced the Treg cell concentration and reduce the IgG antibody level in SLE-prone NZB/W F1 mice (Lee et al. 2013). A study observed that administration of small amount of curcumin can modulate the Th17/Treg balance in SLE patients without affecting the healthy subjects (Handono et al. 2015). Low dose of curcumin also reduced the proliferation of peripheral blood mononuclear cells (PBMCs) in patients with lupus nephritis (Wang et al. 2017).

Virgin olive oil and its phenol fraction was administered in pristane induced mice that showed them as immunomodulators of SLE activity (Aparicio-Soto et al. 2018). The major bioactive polyphenols present in green tea is epigallocatechin-3-gallate (EGCG) that can act as anti-oxidant by enhancing the Nrf2 anti-oxidant signalling pathway (Tsai et al. 2011). EGCG reduced then inflammation in mesangial cells through PI3K/Akt/mTOR pathway by inhibiting the Akt phosphorylation (Peairs et al. 2010). *In-vitro* study on PBMCs isolated from SLE patients showed that the phenol fraction of green tea can also modulate the cytokine production through NF-κB signalling pathway (Aparicio-Soto et al. 2017). A well balance diet with high intake of polyphenols sources like fruits (orange, watermelon, kiwi, and apple) and vegetables (lentils, celery, and lettuce) has been associated with presence of beneficial microorganisms in faecal matter of SLE patients.

Flavonoids such as lycopene has been investigated for its protective role in SLE patients. Lycopene enriched in tomato and red carrot and its high serum level has been associated with reduced SLEDAI activity (Han and Han 2016). Apigenin, a flavonoids rich in thyme, peppermint, and olive inhibits the autoantibody generation by reducing the autoantigen presentation and decreases the expansion of autoreactive Th17 cells (Kang et al. 2009). Vegetables rich in flavonoids has been associated with the presence of beneficial microorganisms such as *Bifidobacterium* and *lactobacillus*. Royal jelly, secreted by worker honey bees, enriched in vitamins, minerals and polyphenols. The SLEDAI score was significantly improved after royal jelly treatment(Islam et al. 2020). The serum level of anti-dsDNA antibody and autoreactive T and B cells was significantly decreased after the royal jelly administration (Mannoor et al. 2009).

CONCLUSION

Patient’s lifestyle may have an important role to play in the pathology of SLE, because stress and diet can directly influence the inflammation milieu in the body (Căruntu et al. 2014). By small improvement in diet and life style, patients may protect themselves from cost effective hospitalization and treatments (Rațiu et al. 2011). Various studies demonstrate different effects of diet that may vary from patient to patient, paving way for a more personalised approach with a very specific diet plan for different SLE patients. SLE patients should prefer the less processed foods e.g. whole grains instead of refined ones, rice instead of sugar and sea salt instead of refined salt (Constantin et al. 2019). At least one fruit daily (oranges, apples) with fresh vegetables (carrots) should be consumed along with the addition of different nuts (almonds, walnuts) and seeds (flaxseeds) in the daily diet. Proper diet in SLE patients can help in maintaining the body homeostasis and can improve the physical and mental health of patients. Because the dietary supplements like macro and micronutrients have immunomodulatory activities, they should be included in SLE patient’s diet.

REFERENCES

Agmon-Levin, Nancy, and Y Shoenfeld. 2016. "Systemic Lupus Erythematosus and the Environment." In *Systemic Lupus Erythematosus*, 63-67. Elsevier.

Aparicio-Soto, Marina, Sergio Montserrat-de la Paz, Marina Sanchez-Hidalgo, Ana Cardeno, Beatriz Bermudez, Francisco JG Muriana, and Catalina Alarcon-de-la-Lastra. 2018. "Virgin olive oil and its phenol fraction modulate monocyte/macrophage functionality: a potential therapeutic strategy in the treatment of systemic lupus erythematosus." *British Journal of Nutrition* 120 (6):681-692.

Aparicio-Soto, Marina, Marina Sánchez-Hidalgo, and Catalina Alarcón-de-la-Lastra. 2017. "An update on diet and nutritional factors in systemic lupus erythematosus management." *Nutrition Research Reviews* 30 (1):118.

Aparicio-Soto, Marina, M Sánchez-Hidalgo, A Cárdeno, M Á Rosillo, S Sánchez-Fidalgo, Jose Utrilla, Inés Martín-Lacave, and Catalina Alarcón-de-la-Lastra. 2016. "Dietary extra virgin olive oil attenuates kidney injury in pristane-induced SLE model via activation of HO-1/Nrf-2 antioxidant pathway and suppression of JAK/STAT, NF-κB and MAPK activation." *The Journal of Nutritional Biochemistry* 27:278-288.

Aparicio-Soto, Marina, Marina Sánchéz-Hidalgo, Ana Cárdeno, Jose Manuel Lucena, Francisca Gonzáléz-Escribano, Maria Jesus Castillo, and Catalina Alarcón-de-la-Lastra. 2017. "The phenolic fraction of extra virgin olive oil modulates the activation and the inflammatory response of T cells from patients with systemic lupus erythematosus and healthy donors." *Molecular nutrition & food research* 61 (8):1601080.

Arriens, Cristina, Linda S Hynan, Robert H Lerman, David R Karp, and Chandra Mohan. 2015. "Placebo-controlled randomized clinical trial of fish oil's impact on fatigue, quality of life, and disease activity in systemic lupus erythematosus." *Nutrition journal* 14 (1):82.

Bergamo, Paolo, D Luongo, F Maurano, G Mazzarella, R Stefanile, and M Rossi. 2006. "Conjugated linoleic acid enhances glutathione synthesis and attenuates pathological signs in MRL/MpJ-Faslpr mice." *Journal of lipid research* 47 (11):2382-2391.

Borges, M Curado, Fabiana de Miranda Moura dos Santos, R W Telles, C C Duarte Lanna, and M Isabel TD Correia. 2012. "Nutritional status and food intake in patients with systemic lupus erythematosus." *Nutrition* 28 (11-12):1098-1103.

Borges, Mariane Curado, Fabiana de Miranda Moura Santos, Rosa Weiss Telles, Maria Isabel Toulson Davisson Correia, and Cristina Costa Duarte Lanna. 2014. "Polyunsaturated omega-3 fatty acids and systemic lupus erythematosus: what do we know?" *Revista Brasileira de Reumatologia (English Edition)* 54 (6):459-466.

Bray, George A, Jennifer C Lovejoy, Steven R Smith, James P DeLany, Michael Lefevre, Daniel Hwang, Donna H Ryan, and David A York. 2002. "The influence of different fats and fatty acids on obesity, insulin resistance and inflammation." *The Journal of nutrition* 132 (9):2488-2491.

Brown, Amy Christine. 2000. "Lupus erythematosus and nutrition: a review of the literature." *Journal of Renal Nutrition* 10 (4):170-183.

Căruntu, Constantin, Daniel Boda, Sorin Musat, Ana Căruntu, and Eugen Mandache. 2014. "Stress-induced mast cell activation in glabrous and hairy skin." *Mediators of inflammation* 2014.

Comstock, GW, AE Burke, SC Hoffman, KJ Helzlsouer, A Bendich, AT Masi, EP Norkus, RL Malamet, and M Eric Gershwin. 1997. "Serum concentrations of α tocopherol, β carotene, and retinol preceding the diagnosis of rheumatoid arthritis and systemic lupus erythematosus." *Annals of the rheumatic diseases* 56 (5):323-325.

Constantin, Maria‑Magdalena, Iuliana Elena Nita, Rodica Olteanu, Traian Constantin, Stefana Bucur, Clara Matei, and Anca Raducan. 2019. "Significance and impact of dietary factors on systemic lupus erythematosus pathogenesis." *Experimental and therapeutic medicine* 17 (2):1085-1090.

Corman, Lourdes C. 1985. "The role of diet in animal models of systemic lupus erythematosus: possible implications for human lupus." Seminars in arthritis and rheumatism.

De Medeiros, Marília Cristina Santos, Jussara Cristina Alves Medeiros, Humberto Jefferson de Medeiros, José Carlos Gomes de Carvalho Leitão, and Maria Irany Knackfuss. 2019. "Dietary intervention and health in patients with systemic lupus erythematosus: a systematic review of the evidence." *Critical reviews in food science and nutrition* 59 (16):2666-2673.

Dos Santos, Fabiana de Miranda Moura, Mariane Curado Borges, Rosa Weiss Telles, Maria Isabel TD Correia, and Cristina Costa Duarte Lanna. 2013. "Excess weight and associated risk factors in patients with systemic lupus erythematosus." *Rheumatology international* 33 (3):681-688.

El Garf, Kamal, Huda Marzouk, Yomna Farag, Laila Rasheed, and Ayman El Garf. 2015. "Vitamin D status in Egyptian patients with juvenile-onset systemic lupus erythematosus." *Rheumatology international* 35 (9):1535-1540.

Elkan, AC, C Anania, T Gustafsson, T Jogestrand, I Hafström, and J Frostegård. 2012. "Diet and fatty acid pattern among patients with SLE: associations with disease activity, blood lipids and atherosclerosis." *Lupus* 21 (13):1405-1411.

Gergely, P, R Gonzalez-Cabello, I Jakab, CV Vien, and I Bodo. 1988. "Effect of vitamin A treatment on cellular immune reactivity in patients with CLL." *Acta medica Hungarica* 45 (3-4):307-311.

Gernand, Alison D, Kerry J Schulze, Christine P Stewart, Keith P West, and Parul Christian. 2016. "Micronutrient deficiencies in pregnancy worldwide: health effects and prevention." *Nature Reviews Endocrinology* 12 (5):274-289.

Halade, Ganesh V, Md Mizanur Rahman, Arunabh Bhattacharya, Jeffrey L Barnes, Bysani Chandrasekar, and Gabriel Fernandes. 2010. "Docosahexaenoic acid-enriched fish oil attenuates kidney disease and prolongs median and maximal life span of autoimmune lupus-prone mice." *The Journal of Immunology* 184 (9):5280-5286.

Han, Guang-Ming, and Xiao-Feng Han. 2016. "Lycopene reduces mortality in people with systemic lupus erythematosus: A pilot study based on the third national health and nutrition examination survey." *Journal of Dermatological Treatment* 27 (5):430-435.

Handono, Kusworini, Mirza Zaka Pratama, Agustina Tri Endharti, and Handono Kalim. 2015. "Treatment of low doses curcumin could modulate Th17/Treg balance specifically on CD4+ T cell cultures of systemic lupus erythematosus patients." *Central-European journal of immunology* 40 (4):461.

Hong, YH, CJ Huang, SC Wang, and BF Lin. 2009. "The ethyl acetate extract of alfalfa sprout ameliorates disease severity of autoimmune-prone MRL-lpr/lpr mice." *Lupus* 18 (3):206-215.

Huerta, Maria Dolores Rodríguez, Maria M Trujillo-Martín, Íñigo Rúa-Figueroa, Leticia Cuellar-Pompa, Raúl Quirós-López, Pedro Serrano-Aguilar, and SLE Spanish. 2016. "Healthy lifestyle habits for patients with systemic lupus erythematosus: a systemic review." Seminars in arthritis and rheumatism.

Islam, Md Asiful, Shahad Saif Khandker, Sayeda Sadia Alam, Przemysław Kotyla, and Rosline Hassan. 2019. "Vitamin D status in patients with systemic lupus erythematosus (SLE): A systematic review and meta-analysis." *Autoimmunity Reviews* 18 (11):102392.

Islam, Md Asiful, Shahad Saif Khandker, Przemysław J Kotyla, and Rosline Hassan. 2020. "Immunomodulatory Effects of Diet and Nutrients in Systemic Lupus Erythematosus (SLE):

A Systematic Review." *Frontiers in immunology* 11:1477.

Jones, Julie Miller. 2014. "CODEX-aligned dietary fiber definitions help to bridge the 'fiber gap'." *Nutrition journal* 13 (1):34.

Kang, Hee-Kap, Diane Ecklund, Michael Liu, and Syamal K Datta. 2009. "Apigenin, a non-mutagenic dietary flavonoid, suppresses lupus by inhibiting autoantigen presentation for expansion of autoreactive Th1 and Th17 cells." *Arthritis research & therapy* 11 (2):1-13.

Katz-Agranov, Nurit, and Gisele Zandman-Goddard. 2017. "The microbiome and systemic lupus erythematosus." *Immunologic Research* 65 (2):432-437.

Kim, Myunghoo, Yaqing Qie, Jeongho Park, and Chang H Kim. 2016. "Gut microbial metabolites fuel host antibody responses." *Cell host & microbe* 20 (2):202-214.

Klack, Karin, E Bonfa, and E F B Neto. 2012. "Diet and nutritional aspects in systemic lupus erythematosus." *Revista brasileira de reumatologia* 52 (3):395-408.

Kotyla, PJ. 2019. "Insulin resistance varies across connective tissue diseases patients: comparison between rheumatoid arthritis, systemic lupus erythematosus and systemic sclerosis." *Clinical and experimental rheumatology* 37 (6):14.

Le-dong, SUN, Kang ZENG, and WANG Qian. 2007. "Study of riboflavin nutritional status in patients with systemic lupus erythematosus." *Modern Preventive Medicine* (1):53.

Lee, Hyojung, Hyunseong Kim, Gihyun Lee, Hwan-Suck Chung, and Hyunsu Bae. 2013. "Curcumin attenuates lupus nephritis upon interaction with regulatory T cells in New Zealand Black/White mice." *British journal of nutrition* 110 (1):69-76.

Leiba, A, H Amital, M Eric Gershwin, and Y Shoenfeld. 2001. "Diet and lupus." *Lupus* 10 (3):246-248.

Liao, Xiaofeng, Jingjing Ren, Cheng-Hsin Wei, A Catharine Ross, Thomas E Cecere, Bernard S Jortner, S Ansar Ahmed, and Xin M Luo. 2015. "Paradoxical effects of all-trans-retinoic acid on lupus-like disease in the MRL/lpr mouse model." *PLoS One* 10 (3):e0118176.

Liu, Yudong, and Mariana J Kaplan. 2018. "Cardiovascular disease in systemic lupus erythematosus: an update." *Current Opinion in Rheumatology* 30 (5):441-448.

Maeshima, Etsuko, Xiang-Ming Liang, Mikako Goda, Haruhisa Otani, and Masatoshi Mune. 2007. "The efficacy of vitamin E against oxidative damage and autoantibody production in systemic lupus erythematosus: a preliminary study." *Clinical rheumatology* 26 (3):401-404.

Makki, Kassem, Edward C Deehan, Jens Walter, and Fredrik Bäckhed. 2018. "The impact of dietary fiber on gut microbiota in host health and disease." *Cell host & microbe* 23 (6):705-715.

Mannoor, MK, I Shimabukuro, M Tsukamotoa, H Watanabe, K Yamaguchi, and Y Sato. 2009. "Honeybee royal jelly inhibits autoimmunity in SLE-prone NZB× NZW F1 mice." *Lupus* 18 (1):44-52.

Milovanov, IuS, LV Lysenko, LIu Milovanova, and IA Dobrosmyslov. 2009. "The role of balanced low-protein diet in inhibition of predialysis chronic kidney disease progression in patients with systemic diseases." *Terapevticheskii arkhiv* 81 (8):52-57.

Milovanov, Yury S, Lyudmila Y Milovanova, AA Mikhailov, and II Aleksandrova. 2013. "Influence of Diet Balanced with Essential Amino Acids/Keto Acid Analogs and High-Nutrient Blend on the Progression of Renal Failure in Patients in the Pre-Dialysis Stage of Chronic Kidney Disease Caused by Systemic Autoimmune Diseases." *Group* 10:8.

Mu, Qinghui, Husen Zhang, and Xin M Luo. 2015. "SLE: another autoimmune disorder influenced by microbes and diet?" *Frontiers in immunology* 6:608.

Oeser, Annette, Cecilia P Chung, Yu Asanuma, Ingrid Avalos, and C Michael Stein. 2005. "Obesity is an independent contributor to functional capacity and inflammation in systemic lupus erythematosus." *Arthritis & Rheumatism* 52 (11):3651-3659.

Pannu, N., and Archana Bhatnagar. 2019a. "Combinatorial therapeutic effect of resveratrol and piperine on murine model of systemic lupus erythematosus."*Inflammopharmacology*: 1-24.

Pannu, Naveet, and Archana Bhatnagar. 2019b. "Resveratrol: From enhanced biosynthesis and bioavailability to multitargeting chronic diseases." *Biomedicine & Pharmacotherapy* 109:2237-2251.

Patavino, Tom, and David M Brady. 2001. "Natural medicine and nutritional therapy as an alternative treatment in systemic lupus erythematosus." *Alternative Medicine Review* 6 (5):460-472.

Peairs, Abigail, Rujuan Dai, Lu Gan, Samuel Shimp, M Nichole Rylander, Liwu Li, and Christopher M Reilly. 2010. "Epigallocatechin-3-gallate (EGCG) attenuates inflammation in MRL/lpr mouse mesangial cells." *Cellular & Molecular Immunology* 7 (2):123-132.

Perricone, Carlo, Nancy Agmon-Levin, Serena Colafrancesco, and Yehuda Shoenfeld. 2013. "Vitamins and systemic lupus erythematosus: to D or not to D." *Expert Review of Clinical Immunology* 9 (5):397-399.

Peters, Harm, Wayne A Border, Matthias Rückert, Stephanie Krämer, Hans-H Neumayer, and Nancy A Noble. 2003. "L-arginine supplementation accelerates renal fibrosis and shortens life span in experimental lupus nephritis." *Kidney international* 63 (4):1382-1392.

Piantoni, S, L Andreoli, M Scarsi, A Zanola, F Dall’Ara, C Pizzorni, M Cutolo, P Airò, and A Tincani. 2015. "Phenotype modifications of T-cells and their shift toward a Th2 response in patients with systemic lupus erythematosus supplemented with different monthly regimens of vitamin D." *Lupus* 24 (4-5):490-498.

Rațiu, MONICA PAULA, IRINA Purcărea, Florian Popa, VICTOR LORIN Purcărea, THEODOR VALENTIN Purcărea, Dumitru Lupuleasa, and Daniel Boda. 2011. "Escaping the economic turn down through performing employees, creative leaders and growth driver capabilities in the Romanian pharmaceutical industry." *Farmacia* 59 (1):119-130.

Ritterhouse, Lauren L, Sherry R Crowe, Timothy B Niewold, Diane L Kamen, Susan R Macwana, Virginia C Roberts, Amy B Dedeke, John B Harley, R Hal Scofield, and Joel M Guthridge. 2011. "Vitamin D deficiency is associated with an increased autoimmune response in healthy individuals and in patients with systemic lupus erythematosus." *Annals of the rheumatic diseases* 70 (9):1569-1574.

Rizk, Amal, Tamer A Gheita, Sahar Nassef, and Abeer Abdallah. 2012. "The impact of obesity in systemic lupus erythematosus on disease parameters, quality of life, functional capacity and the risk of atherosclerosis." *International journal of rheumatic diseases* 15 (3):261-267.

Shahba, Abeer, Noha E Esheba, Abd-Allah Fooda, Samia El-Dardiry, Ayman Wagih, and Omnia el-Deeb. 2015. "Effect of Nigella Sativa and Vitamin E on Some Oxidative/Nitrosative Biomarkers in Systemic Lupus Erythematosus Patients." *Life Science Journal* 12 (7).

Smith, William L. 2005. "Cyclooxygenases, peroxide tone and the allure of fish oil." *Current opinion in cell biology* 17 (2):174-182.

Souto, MID, A Coelho, C Guo, LMC Mendonça, S Argolo, JAS Papi, and MLF Farias. 2011. "Vitamin D insufficiency in Brazilian patients with SLE: prevalence, associated factors, and relationship with activity." *Lupus* 20 (10):1019-1026.

Ţânţu, MONICA, Eduard Belu, Elena Bobescu, Armean P Armean Sm, and Domnariu Cd Constantin Mm. 2014. "Role of angiotensin converting enzyme (ACE) inhibitors in hypertension and cardiovascular protection management." *Trachans, K., Sideris, S., Aggeli, C., Poulidakis, E., Gatzoulis, K., Tousoulis, D., & Kallikazaros, IONNIS (2014) Diabetic Cardiomyopathy: From Pathophysiology to Treatment. Hellenic J Cardiol* 55:411-421.

Tapiero, H, G Mathe, P Couvreur, and KD Tew. 2002. "I. Arginine." *Biomedicine & pharmacotherapy* 56 (9):439-445.

Teng, Xiangyu, Josephine Brown, Seung-Chul Choi, Wei Li, and Laurence Morel. 2020. "Metabolic determinants of lupus pathogenesis." *Immunological Reviews* 295 (1):167-186.

Tsai, Pei-Yi, Shuk-Man Ka, Jia-Ming Chang, Hsiang-Cheng Chen, Hao-Ai Shui, Chen-Yun Li, Kuo-Feng Hua, Wen-Liang Chang, Jiann-Jyh Huang, and Sung-Sen Yang. 2011. "Epigallocatechin-3-gallate prevents lupus nephritis development in mice via enhancing the Nrf2 antioxidant pathway and inhibiting NLRP3 inflammasome activation." *Free Radical Biology and Medicine* 51 (3):744-754.

Van Dam, Rob M, Walter C Willett, Eric B Rimm, Meir J Stampfer, and Frank B Hu. 2002. "Dietary fat and meat intake in relation to risk of type 2 diabetes in men." *Diabetes care* 25 (3):417-424.

Wang, Meiying, Gengmin Zhou, Jiyang Lv, Peiying Zeng, Chengshan Guo, and Qingwen Wang. 2017. "Curcumin modulation of the activation of PYK2 in peripheral blood mononuclear cells from patients with lupus nephritis." *Reumatologia* 55 (6):269.

Wright, Stephen A, Fiona M O'Prey, Michelle T McHenry, William J Leahey, Adrian B Devine, Emeir M Duffy, Dennis G Johnston, Michael B Finch, AL Bell, and GE McVeigh. 2008. "A randomised interventional trial of ω-3-polyunsaturated fatty acids on endothelial function and disease activity in systemic lupus erythematosus." *Annals of the rheumatic diseases* 67 (6):841-848.

Yazdanpanah, Esmaeil, Mahmoud Mahmoudi, Maryam Sahebari, Zahra Rezaieyazdi, Seyed-Alireza Esmaeili, Nafiseh Tabasi, Soheila Jaberi, Amirhossein Sahebkar, and Maryam Rastin. 2017. "Vitamin D3 alters the expression of toll-like receptors in peripheral blood mononuclear cells of patients with systemic lupus erythematosus." *Journal of Cellular Biochemistry* 118 (12):4831-4835.

Yu, Qi, Yingjin Qiao, Dongwei Liu, Fengxun Liu, Congcong Gao, Jiayu Duan, Lulu Liang, Xueqi Di, Yi Yuan, and Yukui Gao. 2019. "Vitamin D protects podocytes from autoantibodies induced injury in lupus nephritis by reducing aberrant autophagy." *Arthritis Research & Therapy* 21 (1):19.

Zhao, Jijun, Jihui Wang, Mianjing Zhou, Mengyuan Li, Meirong Li, and Hechang Tan. 2019. "Curcumin attenuates murine lupus via inhibiting NLRP3 inflammasome." *International immunopharmacology* 69:213-216.

Zhao, Man, Xiu-Hong Duan, Zhen-Zhen Wu, Cong-Cong Gao, Na Wang, and Zhao-Hui Zheng. 2017. "Severe vitamin D deficiency affects the expression of autophagy related genes in PBMCs and T-cell subsets in active systemic lupus erythematosus." *American journal of clinical and experimental immunology* 6 (4):43.

Zheng, Ronghao, Alex Gonzalez, Jing Yue, Xiaolin Wu, Ming Qiu, Lin Gui, Songbai Zhu, and Li Huang. 2019. "Efficacy and safety of vitamin D supplementation in patients with systemic lupus erythematosus: a meta-analysis of randomized controlled trials." *The American Journal of the Medical Sciences* 358 (2):104-114.

Pb. Univ. Res. J (Sci.) Vol. 70, 2020, pp 77-84

EFFICACY OF *PEDALIUM MUREX* (L.) FRUIT EXTRACT TOWARDS HYPEROXALURIA INDUCED RENAL INJURY

Tanzeer Kaur[1]*, Sweety Sindhu[1], Ankita Bhardwaj[1],
Rishi Bhardwaj[1], Nirlep Chhiber[2], Rakesh Kumar Bijarnia[3]
[1]Department of Biophysics, Panjab University, Chandigarh-160014, India
[2]Department of Biochemistry, Panjab University, Chandigarh-160014, India
[3]Medzome lifesciencez, Baddi, H.P, India

ABSTRACT

Phytotherapeutic formulations have gained a considerable reputation in the recent past for the treatment of kidney stone disease for which a study was designed to decipher the anti-urolithiatic influence of Pedalium murex plant extract in hyperoxaluria induced renal injury in male wistar rats. Animals were randomly segregated into three groups: normal control, hyperoxaluric group and hyperoxaluric + P. murex group, respectively. Treatment with P. murex extract significantly curtailed the oxidative stress and rectified the antioxidant enzymes activity in the renal tissue of hyperoxaluric rats along with reduction in calcium oxalate crystals. Therefore P.murex can be a promising phytotherapeutic for kidney stone management and needs to be explored for future prospects.

Keywords: Pedalium murex, plant extract, urolithiasis, oxidative stress

INTRODUCTION

Urolithiasis is a worldwide occurring disease with an enormous socio-economic impact. A kaleidoscope of features contributes towards the formation of renal stones namely hereditary, dietary, geographical etc. Calcium stones comprising oxalate and phosphate, alone or in the combined form constitute approximately 85% of the renal stones present in humans. Urolithiasis or renal stone formation passes through different stages commencing with nidus formation, further provoking adhesion to renal tubular epithelium and growth of crystal which may result in ureter obstruction (Smith et al., 1992). Both *in vivo* and *in vitro* investigations have strengthened the role of oxalate and calcium oxalate crystals in prompting renal epithelial cell injury as an aftermath of lipid peroxidation and reactive oxygen species (Thamiselvam et al., 2003). Studies have substantiated the vital involvement of antioxidants in defending cells against the glomerular inflammatory processes, through a chain of cascades consisting of inflammatory intermediates, highlighting the importance of inhibiting NF-κB activity (Ozaki et al., 1999).

Nature has been benevolent enough in providing mankind a store of house of various remediating resources capable of combating several ailments. Till date, wide range of plant extracts have consolidated their character in counter-acting the occurrence of calcium stone deposition at both the platforms that is *in vitro* and *in vivo*. In addition, literature has supported the proposition of using phytotherapeutic agents either in the form of alternative or adjunct as a possible remediating therapy in modulating urolithiasis (Vanachayangkul et al., 2010). Antioxidants potential of fauna has been deemed helpful in ameliorating the crystal induced renal injury. *Pedalium murex* belonging to the family Pedaliaceae, known as Bada Gokhru commonly, has been predominant in the coastal areas of southern territory of India and tropical Africa. It has been found to be used as an indigenous medicine for the treatment of numerous diseases largely devoted to its free radical scavenger activity. Pharmacologically, the plant has earned its therapeutic character for being nephroprotective, antiulcerogenic, hypolepidemic, aphrodisiac, antimicrobial and insecticidal (Patel et al., 2011). As per the literature available P.murex extract has shown potential as renoprotective agent in myriad of diseases ranging from drug induced nephrotoxicity, nephrolithiasis, in addition to being heptoprotective remedy (Shelke et al., 2009; Ananta et al., 2010; Adikay et al., 2010; Sreedevi et al., 2011; Patel et al., 2016; Kaleeswaran et al., 2019). Thus, the current study aims for better understanding of underlying mechanism by which *P.murex* reverted hyperoxaluria induced renal injury and its activity specifically related to calcium oxalate crystals induced oxidative stress.

---

* Corresponding author e-mail: tanzeer.kaur@pu.ac.in
MS Received: November 17, 2020, Accepted: December 28, 2020

MATERIALS AND METHODOLOGY

Collection and identification of plant materials

Pedalium murex (*P. murex*) fruits was obtained from an authorized herbal shop in Chandigarh (India) which were then sent to Agharkar Research Institute, Pune, India for identification and authentication (voucher specimen no F-252).

Preparation of aqueous extract of *Pedalium murex*

P. murex fruits were properly dried under the shade and were powdered coarsely thereafter. The powder was then suspended in distilled water as aqueous suspension (10% w/v) and used for study.

Inhibitory potential of *P. murex* extract towards calcium phosphate (CaP) mineralization

Mineralization assay was employed to evaluate the calcium phosphate (CaP) precipitation via monitoring the magnitude of *in vitro* mineral phase formation being performed in the absence of any matrix (Herberg et al., 1985). The percent inhibition in the mineral phase was determined as:

$$\% \text{ inhibition} = [(C - T)/C] \times 100$$

Where C stand for the concentration of Ca^{2+} and HPO_4^{2-} ion precipitates formed in control and T represents concentrations of Ca^{2+} and HPO_4^{2-} ions precipitate formed in test.

Animals and experimental model

Healthy male wistar rats weighing 250-300 g were procured from central animal house of Panjab University Chandigarh. Acclimatization of animals was performed with standard animal feed (Aashirwad industries, Punjab, India) and water *ad libitum* for one week. The animal experimental procedures were approved by Institutional Animal Ethics Committee (reference no. 1409/BP dated 12-09-2014) and animal care was taken as per the guidelines mentioned by the Indian National Science Academy Guidelines.

Animals were sorted into three different groups (5-6 animals per group). Group 1 animals performed as normal (NRM) and received normal feed and water *ad libitum* for 9 days. To induce hyperoxaluria (HOX) group 2 rats were administered with 0.4% ethylene glycol (EG) along with 1.0 % ammonium chloride (NH_4Cl) in drinking water for 9 days. Group 3 rats received simultaneous administration of EG and NH_4Cl and treatment regime of *P. murex* extract at the dose of 200 $mg.Kg^{-1}$ body weight orally.

Biochemical estimation in urine and serum

After the completion of duration of the experiment, metabolic cages were utilized to collect 24 h urine samples from rats using 20 µl of 20% sodium azide. Blood was collected from the ocular vein of rats under the influence of anesthesia to separate the serum by centrifugation at 3,000 g. Afterwards levels of urea, creatinine and calcium was estimated by using ERBA kit in blood and urine.

Polarization microscopy of urinary crystal

To analyze the presence of crystals, drop of freshly obtained urine was spread on a glass slide and was visualized under polarized light using Leica DM3000 light microscope.

Tissue collection and Histopathological studies

The rats were anaesthetized under the dose of diethyl ether and sacrificed by decapitation after the completion of treatment schedule. Kidney tissues were thereafter removed, fixed in buffered formaldehyde for histological analysis using transverse sections of 5 µm thickness followed by staining with hematoxylin and eosin and viewed under light microscope (Leica DM3000). Further, portion of tissues were stored at -80°C for other experiments.

RNA isolation and mRNA expression of KIM-1

Total RNA from the renal samples was isolated using TRI- reagent (Sigma) and retrotranscribed to cDNA by cDNA synthesis kit (BIORAD). The primers used for KIM-1 is (r) KIM-1: forward 5'- ATGGACGATC TGTTTCCC-3', reverse 5'-TGAGCAAGGACCCAG ATAGA-3'; GAPDH: forward 5'-GGGCAGCCCAG AACATCAT-3', reverse 5'-CCGTTCAGCTCTGGG ATGAC-3'. PCR amplification using 5x FIRE Pol Master Green PCR reaction mix (Solis Biodyn) was performed and GAPDH was used for normalizing the values obtained for each specific product. Band intensity was measured densitometrically using Image J 1.48 software.

Lipid peroxidation

Lipid peroxidation was estimated by the method described by Wills (1966).

Catalase

The catalase activity was estimated by measuring the breakdown of hydrogen peroxide at 240 nm according to the method of Luck (1963).

Superoxide dismutase (SOD)

Superoxide dismutase activity was estimated by the method of Kono (1978). The activity of superoxide dismutase was expressed as International Units per mg protein (IU/mg protein)

STATISTICAL ANALYSIS

One-way ANOVA and the Tukey's test for multiple comparisons were employed to analyze data using Graph Pad Prism (version 5.0; San Diego, USA). The values were expressed as mean ± SD. Results were considered significant if $p < 0.05$.

RESULTS

The aqueous extract of *P. murex* (10% w/v) was first tested for its potential to inhibit the initiation of calcium and phosphate mineral phase at different concentrations. The dose showing maximum inhibition of calcium ion precipitation (40%) was found to be 250 µl of extract which corresponded to a dose of 200 mg/kg body weight and was thus finalized for the animal study. Additionally, *P. murex* showed highest percentage inhibition (79%) of phosphate ion with 100 µl of the extract (Fig 1).

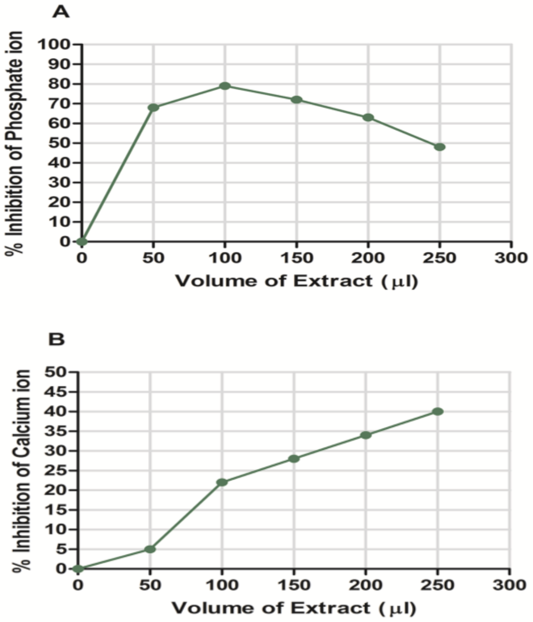

Fig. 1. Effect of varying concentration of *P.murex* extract on % inhibition of phosphate and calcium ion.

Hyperoxaluric rats were treated with *P.murex* extract at a finalized dose of 200 mg/kg body weight. During the treatment schedule all animals were observed for their food and water intake and body weight, and they all progressed well. As shown in Table 1, in hyperoxaluric group animals showed significantly elevated levels of urea and creatinine in serum in contrast to the normal rats. However, rats treated with *P.murex* extract successfully ameliorated the increased creatinine levels in serum, however the amount of urea was not restored to normal levels. On the other hand, the urinary concentration of urea and creatinine was significantly reduced to near normal rats. Urinary calcium was found to be increased in hyperoxaluric rats and it concentration was high even in rats treated with *P.murex* extract.

Table1. Effect of P.murex extract on renal functional markers in hyperoxaluria treated rats.

	NRM	HOX	HOX + PM
Serum			
Urea (mg/dl)	50.49 ± 10.43	105.50 ± 30.92 (+108%)	98.81 ± 6.09 (-6%)
Creatinine (mg/dl)	0.95 ± 0.08	1.17 ± 0.31 (+23%)	0.90 ± 0.12 (-22%)
Urine			
Urea (mg/dl)	30.62 ± 9.39	58.38 ± 33.03* (+89.39%)	18.10 ± 0.28$^{\#\#}$ (-67.08%)
Calcium conc. (mg/24 h urine volume)	1.18± 0.03	13.51 ± 4.42** (+1043%)	13.48 ± 2.32 (-0.20%)

*Hyperoxaluric animals showed higher ranges of standard deviation (S.D.) which can be attributed to the individual capacity of animals to respond to oxalate induced changes. Varying susceptibility towards oxalate toxicity in certain subjects in comparison to other subjects is a probable reason behind higher S.D. values.

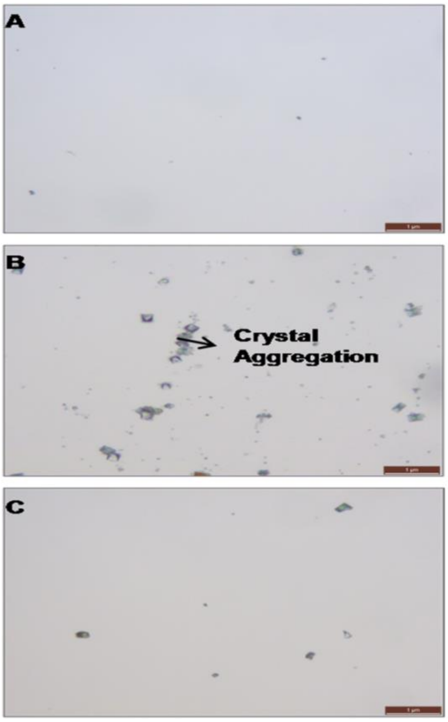

Fig. 2. Polarization micrographs of rat urine. (A) Urine of normal group (NRM); (B) Urine of hyperoxaluric rats (HOX) showing aggregate of COD crystal (bipyramidal) and COM crystals (dumbbell shaped); and (C) Urine of *P. murex* treated hyperoxaluric rats (HOX+PM) showing few COD crystals. Original magnification 200X.

To observe the anti-calcifying properties of *P.murex*, urine from all three groups was evaluated for crystalluria. Polarization microscopy revealed the presence of large number of calcium dihydrate (COD) crystals and their aggregation in the urine of rats subjected to hyperoxaluric abuse whereas in *P.murex* treated rat, urine showed marked decline in the number of urinary crystals (Fig 2). However, urine of normal rats showed absence of any crystals.

To investigate the therapeutic potential of *P.murex* on hyperoxaluria incited oxidative stress and tissue injury in renal tissue, extent of lipid peroxidation (LPO) and mRNA levels of KIM-1 (kidney injury molecule-1) were studied. MDA being an end product of lipid peroxidation exhibited significantly elevated levels in the hyperoxaluric group in comparison to normal group (Fig 3A). However, upon treatment with *P.murex*, MDA levels were found to be significantly diminished. Similarly, expression of renal injury marker KIM-1 was up-regulated in hyperoxaluric rats suggesting the possible role of calcium oxalate crystals in induction of injury (Fig 3B). Furthermore, significantly diminished expression of KIM-1 after *P.murex* treatment exhibited its efficacy in reducing the injury of renal tissue.

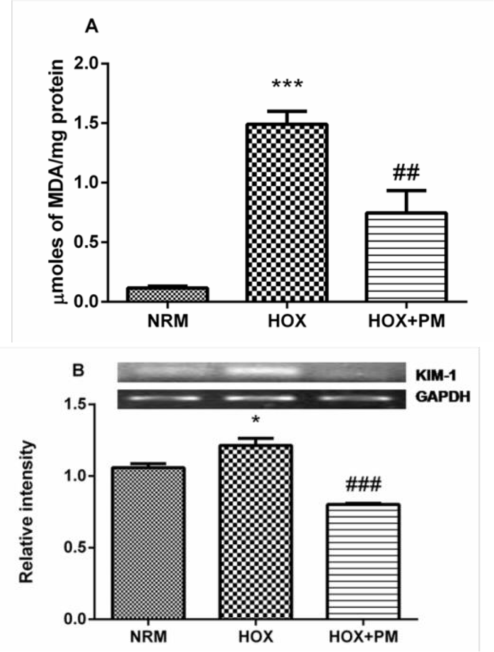

Fig. 3. Alterations in (A) lipid peroxidation (LPO), (B) mRNA expression of Kidney injury marker (KIM-1) in rats exposed to hyperoxaluria (HOX) and subsequent treatment with *P.murex* (HOX+PM). Values are expressed as Mean ± S.D. $^{*}p<0.05$, $^{**}p<0.01$, $^{***}p< 0.001$ compared to normal group; $^{\#}p<0.05$, $^{\#\#}p< 0.01$, $^{\#\#\#}p< 0.001$ compared to hyperoxaluric group.

Further, histological analysis of hyperoxaluric rats revealed tubular epithelial damage, dilation of proximal tubules and excessive shrinkage of glomerulus (Fig 4B). *P.murex* supplementation restored the histoarchitecture of the renal tissue by reducing dilation of proximal tubules and an intact glomerulus was observed (Fig 4C).

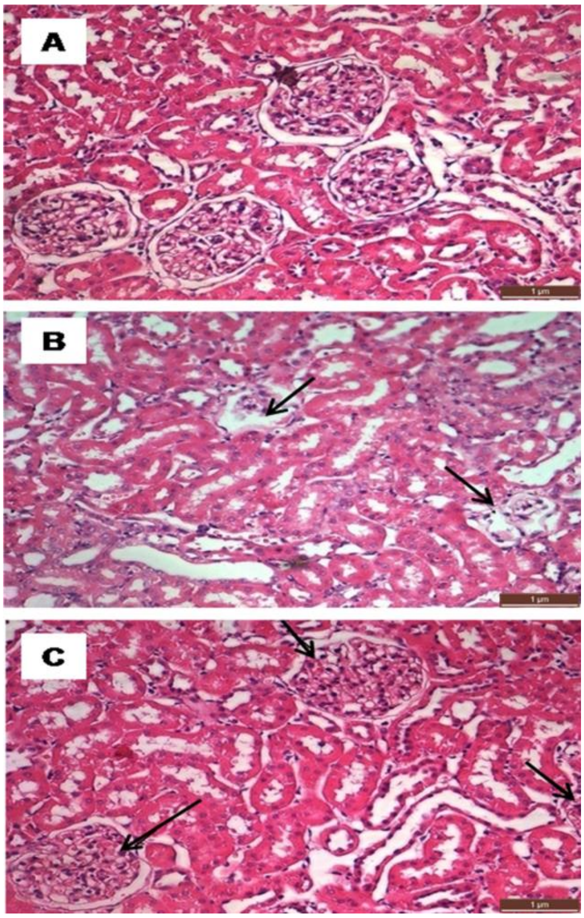

Fig. 4. Renal histological analysis, stained with hematoxylin and eosin (original magnification 200X). (A) Normal animals (NRM), showing normal renal architecture; (B) Hyperoxaluric animals (HOX), showed dilation of proximal tubules and glomerulus damage; and (C) *P. murex* extract treated rats shows less damage and little dilation of tubules (HOX+PM).

To appraise the antioxidant potential of *P.murex*, antioxidant enzymes were estimated. Interestingly, evaluation of antioxidant enzymes (Catalase and Superoxide dismutase) which regulates the redox balance of the cell were found to be significantly higher in hyperoxaluric group in comparison to control group, which may be attributed to the innate nature of cells to combat the oxidative insult incurred by calcium oxalate crystals (Fig 5A and B). Whereas hyperoxaluric animals treated with *P.murex*, showed significant decline in superoxide dismutase activity as compared to the hyperoxaluric rats.

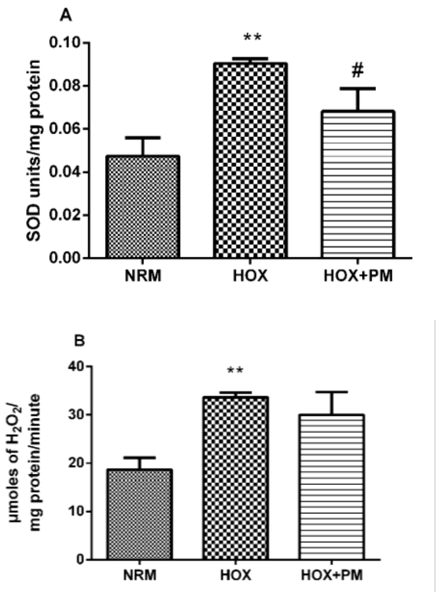

Fig. 5. Alterations in (A) superoxide dismutase (SOD) and (B) catalase (CAT), in the rats exposed to hyperoxaluria (HOX) and subsequent treatment with *P.murex* (HOX+PM).Values are expressed as Mean ± S.D. *p<0.05, **p<0.01, ***p< 0.001 compared to normal group; $^{\#}$p<0.05, $^{\#\#}$p< 0.01, $^{\#\#\#}$p< 0.001 compared to hyperoxaluric group.

DISCUSSION

In the present study, hyperoxaluric induction was achieved by subjecting wistar rats to 0.4% ethylene glycol and 1% ammonium chloride in normal drinking water for 9 days (Kaur et al., 2009). Studies have proved ethylene glycol (EG) a known precursor of oxalate, administration or accidental exposure of which possibly results in hyperoxaluria, CaOx crystalluria, and occasional deposition of CaOx crystals in the kidney. Also, ammonium chloride has been advocated to accelerate the renal stone progression by acidifying the urine environment along with the decrease in urinary citrate excretion, which in turn may be responsible for increased deposition of CaOx crystals in the kidneys (Atmani et al., 2003). Based upon the acute toxicity studies, it was safe to explore the effect of *P. murex* upto 2000 mg.Kg^{-1} body weight in rats (Balasubramanian et al., 2008). In our investigations one tenth (200 mg.Kg^{-1} body weight) of the above described dose of *P. murex* Linn. Fruit was employed. Practitioners usually recommend oral route of administration of traditional medicines, following the similar pattern of drug administration efficacy of *P. murex* in ethylene glycol induced urolithiatic rat model was evaluated.

Oxalate, one of the chief constituents of renal stones has established its reputation of being a potent inducer of free radicals which further vandalize the kidney tissue. Free radicals namely superoxide ions and hydroxyl radicals along with H_2O_2 are the major culprits of oxalate induced renal injury (Saravanan et al., 1995). In the existing study, *P. murex* extract markedly reduced the levels of MDA in renal tissue indicating its potential to quench free radicals. ROS generation in response to hyperoxaluric insult provokes the kidney to uplift the antioxidant defense systems comprising superoxide dismutase (SOD), catalase (CAT), glutathione peroxidase, and glutathione (GSH) in order to resist the possible damage (Green et al., 2005). In the present investigation, oxalate exposure exhibited increased activity of SOD and CAT. Elevation in the SOD activity usually leads to the elevation in the formation of hydrogen peroxide. However, withstanding the increased levels of hydrogen peroxide, Catalase comes to the rescue by decomposing the hydrogen peroxide, for which it can be probably hypothesized that after the workability of SOD in converting the superoxide radical to hydrogen peroxide, an increase in the catalase level was reported. As reported, activities of catalase and manganese superoxide dismutase were found to be increased in the early stages of ethylene glycol induced urolithiasis model in rats; however, attenuation of antioxidant activity of all other enzymes but CAT was observed on day 42 (Huang et al., 2002). The rebalancing of elevated levels of these enzymes in treatment group showed the protective nature of *P. Murex* against hyperoxaluria.

Hyperoxaluria induced free radical generation lead to tubular injury which subsequently resulted in the up-regulation of kidney injury molecule-1 (KIM-1) which is considered as a hallmark of renal injury (Khandrika et al., 2012). *P. murex* extract showed a significant inhibitory potency towards the increased expression levels of KIM-1 in hyperoxaluric rats. Hyperoxaluric conditions resulted to elevated urea and creatinine levels in urine/serum of hyperoxaluric rats indicating the renal dysfunction and crystal deposition in kidney tissue. *P.murex* extract administration moderately restored renal functioning by maintaining the levels of urea and creatinine in serum and urine of rats.

Crystalluria analysis revealed that hyperoxaluric group excreted abundant and large calcium oxalate crystals. *P. murex* treated hyperoxaluric group showed lesser number of crystals. These findings strongly emphasize the ability of *P. murex* to reduce the incidence of crystal formation *in vivo*. Histopathological studies showed extensive shrinkage of glomerulus, loss of membrane integrity and cystic dilation of renal tubules in the hyperoxaluric group, suggesting renal damage. Additionally, several literatures have proactively co-linked the occurrence of crystal retention and renal injury. In accordance to the postulations, under hyperoxaluric conditions, oxalate ions attach to the renal epithelial cells (proximal tubular cells) and are engulfed thereafter. This process of engulfment falls under the term, Crystal-Cell Interaction which is a very well known step in nephrolithiasis and promotes renal injury (Tsujihata, 2008; Davalos et al., 2010; Mulay et al., 2013). Post engulfment, oxalate evokes inflammatory responses and affect the mitochondrial functioning which further results in the generation of free radicals (oxidative stress) which advances the renal injury and affects renal functionality. *P. murex* supplementation restored the histology to near normal levels confirming the protective effect of the extract on kidney by restoring the abnormal changes.

From the present investigation, it is understood that *Pedalium murex* can be considered as an effective drug against calcium oxalate crystallization. Moreover, it is to be noted that reports highlighting the nephroprotective active principle of P. murex are still in the stage of infancy though literature have proactively emphasized the presence of flavanoids and phenolic compounds which are known to possess anti-oxidant and anti-inflammatory properties (Devanesan et al., 2018). However a recent study by Ramadevi et al. (2020) reported the significance of Pedatilin, an active compound of P. murex against bacteria induced struvite renal stones along with literature Concomitant with the reports, P. murex has proven to exhibit promising antioxidant and anti-inflammatory potential which can hypothesized as a mechanism of action of the plant extract in combating deleterious alterations via managing oxidative stress (LPO), antioxidant enzyme status (GSH, Catalae and SOD) and inflammation (Shelke et al., 2009; Patel et al., 2011; Patel et al., 2013; Sangeetha et al., 2016). Our present results put forth the prospect of using this plant as a therapeutic agent to curtail calcium oxalate induced renal stress and subsequently kidney stone management.

CONFLICT OF INTEREST

Authors state that there is no conflict of interest

REFERENCES

Adikay, S., J.P.Y. Latha, and B. Koganti. 2010. Effect of fruits of Pedailum murex against cadmium chloride induced nephrotoxicity in rats, Int. J. Drug Dev. Res., 2:40–46.

Ananta, T., R. Kokilavani., A. Balakrishnan, and K. Gurusamy. 2010. Effect of ethanolic fruit extract of Pedalium murex Linn. in ethylene glycol induced urolithiasis in male wistar albino rats. AncSci. Life, 29:29-34.

Atmani, F., Y. Slimani, M. Mimouni, and B. Hacht. 2003. Prophylaxis of calcium oxalate stones by Herniaria hirsute on experimentally induced nephrolithiasis in rats. BJU Int., 92:137–40.

Balasubramanian, M.N., P. Muralidharan, and G. Balamurugan. 2008. Anti hyperlipidemic activity of Pedalium murex (Linn.) fruits on high fat diet fed rats. Int. J. Pharmacol., 4:310-13.

Davalos, M., S. Konno, M. Eshghi, and M. Choudhury. 2010. First Prize (Tie): oxidative renal cell injury induced by calcium oxalate crystal and renoprotection with antioxidants: a possible role of oxidative stress in nephrolithiasis. J. Endourol., 24:339-45.

Devanesan A.A., T. Zipora, B.A., Smilin, G. Deviram, and S. Thilagar. 2018. Phytochemical and pharmacological status of indigenous medicinal plant Pedalium murex L.—A review. Biomed. Pharmacother., 103:1456-63.

Green, M.L., M. Hatch, and R.W. Freel. 2005. Ethylene glycol induces hyperoxaluria without metabolic acidosis in rats. Am. J. Physiol. Renal Physiol., 289:536-43.

Herzberg, O., and N.G. Michael. 1985. James Structure of the calcium regulatory muscle protein troponin-C at 2.8 Å resolution. Nature. 313:653–9.

Huang, H.S., M.C. Ma, J. Chen, and C.F. Chen. 2002. Changes in the oxidant-antioxidant balance in the kidney of rats with nephrolithiasis induced by ethylene glycol. J. Urol., 167:2584-93.

Kaleeswaran, B., S. Ramadevi, R. Murugesan, S. Srigopalram, T. Suman, and T. Balasubramanian. 2019. Evaluation of anti-urolithiatic potential of ethyl acetate extract of Pedalium murex L. on struvite crystal (kidney stone). J. Tradit. Complement. Med., 9:24-37.

Kaur, T., R.K. Bijarnia, S.K. Singla, and C. Tandon. 2009. *In vivo* efficacy of Trachyspermum ammi anticalcifying protein in urolithiatic rat model. J. Ethnopharmacol., 126:459-462.

Khandrika, L., S. Koul, R.B. Meacham, and H.K. Koul. 2012. Kidney injury molecule-1 is up-regulated in renal epithelial cells in response to oxalate *in vitro* and in renal tissues in response to hyperoxaluria *in vivo*. PLoS One 7:e44174.

Kono, Y. 1978. Generation of superoxide radicals during auto oxidation of hydroxylamine and an assay for superoxide dismutase. Arch. Biochem. Biophys., 186:189-95.

Luck, H. 1963. A spectrophotometric method for the estimation of catalase. In: Methods of enzymatic analysis. Academic Press, New York, 886-7.

Mulay, S.R., A. Evan, and H.J. Anders. 2014. Molecular mechanisms of crystal-related kidney inflammation and injury. Implications for cholesterol embolism, crystalline nephropathies and kidney stone disease. Nephrol. Dial. Transpl., 29:507-14.

Ozaki, H., A.Y. Yu, N. Della, K. Ozaki, J.D. Luna, H. Yamada, S.F. Hackett, N. Okamoto, D.J. Zack, G.L. Semenza, and P.A. Campochiaro. 1999. Hypoxia inducible factor-1alpha is increased in ischemic retina: temporal and spatial correlation with VEGF expression. Invest. Phthalmol. Vis. Sci., 40:182-9.

Patel, D.K., D. Laloo, R. Kumar, and S. Hemalatha. 2011. Pedalium murex Linn.: an overview of its phytopharmacological aspects. Asian. Pac. J. Trop. Med., 4:748–55.

Patel, D.K., R. Kumar, S.K. Prasad, and S. Hemalatha. 2011. Pedalium murex Linn (Pedaliaceae) fruits: a comparative antioxidant activity of its different fractions. Asian Pac. J. Trop. Biomed., 1:395-400.

Patel, M.K., D.R. Mandavia, T.K. Patel, M.J. Barvaliya, and C.B. Tripathi. 2013. Evaluation of anti-inflammatory, analgesic, and antipyretic effects of ethanolic extract of Pedalium murex Linn. fruits. Afr. J. Tradit. Complement. Altern. Med., 10:94-100.

Patel, P.K., B.A. Vyas, and S.V. Joshi. 2016. Evaluation of antiurolithiatic effect of pedalium murex fruit extract in ethylene glycol-induced nephrolithiasis in rat. Indian J. Pharm. Sci., 78:230-9.

Ramadevi S., B. Kaleeswaran, S. Ilavenil, A. Upgade, D. Tamilvendan, R. Rajakrishnan, A.H. Alfarhan, Y.O. Kim, and H.J. Kim. 2020. Effect of traditionally used herb Pedalium murex L. and its active compound pedalitin on urease expression–For the management of kidney stone. Saudi J. Biol. Sci., 27:833-9.

Sangeetha, G, and R. Vidhya. 2016. In vitro anti-inflammatory activity of different parts of Pedalium murex (L.). inflammation. 4:5.

Saravanan, N., D. Senthil, and P. Varalakshmi. 1995. Effect of 1 cysteine on lipid peroxidation in experimental urolithiatic rats. Pharmacol. Res., 32:165–9.

Shelke, T.T., R. Kothai, P.P. Adkar, V.H. Bhaskar, K.C. Juvale, B.B. Kamble, and R.J. Oswal. 2009. Nephroprotective activity of ethanolic extract of dried fruits of Pedalium murex Linn. J. Cell Tissue Res.,.9:1687.

Smith, C.L. and D.R.P. Guay. 1992. Nephrolithiasis. In: Pharmacotherapy: A Pathophysiologic Approach. DiPiro JT, Talbert RL, Hayes PE, Yee GC, Matzke GR, Posey LM (eds.), 2nd Edn, Elsevier, New York, 720.

Sreedevi, A., Y.J. Latha, and K. Bharathi. 2011. Protective effect of fruits of pedalium murex against gentamicin-induced nephrotoxicity in rats. International Journal. 2229:7472.

Thamilselvan, S., S.R. Khan, and M. Menon. 2003. Oxalate and calcium oxalate mediated free radical toxicity in renal epithelial cells: effect of antioxidants. Urol. Res., 31:3–9.

Tsujihata, M. 2008 Mechanism of calcium oxalate renal stone formation and renal tubular cell injury. Int. J. Urol., 15:115-20.

Vanachayangkul, P., K. Byer, S. Khan, and V. Butterweck. 2010. An aqueous extract of Ammi visnaga fruits and its constituents khellin and visnagin prevent cell damage caused by oxalate in renal epithelial cells. Phytomed., 17:653-58.

Wills, E.D. 1966. Mechanisms of lipid peroxide formation in animal tissue. Biochem. J., 99:667-76.

Pb. Univ. Res. J (Sci.) Vol. 70, 2020, pp 85-106

BIOLUMINESCENT SYSTEMS: DIVERSITY AND FUTURE PROSPECTS

***Archana Chauhan, Ahmad Ali and Kirti Kajal**
Department of Zoology, Panjab University, Chandigarh - 160014, India

ABSTRACT

Bioluminescence is a unique chemical phenomenon that is found in many marines as well as terrestrial organisms. It is a form of chemiluminescence in which light is produced inside the living cells. Bioluminescent organisms are commonly distributed throughout the biosphere and most of them are present in the lower phyla. There are almost forty different bioluminescent systems thought to be present in nature, of these only a few light-emitting reactions are well studied. The process of evolution of bioluminescence shows that the light emitting character is advantageous for the organism as it plays a diverse and significant role in the survival and propagation of the luminescent organism. In this review, we attempt to elucidate the diversity of various bioluminescent systems and their applications.

Key words: Bioluminescence, Luciferase, Luciferin-luciferase system, Photoprotein, Luciferase gene

INTRODUCTION

The ability of some organisms to produce light in the darkness has been detected in about 10,000 species from 800 genera (Fleiss and Sarkisyan, 2019). Bioluminescence is defined as an oxygenation reaction that occurs in living organisms and results in the production of light which helps them in their survival and propagation (Haddock et al., 2010). It was reported from different studies that the bioluminescence phenomenon occurs widely in marine organisms as well as terrestrial organisms (Herren et al., 2005; Widder, 2010; Bessho-Uehara et al., 2020). Generally, the chemical reaction that results in bioluminescence requires two unique molecules: luciferase; the enzyme and luciferin; the substrate as well as the presence of some other co-factors that include calcium or magnesium ions and sometimes ATP (McElroy, 1947). Luciferin (derived from the Latin word lucifer, meaning "light bringer") is a group of small molecules that upon oxidation produces an electronically excited intermediate compound that emits light upon its decay to ground state and the energy is released as a by-product of this reaction. The oxidation of these molecules is catalyzed by various non-homologous enzymes which catalyze the light emitting reaction by oxidizing the luciferin molecule (Kaskova et al., 2016). The wavelength of the light emitted depends on the energy of the electronically excited intermediate compound (Seliger et al., 1966).

Light emitting organisms are widely distributed throughout the biosphere and are mostly present in the lower phyla (Widder, 2001). Although their occurrence appears to be randomly distributed among different groups, but till now it has been reported that nearly 17 phyla and 700 genera show the presence of luminous species (Osamu, 2006). The phenomenon of light production and emission is very distinct in marine habitat and has been shown by different species of the organisms which include cephalopods, copepods, ostracods, amphipods, annelids and a few fishes (Widder, 2010; Markova and Vysotski, 2015), whereas terrestrial luminescence is less diverse in occurrence and is found in different types of fungi, bacteria and insects (Viviani, 2002). Insects are one of the most diverse groups of terrestrial luminescent species which contain many organisms that are luminous for example fireflies, glow-worms, click beetles and some dipterans. They produce multiple color light through the similar bioluminescence mechanisms (Yu and Liu, 2020).

TYPES OF BIOLUMINESCENT SYSTEMS

Evolutionary studies, have shown that the light emitting characters have evolved independently during the course of evolution in different terrestrial and marine organisms (Kaskova et al., 2016; Shimomura & Yampolsky, 2019). Till date, nearly forty different bioluminescent systems have been found to exist in nature (Haddock et al., 2010). The chemistry of light emission in the bioluminescent organisms has been classified into two types (figure 1) i.e., i). Luciferase-luciferin chemical pathway in which the luciferin molecule act as substrate and produce light when oxidized by luciferase enzyme (Henry & Michelson, 1978; Shimomura, 2006). ii). Photoprotein based chemical pathway. It's a stable enzyme-substrate complex consisting of a single polypeptide chain such as aequorin, obelin, phialidin and halistaurin with molecular masses of around 20000 Da and contains the same functional group; it emits light like a luciferin in absence of luciferase enzyme (Shimomura, 1985; Vysotski et al., 2006; Daunert & Deo, 2006).

---

* *Corresponding author* archanagenomics@gmail.com, achauhan@pu.ac.in
MS Received: November 28, 2020, Accepted: December 24, 2020

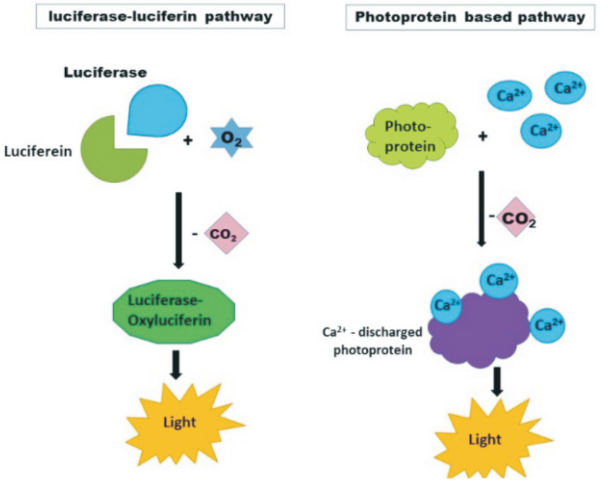

Fig. 1: Different pathways of bioluminescent systems

Luciferase-luciferin Chemical Pathway

On the basis of the luciferin type, the bioluminescent system has been classified into seven types i.e., flavin mononucleotide system in bacteria (Daubner et al., 1987), coelenterazine dependent system in cnidarians (Sharifian et al., 2018), D-luciferin systems in insect (Tiffen et al., 2010), tetrapyrrole based luciferin system in dinoflagellates (Dunlap et al., 1980), N-isovaleryl-3-amino propanol in annelids (Sharifian et al., 2018), enol formate in molluscs (Hastings, 1996) and cypridina luciferin based system in crustacean (Fleiss & Sarkisyan, 2019). Among these seven systems the mechanism of only five systems is well understood and us discussed below:

Flavin mononucleotide bioluminescent system

All the light emitting bacteria utilize the same reaction mechanism in which light is produced by the oxidation of Flavin Mono-Nucleotide (FMN) in the presence of Oxygen (O_2) and Adenosine Triphosphate (ATP, Daubner et al., 1987). In this luminescence reaction the bacterial luciferin which is made up of reduced FMN and a long chain fatty aldehyde react in the presence of luciferase enzyme and molecular oxygen to produce oxidized FMN and result in the emission of blue or green light ($\lambda = 490$ nm) (Tu & Mager, 1995, figure 2).

The emission of distinctive colors by the bioluminescent reaction in bacteria is due to the differences in the energy of photons released when the excited flavin molecule returns to the ground state (Meighen, 1991). Through various experiments, it has been shown that the color of light emitted depends not only on the energy of the photons released but also on the environment of the active binding site of the luciferase enzyme (Meighen, 1993). Although in some strains of bacteria it was seen that they not only carry the luciferase enzyme for light emission but also have the presence of other fluorescent proteins that helps them in light emission and modulation. These fluorescent proteins are known as lumazine protein and are present in *Photobacterium phosphoreum* and *Photocterium leiognathi* (Tu & Mager, 1995).

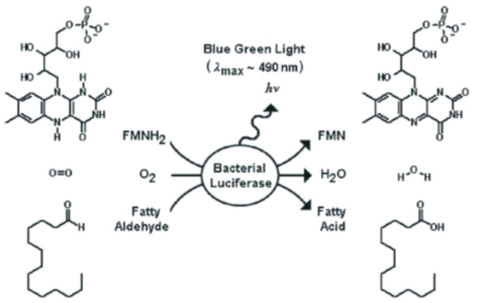

Fig. 2: Mechanism of FMN bioluminescence reaction. (Adopted from: http://photobiology.info/Lin_files/Fig8.png)

These fluorescent proteins not only modulate the color of the light emitted but also change the kinetics of the reaction, because of their ability to interact with the high energy intermediates of the bioluminescent reaction (Meighen, 1991). Apart from the substrate and enzyme, molecular oxygen is also very important for the bacterial bioluminescent reaction (McElroy & Green, 1955). The oxygen is taken up by the bacteria from the surroundings and without the input of oxygen, the bacteria is not able to produce any light. In all the bioluminescent systems, molecular oxygen acts as an energy sink which absorbs the reducing power of the substrates and results in the production of unsteady intermediates which emit light (Tu & Mager, 1995).

D-luciferin dependent system

D-luciferin dependent system is the most important and thoroughly studied terrestrial luminescent system (DeLuca et al., 1979). Among the terrestrial organisms' insects are the most diverse light emitting organisms (Tiffen et al., 2010). The order Collembola, Diptera and Coleoptera shows bioluminescent character (Harvey, 1952), it will be discussed in detail later in this review. The substrate for the bioluminescence reaction is a benzothiazole compound which is synthesized from the amino acid cysteine in all three families of order Coleoptera (McCapra et al., 1963).

Among the insect luciferase, firefly luciferases have been widely studied over the last 50 years with most of the work focused on the North American firefly *Photinus pyralis* luciferase enzyme (McElroy, 1947). Firefly luciferases are grouped under the category of monooxygenase enzymes that results in the production of yellow-green light because of luciferin oxidation in the presence co-factors such as magnesium ions (Mg^{2+}), ATP and oxygen (McCapra et al., 1963).

Luciferases are responsible for catalyzing two essential enzymatic steps in insect bioluminescence reaction i.e., adenylation of D-luciferin (Conti et al., 1996) and oxygenation of adenyl luciferin (DeLuca & McElroy, 1974). In the first step of the insect bioluminescence reaction, the enzyme activates the substrate through adenylation of its carboxyl group in the presence of Mg^{2+} ions and ATP. This reaction results in the formation of luciferase bound luciferyl adenylate (Luc: LH_2-AMP) with the release of inorganic pyrophosphate. This is equivalent to the reaction that results in the activation of amino acids and fatty acids by tRNA synthetase enzyme and acyl CoA ligases respectively (Wood, 1995).

In the subsequent step, the enzyme acts as an oxygenase and catalyzes the oxidation of luciferyl adenylate in presence of O_2 to produce oxyluciferin, Adenosine Mono-Phosphate (AMP) and carbon dioxide (CO_2) (Seliger et al., 1961, figure 3). For the oxidation of luciferin, luciferase must extract C_4 proton from luciferin which will produce carbanion that will undergo electrophilic attack by molecular oxygen. The generation of light takes place when the excited oxyluciferin state comes back to the ground state by releasing photons (Seliger & McElroy, 1960).

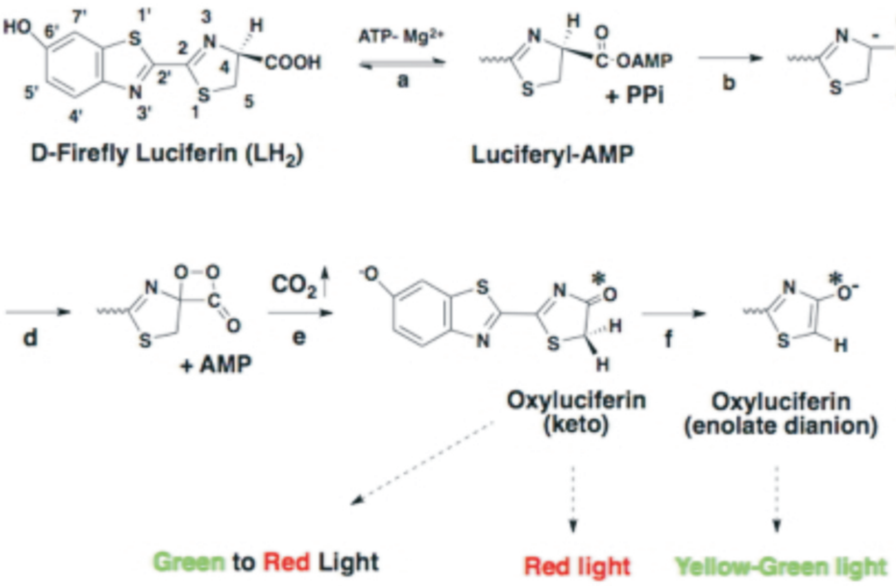

Fig. 3: Mechanism of D-firefly bioluminescence reaction. (Source: Vivani, 2002)

Tetrapyrrole based luciferin system

Marine organism and dinoflagellates are the major group of organisms having tetrapyrrole based luciferin system. The dinoflagellates luciferin, often referred to as LH_2, contains a tetrapyrrole ring which shows a striking similarity to chlorophyll as it possesses a five-member ring attached to the third pyrrole (Dunlap et al., 1980). The existing information about the evolution of light producing enzymes in the ocean comes from the study of the luciferase gene in dinoflagellates (Hasting et al., 1997; Johnsen, 2005). During the light emission reaction in dinoflagellates, luciferin molecule undergoes oxidation in the presence of Ca^{2+} ions and O_2 to form an electronically excited product, a hydroperoxyl adduct (figure 4). This hydroperoxyl adduct then releases energy in the form of photons while returning to its ground state. The photon that is released results in the emission of a blue light with a wavelength of 495 nm.

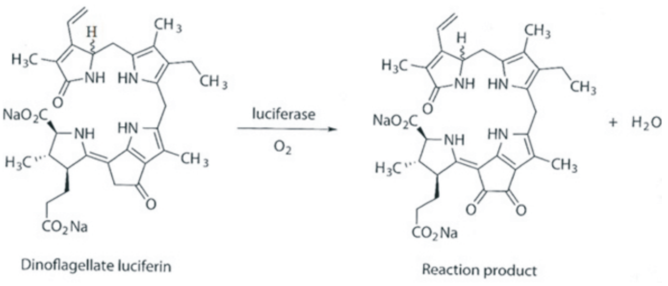

Fig. 4: Mechanism of dinoflagellate bioluminescence reaction (Source: Nakamura et al., 1989)

Coelenterazine dependent system

Coelenterazine is the light emitting molecule that acts as a substrate for cnidarians luciferase (Sharifian et al., 2018). During the bioluminescence reaction, the coelenterazine luciferin is oxidized in the presence of oxygen and calcium to produce a four membered energy rich compound known as phenolate anion as shown in figure 5 (Ohmiya & Hirano, 1996; Shimomura and Yampolsky, 2019). This excited state molecule then emits blue light with emission maxima within the range of 450-500 nm. Green light can also be produced in cases when this luciferin molecule interacts with other fluorescent proteins along with the luciferase enzyme (Vysotski & Lee, 2004). As the evolution of most of the luminescent species has occurred in open waters, the

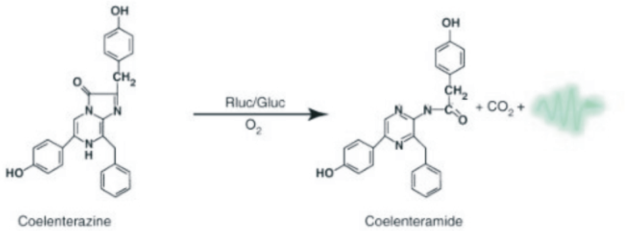

Fig. 5: Mechanism of Coelenterazine bioluminescence reaction (Source: Shimomura & Johnson, 1968)

emission spectra are mostly blue in color because the wavelength (λ = 475 nm) of this color travels farthest through seawater (Widder et al., 1999). But as the turbidity increases in the shallow waters, green becomes the predominant color because particles in the turbid water scatter blue light and this phenomenon encourages the emission of light of longer wavelength for transmission through water (Herring, 1983).

Cypridina luciferin-based system

A modified tripeptide known as cypridina luciferin that emits blue light has also been reported by Oba et al. (2017). This metabolite is found in the bioluminescent midshipman fish, *Porichthys* and ostracod *Cypridina* (Fleiss & Sarkisyan, 2019). Though the biosynthesis of this compound is still not known, it was thought to be produced from tryptophan, isoleucine and arginine (Oba et al., 2017). Such system is commonly found in the crustaceans (Tsuji, 1978).

The emission intensity (λ_{max}) of cypridina luciferin depends on the physiological environment inside the cell (Naumov et al., 2012). In presence of human plasma alpha 1-acid glycoprotein (hAGP), the *Cypridina* luciferin shows maximum wavelength ($\lambda_{max)}$ in the range of 457–458 nm under different pH conditions, whereas in the presence of a recombinant cypridina luciferase, it shows the maximum wave length in the range of 478–483 nm (Kanie et al., 2020).

Ethylene Glycol Tetraacetic Acid (EGTA) and Ethylenediaminetetraacetic acid (EDTA) inhibits the bioluminescent reaction catalyzed by cypridina luciferase (Markova and Vysotski, 2015) which indicates the effect of Ca^{2+} on the enzymatic activity. However, no Ca^{2+} binding sites have been detected in the amino acid sequences of this protein and this is an area of future research (Nakajima et al., 2004).

PHOTOPROTEIN BASED CHEMICAL PATHWAY

In 1962, Shimomura and colleagues discovered bioluminescent protein in the jellyfish *Aequorea* and named it aequorin. This protein has the property to produce light in aqueous solutions in presence of Ca^{2+} ions, later they found a similar protein in the parchment tubeworm *Chaetopterus* (Shimomura and Johnson 1968) which emits light in presence of Fe^{2+} ions and oxygen, without the involvement of luciferase enzyme. Therefore, photoprotein are the bioluminescent protein present in the light emitting organs of luminous organisms as the main component. The total light emission is proportional to the amount of protein used (Shimomura, 1985). Till date, various bioluminescent systems have been identified (Haddock et al., 2010). Half of them involve photoprotein in different organisms such as the Ca^{2+}dependent type in coelenterates i.e., aequorin, obelin etc. (Vysotski, 2006; Stephenson & Sutherland, 1981), the peroxide activation type in brittle star i.e., Ophiopsila (Shimomura, 1986) and the ATP-activation type in Sequoia *millipede* i.e., *Luminodesmus* (Shimomura, 1981). The list of various bioluminescent organisms possessing photoprotein has been summarized in table 1.

Table 1: List of Photoproteins isolated from different organisms

Source	Name	Requirement of luminescence	References
Aequorea aequorea	Aequorin	Ca^{2+}	Shimomora, 1986
Beroe ovata	Berovin	Ca^{2+}	Ward and Seliger, 1974
Hamothoe lunulata	Polynoidin	H_2O_2	Nicolas et al., 1982
Luminodesmus sequoia	sequoia	Mg^{2+}	Shimomura, 1981
Mnemiopsis sp	Mnemiopsin		Ward and Seliger 1974
Ophiopsila californica		H_2O_2	Shimomura 1986
Obelia geniculata	Obelin	Ca^{2+}	Stephanson & Sutherland, 1981
Obelia longissima	Obelin	Ca^{2+}	Illarionov et al., 1995
Phialidium gregarium	Phialidin	Ca^{2+}	Levine and Ward, 1982
Pholas dactylus	Pholasin	Fe^{2+}	Michelson, 1978
Symplectoteuthis oualaniensis	Symplectin	H_2O_2	Fujii et al., 2002
Thalassicola sp	Thalassicolin	Ca^{2+}	Campbell et al., 1981

Table 2: Properties of bioluminescence in different bacteria

Bacteria	Properties of bioluminescence in bacteria	references
Achromobacter fischeri	Requires reduced diphosphopyridine nucleotide and flavin mononucleotide for light emission.	Strehler & Cormier, 1953
Photobacterium fischeri	Upon treatment with trypsin or chymotrypsin they lost luciferase activity. luciferase gene expected size is ~ 2.1 kbp.	Kuwabara et al., 1965
Photobacterium phosphoreum	Stimulate bioluminescence by tetradecanal. NaCl along with nalidixic acid suppress the luminescence.	Karatani & Konaka, 2000
Photobacterium Phosphoreum	At temperature 15? and in the pH range of 7.0-9.0, it shows the maximum luminescence activity.	Kuts & Ismailov, 2009
Vibrio campbellii	They possess thermostable luciferase. Luciferase are bonded to reduced FMN. They emit greater light than native luciferase from *vibrio harveyi and photobacterium.*	Suadee et al., 2007
Vibrio harveyi	At pH 6.8 and temperature 30°C, it shows optimal activity of the luciferase. Diethylcarbonate, phenylmethylsulfonylfluoride, and diethyl-p-nitrophenylphosphate inhibits luciferase by involving the cysteine residue at the binding site of $FMNH_2$.	Reeve & Baldwin, 1981
Vibrio fischeri	The size of the gene is ~2046 bp. The molecular weight of the luciferase protein is 76 kDa.	Tehrani et al., 2011
Leiognathi vibrio harveyi	Luciferase purification can be done using the method FMN oxidoreductases. Suitability of method for various analytical applications based on bacterial bioluminescence enzymes.	Lang et al., 1992
Vibrio harveyi	Inhibited luciferase of *V. harveyi* by ethylacetate (EA) and Methanol:Chloroform (CM).	Lavi et al. (1990)
Photobacterium phosphoreum	Luciferase protein have a dimer of two alpha and two beta subunits. Differ in amino acid sequences of the alpha and beta subunits with other bacterial luciferases.	Karatani & Konaka (2000)

DIVERSITY OF BIOLUMINESCENT ORGANISMS

Diversity of bacterial bioluminescence

Luminescent bacteria are amongst the most widely distributed luminescent organisms (Baumann et al., 1983). They can be found in terrestrial as well as in freshwater environment, though the majority of them are found in marine water (King et al., 1990). They are mostly reported from three genera i.e., *Photobacterium*, *Vibrio* and *Photorhabdus* (Baumann et al., 1983). *Photobacterium* and *Vibrio* mainly dwell in the marine environment whereas *Photorhabdus* is found terrestrially (Engebrecht et al., 1983). Also, it's observed in species of genus *Photobacterium*, which shows symbiotic relation with other marine organisms (Hastings & Nealson, 1977) but the *Vibrio* species can survive in free living as well as symbiotic forms (Engebrecht et al., 1983). Apart from symbiosis, light emitting bacteria can also infect other organisms by acting as parasites. For example, many *Photobacterium* and *Vibrio* families have the ability to pass on a disease to marine organisms like crustaceans (Thomas & Poinar, 1979). *Photorhabdus*, on the other hand can infect the terrestrial living forms such as caterpillars where nematodes act as the intermediate host for the bacteria (Farmer et al., 1989). Table 2 shows the diversity of the bioluminescent bacteria.

Diversity of Insect bioluminescence

The light emitting insects are one of the major terrestrial bioluminescent groups and the light emitting character is shown by the organisms of the order Collembola, Diptera and Coleoptera (Harvey, 1952).

Order Diptera

In Diptera, the luminescent organisms commonly found belong to the family *Mycetophilidae*. The best known are *Arachnocampa* species from New Zealand caves and the Australasian region (Meyer, 1990), whose larvae construct webs on the roof of caves. Other luminescent mycetophilids are found in the genera *Keroplatus* and *Orfelia* (Harvey, 1952). *Orfelia fultoni* is another web-building species, which occurs in stream banks of the Appalachian Mountains of eastern USA (Fulton, 1941).

Order Coleoptera

The order coleopteran has the largest number and variety of light emitting species which are grouped under three different families (figure 6a) i.e., *Elateridae* -click beetles and fire beetles, *Lampyridae* -fireflies and *Phengodidae* -railroad worms (Branham & Wenzel, 2001). Figure 6b shows a representative picture of bioluminescent fly belonging to the order Coleoptera, family *Lampyridae* and genus *yunnana* seen in the Panjab University, Chandigarh campus. Figure 6(c) shows the placement of light organs of various luminescent beetles.

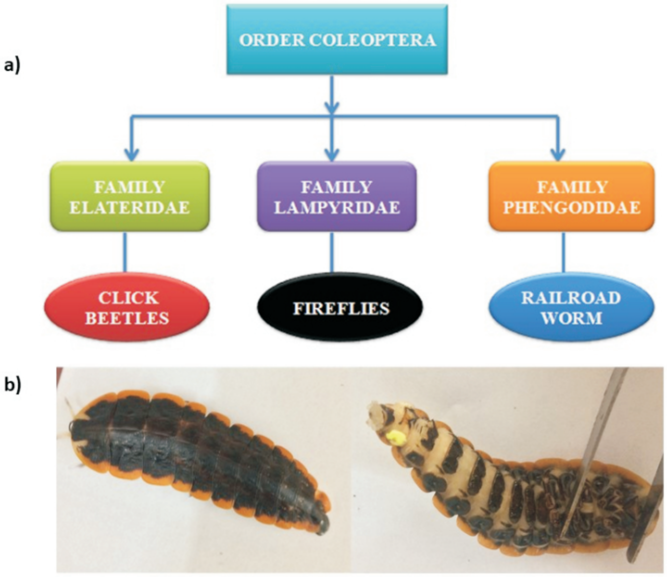

Fig. 6: (a) Distribution of bioluminescent organisms in order Coleoptera, (b) larva of a bioluminescent

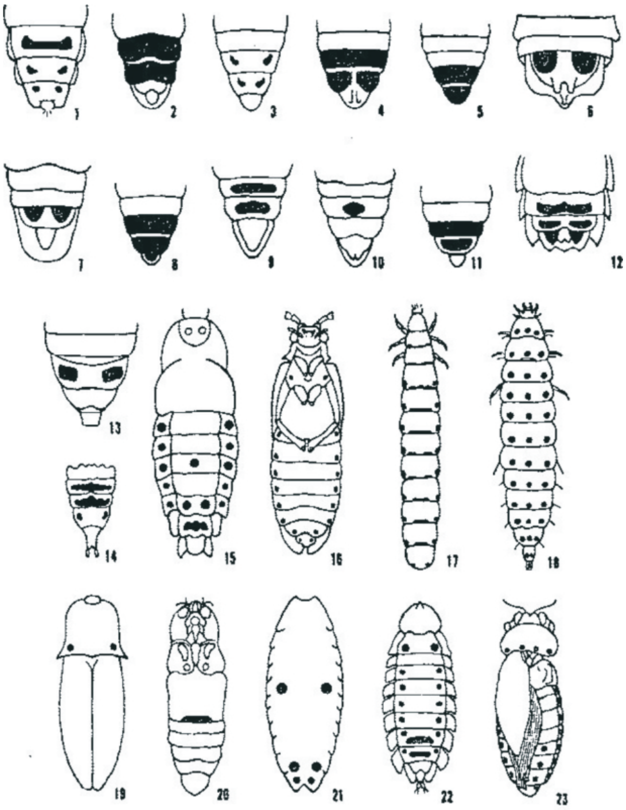

Fig. 6 (c): Light organs of various luminescent beetles, shown in black, image adopted from (James Lloyd, 1971) 1. Lychnurisrofa, female. 2. Phctinusscintillans, male. 3. Pyractomenasp., female. 4. Luciola sp., male. 5. Luciolachinensis, male. 6. Callopisma sp., female. 7. Robopusmontanus, male. 8. Luciolacruciata, male. 9. Photuris sp., female. 10. Photinusreintillans, female. 11. Luciolalateralis, male. 12. Pleotomus sp., female. 13. Luciolaiusitanica, female. 14. Lampyrisnoctiluca, female. 15. Lamprohizasplendidula, female. 16. Harrnateliabilinea, male. 17. Phengodes sp., female. 18. Diplocladonhasselti, female. 19. Pyrophorus sp., male and female, dorsal. 20. Pyrophorus sp., male and female, ventral. 21. Phausisreticulata, female. 22. Lamprohizamulsanti, female. 23. Dioptomaadamsi, male

Family Lampyridae

The insects of this family are commonly known as fireflies or lightning bugs due to their ability to emit light. Bioluminescence in fireflies is produced by distinctive light emitting organs that are present on the lower side of the abdomen. Luciferin is found in these photogenic organs (also known as photocytes) in dissolved as well as granular state whereas the enzyme luciferase can be located in peroxisomes only (Hanna et al., 1976). In case of adult fireflies, green-yellow light is emitted by an abdominal ventral lantern which is made up of thousands of light generating cells. The requisite oxygen for the light emitting reaction is supplied by the tracheolar end cells which are neurally controlled (Buck, 1948).

Table 3: Properties of bioluminescence in eukaryotes

Eukaryotes	Properties of bioluminescence in Eukaryotes	references
Gonyaulax polyedra	Only single chain luciferase present. Molecular mass of the luciferase protein is 130 kDa. It lacks homologies of amino acid sequence with that of any other luciferase.	Bae & Hastings (1994)
Pyrocystis lunula	The amino acid sequence of the luciferase shows homology with that of *Lingulodinium polyedrum.* At pH 8.0 and increase above pH 7.0, it shows optimum activity of the luciferase.	Morishita et al. (2002)
Lingulodinium polyedrum	The bioluminescence present in organelles is called scintillons. Molecular mass of the luciferase protein is 136 kDa. Luciferase with three homologous domains.	Liu et al. (2003)
Noctiluca scintillans	Producing 6 × 1010 ~ photons per cell.	Buskey et al. (1992)
Periphylla periphylla	Luciferase is heat resistant, unstable in solutions of low ionic strength. Luciferase inhibits by Cu^{2+} and thiol compounds.	Shimomura & Flood (1998)
Suberites domuncula	The spicules-luciferase-cryptochrome are the three components of a light signalling system concentrating in the surface layers (cortex) of the body. Upon removing of the cortex, it doesn't emit light. The regeneration and reconstitution of the cortex make it re-gain the capacity to flash light. A SOX-related protein makes the expression of luciferase and cryptochrome.	Wiens et al. (2010)
Suberites domuncula	Large spicules act as light collecting optical fiber. Abundance of luciferase (spicules) produces distinct white-to-red color in light. The size of luciferase gene is 2.3 kb. Molecular weight of the luciferase protein is 63,968 Da Maximum bioluminescence shows at 548 nm and a minor peak at 590 nm.	Müller et al. (2009)
Obelia longissima	Bioluminescence and the Ca^{2+}-discharged fluorescence spectra. Occurring of a complex proton transfer together with the formation of electronically excited coelenteramide.	Chen et al. (2014)
Renilla reniformis	The tendency to self-associate and the high hydrophobicity of luciferase forming inactive dimmers. It produces light at 480 nm. Luciferase is with single polypeptide chain.	Matthews et al. (1977)
Odontosyllis phosphorea	Produce green bioluminescence during mating and swarms. Glowing when stimulation with potassium chloride. Maximum emission between 494 and 504 nm. Optimal luciferase activity shows at temperatures as low as 20^{o}C and degrade above 40 °C.	Deheyn & Latz (2009).
Tomopteris helgolandica	Activation of nicotinic cholinergic receptors. Physiological carbachol concentrations induce flash and higher concentrations induced glows. Tubocurarine shows inhibitory effect.	Gouveneaux & Mallefet (2013)
Metridia longa	Production of blue bioluminescence as a secretion from epidermal glands. Molecular weight of the protein is 23,885 Da. Cysteine-rich luciferase.	Markova et al. (2014)
Oplophorus gracilorostris	Maximum intensity at 462 nm. Optimum activity at pH 9 in presence KaCl at temperature 40 °C. Molecular weight of the protein is 130,000 Da	Inouye & Sasaki (2007)
Watasenia scintillans	Produce flashes of blue light along with ATP, O$_2$ and Mg^{2+}. Oxygenation reaction occurs with a single electron-transfer mechanism. Light emits via the mechanism of gradually reversible charge-transfer-induced luminescence.	Ding & Liu (2017)
Pholas dactylus	Luciferin generally bound to a glycosylated protein. Act as an indicator of reactive oxygen species. Luciferase protein contains 225 amino acids. Fully processed luciferase protein is of 34 kDa.	Müller & Campbell (1990)
Benthosema pterotum	Molecular weight of the protein is 27 kDa. At temperature 40°C and at pH 9, it shows maximum intensity of light. Cu^{2+}, Zn^{2+} and Ni^{2+} inhibit luciferase. Ca^{2+} and Mg^{2+} ions activate luciferase. Blue light emission with a maximum wavelength at 475 nm.	Homaei et al. (2013)
Symplectin oualaniensis	Molecular weight of the protein is 60 kDa. Emits fluorescence under UV light. Shows specific expression of photogenic organ. No sequence similarity to any known photoproteins.	Fujii et al. (2002)

Family Elateridae

In family Elateridae, click beetles have the presence of two sets of light organs which are present on the dorsal surface of the head and ventral surface of the abdomen respectively (Viviani & Bechara, 1997). The light organ that is present on the head emit long pulses of green light when the beetle is in resting state whereas, the light organ which is present on the abdomen emit green- orange light when the beetle is in flight (Lall et al., 2000). The continuous light emission in click beetles is responsible for their courtship behavior and defense mechanisms.

Family Phengodidae

The luminescence in this family is shown by the females and larval forms which emit yellow or orange light by a chain of lateral lanterns (Viviani & Bechara, 1997) present alongside the body surface whereas in some railroad worms, an additional small head lantern may be present which emit red light. In larval stages, bioluminescence is involved in defense whereas in case of adults it acts to attract the mating partners (Sivinski, 1981).

Diversity of dinoflagellate bioluminescence and other eukaryotes

A greater part of luminous organisms exists in the marine environment and nearly 700 marine genera are known to contain bioluminescent species (Shimomura, 2006). Table 3 elucidate the properties and diversity of various eukaryotic bioluminescent organisms.

Dinoflagellates are the chief eukaryotic protists of the marine environment that possess remarkable and unique biochemical system for the generation of light (Haddock et al., 2010). These eukaryotic protists are accountable for majority of luminescence noticed on the surface of the ocean (Widder, 2001). In dinoflagellates, light is produced as a response to the stress caused by breaking waves or upon contact with grazers (Hastings et al., 1993). The bioluminescence systems in dinoflagellates are unique from molecular as well as cellular perspective. A specialized cell called the 'scintillon' are responsible for the light production and consist of all the chemical components that are required for the reaction with special luciferin binding proteins which are peculiarly present in dinoflagellates (Hastings et al., 1972). The photogenic cells contain thick vesicles of about 0.5-0.9 µm in diameter which are abundant on the periphery of the cell (Cline & Hastings, 1972). Table 4 shows the list of various genera with reported bioluminescent species of dinoflagellate (Marcinko et al., 2013; Valiadi et al., 2012).

Diversity of fish bioluminescence

Almost 42 families and 11 orders of bony fishes, including one family of shark have been observed to exhibit bioluminescence (Widder, 2010). Among, them, majority of these fishes have symbiotic relation with luminescent bacteria for the production of light e.g., anglerfishes, flashlight fish like *Photoblepharon* spp and *Leiognathus* spp (Hellinger et al., 2017). However, the other luminous fishes show intrinsic luminescence i.e., they have their own luciferin-luciferase system which match with that of coelenterazine or ostracod luciferin system (Latz & Jeong, 1996; Mallefet & Shimomura, 1995). For example, Myctophids or lantern fishes possess small photophores pointed downward and a large photophores on the tail, which can produce bright, fast (1×1011 photons s-1 for <400 ms) flashes (Anuradha and Maduri, 2016). Also, the genus *Diaphus* has prominent forward-facing photophores which could be used to illuminate or induce fluorescence in their prey (Cavallaro et al., 2004). In the family *Squalidae* of order Chondrichthyes, the luminous lantern sharks use luminescent for both defensive and offensive purposes (Haddock et al., 2005a). In order Stomiiformes fish such as hatchet-fishes, dragon-fishes have the most elaborate arrangements of photophores (Haddock et al., 2005b). Table 5 shows the list of various bioluminescent families and genera of some fishes.

Table 4: List of bioluminescent dinoflagellates

Family	Genus	No. of reported bioluminescent species
Ceratiaceae	Ceratium	4
Goniodomaceae	Alexandrium	7
Goniodomaceae	Pyrodinium	1
Cladopixidaceae	Peridiniella	1
Ceratocoryaceae	Ceratocorys	1
Gonyaulaceae	Gonyaulax	11
Gonyaulaceae	Lingulodinium	1
Pyrocystaceae	Pyrocystis	4
Pyrophacaceae	Fragilidium	4
Pyrophacaceae	Pyrophacus	1
Gymnodiniaceae	Polykrikos	2
Noctilucaceae	Noctiluca	1
Proroperidiniaceae	Protoperidinium	31

GENETIC MAKEUP OF BIOLUMINESCENT ORGANISMS

Luciferase belongs to the class of oxidative enzymes which are responsible for the emission of light in the living organisms. A wide range of organisms use different types of luciferases in order to control light production during light-emitting reactions. Most of the luciferase studies have been performed on organisms that include fireflies, copepods, jellyfish, bacteria etc. In each organism the light emitting reaction is self-contained and uses only ATP, oxygen and luciferase protein. The luciferase protein is varied in different organisms indicating that they all have evolved independently to perform the same function. The genetic structure required for light emission is very complex and its study

Table 5: Diversity of bioluminescent fish

Order	Family	Genus	Reference
Anguilliformes	Congridae	Lumiconger arafura	Castle & Paxton (1984)
Aulopiformes	Chlorophthalmidae	Chlorophthalmus	Herring & Morin (1978)
	Paralepididae	Lestidium, Lestroplepis	Herring (1987)
	Evermannellidae	Cocorella atrata,Odontostomops normalops	Davis & Holcroft (2014)
Aulopiformes	Scopelarchidae	Benthalbella, Scopelarchoides	Merret et al. (1973)
Batrachoidiformes	Batrachoididae	Porichthys	McAllister (1967)
Beryciformes	Anomalopidae	All	Herring (1987)
	Trachichthyidae	Aulotrachiththys	Herring & Morin (1978)
Clupeiformes	Engraulidae	Coilia dussumieri	Carpenter & Niem (1999)
Gadiformes	Macrouridae	Cetonurus, Coelorinchus, Haplomacrurus, Hymenocephalus, Kumba	Herring (1987) Cohen et al, (1990)
	Merlucciidae	Steindachneria argentea	Cohen et al, (1990)
	Moridae	Gadella, Physiculus, Salilota	Herring (1987)
Lophiiformes	Gigantactinidae	Gigantactis	Pietsch (2009)
	Diceratiidae	All	
	Himantolophidae		Davis et al. (2016)
	Ogcocephalidae	Dibranchus atlanticus	
Osmeriformes	Alepocephalidae	Microphotolepis, Photostylus, Rouleina, Xenodermichthys	Herring (1987)
	Opisthoproctidae	Opisthoproctus, Rhynchohyalus, Winteria	Herring (1987)
Perciformes	Acropomatidae	Acropoma, Synagrops	Herring (1987)
	Apogonidae	Apogon,Archamia, Jaydia	Herring (1987) Thacker & Roje (2009)
	Epigonidae	Epigonus, Florenciella, Rosenblattia	Herring (1987)
Squaliformes	Dalatiidae		Claes & Mallefet (2009)
	Somniosidae	Zameus squamulosus	Straube et al. (2015)
Stomiiformes	Gonostomatidae	All	Suntsov et al. (2008)
	Sternoptychidae		
	Stomiidae		

gives us an additional insight about the sequence of evolutionary process that leads to bioluminescence and its importance in the survival of the organism.

Bacterial luciferase gene structure

All luminous bacteria are motile, gram negative, rod-shaped and facultative anaerobic (Meighen, 1991). Till date luminous bacteria have been found mainly in three families namely *Vibrionaceae*, *Shewanellaceae* and *Enterobacteriaceae*, within five main genera *Vibrio*, *Photobacterium*, *Aliivibrio*, *Photorhabdus* and *Shewanella (Dunlap, 2009; Dunlap, 2014; Urbanczyk et al., 2008)*. One of the unique features of bacterial luciferase gene is that it is encoded in an operon of *lux* structural gene with a single promoter and is responsible for coding of the luminescent proteins (Meighen, 1993). The *lux* gene order is conserved in various bacterial strains with the core sequence *luxCDABE* (*Dunlap, 2009,* figure 7a*). The products of lux*A and *luxB* gene encodes for the heterodimeric luciferase enzyme catalyzes the monooxygenation of aliphatic aldehydes to the corresponding acids utilize the reduced flavin mononucleotide ($FMNH_2$) as the redox cofactor (Hastings, 1983), whereas the *luxC*, *luxD*, and *luxE* are responsible for the reaction of fatty acid reductase and *luxG* that encode for flavin reductase. Next to the core genes *luxCDABE(G)*, additional genes are found within the *lux* operon (*luxF*; *ribEBHA; luxI*) or in a separate operon (*luxR*) adjacent to the *lux* operon, where the reading frame is in the oppposite direction (Figure 7b) (Vervoort et al., 1986). The presence of so many genes linked to or part of the *lux* system indicates that the gene duplication played an important role in the evolution of bioluminescent system (O'Kane & Prasher, 1992).

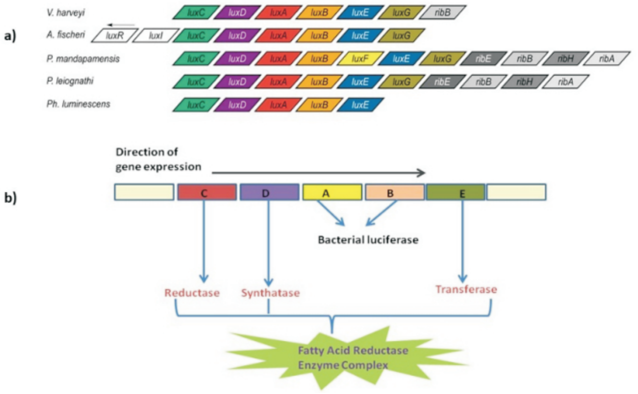

Fig. 7: (a) Structure of bacterial *lux* gene
(Source: lee & Min, 2010)
(b) *lux* operon (Vervoort et al., 1986)

Insect luciferase gene structure

The genetic organization of the luciferase gene in insects has been investigated by different scientists from last 50 years. Till now, the entire luciferase gene has been characterized from six different Lampyridae species namely *Nyctophila caucasica* (Day et al., 2006), *Hotaria species* (Choi et al., 2003), *Luciola lateralis* (Field et al.,

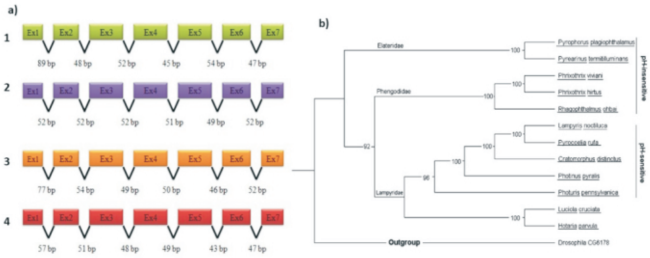

Fig. 8: (a) Organization of luciferase gene in insects (1) Nyctophila caucasica (2) Hotaria species (3) Luciola lateralis (4) Photinus pyralis. (b) Phylogenetic relationship of insect luciferase gene (Source: Arnoldi et al., 2007)

1999), *Photinus pyralis* (Wood, 1995), *Lampyris noctiluca* (deWet et al., 1985), *Pyrocoelia rufa* (Jianhong et al., 2003) and many other fireflies, it was concluded that the firefly luciferase gene is composed of 7 exons and 6 introns which codes for a single polypeptide chain that consists of 545 to 550 amino acid residues (figure 8a). The introns are relatively conserved in size, with the most size variation occurring in intron 1, the largest intron present in *N. caucasica* luciferase gene. Similarly, the sequence comparison of luciferase gene has shown that four TATA boxes, one CCAAT box and two GATA motifs are present nearly 810 bp upstream region of the luciferase coding gene and are all conserved in nature (Day et al., 2006).

Molecular and genetic analysis revealed that the luciferase gene in insects of order Coleoptera codes for proteins that help in fat breakdown. These evidences suggested that the luciferase gene arose from one of the metabolic genes that exhibit bioluminescence after the process of gene duplication. The emission of light of different colors resulted due to the differences in the amino acid sequence of the luciferase enzyme in different organisms of order *Coleoptera* (DeLuca, 1969). These differences in amino acid sequence arise due to the substitution of an ancestral sequences during the course of evolution. Arnoldi et al. (2007) sequenced and compare the mitochondrial genome of the Brazilian light emitting click beetle *Pyrophorus divergens* to get more insights about the evolution of bioluminescence in order *Coleoptera.* The phylogenetic tree constructed on the basis of the sequence comparison showed that the *Rhagophthalmus ohabi* of family *Phengodidae* is closer to click beetles than firefly, suggesting that the evolution of bioluminescence in Phengodidae is independent of Lampyridae evolution (figure 8b). They also observed in the phylogenetic tree that luciferase from *Elateridae* and *Phengodidae* are closer to each other and are pH insensitive whereas, Lampyridae luciferases are pH sensitive. This result also suggests that *Lampyridae* and *Phengodidae* bioluminescence could be independent and could have appeared three time paralleling within *Elateridae.*

Dinoflagellate luciferase gene structure

Luciferase gene from seven genetically related dinoflagellates which includes *Alexandrium, Lingulodinium, Protoceratium* and *Porocystis* have been isolated and sequenced (Devaki & Grossman, 1993). The gene was initially cloned from dinoflagellate *Lingulodinium polyedrum*, it is made up of three tandemly repeated domains named as D1, D2 and D3 separated by an intergenic region (IR) of 0.3 to 3.0 kb (figure 9). Later on, it was observed that this arrangement of genes remains conserved in all other six species of dinoflagellates. However, the coding sequences are highly conserved and the non-coding sequences shows little similarity (Liu et al., 2004). The amino acid sequence of the central region of the three domains (D1, D2 and D3) remain highly conserved in all the species and codes for the active site of the enzyme. The active site is flanked by variable N and C terminal region which mediate the pH activity of the enzyme (Ohmiya et al., 2008). Despite being the similar organization of luciferase gene in the dinoflagellates, different species varied from one another due to the differences in the substitution rate of amino acids in the ORF. Although the significance of these differences is still not clear. The sequence comparison of the domains from different

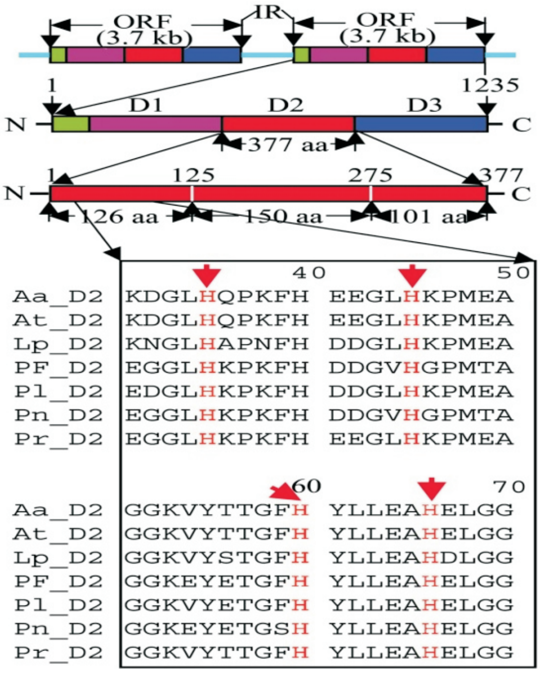

Fig. 9: Organization of luciferase gene in different species of Dinoflagellates. In the picture the three domains of the Dinoflagellate luciferase enzyme are shown with the presence of IR region (Source: Liu et al., 2004)

species has shown that corresponding domains of the luciferase gene are more similar in different organisms (e.g., D1 of *A. tamarense* and *P. reticulatum*) than the different domains within the same organism (e.g., D1 and D2 of *A. tamarense*). This is likely to reflect an ancient triplication of the luciferase gene domain that was then carry forward during the evolution of the different photosynthetic species (Li & Hastings, 1998).

SIGNIFICANCE OF BIOLUMINESCENCE

Ecological significance of bioluminescence

In order to understand the functional aspect of bioluminescence in a particular organism, it is necessary to understand the environment where it lives and evolves (Haddock et al., 2010). For example, in case of marine habitat the visible light disappears below the depth of 1000m as the consequence most of the deep marine organisms live in complete darkness (Widder, 2002). In such living conditions the light emitting character become an advantage and helps the organism in its survival and propagation. On the other hand, the bioluminescence in terrestrial organisms like insects is used as a mechanism of offense, defense and communication.

Commercial significance of bioluminescence

Molecular biology has developed many tools and devices that take advantage of the sensitivity, high detection ability and rapidity of the bioluminescence reactions. These advancements offer inroads to scientists for uninterrupted monitoring of different biological processes.

Bioluminescence reaction in reporter assays

Bioluminescence systems are generally based on the principle of a chemical reaction; that is, the light intensity as the measurable product depends on the amounts of luciferase and luciferin. Luciferase is widely used in reporter assays because of it high sensitivity, easy detection ability in comparison to other reporters like β-galactosidase, β-glucuronidase and green fluorescent protein (Bronstein et al., 1994). For example, using beetle bioluminescence in presence of excess luciferin and luciferase, the bioluminescence intensity correlate, with the amount of ATP (Santos et al., 2003). This system can be applied to detect bacteria in food, as bacteria use ATP as an energy source (Venkateswaran et al., 2003). Moreover, luciferase enzyme reporter assays are most suitable for the measurement of gene expression in prokaryotic and eukaryotic cells (Silverman et al., 1998), because the amount of luciferase correlate with light intensity in presence of excess luciferin and ATP. Figure 10 demonstrate a reporter assay in which the promoter of the gene of interest is present upstream to the luciferase coding gene and the amount of the expressed luciferase protein can be measured from the intensity of the emitted light (Bronstein et al., 1994). Owing to the advancement and ease of detection, many variations of the reporter assay system have been developed over the period of time, such as the single luciferase reporter assay (Bronstein et al., 1994), dual non secreted luciferase reporter assay (Grentzmann et al., 1998), dual secreted luciferase reporter assay (Nakajima et al., 2004; Markova et al., 2004) and multicolor luciferase reporter assay (Nakajima et al., 2005).

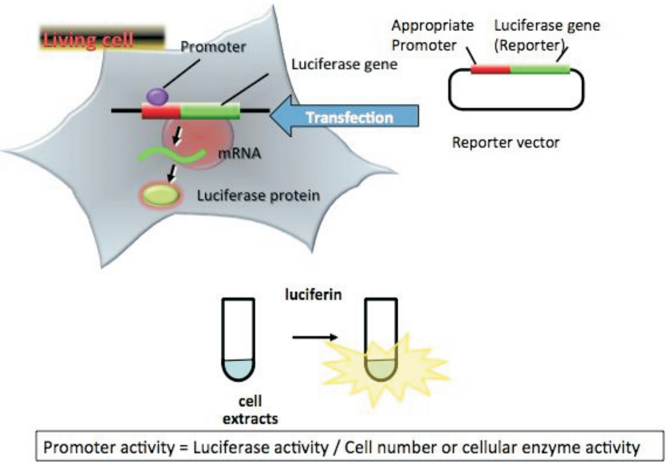

Fig. 10: Demonstration of Luciferase based reporter assay (Source: Bronstein et al., 1994)

Luciferase in detection of microbial growth

All techniques which use bioluminescence reactions are based on the principle that the intensity of emitted light is dependent upon the concentration of luciferase, luciferin and other factors like ATP. The role of ATP in the production of light during bioluminescence reaction was already established (McElroy, 1947). Further, researchers have explored the bioluminescence reaction to measure the microbial growth in packed foods and other dairy products (Venkateshwaram, 2003). For the detection of the microbial growth, beetle luciferase enzyme was used because of its peculiarity, it uses ATP for the emission of light (Seliger, 1987) and due to this ATP was shown to be a reliable marker for microbial growth detection (Kodaka et al., 1996). Therefore, ATP bioluminescence assays have been widely used in monitoring the air and surface cleanliness (Aycicek et al., 2006; Bautista et al., 1995) as well as the quality of food products (Hawronskyj & Holah, 1997).

BIOLUMINESCENCE IMAGING (BLI)

Among the known optical imaging techniques, bioluminescence imaging is the most sensitive, simple and cost-effective procedure. This imaging technique can be used to study the organism via *in vitro* as well as *in vivo* conditions.

IN VITRO BIOLUMINESCENCE IMAGING:

During the *in vitro* imaging, a reporter vector is prepared which has the promoter of the gene of interest present in the upstream region of luciferase gene (DiPilato & Zhang, 2010). This vector is then allowed to transfect the living cell of interest and results in the expression of the luciferase gene with the gene of interest. Figure 11 shows the subcellular localization of the firefly luciferase with high resolution in mammalian cells (Nakajima & Ohmiya, 2010) where firefly luciferin added to the medium enters into the organelle which is then catalyzed by the expressed firefly luciferase to generate light. The expression of the luciferase gene can be measured by the intensity of the light produced after the application of the luciferin substrate (Nakajima & Ohmiya, 2010). The localization of expressed luciferase protein can be visualized by the light signal, which indicate the locality or mobility of organelles in living cells.

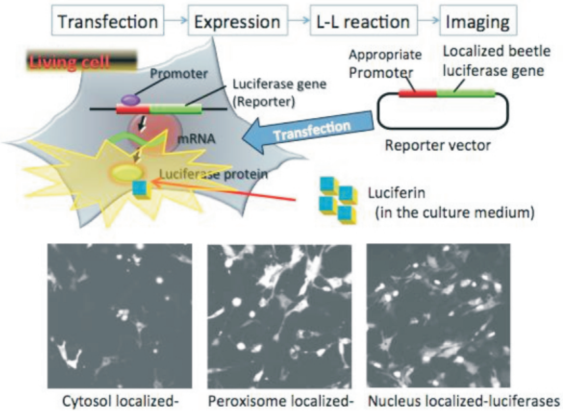

Fig. 11: Demonstration of *in vitro* bioluminescence imaging (Source: Nakajima & Ohmiya, 2010)

In vivo bioluminescence imaging:

In vivo bioluminescence imaging is used to track the pathways of the luciferase expressing stem cells, cancerous cells (Carlsen et al., 2002; Ciana et al., 2003), immune cells, neuronal damages (Zhu et al., 2004) and neuronal developments (Yamaguchi et al., 2000). During the *in vivo* bioluminescence imaging, a reporter plasmid vector is prepared which consists of the luciferase gene and the constitutive promoter sequence; it may also include the antibiotic resistance gene. After transfection of the plasmid into target cells, the expression of the luciferase gene will be regulated by the promoter region (Rehmtulla et al., 2000). Then the luciferase expressed stable cells are administered in the animal model. After an appropriate time, luciferin is injected into the body (Contag et al., 1995). Eventually it enters into the cells from the blood, where it is catalyzed by the expressed luciferase to generate light. The light signals indicate the location and size of monitoring cells in the body. Finally, the bioluminescence imaging is measured by special equipment using a Charge Coupled Device (CCD) photon imaging system (figure 12).

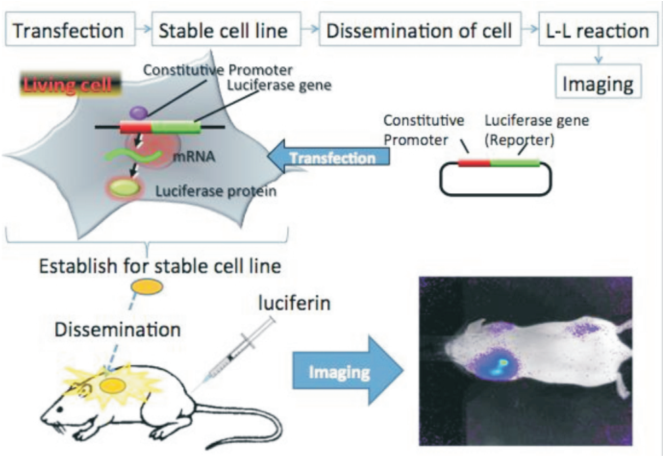

Fig. 12: Demonstration of *in vivo* bioluminescence imaging (Source: Sato et al., 2004)

FUTURE RESEARCH POTENTIAL

Luciferin serves as a substrate for the enzyme luciferase. The products of the bioluminescent reaction have been isolated. However, the gene for luciferin hasn't been isolated as of now. Sequencing of this gene will be beneficial for science as it will help us to detect any conserved sequences and therefore, assist in manipulation of this gene for biotechnological purposes. Apart from that, motifs which assist in the functioning of the luciferase enzyme haven't yet been detected. Detection of the motifs involved in the functioning of luciferase will enable us to understand more about its functioning mechanism and perform mutational studies to manipulate the enzyme's activity. Therefore, the two major areas of research are indicated in figure 13 and would include:

- Gene sequencing of the substrate which metabolizes itself in order to show luminescence- Luciferin.
- Detection of motifs that assist in the functioning of the magic enzyme- Luciferase.

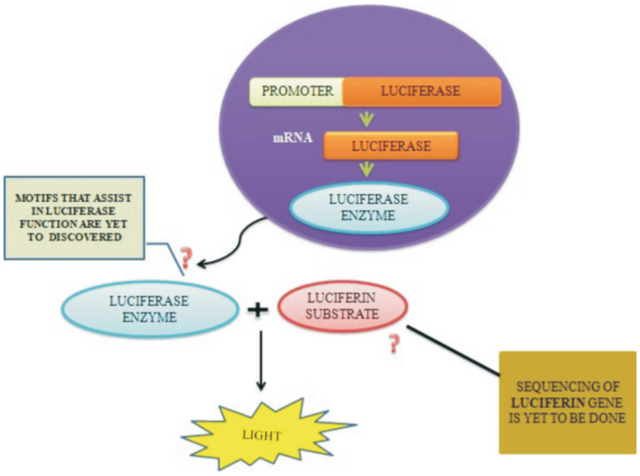

Fig. 13: Future Research potential

Biomarker for air and water pollutants

Bioluminescence reaction is already being used widely for the detection of pollutants in soil. This is done by manipulating the gene for luciferase enzyme using techniques in biotechnology, wherein the sensitivity of the enzyme towards toxins has been increased such that in case a particular pollutant is present, for which the sensitivity has been manipulated, the reaction will show less luminescence as compared to the wild type reaction. Similarly, we can enhance the sensitivity of the enzyme to amplify the luminescence when a particular air pollutant in present (figure 14). Such manipulations can be done by trial-and-error method by testing the enzyme activity and observing changes in it, if any, in presence of the pollutants. This could lead to the development of better methods to test the presence of air and water pollutants in the atmosphere.

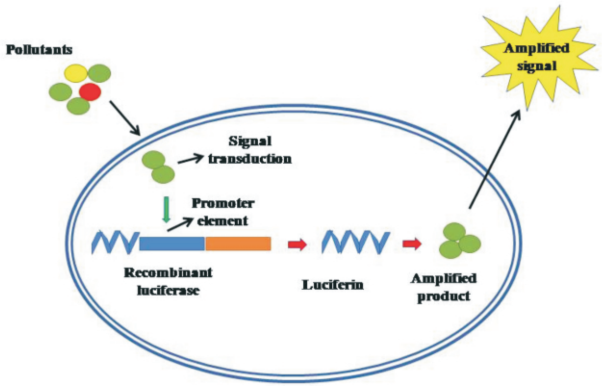

Fig. 14: Bioluminescence as a marker for air pollution

Development of Biolights

The development of biolight has been an interesting area of research, however very less success has been achieved in the same. Biolights, if developed, could become a great alternative for electrical lights and lead to a sustainable future. Luciferin Regenerating Enzyme (LRE) is an enzyme found naturally in fireflies and it converts oxyluciferin, present in the ground state, back to luciferin so that it can act as a substrate for luciferase in the next cycle again to show luminescence. Preparation of biolights has been tested in algae but it sustains only up to 3 days. Hence, this enzyme can be isolated and introduced into a suitable organism using recombinant DNA technology (RDT) to increase the viability and sustainability of biolights. Therefore, for the development of biolights that could work for a longer period of time, we could follow the approach as shown in figure 15.

Bioluminescence as genetic marker

There are various assays and detection techniques used in the field of biology day to day which use probes and markers for easy detection purposes. These probes can be radioactive or non-radioactive. The usage of radioactive probes is very common despite being of the fact that they are tedious to deal with and potentially hazardous to the technician. Non-radioactive probes are also common however the sensitivity of the same is questionable. Enzyme probes are also commonly used for probing but the respective substrate specificity needs to be confirmed so that it doesn't serve as a metabolite for any other compound present in the reaction. The use of luciferase enzyme can replace the use of radioactive probes, being potentially safer and also its specificity to its substrate-luciferin is tremendous, hence it could serve as a better alternative for other enzymatic/non-radioactive probes (figure 16). Also, it won't require any external light source to show luminescence unlike fluorescence assays. Hence, we can elaborate the use of bioluminescence as markers and perform experimentation on those grounds to make it useful in biological assays.

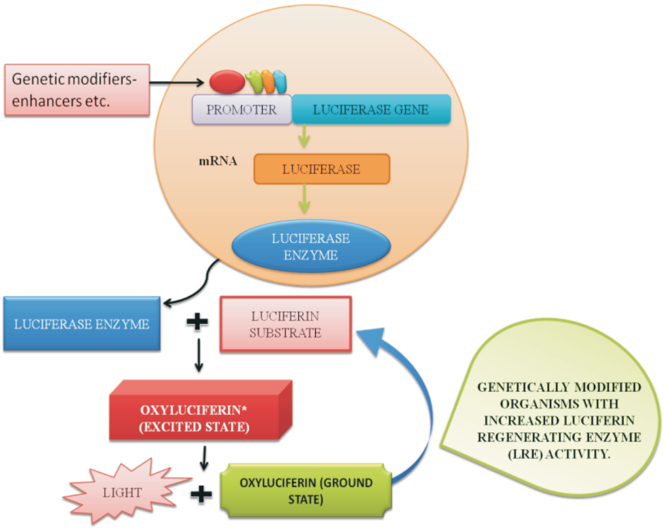

Fig. 15: Use of LRE to develop biolights

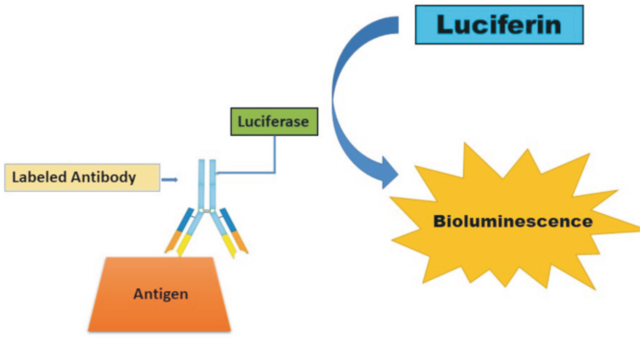

Fig. 16: Use of bioluminescence as a marker for biochemical assays

Bioluminescence in nanoscience

The efficiency of bioluminescence in organisms has developed a way forward to the scientists in Nanotechnology to conduct experiments by manipulating the interaction between the biological and non-biological components (Esimbekova & Kratasyuk, 2005). In fireflies the light emission takes places at nano level when the electrons are excited by an enzyme, when the electrons return the to ground state it becomes dark (Pandey & Sharon, 2017). More particularly scientists simulated the new chemical reaction by combining aequorin with fluorescent protein which results in emission of light known as Bioluminescence Resonance Energy transfer (BRET). Further, we can also use photoprotein/luminescent protein on nano-scale in drug screening and targeting of receptors and junctions using nanotechnology, also BRET can be used to visualize and/or measure intracellular calcium flux and calcium concentrations in different organelles.

SUMMARY & CONCLUSION

Bioluminescence is one of the most fascinating and intriguing processes that is observed in nature. It is a phenomenon that occurs in some organisms due to which they have the ability to produce and emit light (Hastings, 1995). In bioluminescence the light is emitted as a result of oxidation of the substrate molecule named "luciferin" by an enzyme called the "luciferase". During this chemical reaction, the oxidation of the substrate results in the formation of an excited state molecule from which photons are emitted and can be seen as light (Kaskova et al., 2016). The light emitting capability of an organism can be autogenic, which means that they have the machinery to produce light, present within their body (Campbell, 1988). However, in many cases, the light can also be generated by symbiotic organisms living in certain specialized organs of the host (Hastings & Davenpor, 1957).

Hence, from the various studies we could conclude that the occurrence of bioluminescence as a behavioral feature appears to be a clear example of convergent evolution, in which numerous unrelated organisms developed the ability to produce light through separate evolutionary pathways and yet ended up using the same mechanism. The process of evolution of bioluminescence also indicated that the light emitting character is beneficial for the organism as it plays diverse and important roles in the survival and propagation of the luminescent organism, also helping them to eliminate free radicals, which would otherwise be harmful to their body (Widder, 2010). Apart from acting as a free radical scavenger, bioluminescence also helps the organisms in their defense, offense and communication etc. It plays an important role in attracting mating partners and prey for the luminous organisms (Viviani et al., 2008). In the field of science and research, scientists use bioluminescence for different purposes, for example the light emitting character of bacteria has been utilized in order to analyze the contamination in different cell and organ cultures as well as in the food and dietary components. Bioluminescent bacteria and transgenic zebrafishes have also been used as a biosensor for monitoring soil and water pollution due to heavy metals and other organic molecules. Moreover, the light emitting ability of different organisms like bacteria, fireflies and fishes have been explored by scientists for imaging techniques. This technique provides an easy and non-invasive method of visualizing different cells and organs *in vivo* and *in vitro*, which helped the scientists to understand their characters and functioning.

ACKNOWLEDGMENT

We greatly acknowledge the financial help from DST-SERB and UGC.

CONFLICT OF INTEREST

The authors declare no conflict of interest.

REFERENCES

Anuradha Pandey Dubey and Madhuri Sharon. "Culture parameters affect the light emitting property of organisms isolated from two marine fishes". ASMI., 3.5 (2020): 55-61.

Arnoldi, F. G. C., Ogoh, K., Ohmiya, Y., and Viviani, V. R. (2007). Mitochondrial genome sequence of the Brazilian luminescent click beetle *Pyrophorus divergens* (Coleoptera: *Elateridae*): mitochondrial genes utility to investigate the evolutionary history of Coleoptera and its bioluminescence. Gene., 405(1-2), 1-9.

Aycicek, H., U. Oguz, and K. Karci, (2006). Comparison of results of ATP bioluminescence and traditional hygiene swabbing methods for the determination of surface cleanliness at a hospital kitchen. *Int. J. Hyg. Environ. Health,* 209(2), 203-206.

Bae, Y. M., and J. W. Hastings, (1994). Cloning, sequencing and expression of dinoflagellate luciferase DNA from a marine alga, *Gonyaulax polyedra.* Biochim. Biophys. Acta., 1219(2), 449-456.

Baumann, P., Y. Yang, L. Yeh, Y. Cao, L. Baumann, J. S. E. Tang, and B. Beaman, (1983). Characterization of marine luminous bacteria isolated off the coast of China and descripption of *Vibrio orientalis* sp. nov. Curr. Microbiol., 8(2), 95- 100.

Bautista, D. A., J. P. Vaillancourt, R. A. Clarke, S. Renwick, and M. W. Griffiths, (1995). Rapid assessment of the microbiological quality of poultry carcasses using ATP bioluminescence. J. Food Prot., 58(5), 551-554.

Bessho-Uehara, M., W. R. Francis, and S. H. Haddock, (2020). Biochemical characterization of diverse deep-sea anthozoan bioluminescence systems. Marine Biology, 167(8), 1-19.

Branham, M. A., and J. W. Wenzel, (2001). The evolution of bioluminescence in cantharoids (Coleoptera: Elateroidea). Fla. Entomol., 84(4), 565.

Bronstein, I., J. Fortin, P. E. Stanley, G. S. Stewart, and L. J. Kricka, (1994). Chemiluminescent and bioluminescent reporter gene assays. *Anal. Biochem.,* 219(2), 169-181.

Buck, J. B. (1948). The anatomy and physiology of the light organ in fireflies. Ann. N. Y. Acad. Sci., 49(1), 397-485.

Buskey, E. J., S. Strom, and C. Coulter, (1992). Biolumiscence of heterotrophic dinoflagellates from Texas coastal waters. *J. Exp. Mar. Biol. Ecol.,* 159(1), 37-49.

Campbell, A. K., and A. K. Campbell, (1988). Chemiluminescence: principles and applications in biology and medicine. JRPS.,78(9), 787.

Campbell, A. K., M. B. Hallett, R. A. Daw, M. E. Ryall, R. C. Hart, and P. J. Herring, (1981). Application of the photoprotein obelin to the measurement of free Ca^{2+} in cells. In Bioluminescence and chemiluminescence (pp. 601-607). Academic Press.

Carlsen, H., J. Q. Moskaug, S. H. Fromm, and R. Blomhoff, (2002). *In vivo* imaging of NF-κB activity. J. Immunol., 168(3), 1441-1446.

Carpenter, K. E., and V. H. Niem, (Eds.). (1999). The living marine resources of the western central pacific: Batoid fishes, chimaera and bony fishes' part 1 (*Elopidae to Linophrynidae*) (Vol. 3). FAO.

Castle, P. H. J., and J. R. Paxton, (1984). A new genus and species of luminescent eel (Pisces: Congridae) from the Arafura Sea, Northern Australia. Copeia, 72-81.

Cavallaro, M., C. L. Mammola, and R. Verdiglione, (2004). Structural and ultrastructural comparison of photophores of two species of deep sea fishes: *Argyropelecus hemigymnus and Maurolicus muelleri*. J. Fish Biol., 64(6), 1552-1567.

Chen, S., I. Navizet, R. Lindh, Y. Liu, and N. Ferré, (2014). Hybrid QM/MM simulations of the obelin bioluminescence and fluorescence reveal an unexpected light emitter. J. Phys. Chem B., 118(11), 2896-2903.

Choi, Y. S., J. S. Bae, K. S. Lee, S. R. Kim, I. Kim, J. G. Kim, and H. D. Sohn, (2003). Genomic structure of the luciferase gene and phylogenetic analysis in the Hotaria-group fireflies. Comparative Biochemistry and Physiology Part B: BMB., 134(2), 199-214.

Ciana, P., M. Raviscioni, P. Mussi, E. Vegeto, I. Que, M. G. Parker, and A. Maggi, (2003). In vivo imaging of transcriptionally active estrogen receptors. Nat. Med., 9(1), 82.

Claes, J. M., and J. Mallefet, (2009). Hormonal control of luminescence from lantern shark (Etmopterus spinax) photophores. J. Exp. Biol., 212(22), 3684-3692.

Cline, T. W., and J. W. Hastings, (1972). Mutationally altered bacterial luciferase. Implications for subunit functions. *Biochemistry.,* 11(18), 3359-3370.

Cohen, D. M., T. Inada, T. Iwamoto, N. Scialabba, and P. J. P. Whitehead, (1990). FAO species catalogue: vol. 10 gadiform fishes of the world (order gadiformes), an annotated and ilustrated catalogue of Cods. Hakes, grenadiers and other gadiform fishes known to date (No. Sirsi) a324545). FAO.

Contag, C. H., P. R. Contag, J. I. Mullins, S. D. Spilman, D. K. Stevenson, and D. A. Benaron, (1995). Photonic detection of bacterial pathogens in living hosts. Mol. Microbiol., 18(4), 593-603.

Conti, E., N. P. Franks, and P. Brick, (1996). Crystal structure of firefly luciferase throws light on a superfamily of adenylate-forming enzymes. Structure, 4(3), 287-298.

Daubner, S. C., A. M. Astorga, G. B. Leisman, and T. O. Baldwin, (1987). Yellow light emission of *Vibrio fischeri* strain Y-1: purification and characterization of the energy-accepting yellow fluorescent protein. *PNAS.*, 84(24), 8912-8916.

Daunert, S., and S. K. Deo, (Eds.). (2006). Photoproteins in bioanalysis (p. 240). Weinheim, DE: Wiley-VCH.

Davis, M. P., N. I. Holcroft, E. O. Wiley, J. S. Sparks, and W. L. Smith, (2014). Species-specific bioluminescence facilitates speciation in the deep sea. Mar. Biol., 161(5), 1139-1148.

Davis, M. P., J. S. Sparks, and W. L. Smith, (2016). Repeated and widespread evolution of bioluminescence in marine fishes. PloS one., 11(6), e0155154.

Day, J. C., M. J. Chaichi, I. Najafil, and A. S. Whiteley, (2006). Genomic structure of the luciferase gene from the bioluminescent beetle, *Nyctophila* cf. *caucasica*. *J. Insect Sci.*, 6(1), 598 600.

De Wet, J. R., K. V. Wood, D. R. Helinski, and M. DeLuca, (1985). Cloning of firefly luciferase cDNA and the expression of active luciferase in *Escherichia coli*. PNAS., 82(23), 7870-7873.

Deheyn, D. D., and M. I. Latz, (2009). Internal and secreted bioluminescence of the marine polychaete *Odontosyllis phosphorea* (Syllidae). Invertebr. Biol., 128(1), 31-45.

DeLuca, M. (1969). Hydrophobic nature of the active site of firefly luciferase. *Biochemistry*, 8(1), 160-166.

DeLuca, M., and W. D. McElroy, (1974). Kinetics of the firefly luciferase catalyzed reactions. *Biochemistry,* 13(5), 921-925.

DeLuca, M., L. G. Strause, and J. F. Case, (1979). Biochemical and morphological changes accompanying light organ development in the firefly, *Photuris pennsylvanica*. J. Insect Physiol., 25(4), 339-347.

Devaki, B., and A. R. Grossman, (1993). Characterization of gene clusters encoding the fucoxanthin chlorophyll proteins of the diatom *Phaeodactylum tricornutum*. Nucleic Acids Res., 21(19), 4458-4466.

Ding, B. W., and Y. J. Liu, (2017). Bioluminescence of firefly squid via mechanism of single electron-transfer oxygenation and charge-transfer-induced luminescence. J. Am. Chem. Soc., 139(3), 1106-1119.

DiPilato, L. M., and J. Zhang, (2010). Fluorescent protein-based biosensors: resolving spatiotemporal dynamics of signaling. *Curr. Opin. Chem. Biol.,* 14(1), 37-42.

Dunlap, J. C., R. Krasnow, W. Taylor, J. W. Hastings, W. Vetterling, and V. Gooch, (1980). Circadian spontaneous bioluminescent glow and flashing of *Gonyaulax polyedra*. *J. Comp. Physiol.,* 138(1), 19-26.

Dunlap, P. (2014). Biochemistry and genetics of bacterial bioluminescence. In Bioluminescence: *Fundamentals and Applications in Biotechnology-Volume 1 (pp. 37-64). Springer, Berlin, Heidelberg.*

Dunlap, P. V. (2009). Bioluminescence, microbial. 41-61.

Engebrecht, J., K. Nealson, and M. Silverman, (1983). Bacterial bioluminescence: isolation and genetic analysis of functions from *Vibrio fischeri*. *Cell, 32*(3), 773-781.

Esimbekova EN., and VA Kratasyuk (2005) in: A. Tsuji Akio (Ed.), Bioluminescence & Chemiluminescence: Progress and Perspectives, world scientific publishing Co Pvt Ltd Singapore: 237.

Farmer, J. J., M. W. Reeves, G. M. Evins, A. A. Heiba, and B. D. Plikaytis, (1989). Clonal nature of *Salmonella typhi* and its genetic relatedness to other salmonellae as shown by multilocus enzyme electrophoresis, and proposal of *Salmonella bongori*. *JCM.,* 27(2), 313-320.

Field, L. M., A. A. James, K. H. Cho, J. S. Lee, Y. D. Choi, and K. S. Boo, (1999). Structural polymorphism of the luciferase gene in the firefly, *Luciola lateralis*. *Insect Mol. Biol.,* 8(2), 193-200.

Fleiss, A., and K. S. Sarkisyan, (2019). A brief review of bioluminescent systems (2019). Curr. Genet., 1-6.

Fujii, T., J. Y. Ahn, M. Kuse, H. Mori, T. Matsuda, and M. Isobe, (2002). A novel photoprotein from oceanic squid (*Symplectoteuthis oualaniensis*) with sequence similarity to mammalian carbon–nitrogen hydrolase domains. Biochem. Biophys. Res. Commun., 293(2), 874-879.

Fulton, B. B. (1941). A luminous fly larva with spider traits (Diptera, Mycetophilidae). Ann. Entomol. Soc. Am., 34(2), 289-302.

Gouveneaux, A., and J. Mallefet, (2013). Physiological control of bioluminescence in a deep-sea planktonic worm, *Tomopteris helgolandica*. J. Exp. Biol., 216(22), 4285-4289.

Grentzmann, G., J. A. Ingram, P. J. Kelly, R. F. Gestaland, and J. F. Atkins, (1998). A dual- luciferase reporter system for studying recoding signals. RNA, 4(4), 479-486.

Haddock, S. H., C. W. Dunn, and P. R. Pugh, (2005a). A re-examination of siphonophore terminology and morphology, applied to the description of two new prayine species with remarkable bio-optical properties. J. Mar. Biol. Assoc., 85(3), 695-707.

Haddock, S. H., C. W. Dunn, P. R. Pugh, and C. E. Schnitzler, (2005b). Bioluminescent and red-fluorescent lures in a deep-sea siphonophore. Science, 309(5732), 263-263.

Haddock, S. H., M. A. Moline, and J. F. Case, (2010). Bioluminescence in the sea. Annu. Rev. Mar. Sci., 2, 443-493.

Hanna, C. H., T. A. Hopkins, and J. Buck, (1976). Peroxisomes of the firefly lantern. J. Ultrastruct. Res., 57(2), 150-162.

Harvey, E. N. (1952). Bioluminescence. New York: Academic Press.

Hastings, J. W. (1983). Biological diversity, chemical mechanisms and evolutionary origins of bioluminescent systems. J. Mol. Evol, 19, 309-321.

Hastings, J. W. (1995). Bioluminescence: similar chemistries but many different evolutionary origins. Photochem. Photobiol., 62, 599-600.

Hastings, J. W. (1996). Chemistries and colors of bioluminescent reactions: a review. Gene, 173(1), 5-11.

Hastings, J. W., and D. Davenpor, (1957). The luminescence of the millipede, *Luminodesmus sequoiae*. *Biol. Bull.,* 113(1), 120-128.

Hastings, J. W., and K. H. Nealson, (1977). Bacterial bioluminescence. *Annu. Rev. Microbiol.*, 31(1), 549-595.

Hastings, J. W., P. Colepicolo, T. Roenneberg, D. Morse, and W. R. Taylor, (1993). Circadia regulation of bioluminescence in the dinoflagellate *Pyrocystis lunula*. J. Phycol., 29(2), 173-179.

Hastings, J. W., M. Fogel, and R. Schmitter, (1972). On the physical identity of scintillons: bioluminescent particles in *Gonyaulax polyedra*. *J. Cell. Sci.,* 11(1), 305-317.

Hastings, J. W., L. J. Kricka, and P. E. Stanley, (1997). Bioluminescence and chemiluminescence: Molecular reporting with photons. *Photochem. Photobiol. Sci.,* 8(2), 90-92.

Hawronskyj, J. M., and J. Holah, (1997). ATP: a universal hygiene monitor. *Trends Food Sci. Technol.,* 8(3), 79-84.

Hellinger, J., M. Huhn, and S. Herlitze, (2017). Bioluminescence in fishes: Diversity and functions. OFOAJ., 2(3), e555587.

Henry, J. P., and A. M. Michelson, (1978). Bioluminescence: physiological control and regulation at the molecular level. Photochem. Photobiol., 28(2), 293-310.

Herren, C. M., S. H. Haddock, C. Johnson, C. M. Orrico, M. A. Moline, and J. F. Case, (2005). A multi platform bathyphotometer for fine scale, coastal bioluminescence research. *Limnol. Oceanogr*: Methods, 3(5), 247-262.

Herring, P. J. (1983). The spectral characteristics of luminous marine organisms. Proc. R. Soc. London, Ser. B., 220(1219), 183-217.

Herring, P. J. (1987). Systematic distribution of bioluminescence in living organisms. Luminescence, 1(3), 147-163.

Herring, P. J., and J. G. Morin, (1978). Bioluminescence in fishes. Bioluminescence in action, 273, 329.

Homaei, A. A., A. B. Mymandi, R.Sariri, E. Kamrani, R. Stevanato, S. M. Etezad, and K. Khajeh, (2013). Purification and characterization of a novel thermostable luciferase from *Benthosema pterotum*. J. Photochem. Photobiol., 125, 131-136.

Illarionov, B. A., V. S. Bondar, V. A. Illarionova, and E. S. Vysotski, (1995). Sequence of the cDNA encoding the Ca^{2+}-activated photoprotein obelin from the hydroid polyp *Obelia longissima*. Gene, 153(2), 273-274.

Inouye, S., and S. Sasaki, (2007). Overexpression, purification and characterization of the catalytic component of Oplophorus luciferase in the deep-sea shrimp, *Oplophorus gracilirostris*. Protein

Expr. Purif., 56(2), 261-268.

Jianhong, L., Y. S. Park, S. C. Lee, S. M. Lee, J. G. Kim, I. Kim, and B. R. Jin, (2003). Genomic structure of the luciferase gene of the firefly, *Lampyris noctiluca*. Int. J. Ind. Entomol., 7(2), 155-159.

Johnsen, S. (2005). The red and the black: bioluminescence and the color of animals in the deep sea. Integr. Comp. Biol., 45(2), 234-246.

Karatani, H., and T. Konaka, (2000). Activities of the bimodal fluorescent protein produced by *Photobacterium phosphoreum* strain bmFP in the luciferase reaction *in vitro*. *Photochem. Photobiol.,* 71(2), 237-242.

Karatani, H., T. Konaka, and C. Katsukawa, (2000). Properties of the bimodal fluorescent protein produced by *Photobacterium phosphoreum*. Photochem. Photobiol., 71(2), 230-236.

Kaskova, Z. M., A. S. Tsarkova, and I. V. Yampolsky, (2016). 1001 lights: luciferins, luciferases, their mechanisms of action and applications in chemical analysis, *biology and medicine.* Chem. Soc. Rev., 45(21), 6048-6077.

King, A., W. R. Gransden, I. Phillips, and S. J. Eykyn, (1990). The antibiotic sensitivity of bacteria isolated from the blood of patients in St Thomas' Hospital, 1969-1988. *J. Antimicrob. Chemother.,* 25, 59-80.

Kodaka, H., K. Fukuada, S. Mizuochi, and K. Horigome,(1996). Adenosine triphosphate content of microorganisms related with food spoilage. *Jpn. J. Food Microbiol.,* 13(1), 29-34.

Kuts, V. V., and A. D. Ismailov, (2009). Physiological and emission characteristics of the luminescent bacterium Photobacterium phosphoreum from the white Sea. *Microbiology*, 78(5), 554.

Kuwabara, S., M. J. Cormier, L. S. Dure, P. Kreiss, and P. Pfuderer, (1965). Crystalline bacterial luciferase from *Photobacterium fischeri*. *PNAS.,* 53(4), 822.

Lall, A. B., D. S. Ventura, E. J. Bechara, de J. M. Souza, P. Colepicolo-Neto, and V. R. Viviani, (2000). Spectral correspondence between visual spectral sensitivity and bioluminescence emission spectra in the click beetle *Pyrophorus punctatissimus* (Coleoptera: *Elateridae*). J. Insect Physiol., 46(7), 1137-1141.

Lang, D., H. Erdmann, and R. D. Schmid, (1992). Bacterial luciferase of *Vibrio harveyi* MAV: purification, characterization and crystallization. Enzyme Microb. Technol., 14(6), 479-485.

Latz, M. I., and H. J. Jeong, (1996). Effect of red tide dinoflagellate diet and cannibalism on the bioluminescence of the heterotrophic dinoflagellates *Protoperidinium* spp. Mar. Ecol. Prog. Ser., 132, 275-285.

Lavi, J. T., R. P. Raunio, and T. H. Stahlberg, (1990). Affinity purification of bacterial luciferase and NADPH: FMN oxidoreductases by FMN sepharose for analytical applications. *J. Biolumin. Chemilumin.,* 5(3), 187-192.

Levine, L. D., and W. Ward, (1982). Isolation and characterization of a photoprotein," phialidin", and a spectrally unique green-fluorescent protein from the bioluminescent jellyfish *Phialidium gregarium*. Comp. Biochem. Physiol. B., 72(1), 77-85.

Li, L., and J. W. Hastings, (1998). The structure and organization of the luciferase gene in the photosynthetic dinoflagellate *Gonyaulax polyedra*. Plant Mol. Biol., 36(2), 275-284.

Liu, L., H. Im, M. Cegielski, P. LeMagueres, L. W. Schultz, K. L. Krause, and J. W. Hastings, (2003). Characterization and crystallization of active domains of a novel luciferase from a marine dinoflagellate. Acta Crystallogr. D., 59(4), 761-764.

Liu, L., T. Wilson, and J. W. Hastings, (2004). Molecular evolution of dinoflagellate luciferases, enzymes with three catalytic domains in a single polypeptide. *PNAS.,* 101(47), 16555- 16560.

Lloyd, J. E. (1971). Bioluminescent communication in insects. Annu. Rev. Entomol., 16(1), 97-122.

Mallefet, J., and O. Shimomura, (1995). Presence of coelenterazine in mesopelagic fishes from the Strait of Messina. Mar. Biol., 124(3), 381-385.

Marcinko, C. L., S. C. Painter, A. P. Martin, and J. T. Allen, (2013). A review of the measurement and modelling of dinoflagellate bioluminescence. *Prog. Oceanogr.*, 109, 117-129.

Markova, S. V., and E. S. Vysotski, (2015). Coelenterazine-dependent luciferases. Biochemistry, 80(6), 714-732.

Markova, S. V., S. Golz, L. A. Frank, B. Kalthof, and E. S. Vysotski, (2004). Cloning and expression of cDNA for a luciferase from the marine *copepod Metridia longa* a novel secreted bioluminescent reporter enzyme. *J. Biol. Chem.,* 279(5), 3212-3217.

Markova, S. V., M. D. Larionova, L. P. Burakova, and E. S. Vysotski, (2015). The smallest natural high-active luciferase: cloning and characterization of novel 16.5-kDa luciferase from copepod *Metridia longa*. Biochem. Biophys. Res. Commun., 457(1), 77-82.

Matthews, J. C., K. Hori, and M. J. Cormier, (1977). Purification and properties of *Renilla reniformis* luciferase. *Biochemistry*, 16(1), 85-91.

McAllister, D. E. (1967). The significance of ventral bioluminescenee in fishes. J. Fish. Res. Board Can., 24(3), 537-554.

McCapra, F., E. H. White, and G. F. Field, (1963). The structure and synthesis of firefly luciferin. J. Am. Chem. Soc., 85(3), 337-343.

McElroy, W. D. (1947). The energy source for bioluminescence in an isolated system. PNAS., 33(11), 342.

McElroy, W. D., and A. A. Green, (1955). Enzymatic properties of bacterial luciferase. Arch. Biochem. Biophys., 56(1), 240-255.

Meighen, E. A. (1991). Molecular biology of bacterial bioluminescence. *Microbiol. Mol. Biol. Rev.,* 55(1), 123-142.

Meighen, E. A. (1993). Bacterial bioluminescence: organization, regulation, and application of the lux genes. FASEB. J., 7(11), 1016-1022.

Merrett, N. R., J. Badcock, and P. J. Herring, (1973). The status of *Benthalbella infans* (Pisces: *Myctophoidei*), its development, bioluminescence, general biology and distribution in the eastern North Atlantic. J. Zool., 170(1), 1-48.

Meyer-Rochow VB (1990). The New Zealand Glowworm. Waitomo Caves Museum Society Inc., Waitomo, New Zealand. 60 pp.

Meyer Rochow, V. B. (2007). Glowworms: a review of *Arachnocampa spp*. and kin. Luminescence, 22(3), 251-265.

Morishita, H., S. Ohashi, T. Oku, Y. Nakajima, S. Kojima, M. Ryufuku, and Y. Ohmiya, (2002). Cloning and characterization of an active fragment of luciferase from a luminescent marine alga, *Pyrocystis lunula*. Photochem. Photobiol., 75(3), 311-315.

Müller, T., and A. K. Campbell, (1990). The chromophore of *pholasin*: a highly luminescent protein. *J. Biolumin. Chemilumin.,* 5(1), 25-30.

Müller, W. E. G., M. Kasueske, X. Wang, H. C. Schröder, Y. Wang, D. Pisignano, and M. Wiens, (2009). Luciferase a light source for the silica-based optical waveguides (spicules) in the demosponge *Suberites domuncula*. Cell. Mol. Life Sci., 66(3), 537.

Nakajima, Y., and Y. Ohmiya, (2010). Bioluminescence assays: multicolor luciferase assay, secreted luciferase assay and imaging luciferase assay. Expert Opin. Drug Discov., 5(9), 835-849.

Nakajima, Y., T. Kimura, K. Sugata, T. Enomoto, A. Asakawa, H. Kubota, and Y. Ohmiya, (2005). Multicolor luciferase assay system: one-step monitoring of multiple gene expressions with a single substrate. *Biotechniques,* 38(6), 891-894.

Nakajima, Y., K. Kobayashi, K. Yamagishi, T. Enomoto, and Y. Ohmiya, (2004). cDNA cloning and characterization of a secreted luciferase from the luminous japanese ostracod, *Cypridina noctiluca*. *Biosci. Biotechnol. Biochem.,* 68(3), 565-570.

Nakamura, H., Y. Kishi, O. Shimomura, D. Morse, and J. W. Hastings, (1989). Structure of dinoflagellate luciferin and its enzymic and nonenzymic air-oxidation products. J. Am. Chem. Soc., 111(19), 7607-7611.

Naumov, P., C. Wu, Y. J. Liu, and Y. Ohmiya, (2012). Spectrochemistry and artificial color modulation of Cypridina luminescence: indirect evidence for chemiexcitation of a neutral dioxetanone and emission from a neutral amide. Photochem. Photobiol. Sci., 11(7), 1151-1155.

Nicolas, M. T., J. M. Bassot, and O. Shimomura, (1982). Polynoidin: a membrane photoprotein isolated from the bioluminescent system of scale worms. Photochem. Photobiol., 35(2), 201-207.

Oba, Y., Bessho-Uehara, M., and K. Konishi, (2017). Biochemical characteristics and gene expression profiles of two paralogous luciferases from the japanese firefly *Pyrocoelia atripennis* (Coleoptera, Lampyridae, Lampyrinae): insight into the evolution of firefly luciferase genes. *Photochem. Photobiol.,* 16(8), 1301-1310.

Ohmiya, Y., and T. Hirano, (1996). Shining the light: the mechanism of the bioluminescence reaction of calcium-binding photoproteins. *Chem. Biol.*, 3(5), 337- 347.

Ohmiya, Y., C. Wu, and C. Suzuki-Ogoh, (2008). C-terminal region of the active domain enhances enzymatic activity in dinoflagellate luciferase. *Photochem. Photobiol. Sci.*, 7(2), 208-211.

O'Kane, D. J., and D. C. Prasher, (1992). Evolutionary origins of bacterial bioluminescence. Mol. Microbiol., *6*(4), 443-449.

Osamu. S. (2006) "The coelenterazines." In Bioluminescence: Chemical Principles and Methods, pp. 159-179. World Scientific.

Pietsch, T., R. Arnold, and D. Hall, (2009). A bizarre new species of frogfish of the genus *Histiophryne* (Lophiiformes: *Antennariidae)* from Ambon and Bali, Indonesia. Copeia, 2009(1), 37-45.

Reeve, C. A., and T. O. Baldwin, (1981). Luciferase inactivation in the luminous marine bacterium *Vibrio harveyi*. J. Bacteriol., 146(3), 1038-1045.

Rehemtulla, A., L. D. Stegman, S. J. Cardozo, S. Gupta, D. E. Hall, C. H. Contag, and B. D. Ross, (2000). Rapid and quantitative assessment of cancer treatment response using *in vivo* bioluminescence imaging. *Neoplasia*, 2(6), 491-495.

Renwart, M. (2013). " Ultrastructure and biochemistry of the light-emitting system of lantern shark (*Etmopterus spinax*) photophores. Mar. Biol. Res*.,* 223.

Santos, D. A., A. I. Salgado, and R. A. Cunha, (2003). ATP is released from nerve terminals and from activated muscle fibres on stimulation of the rat phrenic nerve. Neurosci. Lett., 338(3), 225-228.

Sato, A., B. Klaunberg, and R. Tolwani, (2004). *In vivo* bioluminescence imaging. Comp. Med., 54(6), 631-634.

Seliger, H. H. (1987). The evolution of bioluminescence in bacteria. Photochem. Photobiol., 45(2), 291-297.

Seliger, H. H., and W. D. McElroy, (1960). Spectral emission and quantum yield of firefly bioluminescence. Arch. Biochem. Biophys., 88(1), 136-141.

Seliger, H. H., J. B. Buck, W. G. Fastie, and W. D. McElroy, (1966). Flash patterns in jamaican fireflies. *The Bio. Bull.,* 127(1), 159-172.

Seliger, H. H., W. D. McElroy, E. H. White, and G. F. Field, (1961). Stereospecificity and firefly bioluminescence, a comparison of natural and synthetic luciferins. PNAS., 47(8), 1129.

Sharifian, S., A. Homaei, R. Hemmati, R. B. Luwor, and K. Khajeh, (2018). The emerging use of bioluminescence in medical research. Biomed. Pharmacother., 101, 74-86.

Shimomura O., and IV Yampolsky (2019) Bioluminescence, chemical principles and methods, 3rd Edn. World Scientific Publishing Co Pte Ltd, Hackensack.

Shimomura, O. (1981). A new type of ATP activated bioluminescent system in the millipede *Luminodesmus sequoiae*. FEBS. Letters, 128(2), 242-244.

Shimomura, O. (1985). Physiological adaptations of marine animals. Bioluminescence in the Sea: Photoprotein Systems, University Press, Cambridge, 351-372.

Shimomura, O. (1986). Bioluminescence of the brittle star *Ophiopsila californica*. Photochem. Photobiol., 44(5), 671-674.

Shimomura, O. (2006). Discovery of green fluorescent protein. Methods Biochem. Anal., 47, 1-14.

Shimomura, O., and P. R. Flood, (1998). Luciferase of the scyphozoan medusa *Periphylla periphylla*. The Bio. Bull., 194(3), 244-252.

Shimomura, O., and F. H. Johnson, (1968). *Chaetopterus* photoprotein: crystallization and cofactor requirements for bioluminescence. Science, 159(3820), 1239-1240.

Shimomura, O.; I. Yampolsky, Bioluminescence: Chemical Principles and Methods, 3rd ed.; World Scientific Publishing: Singapore, 2019.

Silverman, L., R. Campbell, and J. R. Broach, (1998). New assay technologies for high- throughput screening. *Curr. Opin. Chem. Biol.*, 2(3), 397-

403.

Sivinski, J. (1981). The nature and possible functions of luminescence in coleoptera larvae. Coleopt. Bull., 167-179.

Stephenson, D. G., and P. J. Sutherland, (1981). Studies on the luminescent response of the Ca^{2+}-activated photoprotein, obelin. Biochim. Biophys. Acta., *678*(1), 65-75.

Straube, N., C. Li, J. M. Claes, S. Corrigan, and G. J. Naylor, (2015). Molecular phylogeny of Squaliformes and first occurrence of bioluminescence in sharks. BMC Evol. Biol., 15(1), 162.

Strehler, B. L., and M. J. Cormier, (1953). Factors affecting the luminescence of cell-free extracts of the luminous bacterium, *Achromobacter fischeri*. Arch. Biochem. Biophys., 47(1), 16-33.

Suadee, C., S. Nijvipakul, J. Svasti, B. Entsch, D. P. Ballou, and P. Chaiyen, (2007). Luciferase from *Vibrio campbellii* is more thermostable and binds reduced FMN better than its homologues. J. Biochem., 142(4), 539-552.

Suntsov, A. V., and R. D. Brodeur, (2008). Trophic ecology of three dominant myctophid species in the northern California current region. Mar. Ecol. Prog. Ser., 373, 81-96.

Tehrani, G. A., S. Mirzaahmadi, M. Bandehpour, F. Laloei, A. Eidi, T. Valinasab, and B. Kazemi, (2011). Molecular cloning and expression of the luciferase coding genes of *Vibrio fischeri*. Afr. J. Biotechnol., 10(20), 4018-4023.

Thacker, C. E., and D. M. Roje, (2009). Phylogeny of cardinalfishes (Teleostei: Gobiiformes: Apogonidae) and the evolution of visceral bioluminescence. Mol. Phylogenet. Evol., 52(3), 735-745.

Thomas, G. M., and G. O. Poinar, (1979). *Xenorhabdus* gen. nov., a genus of entomopathogenic, nematophilic bacteria of the family *Enterobacteriaceae*. *Int. J. Syst. Evol. Microbiol.*, 29(4), 352-360.

Tiffen, J. C., C. G. Bailey, C. Ng, J. E. Rasko, and J. Holst, (2010). Luciferase expression and bioluminescence does not affect tumor cell growth *in vitro* or *in vivo*. Mol. Cancer, *9*(1), 1-8.

Tsuji, F. I. (1978). Cypridina luciferin and luciferase. In *Meth. Enzymol.,* (Vol. 57, pp. 364-372). Academic Press.

Tu, S. C., and H. I. Mager, (1995). Biochemistry of bacterial bioluminescence. *Photochem. Photobiol.,* 62(4), 615-624.

Urbanczyk, H., J. C. Ast, A. J. Kaeding, J. D. Oliver, and P. V. Dunlap, (2008). Phylogenetic analysis of the incidence of *lux* gene horizontal transfer in *Vibrionaceae*. J. Bacteriol., 190(10), 3494-3504.

Valiadi, M., M. Debora Iglesias Rodriguez, and A. Amorim, (2012). Distribution and genetic diversity of the luciferase gene within marine dinoflagellates. J. Phycol., 48(3), 826-836.

Venkateswaran, K., N. Hattori, M. T. La Duc, and R. Kern, (2003). ATP as a biomarker of viable microorganisms in clean-room facilities. J. Microbiol. Methods, 52(3), 367-377.

Vervoort, J., F. Muller, J. Lee, W. A. Van den Berg, and C. T. Moonen, (1986). Identifications of the true carbon-13 nuclear magnetic resonance spectrum of the stable intermediate II in bacterial luciferase. *Biochemistry.,* 25(24), 8062- 8067.

Viviani, V. R. (2002). The origin, diversity, and structure function relationships of insect luciferases. *Cell. Mol. Life Sci.,* 59(11), 1833-1850.

Viviani, V. R., and E. J. Bechara, (1997). Bioluminescence and biological aspects of Brazilian railroad-worms (Coleoptera: Phengodidae). *Ann. Entomol. Soc. Am.,* 90(3), 389-398.

Viviani, V. R., F. G. C. Arnoldi, A. S. Neto, T. L. Oehlmeyer, E. J. H. Bechara, and Y. Ohmiya, (2008). The structural origin and biological function of pH-sensitivity in firefly luciferases. Photochem. Photobiol. Sci., 7(2), 159-169.

Vysotski, E. S., and J. Lee, (2004). Ca^{2+} regulated photoproteins: structural insight into the bioluminescence mechanism. Acc. Chem. Res., 37(6), 405-415.

Vysotski, E. S., S. V. Markova, and L. A. Frank, (2006). Calcium-regulated photoproteins of marine coelenterates. Mol. Biol., 40(3), 355-367.

Ward, W. W., and H. H. Seliger, (1974). Extraction and purification of calcium-activated photoproteins from the ctenophores *Mnemiopsis* species and *Beroe ovata*. Biochemistry, 13(7), 1491-1499.

Widder, E. (2002). Bioluminescence and the pelagic visual environment. *Mar. Freshw. Behav. Physiol.,* 35(1-2), 1-26.

Widder, E. A. (2001). Marine bioluminescence. Why do so many animals in the open ocean make light. *BioScience*, 1(1), 78.

Widder, E. A. (2010). Bioluminescence in the ocean: origins of biological, chemical, and ecological diversity. *Science.*, 328(5979), 704-708.

Widder, E. A., S. Johnsen, E. J. Balser, and E. C. Fisher, (1999). Bioluminescence in the deep- sea cirrate octopod *Stauroteuthis syrtensis Verrill* (Mollusca: Cephalopoda). *Biol. Bull.*, 197(1), 26-39.

Wiens, M., X. Wang, A. Unger, H. C. Schröder, V. A. Grebenjuk, D. Pisignano, and W. E. Müller, (2010). Flashing light signaling circuit in sponges: endogenous light generation after tissue ablation in *Suberites domuncula*. J. Cell. Biochem., 111(6), 1377-1389.

Wood, K. V. (1995). The chemical mechanism and evolutionary development of beetle bioluminescence. *Photochem. Photobiol.*, 62(4), 662-673.

Yamaguchi, M., H. Saito, M. Suzuki, and K. Mori, (2000). Visualization of neurogenesis in the central nervous system using nestin promoter-GFP transgenic mice. *NeuroReport.*, 11(9), 1991-1996.

Yu, M., and Y. J. Liu, (2020). Same luciferin in different luciferases emitting different-color light-a theoretical study on beetle bioluminescence. J. Chem. Theory Comput., 16 (6), 3904-3909.

Zhu, Y., R. L. Stornetta, and J. J. Zhu, (2004). Chandelier cells control excessive cortical excitation: characteristics of whisker-evoked synaptic responses of layer 2/3 nonpyramidal and pyramidal neurons. J. Neurosci., *24*(22), 5101-5108.

Pb. Univ. Res. J (Sci.) Vol. 70, 2020, pp 107-114

REGENERATED SCALE STRUCTURE - A TOOL FOR DIFFERENTIATING STOCKS OF *LABEO ROHITA* (HAMILTON)

Apneet Kaur and Yogesh Kumar Rawal*
Department of Zoology, Panjab University, Chandigarh - 160014, India

ABSTRACT

The fish scale contains important information for age and growth parameters of a fish besides being of taxonomic importance for differentiating the species of a genus. Of late, the sculptural details of the fish scale have also been employed for the discrimination of stocks of commercial fish species as correct identification is primary to the conservation and the management of the stocks. The regenerated scales of a commercial fish, *Labeo rohita* (Hamilton) were studied from four ecologically different localities, Gobindsagar reservoir; Ropar wetland; Fish pond at Ropar and Harike wetland. The scanning electron microscopic studies of the focus region of the regenerated scale shows differences in the pattern of regeneration in the stocks of *L. rohita* from different localities. The microridges seen in the focus region of the regenerated scale shows different interlacing patterns in different stocks on account of the difference in the mineral composition in the different localities. The ultrastructural detail of the regenerated scale can thus serve as an alternate tool for distinguishing the stocks of fish from different localities.

Key words: Fish; Stock; Regenerated scale; SEM; Ultrastructure

INTRODUCTION

On first glance, the most noticeable feature of most carps are that their body is covered with scales and so much information can be obtained about the growth, history and longevity of fish by studying the finer details of the scale. The carved pattern of circuli on the scale tells about the physiological events of fish life as well as the growth history (Kaur and Dua, 2004). The circuli form a concentric pattern over the course of a year that is related to environmental and growth conditions (Schneider *et al*., 2000). The scales have many concealed details in their design that are helpful for fish identification and classification (Jawad, 2005a,b; Poulet *et al*., 2005; Rawal *et al*., 2020). The fish scale has also been employed for identification of fish species with a large number of overlapping characters, which makes it hard for a taxonomist to identify a species correctly (Johal and Dhiman, 2007; Kaur and Dua, 2004).

The use of scale morphology gained importance for the identification of fish species and stocks with the introduction of scanning electron microscopy (Roberts, 1993; Jawad, 2005a, b; Rawal *et al*., 2020). The concept of stock used in the present work follows the definition given by Gulland (1969) which says that “A stock is a separate reproducing population or subpopulation of a species”. For fish conservation and fishery management, it is of utmost important to understand the significance and distribution of the fish stocks.

The fish stocks have been identified employing a wide variety of techniques such as morphometrics (Rawat *et al*., 2017; Khan and Nazir, 2018), otolith chemistry (Tanner *et al*., 2016; Avigliano *et al*., 2017) and shape (Mapp *et al*., 2017; Mahe *at al*., 2019). Attempts have also been made to identify the fish stocks studying the structure of the regenerated scale (Johal *et al*., 2014). The regenerated scales appear in place of normal scales as a result of erosion of scales, which might happen naturally as result of overcrowding; while passing through the macrophytes or because of some other natural events or hard conditions (Miranda and Escala, 2002). The regenerated scale is different from the normal scale as the focus area is diffusely spread over a large area and the circuli start beyond this diffused area unlike the normal scale where the focus is sharp and circuli start immediately around the focus (Fig. 1). The regenerated scales are easy to identify even under a light microscope and

---

* Corresponding author e-mail: ykrawal@pu.ac.in
MS Received: September 20, 2020, Accepted: November 15, 2020

sometimes, the larger scale samples can be identified even with naked eyes.

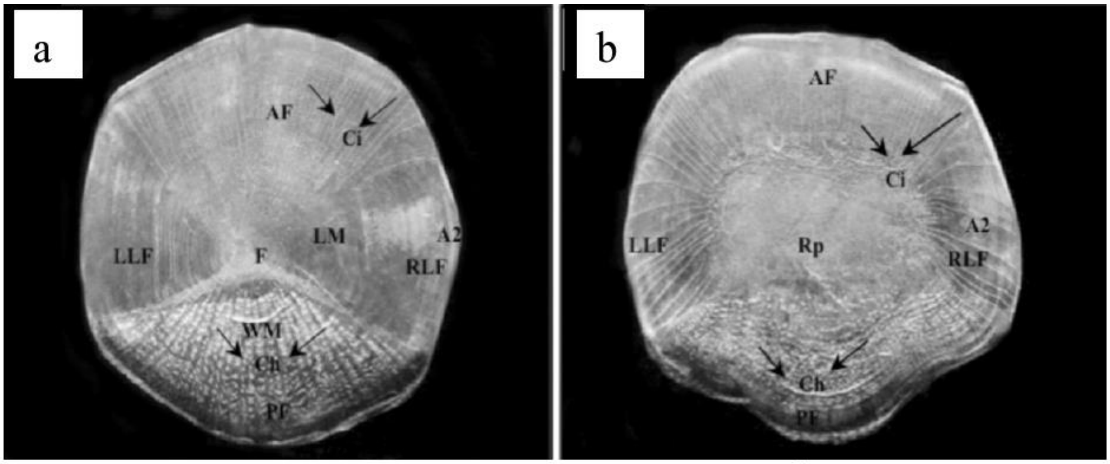

Fig. 1: (a) Normal Scale, (b) Regenerated Scale (Johal et al., 2017) A, Annulus; AF, Anterior field; Ch, Chromatophores; Ci, Circuli; F, Focus; LM, Larval mark; LLF, Left lateral field; PF, Posterior field; RLF, Right lateral field; Rp, Regenerated part; WM, Winter mark.

The present work has been carried out to study the stocks of a commercial fish, *Labeo rohita*, which occurs naturally in the riverine waters of north India and is also cultured extensively. It is considered that fish respond to the changing environmental conditions and invariably, pre-pone or postpone their spawning periods in response to changing environmental conditions. Keeping these factors in mind, it has been considered appropriate to study the occurrence of various sub-populations of this fast growing culturable fish species under different ecological conditions.

The samples of the *L. rohita* were collected from Gobindsagar reservoir (31^0′4′39′′N & $76^0$26′0’’E), Ropar wetland ($30^0$58′N & $76^0$30′E), Katli Fish Farm, Ropar ($30^0$58′N & $76^0$30′E) and Harike wetland ($31^0$3′N & $75^0$12′E) (Fig.2). The average length (≈50 cm) and weight (≈600 gm) of the specimens from all the four localities were approximately the same and they were all with age group of 2+. The regenerated scales were taken from the left side of fish below the dorsal fin and above the lateral line from the second or third row.

The scales were washed in tap water to remove the mucous and dirt particles. The scales were sonicated for 2-3 minutes to remove any trace of dust particles. The scales were kept in dessicator overnight to dry them completely. The scales were then mounted on aluminum stubs with the ventral part of the scale touching the stub. They were then coated with a layer of gold (100 Å) in a gold sputtering unit. The images were taken at an accelerating voltage of 20 kV in JEOL SEM Model JSM 6100.

For ultrastructural details of the regenerated scale, only the dorsal part of the scale was studied under scanning electron microscope. All the SEM photomicrographs were taken at the same magnification (150X, 500X, 700X and 1500X).

The SEM of regenerated scale of *L. rohita* showed unique patterns of regeneration in the focus region in each of the four ecologically different localities. The regenerated part of the focus is made up of raised structures called microridges. These microridges are made up of various minerals which contribute to speedy development of the scale in order to cover the naked area of the fish. A greater part of these minerals comprise of calcium and magnesium salts. The focus region of the regenerated scales of *L. rohita* under scanning microscope shows an obscure network of interlacing ridges in all the four localities. (Fig. 3).

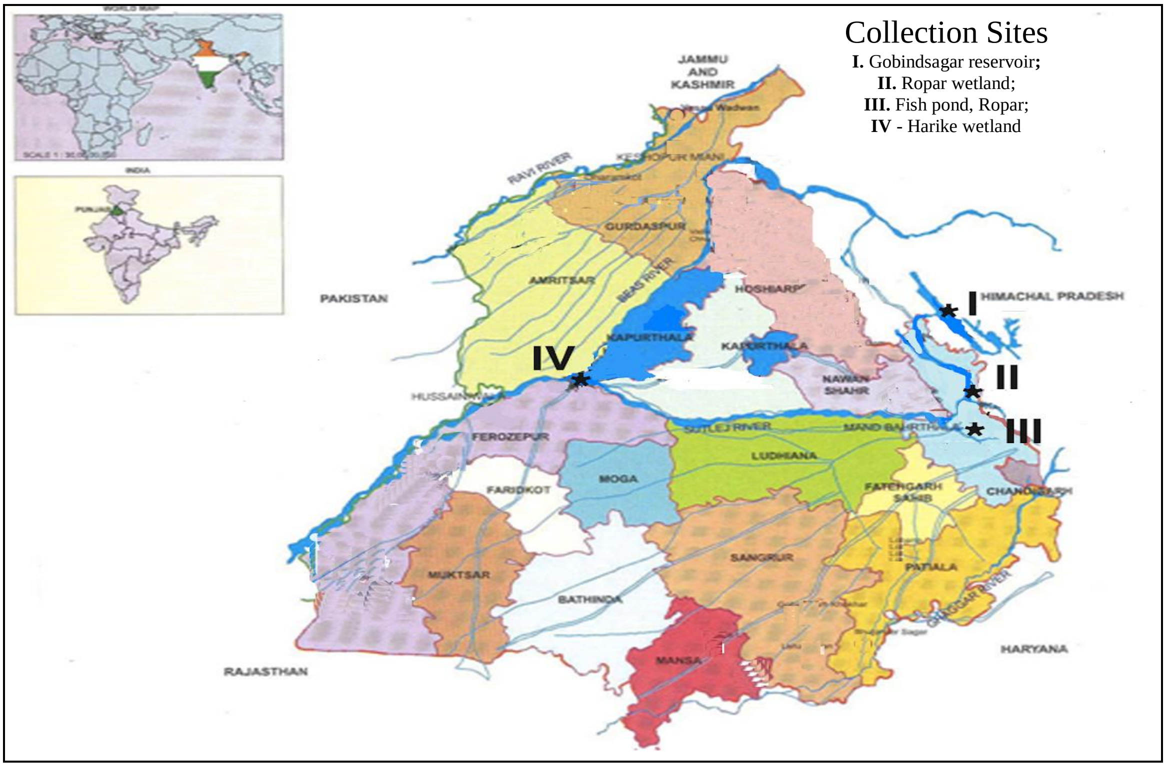

Fig. 2: Collection sites (Modified after Ladhar, 2005)

As can be seen in micrographs of the focus area at 150X, the four localities, Gobindsagar reservoir; Ropar wetland; Fish pond at Ropar and Harike wetland have all different regeneration patterns (Fig. 3a-d). The microridges are compact in Ropar and Harike wetlands as compared to the Gobindsagar and fish pond. The same gets clearer at higher magnification of 500X. The microridges form a compact interlacing network in Ropar and Harike wetlands, whereas in case of Gobindsagar, the microridges are forming interlacing patterns at some places and at other points, they are far apart. The pattern of the microridges at Fish pond at Ropar is having intact pattern but they are widely spaced. The higher magnification showed the pattern of newly formed focus to be different from each other. Thus the focus region on higher magnification (500X) clearly shows the pattern of deposition of the minerals to be different and unique at each locality. At Harike wetland, the microridges form structure with 5-7 edges whereas the focus region of the regenerated scale of fish from the farm showed network in the form of non-continuous deposits (Fig.3 e-h).

The microridges become much clearer on higher magnifications of 700X and 1500X but the overall pattern gets diffused as only a few microridges are visible at higher magnification of 700X and 1500X (Fig.3 i-l & m-p)

An unusual large indistinct and amorphous focus is an identifiable mark in regenerated type of scales, which are developed as a replacement of the lost scales (Creaser, 1926; Matondo *et al*., 2012). In the regenerated scales, the initial growth is very fast without circuli formation (Blair, 1942). In the scales of *L. rohita*, the focus region of the regenerated scale is a large diffused area as in most of the regenerated scales of other fishes. The focus region bears a mesh of raised structures called as microridges which are formed of the various minerals. Jawad and Al-Jufaili (2007) also observed the focus region to having random deposit of tubercles and ridges. They also observed that the boundary between overlapped and free regions (anterior limit of the epidermal-dermal cover) divides the regenerated focus into two distinct ornamented areas with the number of tubercles and granules to be much higher in the free region than in the overlapped one.

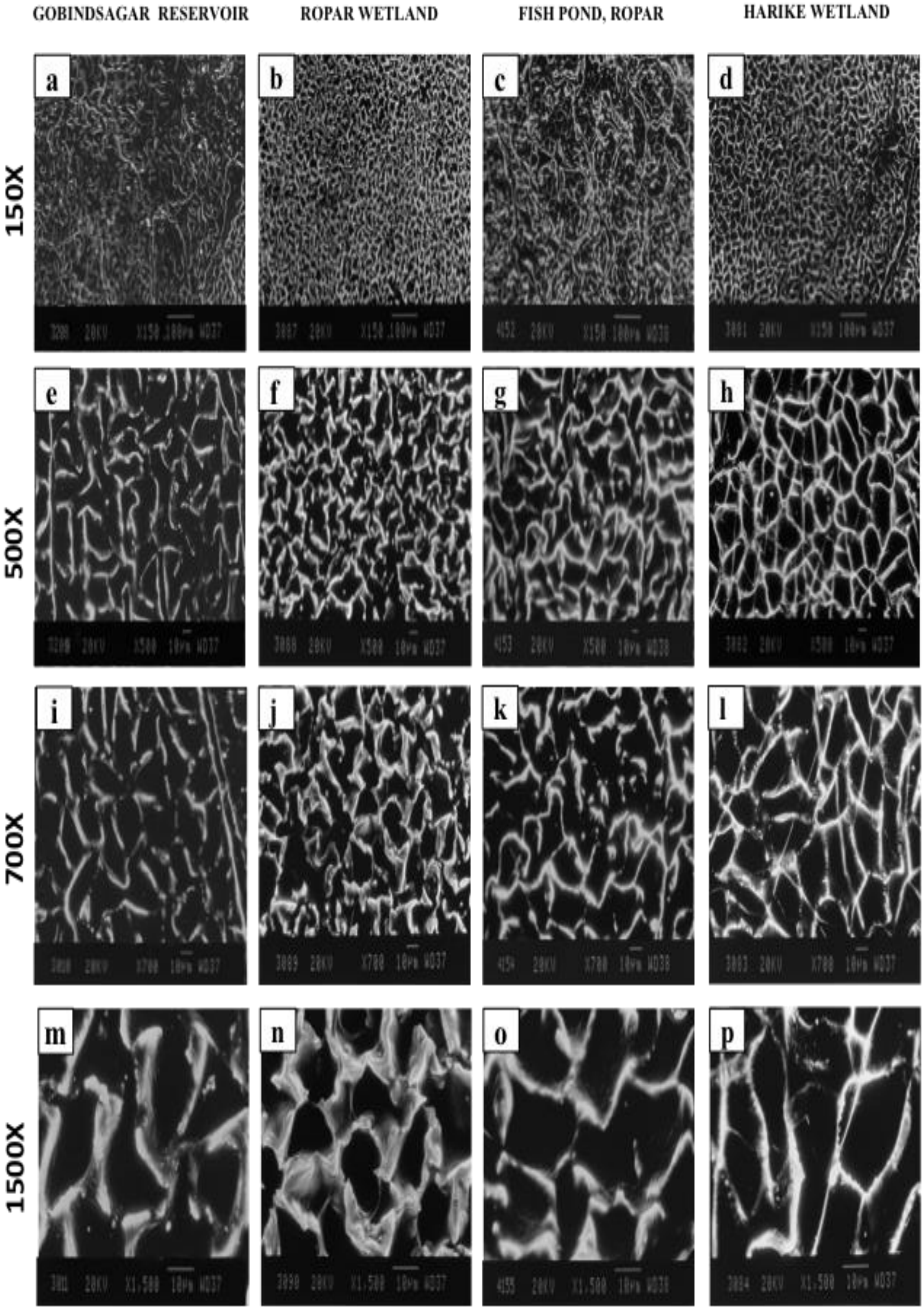

Fig. 3: Micrographs of focus region of the regenerated cycloid scale of *Labeo rohita* (Hamilton) of different fish stocks.

Sire (1986) suggested that the regenerated focus exhibits a characteristic pattern of tubercles of various sizes, forming short ridges that are not found on ontogenetic scales and that are laid at random on the regenerated focus. This large heterogeneous region of focus and the arrangement of the grooves is because of the quick process of replacement of scale through activation of innumerable number of scale-pocket living cells (Sire *et al*., 2000). The regenerated scale never recovers its superficial pattern characteristics of the original ontogenic scale. The regenerated scales show a central area lacking concentric ridges with a grooved network and many radial grooves which are connected with the central network (Yamada, 1961). This is in reference to the viewpoint of mechanism of ridge formation.

The particular pattern of circuli on regenerated scale is significant for discrimination of taxa (Casselman *et al*., 1986). Such distinctness with regard to regeneration pattern has also been found for *Labeo* species. The regenerated scales of *L. rohita* from different ecological localities grossly showed differences in terms of interlacing patterns and shape of the microridges. The differences between the stocks are much clearer at low magnifications (150X and 150X) than at higher magnifications (700X and 1500X) as fewer microridges are visible at higher magnification and pattern gets lost. These microridges patterns are different in different fish stocks as the mineral composition is different at different places consequently leading to differences in the formation pattern of the microridges. Kaur and Dua (2004) while working on 4 species of *Labeo* spp. found the arrangement of ridges and their relative interspace to be of taxonomic significance for differentiating different species of *Labeo.* Similar observations were made in the regenerated scales of the *C. carpio* stocks with observed variation in the pattern of the villi and the inter-villous space (Johal *et al.*, 2014). They called the structures in the focus to be villi but it is better to call these structures as microridges as villi are finger like projections and generally they do not form a network but microridges do. A lot of studies have been conducted wherein the investigators have employed the otolith chemistry in relation to water chemistry for separating the stocks of different fish species (Miyan *et al*., 2016; Nazir and Khan, 2019). The underlying principle for differentiation of stocks of *Labeo* spp. in the present study is the same as otolith chemistry. The present studies revealed that the ultrastructural details of the focus region of the regenerated scale can also be employed for the discrimination of the fish stocks from different zoogeographical areas occupying different ecological conditions.

ACKNOWLEDGEMENT

Authors are thankful to Dr. Harpreet Kaur, Chairperson, Department of Zoology, Panjab University, Chandigarh for providing the laboratory facilities. We also owe our thanks to the DST-INSPIRE for providing the financial assistance. The authors are also grateful to Indian Institute of Technology (IIT), Ropar, Punjab and Department of Geology, Panjab University, Chandigarh for providing the SEM facilities.

REFERENCES

Avigliano, E., M.C. Barbara, L. Mathieu, R. Rurik, V. Gonzalo, V. Marcelo, B. Fernando and V.V. Alejandra. 2017. Otolith edge fingerprints as approach for stock identification of *Genidens barbus*. *Estuar. Coast. Shelf Sci.*, 194: 92-96

Blair, A.A. 1942. Regeneration of the Scales of Atlantic Salmon. *J. Fish. Res. Board Can*., 5c(5): 440-447.

Casselman, J.M., E.J. Crossman, P.E. Ihssen, J.D. Reist and H.E. Booke. 1986. Identification of muskellunge northern pike, and their hybrids. *Am. Fish. Soc. Spl. Publ.,* 15: 14-46.

Creaser, C. 1926. The structure and growth of the scales of fishes in relation to the interpretation of their life history, with special reference to the sunfish *Eupomotis gibbosus*. Museum of Zoology, University of Michigan, Miscellaneous Publications

No. 17. 84 pp. Published by the University, Ann Harbor, Michigan.

Gulland, J.A. 1969. Manual for Methods of Fish Stock Assessment. Part 1. Food and Agricultural Organization, Rome FRS/M4. pp154.

Jawad, L.A. 2005a. Comparative morphology of scales of four teleost fishes from Sudan and Yemen. *J. Nat. Hist*., 39(28): 2643-2660.

Jawad, L.A. 2005b. Comparative scale morphology and squamation pattern in triplefins (Pisces: Teleostei: Perciformes: Tripterygiida). *Tuhinga*., 16: 137-167.

Jawad, L.A. and S.M. Al-Jufaili. 2007. Scale morphology of greater lizardfish *Saurida tumbil* (Bloch, 1795) (Pisces: Synodontidae). *J. Fish Biol.*,70(4): 1185-1212.

Johal, M.S. and M. Dhiman. 2007. Ultrastructure of fish scales as a tool in fish identification up to species level of Genus *Puntius* Hamilton. *Pb. Univ. Res. J.* (Sci.)., 57:73-81.

Johal, M.S., Y.K. Rawal, A. Kaur and A. Kaur. 2014. Ultrastructure of the focus region of the regenerated cycloid scale of an exotic fish *Cyprinus carpio communis* L as a possible key to comprehensive understanding of populations. *Curr. Sci*., 106(5):744-748.

Kaur, N. and A. Dua. 2004. Species specificity as evidenced by scanning electron microscopy of fish scales. *Curr. Sci*., 87: 692-696.

Khan, M.A. and A. Nazir. 2018. Stock delineation of the long-whiskered catfish, *Sperata aor* (Hamilton 1822), from River Ganga by using morphometrics. *Mar. & Freshwat. Res*. 70: 107-113.

Ladhar, S.S. 2005. Ropar wetland. Chandigarh: Punjab State Council for Science and Technology, pp. 1-64.

Mahé, K., D. Ider, A. Massaro, O. Hamed, A. Jurado-Ruzafa, P. Gonçalves, A. Anastasopoulou, A. Jadaud, C. Mytilineou, R. Elleboode, Z. Ramdane, M. Bacha, R. Amara, H. Pontual and B. Ernande. 2019. Directional bilateral asymmetry in otolith morphology may affect fish stock discrimination based on otolith shape analysis. ICES *J. Mar. Sci.*, 76(1): 232–243.

Mapp, J., E. Hunter, J.V.D. Kooij, S. Songer and M. Fisher. 2017. Otolith shape and size: The importance of age when determining indices for fish-stock separation. *Fish. Res*., 190:43-52.

Matondo, D.P., M.A.J. Torres, J.G. Gorospe and C.G. Demayo. 2012. Describing Scale Shapes of the Male and Female *Glossogobius aureus* Akihito and Meguro, 1975 from Tumaga River, Zamboanga City, Philippines. *Egypt. Acad. J. Biol. Sci*., 4(1): 47-58.

Miranda, R. and M. C. Escala. 2002. Identification Guide to Osseous Remains of Cyprinids of Spain. Pamplona: Seviciode publicaciones de la Universidad de Navarra.

Miyan, K., M.A. Khan, D.K. Patel, S. Khan and N.G. Ansari. 2016.Truss morphometry and otolith microchemistry reveal stock discrimination in *Clarias batrachus* (Linnaeus, 1758) inhabiting the Gangetic river system. *Fish. Res.*, 173(3): 294-302

Nazir, A. and M.A. Khan. 2019. Spatial and temporal variation in otolith chemistry and its relationship with water chemistry: stock discrimination of *Sperata aor. Ecol. Freshw. Fish.*, 28:499-511.

Poulet, N., Y. Reyjol, H. Collier and S. Lek. 2005. Does fish scale morphology allow the identification of populations at a local scale? A case study for rostrum dace *Leuciscus leuciscus burdigalensis* in River Viaur (SW France). *Aquat. Sci.*, 67:122-127.

Rawal, Y.K., O. Dhillon and I.S. Sidhu. 2020. Distinction of two featherback species (Osteoglossiformes: Notopteridae) in India based on scale structure. *Rec. Zool. Surv. India.*, 120(3): 241–246.

Rawat, S., S. Benakappa, J. Kumar, K. Naik, G. Pandey and C.W. Pema. 2017. Identification of fish stocks based on Truss Morphometric: A review. *J. Fish. Life Sci.*, 2(1): 9-14.

Roberts, C.D. 1993. Comparative morphology of spined scales and their phylogenetic significance in the Teleostei. *Bull. Mar. Sci.*, 52: 60-113.

Schneider, J.C., P.W. Laarman and H. Gowing. 2000. Length-weight relationships. In: Manual of Fisheries Survey Methods II: with Periodic Updates (Ed. J.C. Schneider). Michigan Department of Natural Resources, Fisheries Special Report 25, Ann Arbor.

Sire, J.Y. 1986. Ontogenic development of surface ornamentation in the scales of *Hemichromis bimaculatus* (Cichlidae). *J. Fish Biol.*, 28: 713-724.

Sire, J.Y., M. Girondot and O. Babiar. 2000. Marking Zebrafish, *Danio rerio* (Cyprinidae), Using Scale Regeneration. *J. Exp. Biol.*, 286: 297-304.

Tanner, S.E., P. Patrick Reis-Santos and H.N. Cabral. 2016. Otolith chemistry in stock delineation: A brief overview, current challenges and future prospects. *Fish. Res.*, 173(3): 206-213.

Yamada, J. 1961. Studies on the structure and growth of the scales in the goldfish. *Memoirs of the Faculty of Fisheries, Hokkaido University,* 9(2): 181-226.

Pb. Univ. Res. J (Sci.) Vol. 70, 2020, pp 115-126

"PERAMPANEL: A PROMISING ANTIEPILEPTIC DRUG ACTING VIA A NOVEL TARGET"

Suruchi Aditya[1*] and Aditya Rattan[2]
[1] *Deptt. of pharmacology,*
Dr Harvansh Singh Judge Institute of Dental Sciences, Panjab University, Chandigarh-160014, India
[2]*Consultant cardiologist, Heartline, SCO 60, Sector 6, Panchkula - 134109, India*

ABSTRACT

Despite advances in the treatment of epilepsy, more than 30% of patients remain uncontrolled on a single antiepileptic drug and need a combination therapy. Drugs with a new mechanism of action offer hope to these refractory cases. Activation of α-amino-3-hydroxy-5-methyl-4-isoxazolepropionic acid (AMPA) receptors by glutamate causes fast-excitatory synaptic transmission in the brain. Perampanel hydrate is a highly selective, non-competitive AMPA-type glutamate receptor antagonist approved by the US Food and Drug Administration (FDA) for monotherapy and an adjunctive treatment of patients aged 4 years and above having partial-onset seizures with or without secondary generalization, and as an adjunctive treatment for primarily generalized tonic-clonic seizures in patients aged 12 years and above. Common side-effects are dizziness and somnolence. However, perampanel may provoke psychiatric and behavioral problems in a dose-related fashion. The use of this novel drug as a once-daily treatment of uncontrolled partial-onset seizures and as an add-on therapy in generalized tonic-clonic seizures is promising.

Keywords: AMPA, focal seizures, perampanel, glutamate

INTRODUCTION

Epilepsy is a disabling chronic neurological disorder associated with a low quality of life, resulting from physical and psychosocial issues (Rassart, 2020). The associated social isolation, dependency, low marriage rates, and unemployment compound the problem by adding to the stigma (Beghi, 2020; Sharma, 2019). The identification of structural, metabolic, genetic, and autoimmune linkages underlying epilepsy have paved the way for precision medicine (Loscher, 2020). Focal epilepsies of unknown etiology represent the most common subtype in newly diagnosed patients (Beghi, 2020).

There are more than 12 million persons with epilepsy (PWE) in India, contributing to one-sixth of the global burden (Amudhan, 2015). The prevalence of epilepsy is estimated to be 3.0-11.9 per 1000 while incidence is 0.2-0.6 per 1,000 population per year in India (Amudhan, 2015). Cardiorespiratory alterations may lead to sudden unexpected death in epilepsy (SUDEP), which has an incidence of 1.2 per 1000 person-years (Panelli, 2020). However, improved access to treatments and the development of new antiepileptic drugs (AEDs) offers hope to PWE (Beghi, 2020). With judicious use of drugs, around 68% of patients attain prolonged seizure remission (Beghi, 2020). About one-third of PWE fail to respond to first-line treatments, paving the way for combination therapy. However, a combination of AEDs acting via a similar mechanism increases the chance of neurotoxicity (Trinka,2016). The addition of drugs with novel mechanism offers a good option for rational combination therapy for control of seizures with minimal toxicity. The selection of an AED is challenging for the physician. It has been observed that the efficacy of the newer drugs, as measured by seizure control, is not much different from the older agents. However, the newer AEDs such as gabapentin, lamotrigine, and levetiracetam are better tolerated than older agents such as phenytoin and phenobarbital (Wahab, 2010).

Drugs used to treat epilepsy work by decreasing the electrical activity of the brain, either by preventing neuronal depolarization by blocking sodium or calcium channels, enhancing potassium channel function, inhibiting glutamate-mediated excitation, or promoting gamma amino butyric acid (GABA)-mediated inhibition (Stafstrom, 2015).

Ionotropic glutamate α-amino-3-hydroxy-5-methyl-4-isoxazolepropionic acid (AMPA) receptors are critical to the generation, spread, and synchronization of epileptic discharges (Rogawski,

---

* Corresponding author e-mail: suruchiaditya@rediffmail.com
MS Received: August 03, 2020, Accepted: December 24, 2020

2013). Perampanel, a third-generation AED, was designed specifically as an antagonist to the AMPA receptors and is the only Food and Drug Administration (FDA) approved drug acting primarily via these receptors. It is indicated for monotherapy and as an adjunctive treatment of patients aged 4 years and above having partial-onset seizures with or without secondary generalization, and as an adjunctive treatment for primarily generalized tonic-clonic seizures in patients aged 12 years and above.

Multifaceted actions of perampanel have led researchers to explore its use in various other neurological disorders (Suda, 2019). The ease of once-daily oral administration and the novel approach of targeting excitatory ionotropic glutamate AMPA receptor makes it a promising drug in epilepsy. It has a favorable safety profile though caution is advised in patients with a history of anger or aggressive behavior. This review discusses the mechanism of action and clinical studies of perampanel, a first-in-class AED.

CURRENT TREATMENT OF EPILEPSY

Unmanaged chronic epilepsy results in increased mortality, physical injury as well as significant comorbidities (Ko, 2013). The goal of pharmacotherapy is to make the patient seizure-free without side effects. Factors affecting the choice of an AED are type of seizure, presence of an epilepsy syndrome, use of other drugs, comorbidities, lifestyle, and patient preference.

First-line AEDs for primarily generalized tonic-clonic seizures (PGTCS) are valproic acid, topiramate, or lamotrigine. Phenobarbital, phenytoin, carbamazepine, oxcarbazepine, levetiracetam, and felbamate are alternative drugs (Liu, 2017; Jameson, 2018; Ko, 2020).

In focal-onset seizures, monotherapy with carbamazepine, phenytoin, lamotrigine, oxcarbazepine, and levetiracetam is approved. Alternative therapy with tiagabine, topiramate, gabapentin, phenobarbital, lacosamide, or valproic acid is considered if the first or second trial with first-line drugs fails (Liu, 2017; Jameson, 2018; Ko, 2020).

An imbalance in excitatory (glutamatergic) and inhibitory (GABAergic) neurotransmission underlies the pathophysiology of epilepsy (Yuan, 2019). Few drugs target the glutamatergic neurotransmission (Table1). First-generation drugs like phenytoin and carbamazepine are associated with vestibulocerebellar symptoms, skin rash, and hepatotoxicity. Many AEDs cause deleterious effects on cognition. Thus, the currently available AEDs are not completely safe (Table 2).

Table 1. Mechanism of action of antiepileptic drugs (Loscher, 2020; Stafstrom, 2015).

Antiepileptic drug	**Mechanism of action**
Benzodiazepines	$GABA_A$ receptor inhibition
Carbamazepine	Inhibit voltage-gated sodium channels
Ethosuximide	Inhibit voltage-gated calcium (T-type) channels
Gabapentin	α2δ calcium channel subunit-decrease glutamate
Lacosamide	Enhances slow inactivation of voltage-gated sodium channels
Lamotrigine	Inhibit voltage-gated sodium channels
Levetiracetam	Inhibit presynaptic release of neurotransmitters by binding to SV2A
Perampanel	Negative allosteric modulator of AMPA receptors
Phenobarbital	$GABA_A$ receptor inhibition
Phenytoin	Inhibit voltage-gated sodium channels
Pregabalin	Inhibit α2δ subunit of voltage-dependent calcium channels
Tiagabine	Inhibit GAT-1 GABA transporter
Topiramate	Inhibit voltage-gated sodium channels
Valproic acid	Mixed-Inhibit voltage-gated sodium and calcium channels/ increase GABA levels/partly unknown
Zonisamide	Inhibit voltage-gated sodium channels

Table 2. Adverse drug reactions of commonly used anti-epileptic drugs (Wahab, 2010; Jameson, 2018; Kim, 2020).

Antiepileptic drug	**Adverse effects**	**Contraindications and life-threatening adverse effects**
Benzodiazepines (Clobazam, Clonazepam, others)	Sedation, lethargy, drowsiness, dizziness.	-
Carbamazepine	Ataxia, dizziness, diplopia, hyponatremia, vertigo, aplastic anemia, agranulocytosis, hepatotoxicity	Stevens-Johnson syndrome, bone marrow suppression, atrio-ventricular blocks, use of monoamine oxidase inhibitors
Ethosuximide	Ataxia, lethargy, headache, rash, bone marrow suppression	Stevens-Johnson syndrome, pancytopenia,
Gabapentin	Sedation, dizziness, ataxia, weight gain	Pancreatitis, absence seizures
Lacosamide	Dizziness, ataxia, diplopia, somnolence, cardiac arrhythmias	-
Lamotrigine	Dizziness, diplopia, sedation, ataxia, rash	Stevens-Johnson syndrome
Levetiracetam	Sedation, incoordination, mood changes	Suicidal tendency, pancytopenia, Stevens-Johnson syndrome,
Perampanel	Drowsiness, dizziness, ataxia, somnolence, increased weight	Severe hepatic failure, moderate to severe renal failure suicide ideation
Phenobarbital	Sedation, lethargy, ataxia, dizziness, decreased libido, mood disorder, hepatotoxicity, rash, osteomalacia	Stevens-Johnson syndrome
Phenytoin	Ataxia, diplopia, dizziness, gingival hyperplasia, hirsutism, osteomalacia, rash, facial coarsening	Stevens-Johnson syndrome, bone marrow suppression, coronary ischemia, atrioventricular blocks
Pregabalin	Somnolence, dizziness, ataxia, weight gain, Peripheral edema	Renal failure, congestive heart failure
Tiagabine	Dizziness, fatigue, tremor, emotional lability	Acute porphyria, abrupt stoppage
Topiramate	Sedation, psychomotor slowing, paresthesia, word finding difficulty, kidney stones, glaucoma	Glaucoma, hyperammonemia, hypohidrosis, urolithiasis
Valproic acid	Ataxia, sedation, tremor, weight gain, alopecia, thrombocytopenia, hepatotoxicity, hyperammonemia	Hepatic/pancreatic dysfunction, porphyria, urea cycle
Zonisamide	Sedation, dizziness, headache, renal stones, hypohidrosis	Stevens-Johnson syndrome, urolithiasis, hypohidrosis

Almost one-third of patients show resistance to the prescribed treatment and need alternative pharmacological options (Loscher, 2020). According to the International League Against Epilepsy (ILAE), drug-resistant epilepsy (DRE), also known as medically intractable epilepsy is defined as “a failure of trials of two tolerated and appropriately chosen drugs (as monotherapies or in combination)”. Topiramate and levetiracetam have shown good long-term efficacy for such patients (Zhuo, 2017).

Thus, resistance to medication, adverse effects of available drugs, inability to undergo surgical treatment has driven the need to develop new AEDs with different mechanism of action and fewer adverse effects.

THE ROLE OF AMPA RECEPTORS IN PATHOPHYSIOLOGY OF EPILEPSY

According to the ILAE, seizures are divided into three categories: focal (earlier called partial), generalized and epileptic spasms. Focal epilepsy can appear as- focal aware seizures (simple partial), focal impaired awareness seizures (complex partial or dyscognitive), and focal to bilateral tonic-clonic (partial-onset with secondary generalization) (Sharma, 2019). The main subtypes of generalized seizures are absence, generalized tonic-clonic seizures (GTCS), myoclonic, and atonic. The clinical symptoms depend on the area of cortex involved; arising from the occipital lobe, a focal seizure may present with visual phenomena; rhythmic clonic or tonic movements from the precentral gyrus and sensory symptoms, if arising from the postcentral gyrus (Stafstrom, 2015; Liu, 2017; Ko, 2020).

The underlying causes of focal seizures include structural lesions such as traumatic scars (exemplified by mesial temporal sclerosis), strokes, neoplasms, vascular malformations, and neuronal heterotopias (Cendes, 2016).

Glutamate, the most important excitatory neurotransmitter in the brain, binds a series of ionotropic postsynaptic receptors known as AMPA- the most abundant, kainate, and N-methyl-D-aspartate (NMDA). It has been documented that levels of glutamate rise during the ictal phase. Additionally, glutamate receptor agonists as well as AMPA, NMDA and kainate can induce seizures in rodent models- implicating a major role of glutamate in seizure genesis (Hanada, 2020).

Being responsible for fast excitatory signaling, AMPA receptors are a critical component of all neuronal networks (Rektor, 2013; Rogawski, 2011). AMPA receptors are heterotetramers comprising of four subunits- GluA1, GluA2, GluA3, and GluA4, which assemble to form an ion channel. The GluA2 protein subunit is the main determinant of calcium permeability (Leo, 2018). The two subtypes of AMPA receptors are calcium-permeable (lacking GluA2 subunit or containing it in unedited form) and calcium-impermeable AMPA receptors. The latter are mainly expressed in excitatory projection neurons while the former subtypes are expressed in inhibitory interneurons (Hanada, 2020). The electrophysiological properties and ion permeability is determined by alternative splicing (flip/flop) and RNA editing (at R/G and Q/R sites of GluA2) (Wen, 2017).

The hippocampal and neocortical tissues from epileptic patients show hypersensitivity, upregulation, and increased density of AMPA receptors (Lattanzi, 2019). AMPA mediated neurotransmission during status epilepticus (SE) is associated with increased surface expression of GluA1 and decreased expression of GluA2 subunit (Leo, 2018). Mutation of the enzyme (thorase- also called AAA+ATPase, coded by *ADAD1*) that regulates the surface expression of AMPA receptors is associated with seizures, and perampanel was found to improve the seizure-related symptoms and slow neurodegeneration in both animal models and human cases (Ahrens-Nicklas, 2017). Impairments of AMPA receptor subunit composition, function, or desensitization kinetics result in overactivation of cascading pathways further leading to GABA receptor inhibition, promoting hyperexcitation (Lattanzi, 2019).

AMPA receptors open after glutamate binds to them and allow cations, mainly sodium, to enter causing a brief depolarization of the postsynaptic membrane. Summation of excitatory postsynaptic potentials (EPSPs) leads to the firing of action potentials by the postsynaptic neuron, completing the transmission of the synaptic signal (Rheims, 2013). The effectiveness of the AMPA antagonists validates the role of glutamate receptors in epileptogenesis. Attempts to produce AEDs that act on NMDA receptors have been disappointing as they play a crucial role in memory and learning. Unlike NMDA antagonists, AMPA receptor antagonists have a broader spectrum of anticonvulsant action as they are effective against kindled seizures also.

MECHANISM OF ACTION

Perampanel [2-(2-oxo-1-phenyl-5-pyridin-2-ylpyridin-3-yl) benzonitrile; trihydrate], is a non-competitive antagonist of the AMPA glutamate receptor (Figure 1). Its predecessor, talampanel has been discontinued due to tolerability and pharmacokinetic issues.

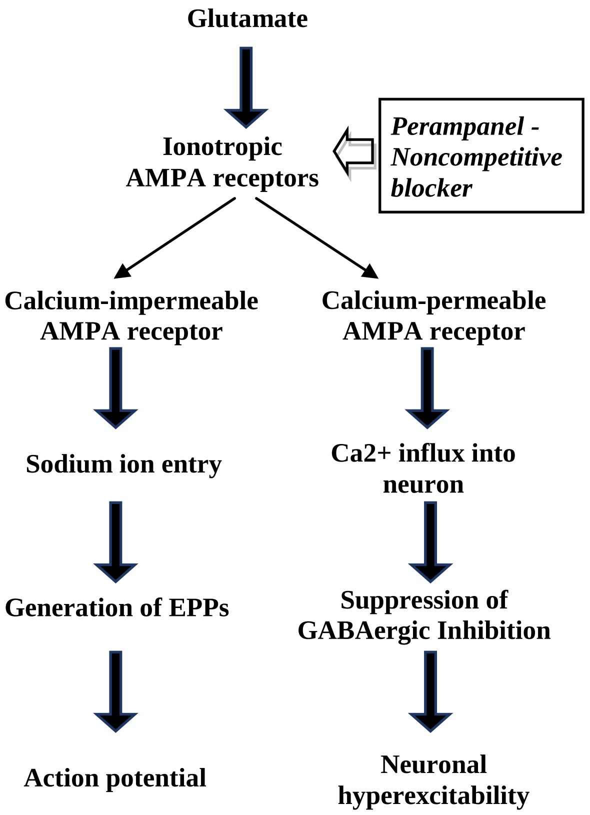

Fig.1. Mechanism of action of perampanel (Hanada, 2020; Charsouei, 2020). By blocking the AMPA receptors, perampanel inhibits the ion influx and subsequent enhanced excitatory neurotransmission seen in epilepsy.

AMPA-α-amino-3-hydroxy-5-methyl-4-isoxazole-propionic acid; **EPSP**-Excitatory postsynaptic potential; **GABA**- Gamma amino butyric acid.

A single AMPA receptor channel exposed to 5 mM L-glutamate can open to four conductance levels (designated O1−O4) of around 10, 23, 33, and 47 pS. The highest conductance level (O4) occurs when glutamate is bound to all four subunits and all of them are in the open conformation. The lowest conductance level (O1) arises from the gating of a single subunit. Each of the four subunits in the receptor contributes an extracellular amino-terminal domain (ATD), an intracellular C-terminal domain, a ligand-binding domain (LBD), and a transmembrane/ion channel domain (TMD). The receptor shows four binding sites- one per AMPA receptor subunit (Yuan, 2018). Three structural elements: pre-M1 and extracellular portions of M3 and M4, form each one of the four equivalent noncompetitive inhibitor binding sites located at the interface between the ion channel and TMD-LBD linkers (Yelshanskaya, 2016). Perampanel binds between pre-M1 and the extracellular portions of M1 and M4, with a possible contact to M3 of an adjacent subunit immobilizing the transmembrane segments relative to each other - stabilizing the closed state of AMPA receptor and preventing the pore opening. The open channel has at least one binding site. Perampanel shifts the distribution of open channels to lower conductances, leading to a more graded response. This response may have beneficial consequence in that it allows channel activity with lower amplitude, letting the affected neurons to function normally despite dealing with an epileptic challenge (Yuan, 2018).

The paroxysmal depolarization shift- abnormal discharges or spikes of action potentials that last few minutes, is said to be mediated by AMPA- mediated synaptic currents (Kubista, 2019). AMPA antagonists inhibit the early phase of paroxysmal depolarization shift, suppressing synchronized activity (Hanada, 2020). Perampanel works as an antiepileptic drug, partly by disrupting these co-ordinated network burst oscillations tuned by dynamic glutamatergic and GABAergic transmission (Yang, 2020).

Animal studies: Perampanel, is active in the mouse maximal electroshock (MES) test, the mouse audiogenic seizure model, pentylenetetrazol (PTZ)-induced clonic seizures, and the psychomotor seizure test (Rogawski, 2013). AMPA antagonists evaluated in experimental models of SE (kainate, pilocarpine, amygdala electrical stimulation) show a dose-dependent effect in stopping seizures (Leo, 2018). Perampanel was able to abort seizures in rodents with severe pilocarpine-induced SE that was resistant to diazepam (Hanada, 2014). Moreover, co-administration of perampanel with diazepam and zonisamide led to synergistic effects, implying that the combined use of low doses of these drugs may help to reduce the side effects (Hanada, 2014; Russman, 2016; Mohammad, 2019). In genetically epilepsy-prone rats, perampanel decreased the development of tolerance to clobazam (Citraro, 2018). Thus, targeting AMPA transmission is a promising strategy to overcome refractoriness and time-dependent drug resistance to GABAergic drugs (Lattanzi, 2019).

PHARMACOKINETICS

Oral perampanel is nearly 100% bioavailable. Food may delay its absorption. Peak plasma levels occur between 15 min and 2 h. It is highly plasma protein bound (95%) and metabolized by CYP3A4. About one-third of the oral dose is excreted in the urine. The elimination half-life of perampanel is long (105 hours) and allows for once-daily dosing (Heyman, 2017). In mild and moderate hepatic impairment, the dose should not exceed 6 mg and 4 mg once daily at bedtime, respectively. Perampanel is contraindicated in pregnancy, severe hepatic, or renal impairment. Its excretion in milk has not been studied. It decreased clearance of oxcarbazepine by 26%. At 12mg/day dose, it decreased effectiveness of progestin containing contraceptive (Patsalos, 2015).

Dosage and Administration:

Supplied as 2-mg to 12-mg tablets, the initial dose of perampanel is 2 mg once daily at bedtime or 4 mg in patients taking enzyme-inducing drugs. The dosage can be up-titrated every 2 weeks. An oral suspension formulation for patients having difficulty in swallowing tablets is available.

CLINICAL EXPERIENCE WITH PERAMPANEL

Perampanel has been evaluated in focal seizures via three major clinical trials (Studies 304, 305, and 306), all of which were part of the Examining Perampanel Observations from Research Experience (EXPLORE) program (Kerling, 2013). These three studies were double-blind, placebo-controlled, dose-escalation, parallel-group studies to evaluate the efficacy and safety of E2007 (perampanel) given as adjunctive therapy in subjects with refractory partial seizures.

In study 304, the median percent change in seizure frequency was -21.0%, -26.3%, and -34.5% for placebo and perampanel 8 and 12 mg, respectively (statistically significant decrease for both doses). Fifty percent responder rates were 26.4%, 37.6%, and 36.1%, for these three groups (French, 2012).

Study 305 also evaluated placebo with 8 mg or 12 mg perampanel once daily for 19 weeks (6 weeks titration and 13 weeks maintenance therapy), in addition to their regular therapy. The median percent change from baseline in seizure frequency per 28 days was −9.7% (placebo), −30.5% (8mg), and −17.6% (12mg) with significant reductions compared with placebo for both doses. For complex partial seizures and secondarily generalized partial seizures, the change in seizure frequency was −8.1% (placebo), −32.7% (8 mg; $p < 0.001$), −21.9 (12 mg; $p < 0.001$). Dizziness, somnolence, fatigue, and headache were observed (French, 2013).

In study 306, 706 patients with persistent partial-onset seizures despite treatment with up to three AEDs were randomized to receive adjunctive placebo or perampanel at 2, 4, or 8 mg/day for 13 weeks. The median change in seizure frequency from baseline in the four arms was -10.7%, -13.6%, -23.3%, and -30.8%, respectively, which was found to be significant for 4 and 8 mg doses. The most frequent side effect was dizziness. This study defined the minimum effective perampanel dose as 4 mg/day (Krauss, 2012).

In an interim analysis of study 307, an extension study for patients completing the double-blind phase of studies 304, 305, and 306, the frequency of all seizures decreased over the first 26 weeks of perampanel treatment (n = 1,006 [83.3%]); and was maintained for at least 1 year (n = 588 [48.7%]). The overall median percent change in seizure frequency was -58.1% for weeks 92-104 (Krauss, 2013). Adjunctive treatment with perampanel for up to 4 years (open-label extension study 307) was safe and showed a sustained improvement in seizure control, especially in secondarily generalized seizures (Krauss, 2018). A good tolerability profile was observed in refractory partial-onset seizures for up to 4 years in study 207 (Rektor, 2012).

Seizure frequency decreases of 50%, 75%, and 100% were observed in 80.0%, 71.8%, and 47.1% patients respectively in an open-label trial in focal-onset seizures with a 3-month titration and 6-month maintenance period. The decrease in seizure frequency was higher in the subset of secondarily GTCS (87.5%, 87.5%, and 75.0% of patients). Adverse effects observed were dizziness (50.0%), somnolence (9.8%), and headache (8.8%) (Kim, 2020).

In a study in Spain, an early add-on of perampanel in focal seizures was evaluated. At 12 months, 68.1% and 26.5% of the patients were responders and seizure-free (respectively), relative to baseline (Abril

Jaramillo, 2019). A clinical study to evaluate its safety and efficacy in Indian subjects is underway (NCT03836924).

Patients aged ≥12 years with drug-resistant PGTCS and idiopathic generalized epilepsy (IGE) were randomized to receive placebo or perampanel during a 4-week titration period and 13-week maintenance period. Perampanel led to a greater median percent change in PGTCS frequency per 28 days (-38.4%vs -76.5%; p< 0.0001) and greater 50% PGTCS responder rate (39.5% vs 64.2%; p = 0.0019) compared with placebo. During maintenance, 30.9% of the perampanel group achieved PGTCS freedom compared to placebo (12.3%). Dizziness (32.1%) and fatigue (14.8%) were observed (Study 332) [French, 2015].

In the IGE study by Villanueva (2018) et al, at 12 months, the seizure-free rate was 59% for all seizures; 63% for GTCS, 65% for myoclonic seizures, and 51% for absence seizures. Perampanel was more effective in the early add-on setting (72% seizure-free) than after the use of ≥3 AEDs (52% seizure-free). In this study, the GTC seizure-free rate (63%) was higher than reported in the study of adjunctive perampanel in refractory IGE (31%), which recruited patients with more refractory and frequent GTCS (French, 2015).

In SE, refractory SE (RSE), or super-refractory SE (SRSE) patients, who had failed benzodiazepines and a median of five other AEDs, the addition of perampanel as the last drug in 61.5% patients led to seizure cessation rate of 36.5% - a noteworthy response (Strzelczyk, 2019). In study 232, an oral suspension formulation was shown to be well-tolerated and efficacious in epileptic children aged ≥2 to <12 years (Renfroe, 2019). In the PERADET study, the addition of perampanel led to high responder rates in brain tumor-related epilepsy (Coppola, 2020).

Perampanel as the first add-on drug resulted in seizure freedom in 17 out of 18 patients in glioma patients with levetiracetam-uncontrollable epilepsy (Izumoto, 2018; Chonan, 2020). It has also shown a good response in Dravet syndrome (Chang, 2019), myoclonus (Iijima, 2019), and Lennox-Gastaut syndrome (Crespel, 2019). Perampanel has shown effectiveness in progressive myoclonic epilepsies- a group of rare types of epilepsy, mostly identified as intracellular substance storage disorders, such as Unverricht–Lundborg disease, Lafora disease, dentatorubral-pallidoluysian atrophy (DRPLA), MELAS (mitochondrial encephalomyopathy, lactic acidosis, and stroke-like episodes) and ceroid lipofuscinosis (Oi, 2019, Santamarina, 2019).

Perampanel exerts a neuroprotective effect against brain injury in experimental models, such as cerebral ischemia, traumatic brain injury (TBI), and intraventricular hemorrhage (Suda, 2019). Inhibition of microglial activation, pro-inflammatory cytokines, and oxidative stress-related molecules, as well as downregulation of Bcl-2 associated X protein and upregulation of Bcl-extra-large are involved in its neuroprotective potential (Nakajima, 2018).
However, when evaluated for Parkinson’s patients experiencing motor fluctuations, adjunctive perampanel did not improve the motor state (Lattanzi, 2018).

ADVERSE EFFECTS

The most common side effects of perampanel are dizziness, drowsiness, irritability, nausea, falls, and ataxia, which may limit its use in drivers and machine operators (Serratosa, 2013; Trinka, 2016).

The drug's label includes a boxed warning about the risk for serious neuropsychiatric events, including irritability, aggression, anger, anxiety, paranoia, euphoric mood, agitation, mental status changes, and suicidal or homicidal ideation (Renfroe, 2019). The concomitant use of alcohol should be avoided as mood changes may be worsened.

The frequency of psychiatric adverse events observed in collective studies was 17.2% and 22.4 % in children treated with 8mg/day and 12mg/day perampanel respectively (Heyman, 2017). These included nervousness, restlessness, behavioral deterioration, violence, insomnia, and psychosis. Perampanel did not affect the Cognitive Drug Research (CDR) system global cognition score, continuity of attention, quality of episodic and working memory, or speed of memory but was associated with a significant decline in power of attention at the end of treatment compared with baseline (p=0.03) (Pina-Garza, 2018). The once-daily night-time dosing, simple titration schedule, and long half-life offers ease of use and can improve adherence in the adolescent group (Kim, 2016).

Other less frequent adverse events reported are excessive sputum production, drooling, dysphagia, nausea, increase in triglycerides, memory impairment, and bizarre feeling (Youn, 2018). A weight gain of more than 7% was seen (11.6%-19.2% patients) compared to placebo (4.4%-8.3% patients) (Schulze-Bonhage, 2015). Researchers advocate that weight gain is consistent with that expected for the adolescent population (Kim, 2016). It has been approved by CDSCO and is available in India at a nominal price -2 mg, 4 mg, and 6 mg with per day cost to patients being Rs 35, Rs 55, and Rs70 for each strength.

CONCLUSION

Perampanel is a highly selective, non-competitive AMPA-type glutamate receptor antagonist approved by the FDA for the therapy of focal seizures for patients ≥4 years old, with or without secondary generalization, and as an adjunctive therapy in PGTCS for patients aged ≥12 years. Potential candidates for its use include those unresponsive to the new antiseizure drugs, such as levetiracetam, lamotrigine, and topiramate. The most common adverse effects are dizziness and somnolence. Although it is well-tolerated, the risk of serious neuropsychiatric side effects such as aggression and irritability is a drawback. A good efficacy, once-daily administration and a novel mechanism of action make this drug a welcome addition to the armamentarium of AEDs.

REFERENCES

Abril Jaramillo J, Estévez María JC, Girón Úbeda JM, Vega López Ó, Calzado Rivas ME, Pérez Díaz H, et al. 2019. Effectiveness and safety of perampanel as early add-on treatment in patients with epilepsy and focal seizures in the routine clinical practice: Spain prospective study (PERADON). Epilepsy Behav.,102:106655.

Ahrens-Nicklas RC, Umanah GK, Sondheimer N, Deardor M A, Wilkens AB, Conlin LK, et al. 2017. Precision therapy for a new disorder of AMPA receptor recycling due to mutations in ATAD1. Neurol Genet.,3: e130.

Amudhan S, G Gururaj, P Satishchandra. 2015. Epilepsy in India I: Epidemiology and public health. Ann Indian Acad Neurol., 18:263–77.

Beghi E.2020. The epidemiology of epilepsy. Neuroepidemiology., 54:185-91.

Cendes F, WH Theodore, BH Brinkmann, V Sulc, GD Cascino. 2016. Neuroimaging of epilepsy. Handb Clin Neurol.,136:985-1014.

Chang FM, PC Fan, WC Weng, CH Chang. 2019. The efficacy of perampanel in young children with drug-resistant epilepsy. Seizure.,75:82-6.

Charsouei S, MR Jabalameli and Karimi-Moghadam A. 2020. Molecular insights into the role of AMPA receptors in the synaptic plasticity, pathogenesis and treatment of epilepsy: therapeutic potentials of perampanel and antisense oligonucleotide (ASO) technology. Acta Neurol Belg., 120:531-44.

Chonan M, R Saito, M Kanamori, S-I Osawa, M Watanabe, H Suzuki, et al. 2020. Experience of low dose perampanel to add-on in glioma patients with levetiracetam-uncontrollable epilepsy. Neurol Med Chir (Tokyo)., 60:37-44.

Citraro R, C De Sarro, A Leo, E Donato di Paola, E Palma, E Russo, et al. 2018. Perampanel chronic treatment does not induce tolerance and decreases tolerance to clobazam in genetically epilepsy prone rats. Epilepsy Res. ,146: 94-102.

Coppola A, A Zarabla, A Maialetti, V Villani, T Koudriavtseva, E Russo, et al. 2020. Perampanel confirms to be effective and well-tolerated as an add-on treatment in patients with brain tumor-related epilepsy (PERADET Study). Front Neurol.,11:592.

Crespel A, NPL Tang, G Macorig, P Gelisse, P Genton. 2019. Open-label, uncontrolled retrospective study of perampanel in adults with Lennox-Gastaut syndrome. Seizure., 75:66-9.

French JA, GL Krauss, V Biton, D Squillacote, H Yang, A Laurenza, et al. 2012. Adjunctive perampanel for refractory partial-onset seizures: randomized phase III study 304.Neurology., 79:589-96.

French JA, GL Krauss, BJ Steinhoff, D Squillacote, H Yang, D Kumar et al. 2013. Evaluation of adjunctive perampanel in patients with refractory partial-onset seizures: results of randomized global phase III study 305. Epilepsia., 54: 117-25.

French JA, GL Krauss, RT Wechsler, XF Wang, B DiVentura, C Brandt, et al. 2015. Perampanel for tonic-clonic seizures in idiopathic generalized epilepsy: A randomized trial. Neurology., 85:950-7.

Hanada T, K Ido, T Kosasa. 2014. Effect of perampanel, a novel AMPA antagonist, on benzodiazepine-resistant status epilepticus in a lithium-pilocarpine rat model. Pharmacol Res Perspect., 2: e00063.

Hanada T. 2020. Ionotropic glutamate receptors in epilepsy: A review focusing on AMPA and NMDA receptors. Biomolecules.,10:464.

Heyman E, E Lahat, N Levin, O Epstein, M Azinger, M Berkovitch, et al. 2017.Tolerability and efficacy of perampanel in children with refractory epilepsy. Dev Med Child Neurol.,59:441-4.

Iijima M, H Oguni, M Kobayashi, K Kitagawa. 2019. Perampanel improved intractable myoclonus in two patients with myoclonus epilepsy. eNeurologicalSci., 17:100215.

Izumoto S, M Miyauchi, T Tasaki, T Okuda, N Nakagawa, N Nakano, et al. 2018. Seizures and tumor progression in glioma patients with uncontrollable epilepsy treated with perampanel. Anticancer Res., 38:4361–6.

Jameson J, AS Fauci, DL Kasper, SL Hauser, DL Longo, J Loscalzo. eds. 2018. Harrison's Principles of Internal Medicine, 20e. New York, NY: McGraw-Hill., vol 2;3062-3.

Kerling F, BS Kasper. 2013. Efficacy of perampanel: a review of clinical trial data. Acta Neurol Scand., 127(s197):25-9.

Kim HD, CS Chi, T Desudchit, M Nikanorova, A Visudtibhan, C Nabangchang, et al. 2016. Review of clinical studies of perampanel in adolescent patients. Brain and Behavior., 6: e00505.

Kim JH, DW Kim, SK Lee, DW Seo, JW Lee, HJ Park, et al. 2020. First add-on perampanel for focal-onset seizures: An open-label, prospective study. Acta Neurol Scand., 141:132–40.

Kim KT, DW Kim, KI Yang, ST Lee, JI Byun, JG Seo, et al, on behalf of the Drug Committee of Korean Epilepsy Society. 2020. Refining general principles of antiepileptic drug treatments for epilepsy. J Clin Neurol., 16:383-9.

Ko D, Ramsay RE. 2013. Perampanel: expanding therapeutic options for patients with medically refractory secondary generalized convulsive seizures. Acta Neurol Scand., 127(s197):36-43.

Ko DY. Epilepsy and seizures treatment & management. Updated on Aug 6,2020 Available from https://emedicine.medscape.com/article/1184846-treatment#d11.Last cited on Aug 12 2020.

Krauss GL, JM Serratosa, V Villanueva, M Endziniene, Z Hong, J French, et al. 2012. Randomized phase III study 306: adjunctive perampanel for refractory partial-onset seizures. Neurology., 78:1408-15.

Krauss GL, E Perucca, E Ben-Menachem, P Kwan, JJ Shih, D Squillacote, et al. 2013. Perampanel, a selective, noncompetitive α-amino-3-hydroxy-5-methyl-4-isoxazolepropionic acid receptor antagonist, as adjunctive therapy for refractory partial-onset seizures: interim results from phase III, extension study 307.Epilepsia .,54:126-34.

Krauss GL, E Perucca, P Kwan, Ben- E Menachem, X-F Wang, JJ Shih, et al. 2018. Final safety, tolerability, and seizure outcomes in patients with focal epilepsy treated with adjunctive perampanel for up to 4 years in an open-label extension of phase III randomized trials: Study 307. Epilepsia., 59:866-76.

Kubista H, S Boehm, M Hotka. 2019. The paroxysmal depolarization shift: reconsidering its role in epilepsy, epileptogenesis and beyond. Int J Mol Sci.,20:577.

Lattanzi S, E Grillo, F Brigo, M Silvestrini. 2018. Efficacy and safety of perampanel in Parkinson's disease. A systematic review with meta-analysis. J Neurol.,265: 733–40.

Lattanzi S, P Striano. 2019. The impact of perampanel and targeting AMPA transmission on anti-seizure drug discovery. Expert Opin Drug Discov.,14:195-7.

Leo A, G Giovannini, E Russo, S Meletti. 2018. The role of AMPA receptors and their antagonists in status epilepticus.Epilepsia.,59:1098-108.

Liu G, N Slater, A Perkins. 2017. Epilepsy: Treatment options. Am Fam Physician., 96:87-96.

Löscher W, H Potschka, SM Sisodiya, A Vezzani. 2020. Drug Resistance in Epilepsy: Clinical Impact, Potential Mechanisms, and New Innovative Treatment Options. Pharmacol Rev.,72:606-38.

Mohammad H, S Sekar, Z Wei, F Moien-Afshari, C Taghibiglou. 2019. Perampanel but not amantadine prevents behavioral alterations and epileptogenesis in pilocarpine rat model of status epilepticus. Mol Neurobiol., 56: 2508–23.

Nakajima M, S Suda, K Sowa, Y Sakamoto, C Nito, Y Nishiyama, et al. 2018. AMPA receptor antagonist perampanel ameliorates post-stroke functional and cognitive impairments. Neuroscience., 386:256–64.

Oi. K., S Neshige, T Hitomi, K Kobayashi, M Tojima, M Matsuhashi, et al. 2019.Low-dose perampanel improves refractory cortical myoclonus by the dispersed and suppressed paroxysmal depolarization shifts in the sensorimotor cortex. Clin Neurophysiol., 130:1804–12.

Panelli, RJ. 2020. SUDEP: A global perspective. Epilepsy Behav., Feb; 103(Pt B):106417.

Patsalos, P N. 2015. The clinical pharmacology profile of the new antiepileptic drug perampanel: A novel noncompetitive AMPA receptor antagonist. Epilepsia.,56:12-27.

Piña-Garza JE, L Lagae, V Villanueva, JB Renfroe, A Laurenza, B Williams, et al. 2018. Long-term effects of adjunctive perampanel on cognition in adolescents with partial seizures. Epilepsy Behav.,83:50-8.

Rassart J, K Luyckk, L Verdyck, T Mijnster, Mark RE. 2020. Personality functioning in adults with refractory epilepsy and community adults: Implications for health-related quality of life. Epilepsy Res., 159:106251.

Rektor I, GL Krauss, M Bar, V Biton, JA Klapper, N Vaiciene-Magistris, et al. 2012.Perampanel Study 207: long-term open-label evaluation in patients with epilepsy., Acta Neurol Scand.,126:263-9.

Rektor I. 2013. Perampanel, a novel, non-competitive, selective AMPA receptor antagonist as adjunctive therapy for treatment-resistant partial-onset seizures. Expert Opin Pharmacother ., 14: 225-35.

Renfroe, J. B., M Mintz, R Davis, J Ferreira, S Dispoto, J Ferry, et al. 2019. Adjunctive perampanel oral suspension in pediatric patients from 2 to <12Years of age with epilepsy: Pharmacokinetics, safety, tolerability, and efficacy. J Child Neurol., 34: 284-94.

Rheims S, P Ryvlin. 2013. Profile of perampanel and its potential in the treatment of partial onset seizures. Neuropsychiatr Dis Treat., 9: 629–37.

Rogawski MA. 2011. Revisiting AMPA receptors as an antiepileptic drug target. Epilepsy Curr.,11: 56–63.

Rogawski MA and T Hanada. 2013. Preclinical pharmacology of perampanel, a selective non-competitive AMPA receptor antagonist. Acta Neurol Scand., 127(s197):19-24.

Russman V, JD Salvamoser, ML Rettenbeck, T Komori, H Potschka, et al. 2016.Synergism of perampanel and zonisamide in the rat amygdala kindling model of temporal lobe epilepsy. Epilepsia.,57:638-47.

Santamarina E, A Alpuente, O Maisterra, M Sueiras, S Sarria, L Guzman, et al. 2019.Perampanel: A therapeutic alternative in refractory status epilepticus associated with MELAS syndrome. Epilepsy Behav Case Rep., 11:92-5.

Schulze-Bonhage A, and M Hintz. 2015. Perampanel in the management of partial-onset seizures: a review of safety, efficacy, and patient acceptability. Patient Prefer Adherence., 9:1143–51.

Serratosa JM, V Villanueva, F Kerling, and BS Kasper. 2013. Safety and tolerability of perampanel: a review of clinical trial data. Acta Neurol Scand., 127(s197):30-5.

Sharma P, A Hussain, and R Greenwood. 2019. Precision in pediatric epilepsy. F1000Res., 8: F1000 Faculty Rev-163.

Stafstrom CE, and L Carmant. 2015. Seizures and epilepsy: an overview for neuroscientists. Cold Spring Harb Perspect Med.,5: a022426.

Strzelczyk A, S Knake, R, Kälviäinen E Santamarina, M Toledo, S Willig, et al. 2019. Perampanel for treatment of status epilepticus in Austria, Finland, Germany, and Spain. Acta Neurol Scand., 139:369–76.

Suda S, and K Kimura. 2019. Therapeutic potential of AMPA receptor antagonist perampanel against cerebral ischemia: beyond epileptic disorder. Neural Regen Res.,14:1525-6.

Trinka E, Steinhoff BJ, Nikanorova M, Brodie MJ. 2016.Perampanel for focal epilepsy: insights from early clinical experience. Acta Neurol Scand.,133: 160–72.

Villanueva V, J Montoya, A Castillo, JA Mauri-Llerda, P Pau Giner, FJ López-González, et al. 2018. Perampanel in routine clinical use in idiopathic generalized epilepsy: The 12-month GENERAL study. Epilepsia., 59:1740-52.

Wahab A. 2010. Difficulties in treatment and management of epilepsy and challenges in new drug development. Pharmaceuticals (Basel).,3: 2090-110.

Wen W, CY Lin and L Niu. 2017. R/G editing in GluA2R flop modulates the functional difference between GluA1 flip and flop variants in GluA1/2R heteromeric channels. Sci Rep., 7:13654.

Yang YC, GH Wang, AY Chuang and SW Hsueh. 2020. Perampanel reduces paroxysmal depolarizing shift and inhibitory synaptic input in excitatory neurons to inhibit epileptic network oscillations. Br J Pharmacol., 177:5177–94.

Yelshanskaya MV, AK Singh, JM Sampson, C Narangoda, M Kurnikova and AI Sobolevsky. 2016. Structural bases of noncompetitive inhibition of AMPA-subtype ionotropic glutamate receptors by antiepileptic drugs. Neuron.,91:1305-15.

Youn SE, SH Kim, A Koa, SH Lee, YM Lee, HC Kang, et al. 2018. Adverse events during perampanel adjunctive therapy in intractable epilepsy. J Clin Neurol.,14:296-302.

Yuan CL, EY Shi, J Srinivasan, CP Ptak, RE Oswald and LM Nowak. 2018. Modulation of AMPA receptor gating by the anticonvulsant drug, perampanel. ACS Med Chem Lett.,10:237-42.

Zhuo C, R Jiang, G Li, M Shao, C Chen, G Chen, et al. 2017. Efficacy and tolerability of second and third generation anti-epileptic drugs in refractory epilepsy: A network meta-analysis. Sci Rep.,7: 2535.

FORM IV
(See rule 8)

1.	Registration No.	:	ISSN-0555-7631
2.	Place of Publication	:	Old Correspondence Building Panjab University, Chandigarh – 160014 (India)
3.	Periodicity of Publication	:	Annual
4.	**Publisher's & Editors' Name**	:	
	Editor-in-Chief	:	Professor Devinder Mehta
	Nationality	:	Indian
	Editor	:	Professor Jagtar Singh
	Nationality	:	Indian
	Address	:	Research Journal (Science) Room No. 28-29, Old Correspondence Building, Panjab University, Chandigarh- 160014 (India)
5.	Printer's Name	:	Mr. Jatinder Moudgill
	Nationality	:	Indian
	Address	:	Manager Panjab University Printing Press Chandigarh – 160 014.
6.	Name and address of the Individuals who own the newspaper and partners or shareholders holding more than one percent of the total capital.	:	Panjab University, Chandigarh

Professor Devinder Mehta, hereby declare that the particulars given above are true to the best of my knowledge and belief.

Professor Devinder Mehta
Editor-in-Chief

PANJAB UNIVERSITY RESEARCH JOURNAL (SCIENCE)

LIFE MEMBERSHIP FORM

Name	___________________________________
Qualification	___________________________________
Area of Specialization	___________________________________
Present Designation	___________________________________

Address: (Tick the address on which you would like to receive the journal.
Local members would receive the journal by hand)

i. Office	____________________________________
	____________________________________
ii. Residence	____________________________________
	____________________________________
Telephone (O)	____________________________________
(R)	____________________________________
(Mobile)	____________________________________
Fax	____________________________________
Email.	____________________________________

Payment Mode:

(Only local cheques are acceptable. Draft to be drawn in favour of
The Registrar, Panjab University, Chandigarh

If by cheque/Draft:
Cheque/D.DNo. ___________ Date _____________ Amount___________
Name of the Bank: ____

Date ______________
Place: _____________

SIGNATURES

Subscription fee:

	Inland	Foreign
Life Membership:	Rs. 3000/-	US $ 250
Annual Subscription:	Rs. 400/-	US $ 50

Send to:
The Editor-in-Chief
Research Journal (Science)
Old Correspondence Building
Panjab University, Chandigarh-160014(India)

INSTRUCTIONS FOR AUTHORS

Panjab University Research Journal of Science (PURJS) is an international peer-reviewed journal covering wide-range of research activities in all disciples of science.

PURJS provides opportunity to scientists, engineers and medical experts to publish original full research articles, rapid communications, state-of-the-art reviews in all disciplines of the science, engineering and medicine.

JOURNAL POLICY: It is PURJS policy to publish only original and unpublished research work, therefore, PURJS does not wish to receive any papers on research work that has already been reported in parts or contains already published text, data, figures, tables or other illustrations or any copyright materials whatsoever that has been submitted or accepted for publication either in a journal or conference proceedings elsewhere in any form, in print or in electronic media. When submitting a manuscript, authors should make a full statement to the Editors that the research work contained in their manuscript is completely original and unpublished. If redundant or duplicate publication is attempted or occurs authors should expect immediate editorial action to be taken including prompt rejection of the submitted manuscript. Submission of any manuscript that contains redundant or duplicate publication of the same or very similar research work violates the policies of this journal

ETHICAL COMPLIANCE: Research papers reporting animal or clinical studies should, where appropriate, contain a statement that they have been carried out with animal or human ethics committee approval. All scientific studies should be carried out in accordance with the relevant national and local guidelines. Each author(s) warrants that his or her research institution has fully approved the protocol for all scientific studies involving animals or humans and that all experiments of any kinds were conducted in compliance with ethical and humane principles of research after ethics committee approval.

SUBMISSION OF MANUSCRIPT: Authors are requested to read PURJS policy before submitting their manuscript to Editors. Authors are encouraged to submit high quality original research work that has not been published or nor under consideration by other journals or conference proceedings elsewhere. Authors should submit manuscript electronically as a Microsoft Word file to the Editor-in-Chief. Authors are highly encouraged to submit manuscript electronically as a MS Word file (preferred) or a PDF file to save time for the reviewing process.

Authors should submit a list of SIX (6) potential referees accompanied with their complete mailing address, telephone, fax and email address, who may be contacted for reviewing the manuscript though refereeing, is done by anonymous reviewers selected by the Editor-in-Chief or Editor. (The selection of the reviewer is the discretion of Editors –in-chief and reviewers may not necessarily be from the list provided).

MANUSCRIPTS - The manuscripts should be typewritten (double spaced) with ample margins.

Page 1 should contain only title of manuscript, author(s) name(s) and affiliation(s), a short running title (abbreviated from the title) not exceeding 40 characters, name & complete mailing address of the person to whom correspondence should be addressed.

Page 2 should contain an abstract not exceeding 150 words. The abstract should contain no illustration or reference to the figures, tables, or authors. The abstract should be followed by 3-4 key words.

Rest of the content also continue from this page and should be described under Headings, Introduction, Results and Discussions. Acknowledgements should be inserted at the end of the text before References.

SHORT COMMUNICATION: A short communication should be a record of completed short investigation giving details of new methods or findings. It should not exceed 4 to 5 typed pages with an Abstract followed by Key words. Body of the text should not have any separate title, like Abstract, Materials and Methods, Results and Discussion except the Acknowledgements and References.

REFERENCES:
While citing references in the text it should conform to the following style:-
Adherence of *E. coli* to intestinal mucosal surface...pathogenesis (Beachey, 1981). According to Arnoldi (1976), these feathers....

The references at the end of article should be in alphabetical order and presented as follows:-

Ahuja, D.B. 1990. Population dynamics of mustard aphid, Lipaphis erysimi (Kalt.) on Indian mustard Brassica juncea. Indian J. Plant Protection, 18 : 233-235.
Bener, A. and F.C. Erk. 1979. The analysis of whorls on specific fingerstips with respect to sex, bilateral asymmetry and genetic relationship. Ann. Hum. Biol., 6 : 349 - 356.
Buskrik, E.R., K.L. Anderson, and J. Brozek. 1956. Unilateral activity and bone and muscle development in the forearm. Res. Quart., 27 : 127-131.
Jain, S.K. 1986. Orchid Wealth of India. In: Biology, Conservation, and Culture of Orchid
s (Ed.S.P.Vij) pp. 319-22. Affiliated East - West Press (New Delhi).

ILLUSTRATIONS: The illustrations, preferably be in the form of text-figures, should also be submitted electronically. All figures whether photographs or drawing, must be numbered in single series (Fig. 1, 2, 3.etc.). The figures should be arranged and numbered in the order in which they are referred to in the text. The figures or photographs (plates) submitted for publication must not be less than 300 DPI. The ratio of length & width of the full figure plate must necessarily be in proportion to the page size of the journal i.e. 23 cm x 18 cm. Figures must carry magnification bars.
Legends to figures should be typed on a separate sheet of paper to be inserted after References. Abbreviations used for the figures should be given in an alphabetical order after the legends.

TABLES: Tables 1, 2, 3 should be single-spaced on separate page and numbered. Each table must bear a short descriptive heading.

PROOFS: Page proof will be sent to corresponding author.

Manuscripts and Correspondence should be addressed:

Editor-in-Chief
Research Journal of Science
Old Correspondence Building
Panjab University,
Chandigarh. 160 014 (India)
Telephone: 0172-2534376
E.mail : resjoursci@pu.ac.in

210

Published by :
EDITOR-IN-CHIEF
Research Journal (Science)
Panjab University, Chandigarh-160 014
INDIA

www.puchd.ac.in

ISSN-0555-7631